Low-thrust horizontal Lyapunov orbits in the circular restricted Earth-Moon system

A numerical exploration of the planar periodic solution structure within a combined low-thrust three-body dynamical model

by

S.H.F. Martens

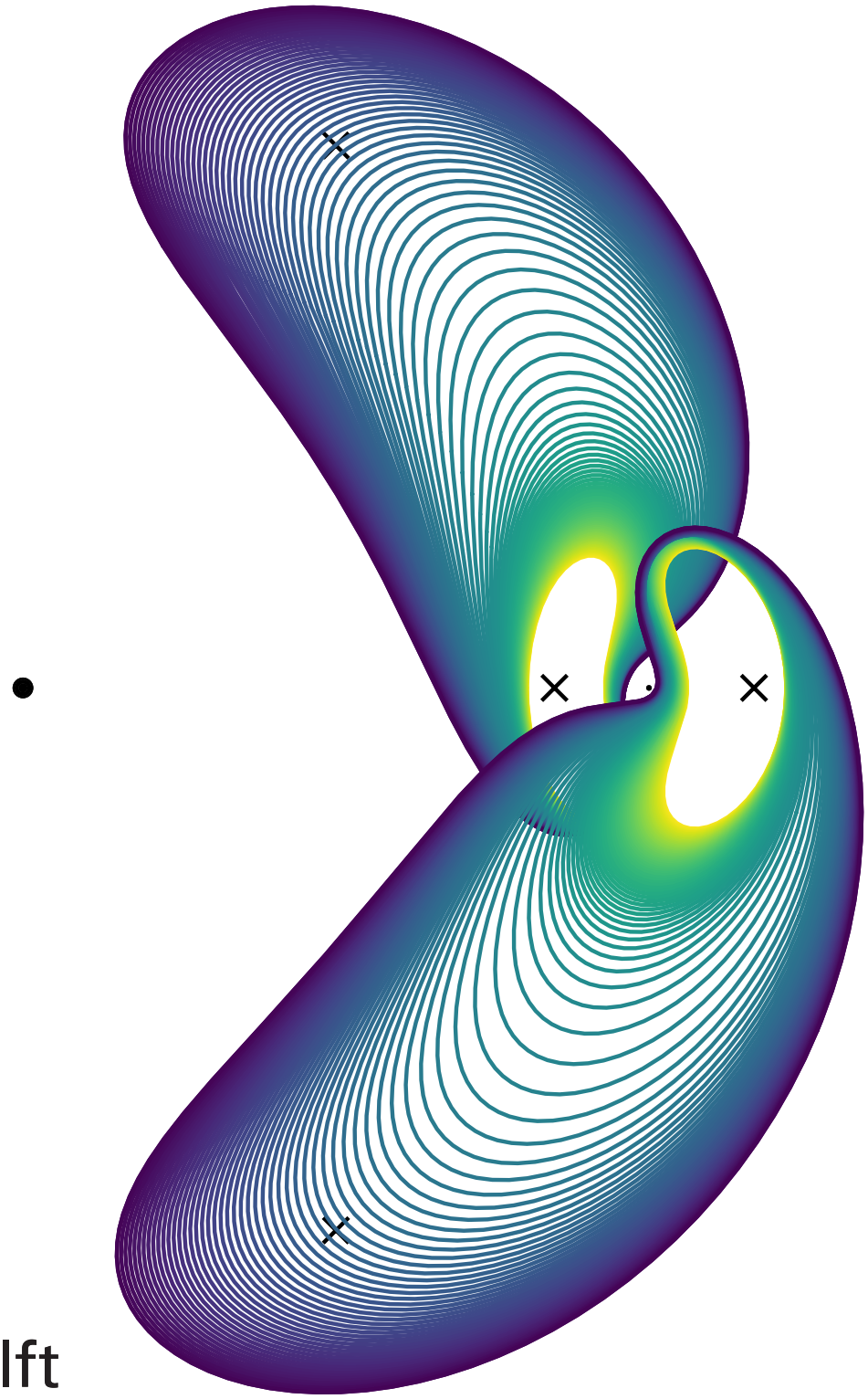

Technische Universiteit Delft

TU Delft

This page is intentionally left blank.

Low-thrust horizontal Lyapunov orbits in the circular restricted Earth-Moon system

A numerical exploration of the planar periodic solution structure within a combined low-thrust three-body dynamical model

by

S.H.F. Martens

to obtain the degree of Master of Science

at the Delft University of Technology,

to be defended publicly on Friday February 14, 2020 at 14:00.

Cover image: Two acceleration-varying families of horizontal Lyapunov orbits the Earth-Moon system.

Student number: 4149610
Project duration: October 1, 2018 – February 14, 2020

Thesis committee:

Prof. dr. ir. P.N.A.M Visser	*Astrodynamics and Space Missions, Professor*	Committee chair
Ir. K.J. Cowan MBA	*Astrodynamics and Space Missions, Lecturer*	Daily supervisor
Dr. B.V.S Jyoti	*Space Systems Engineering, Lecturer*	External examiner

An electronic version of this thesis is available at `http://repository.tudelft.nl/`.

TU Delft

This page is intentionally left blank.

Contents

List of Figures

This page is intentionally left blank.

List of Tables

This page is intentionally left blank.

Nomenclature

The entirety of acronyms and symbols used in the Appendices A-G is presented in the lists below. The nomenclature used in Chapter 1 is presented in the article itself.

List of acronyms

Acronym	Definition	Chapter
BVP	Boundary value problem	B
CR3BP	Circular restricted three-body problem	A
CR3BP-LT	Low-thrust circular restricted three-body problem	A
FT	Floquet targeter	A
H_{lt}-varying	Hamiltonian-varying	A
a_{lt}-varying	Acceleration-varying	A
α-varying	Orientation-varying	A
l.p.o	libration point orbit	A
NR	Newton-Raphson	A
RKF78	Runge-Kutta-Fehlberg 7(8)	A
SPM	State propagation matrix	C
STM	State transition matrix	C
TLT	Two-level targeter	A
TPBVP	Two-point boundary value problem	C
TUDAT	TU Delft Astrodynamics Toolbox	A

List of symbols

Symbol	Description	Equation of first appearance
Latin symbols		
A_x	In-plane amplitude	C.19
$\bar{a}_k$	Acceleration vector at node k	C.29
a_{lt}	Low-thrust acceleration magnitude	C.6
B_i	Polynomial time matrix	B.11
$\boldsymbol{b}$	Last column of the inverse of B_i	B.18
b^i_j	Constants for defect computation	B.12
C	Computable constant for error control	B.16
C_i	Polynomial coefficient matrix	B.11
$D\boldsymbol{F}$	Jacobian	C.3
$\bar{e}_i$	i^{th} column of the Floquet modal matrix	C.11
e	Local truncation error estimate	B.6
$\boldsymbol{F}$	Defect vector	C.1
$\bar{f}_i$	Field vector evaluation	B.10
$G(t)$	Perturbation decomposition matrix	C.12
$\bar{g}_i$	i^{th} column of the perturbation decomposition matrix	C.11
H_{lt}	Low-thrust Hamiltonian	C.38
h	Stepsize in explicit propagation schemes	B.1
I	Collocation error integral	B.19
l	Relaxation parameter	C.8

l_*	Characteristic length	A.2
n	Number of nodes	B.15
$\boldsymbol{p}$	Piecewise polynomial	B.9
$\bar{R}$	Position vector	
r_{ij}	Distance from body i to body j	C.6
T	Orbital period	C.18
t_*	Characteristic time	A.2
S	Eigenvector matrix	C.13
$\bar{V}$	Velocity vector	C.14
w_j^i	Constants for defect computation	B.12
$\boldsymbol{X}$	Design vector	C.1
Z_j	Runge-Kutta local function evaluation	B.3

Greek symbols

α	Low-thrust acceleration orientation	C.6
α_i	Runge-Kutta nodes	B.3
β_{ij}	Runge-Kutta internal weights	B.5
γ_j	External weights of the Runge-Kutta scheme	B.3
Δ	Difference	B.10
∂	Partial derivative	C.3
ϵ	Truncation error	A.3
η_k	Two-level targeter constraint at node k	C.32
θ	Angle from synodic frame x-axis to equilibrium	C.19
ζ	Defect constraint	B.12
ι_j	Floquet targeter coefficients	C.14
κ	Line search attenuation parameter	C.47
μ	Mass ratio parameter	A.1
ξ	Eighth-order derivative estimate	B.16
Π	Mesh of the collocation procedure	B.15
σ	Complex step increment	C.46
τ	Normalized segment time	B.9
ϕ	Orbital phase	C.49
Φ	State transition matrix	C.10

Superscripts

*	Constraint reference value	C.33
$^+$	Incoming quantity	B.10
$^-$	Outgoing quantity	B.10
^{T}	Matrix transpose	B.9

Subscripts

$_*$	characteristic	A.2
$_{\text{abs}}$	Absolute	Table A.3
$_{\text{lt}}$	Low-thrust	A.4
$_{\text{m}}$	Machine	A.3
$_{\text{max}}$	Maximum	Table A.3
$_{\text{min}}$	Minimum	Table A.3
$_{\text{rel}}$	Relative	A.3
$_{\text{tol}}$	Tolerance	B.6

Other notation

$\lvert\ \rvert$	Absolute value	B.6
$\lvert\lvert\ \rvert\rvert$	Euclidian norm	C.50
$\langle\ ,\ \rangle$	Inner product	C.49

1

Journal article

LOW-THRUST HORIZONTAL LYAPUNOV ORBITS IN THE EARTH-MOON RESTRICTED THREE-BODY PROBLEM

Sjors Martens* **and Kevin J. Cowan†**

Preliminary design of low-thrust trajectories in the circular restricted three-body problem (CR3BP) frequently relies upon ballistic dynamical structures and optimization algorithms. A fundamental understanding of how these dynamical structures change due to presence of a low-thrust force may lead to trajectories that cannot be obtained otherwise. This paper investigates the effect of a constant low-thrust acceleration on the horizontal Lyapunov (H-L) families in the CR3BP. Families of low-thrust periodic solutions are constructed in vicinity of L_1 and L_2 using numerical continuation methods. By either varying the Hamiltonian, acceleration magnitude, or acceleration orientation along the solution family, the effect of a low-thrust acceleration on H-L orbits is characterized. Investigating the geometry, bifurcations and hyperbolic unwinding behaviour of these families provides insight into the low-thrust periodic solution structure of the Earth-Moon system. The introduction of a constant low-thrust acceleration distorts the geometry of ballistic H-L orbits into 'ear-shaped' periodic solutions. The bifurcations of the low-thrust periodic solution families imply the existence of low-thrust halo, low-thrust axial, and low-thrust planar double-period families. Finally, low-thrust periodic solutions are identified that possess a higher rate of hyperbolic unwinding behaviour than the ballistic L_1 and L_2 H-L families.

INTRODUCTION

Libration point orbits have been key to the realization of numerous space missions. An increased understanding of the solar wind[1] and early Universe[2] are just some of the valuable scientific insights which have been obtained by utilization of these non-Keplerian geometries. The significance of these libration point orbits will only increase in the near future as NASA aims to deploy the successor of the International Space Station in the vicinity of the Earth-Moon L_2 point.[3] Recent advancements in low-thrust propulsion technology have sparked the interest of the scientific community into investigation of nonballistic libration point orbits. Research efforts have led to the discovery of novel mission concepts like continuous observation of lunar poles via deformed Halo orbits.[4] These so-called 'pole-sitter' orbits illustrate the possibility to discover new mission concepts by combining low-thrust technology and non-Keplerian geometries.

Initial designs of space missions involving libration point orbits are commonly obtained from low-fidelity multi-body models like the CR3BP. Extensive research towards the dynamical structures of this model has revealed a rich set of periodic solutions in the vicinity of the Lagrangian points.[5] Furthermore, invariant manifolds emanating from these equilibria have opened up new opportunities for low-energy space travel.[6] The common approach for preliminary design of missions involving nonballistic libration point orbits is to specify a ballistic trajectory in the CR3BP and

*Graduate Student, Aerospace Engineering, Delft University of Technology, Kluverweg 1, 2629 HS Delft, The Netherlands
†Lecturer, Aerospace Engineering, Delft University of Technology, Kluverweg 1, 2629 HS Delft, The Netherlands

find a control history via trajectory optimization techniques. The mass- or time-optimal trajectories resulting from this design philosophy may satisfy mission-specific constraints but fail to provide an understanding how the fundamental flow in the CR3BP changes under influence of low-thrust propulsion. Such an understanding can be obtained by studying the flow of a multi-body model whose dynamics allow the formulation of a low-thrust force.

Investigation of dynamical structures in low-thrust multi-body models is an emerging field of research, especially in the context of solar sailing. Studies towards the deformation of Halo orbits in the Sun-Earth radial solar sail CR3BP[7] and the existence of libration point orbits in the Earth-Moon solar sail CR3BP[8] are just some of the examples that have revealed new geometries. Multi-body models which incorporate a low-thrust force via electric propulsion have received far less attention despite the widespread use of electric propulsion in today's space missions. Recent studies that investigate multi-body models that incorporate a low-thrust force in the form of electric propulsion show that key dynamical structures like equilibria, periodic motion and invariant manifolds exist.[9–11] However, the phase space of this model remains largely unexplored. This paper increases the understanding of dynamical structures in these low-thrust multi-body models by investigating the planar periodic solution structure in the Earth-Moon system.

This article starts with a formulation of the dynamics of the low-thrust multi-body model. Next, the characteristics of the planar equilibrium solutions within this system are discussed. Three different types of periodic solution families are presented in the vicinity L_1 and L_2 at a variety of thrust parameters. Studying the geometry and linear stability of these periodic solution families aids to an increased understanding of the low-thrust multi-body dynamics.

DYNAMICAL MODEL

Before periodic motion in a low-thrust multi-body model can be investigated, it is necessary to formulate the dynamics of such a system. The dynamical model adopted in this investigation is known as the low-thrust circular restricted three-body problem (CR3BP-LT).[11] A graphical representation of this dynamical model is presented in Figure 1.

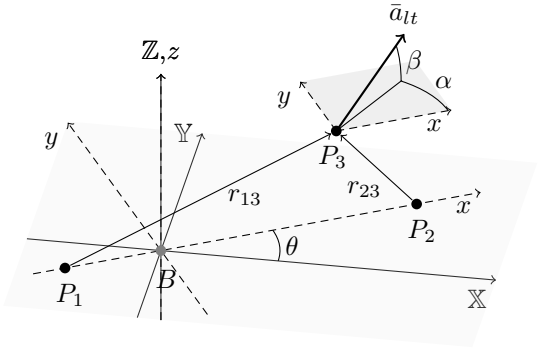

Figure 1. The configuration of the CR3BP-LT. The light grey shaded area denotes the plane of motion of the two primaries and coincides with the xy and $\mathbb{XY}$-plane. The orientation of the dark grey shaded area is parallel to the xy plane.

The CR3BP-LT is a combination of the CR3BP and a low-thrust acceleration $\bar{a}_{lt}$ provided by an electric propulsion system. The dynamics of the CR3BP are explained first followed by a discussion on these ballistic dynamics are affected by the introduction of a low-thrust acceleration.

The circular restricted three-body problem

The CR3BP concerns the motion of three bodies resulting from their mutual gravitational attraction. The two celestial bodies, from now on referred to as the primary (P_1) and secondary (P_2), rotate around their mutual barycenter B in a coplanar and circular fashion. The artificial body (P_3) is unrestricted in its movement and has a negligible mass so its gravitational pull can be ignored. It is a common strategy to study the three-body problem in a rotating reference frame (x, y, z) where the x-axis coincides with the primary and secondary. This so-called synodic reference frame removes the time dependency of the dynamics which simplifies its analysis.[12] It is worth noting that the introduction of a rotating reference frame gives rise to a centrifugal force and Coriolis force. Hence, the motion in the synodic frame is the result of the gravitational pull and the two aforementioned forces.

Another standard simplification is the nondimensionalization of the CR3BP which is achieved by assuming three quantities to unity. These quantities are the total mass in the system, the mean motion of the synodic reference frame, and the distance between the primary and secondary.[12] Nondimensionalization of the system allows full parametrization of the CR3BP via the mass ratio parameter $\mu = \frac{M_2}{M_1+M2}$. This research assumes $\mu \approx 0.0121506^*$ to simulate motion in the Earth-Moon version of the CR3BP. Since the positions of P_1 and P_2 are fixed in the synodic reference frame at ($-\mu$,0,0) and ($1-\mu$,0,0) respectively, the distances of P_3 with respect to the spacecraft can be calculated according to Eq. (1).

$$r_{13} = \sqrt{(x+\mu)^2 + y^2 + z^2}, \quad , r_{23} = \sqrt{(x-1+\mu)^2 + y^2 + z^2} \tag{1}$$

The motion of P_3 is defined through three second order nonlinear differential equations,[12] which are shown below in Eq. (2).

$$\begin{aligned}
\ddot{x} &= 2\dot{y} + x - \frac{1-\mu}{r_{13}^3}(x+\mu) - \frac{\mu}{r_{23}^3}(x-1+\mu) = 2\dot{y} + \Omega_x \\
\ddot{y} &= -2\dot{x} + y - \frac{1-\mu}{r_{13}^3}y - \frac{\mu}{r_{23}^3}y = -2\dot{x} + \Omega_y \\
\ddot{z} &= -\frac{1-\mu}{r_{13}^3}z - \frac{\mu}{r_{23}^3}z = \Omega_z
\end{aligned} \tag{2}$$

Ω represents the pseudo-potential of the system, which is formed by the sum of the centrifugal force and gravitational potential of $P1$ and P_2 as shown in Eq. (3).[12]

$$\Omega = \frac{1}{2}(x^2 + y^2) + \frac{1-\mu}{r_{13}} + \frac{\mu}{r_{23}} \tag{3}$$

The aforementioned time independence of the CR3BP implies the existence of a first integral in the dynamical model according to the theory Hamiltonian mechanics.[14] The conserved quantity is known as the Jacobi integral and is an important parameter for characterizing motion in the dynamical model. The Hamiltonian of the CR3BP is proportional to the Jacobi integral and is computed via Eq. (4).[11]

$$C = -2H_{nat} = 2\Omega - V^2 \tag{4}$$

*The exact value of μ is obtained directly from the publicly available TUDAT software package[13]

The low-thrust circular restricted three-body problem

The CR3BP-LT arises from the CR3BP by introduction of a dimensionless low-thrust acceleration ($\bar{a}_{lt}$) in the form of Eq. (5). The magnitude of this acceleration is represented as a_{lt} whereas its orientation is captured via a pointing vector $\hat{u}$. The acceleration pointing vector is defined via an in-plane angle (α) and out-of-plane angle (β) as shown in Figure 1.

$$\bar{a}_{lt} = \frac{f}{m}\hat{u}, \quad \hat{u} = \begin{bmatrix} \hat{u}_x \\ \hat{u}_y \\ \hat{u}_z \end{bmatrix} = \begin{bmatrix} \cos(\beta)\cos(\alpha) \\ \cos(\beta)\sin(\alpha) \\ \sin(\beta) \end{bmatrix}, \quad f = \frac{Ft_*^2}{l_* M_{3,0}} \tag{5}$$

In Eq. (5), f denotes the dimensionless thrust magnitude and $m = \frac{M_3}{M_{3,0}}$ represents the dimensionless spacecraft mass with $M_{3,0}$ defined as the initial spacecraft mass in kilograms. F symbolizes the dimensional thrust force in kilonewtons whereas l_* and t_* are referred to as the characteristic length and characteristic time respectively.[11] The characteristic length represents the distance between P_1 and P_2 in kilometers whereas the characteristic time represents the inverted mean motion of the system in seconds. This research adopts $l_* = 384400$ from which the characteristic time can be computed with Kepler's third law. Furthermore, this research assumes $f \in$[0.0,0.1] which is in line with today's low-thrust propulsion technology as shown in Appendix A.

The low-thrust dynamics of P_3 can be defined via four second order differential equations as shown in Eq. (6).[11] The first three different equations define the dynamics of P_3 whereas the fourth differential equation governs the dimensionless mass flow of the system. I_{sp} denotes the specific impulse in seconds and $g_0 = 9.80665 m/s^{-2}$ represents the gravitational acceleration at sea level.

$$\begin{aligned} \ddot{x} &= 2\dot{y} + \Omega_x + a_{lt}\hat{u}_x \\ \ddot{y} &= -2\dot{x} + \Omega_y + a_{lt}\hat{u}_y \\ \ddot{z} &= \Omega_z + a_{lt}\hat{u}_z \\ \dot{m} &= \frac{f_{lt} l_*}{I_{sp} g_0 t_*} \end{aligned} \tag{6}$$

Contrary to the CR3BP, the Hamiltonian of the CR3BP-LT, shown in Eq. (7), is not a conserved quantity since it varies with a change in the acceleration vector.

$$H_{lt} = H_{nat} - \langle \bar{r}, \bar{a}_{lt} \rangle, \quad \frac{\partial H_{lt}}{\partial \tau} = \langle \bar{r}, \dot{\bar{a}}_{lt} \rangle \tag{7}$$

The time-varying nature of the spacecraft mass gives rise to a non-autonomous dynamical system. Dynamical structures in time-variant systems are challenging to characterize due to the absence of a first integral. This research employs three simplifications to transform the CR3BP-LT into an autonomous dynamical system. First of all, the acceleration orientation vector $\hat{u}$ is fixed in the rotating fame. Secondly the thrust magnitude f is held constant. Finally it is assumed that $\dot{m} = 0$. These assumptions ensure a constant low-thrust acceleration vector in the rotating frame which give rise to an integral of motion in the form of H_{lt}. The remainder of this work considers a_{lt} and H_{lt} as constant quantities since a varying spacecraft mass has a negligible influence in the Earth-Moon system, as suggested in previous literature.[11] The validity of this assumption is discussed in Appendix B. This section is concluded with the notice that the dynamics of P_3 are constrained to planar motion.

LOW-THRUST EQUILIBRIUM SOLUTIONS

The CR3BP posseses five locations where a spacecraft experiences a net zero acceleration. Analysis of the dynamics around these Lagrangian points reveals the existence of dynamical structures like libration point orbits and/or invariant manifolds.[15] Hence, the characterization of the CR3BP-LT phase space starts with an investigation towards the low-thrust equilibria. This section presents the methodology to locate these equilibria and subsequently characterize the dynamics around them. Furthermore, it discusses the effect of a constant low-thrust acceleration on the equilibria locations and the surrounding dynamics.

Equilibria localization and characterization methodology

Previous research has shown that a low-thrust acceleration can considerably shift the locations of the equilibria.[9] The low-thrust equilibrium solutions are located via a multivariate relaxed Newton-Rapshon root-finding method[16] which finds a position in the rotating frame that satisfies the conditions listed in Eq. 8.

$$\begin{aligned} \ddot{x} = &\quad 2\dot{y} + \Omega_x + a_{lt}\cos(\alpha) = 0 \\ \ddot{y} = &-2\dot{x} + \Omega_y + a_{lt}\sin(\alpha) = 0 \end{aligned} \tag{8}$$

This multivariate root-finding algorithm is employed to compute two types of structures. The first structure comprises a set of low-thrust equilibrium solutions with an identical acceleration magnitude but different acceleration orientations ($\alpha \in [0, 2\pi]$). This structure is referred to as an α-varying zero acceleration contour (ZAC). The second structure, referred to as the a_{lt}-varying ZAC, consists of low-thrust equilibrium solutions that have an identical acceleration orientation but different acceleration magnitudes. ($a_{lt} \in [0, 0.1]$). These two contours isolate the effect of a_{lt} and α so their influence on the equilibrium solutions can be investigated separately.

The multivariate root-finding procedure is initialized with seed solutions that differ per type of contour. Two types of seed solutions are employed for the α-varying ZAC. The first type of seed solutions are low-thrust equilibria located on the x-axis of the CR3BP-LT. These seed solutions are straightforwardly calculated via a univariate Newton-Raphson procedure. The second type of seed solutions are noncollinear low-thrust equilbria with $\alpha = 0$ obtained via analytical Eqs. (9-11).[11]

$$\begin{aligned} \bar{r}_{L_4} &= \begin{bmatrix} -\mu + r_{13}\cos(\kappa) & r_{13}\sin(\kappa) & 0 \end{bmatrix}^T \\ \bar{r}_{L_5} &= \begin{bmatrix} -\mu + r_{13}\cos(\kappa) & -r_{13}\sin(\kappa) & 0 \end{bmatrix}^T \end{aligned} \tag{9}$$

$$\begin{aligned} r_{13} &= \left(\frac{1-\mu}{1-\mu+a_{lt}}\right)^{\frac{1}{3}} \\ r_{23} &= \left(1 - \frac{a_{lt}}{\mu}\right)^{-\frac{1}{3}} \end{aligned} \tag{10}$$

$$\kappa = \left(\frac{1 + r_{13}^2 + r_{23}^2}{2r_{13}}\right) \tag{11}$$

In the Eq.s above, κ represents the angle between the positive x-axis and the r_{13} vector. The seed solutions of a_{lt}-varying ZAC's are the Lagrangian points of the CR3BP.

The dynamics in vicinity of the equilibrium can be characterized via analysis of the CR3BP-LT linearized dynamics at the known equilibrium location. An expression of these linearized dynamics is shown in Eq. 12 in the form of a first-order Taylor series expansion

$$\frac{d}{dt}\begin{bmatrix} x \\ y \\ z \\ \dot{x} \\ \dot{y} \\ \dot{z} \\ f \\ \alpha \\ \beta \\ m \end{bmatrix} = \begin{bmatrix} 0 & 0 & 0 & 1 & 0 & 0 & 0 & 0 & 0 & 0 \\ 0 & 0 & 0 & 0 & 1 & 0 & 0 & 0 & 0 & 0 \\ 0 & 0 & 0 & 0 & 0 & 1 & 0 & 0 & 0 & 0 \\ \Omega_{xx} & \Omega_{xy} & \Omega_{xz} & 0 & 2 & 0 & \frac{\mathrm{C}_\alpha \mathrm{C}_\beta}{m} & -\frac{f\mathrm{S}_\alpha \mathrm{C}_\beta}{m} & -\frac{f\mathrm{C}_\alpha \mathrm{S}_\beta}{m} & -\frac{f\mathrm{C}_\alpha \mathrm{C}_\beta}{m^2} \\ \Omega_{yx} & \Omega_{yy} & \Omega_{yz} & -2 & 0 & 0 & \frac{\mathrm{S}_\alpha \mathrm{C}_\beta}{m} & \frac{f\mathrm{C}_\alpha \mathrm{C}_\beta}{m} & -\frac{f\mathrm{S}_\alpha \mathrm{S}_\beta}{m} & -\frac{f\mathrm{S}_\alpha \mathrm{C}_\beta}{m^2} \\ \Omega_{zx} & \Omega_{zy} & \Omega_{zz} & 0 & 0 & 0 & \frac{\mathrm{S}_\beta}{m} & 0 & f\frac{\mathrm{C}_\beta}{m} & -\frac{f\mathrm{S}_\beta}{m^2} \\ 0 & 0 & 0 & 0 & 0 & 0 & 0 & 0 & 0 & 0 \\ 0 & 0 & 0 & 0 & 0 & 0 & 0 & 0 & 0 & 0 \\ 0 & 0 & 0 & 0 & 0 & 0 & 0 & 0 & 0 & 0 \\ 0 & 0 & 0 & 0 & 0 & 0 & \frac{l_*}{I_{sp} g_0 t_*} & 0 & 0 & 0 \end{bmatrix}_{eq} \begin{bmatrix} x \\ y \\ z \\ \dot{x} \\ \dot{y} \\ \dot{z} \\ f \\ \alpha \\ \beta \\ m \end{bmatrix} = \bar{A}|_{eq} \bar{X}(t) \quad (12)$$

$\bar{X}$ denotes the state vector and A represents its Jacobian, commonly referred to as the state propagation matrix (SPM). C_k and S_k refer to sine and cose operator respectively where subscript k denotes the argument of these operators. The dynamics are defined by the upper 6×6 block of the SPM since this research assumes a constant thrust magnitude, thrust orientation, and spacecraft mass.[11] The six eigenvalues of the upper block, which occur as three pairs with opposite signs, reveal the stability components in the neighbourhood of the equilibrium point. A pair of real eigenvalues with opposite sign indicates a so-called saddle (S) mode which suggests the existence of hyperbolic invariant manifolds. Secondly, a conjugate pair of purely imaginary eigenvalues gives rise to a center (C) mode which indicates the existence of periodic solutions. Finally, a conjugate pair of complex eigenvalues denotes a mixed (M) mode which suggests spiral behaviour. The combination of two (three) stability modes defines the planar (spatial) linear stability of the equilibrium point.

Low-thrust acceleration effect on the equilibrium solutions

The root-finding method presented in the previous section allows the construction of the α-varying ZAC's and a_{lt}-varying ZAC's. An α-varying ZAC that arises from L_i is denoted with E_i and these structures are displayed in Figure 2 for three distinct acceleration magnitudes. In an analogous way, a_{lt}-varying ZAC's are indicated via E_i^α where α indicates the acceleration orientation. These structures are displayed in Figure 3. Both images show the planar linear stability at each location in the rotating frame, also referred to as a stability portrait.[11]

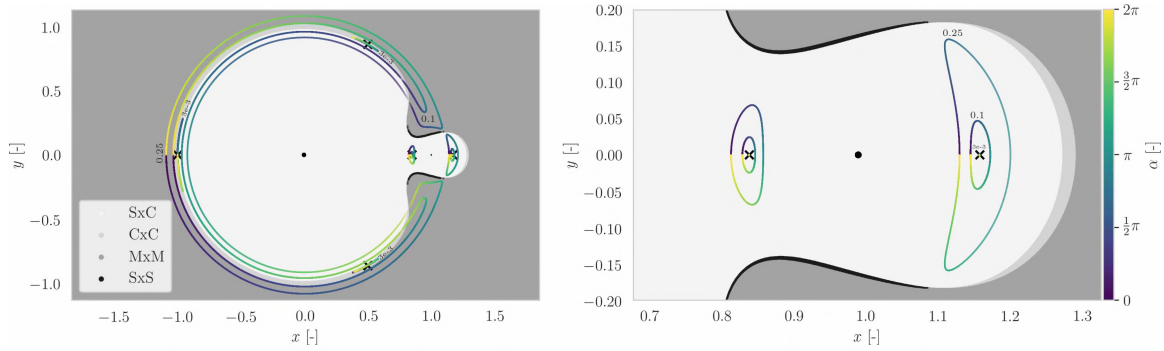

Figure 2. The α-varying ZAC contours at three distinct acceleration magnitudes $a_{lt} = [0.003, 0.1, 0.25]$ over the complete range of thrust orientations $\alpha \in [0, 2\pi]$. The natural Lagrangian points are plotted as black crosses whereas the two primaries are symbolized as filled black circles. a_{lt} = 0.025 lies outside the feasible range of acceleration magnitudes but is added to illustrate the impact of a high a_{lt} value.

The stability portrait reveals the presence of four stability regions in the planar CR3BP-LT. The neighbourhood around the $P_{1,2}$ characterized by $S \times C$ stability, indicating that planar periodic solutions and invariant manifolds are present. The $S \times C$ stability realm is surrounded by two small bands characterized by $C \times C$ and $S \times S$ stability. $C \times C$ stability suggests that only bounded motion exists within this field whereas only asymptotic motion can be found within the $S \times S$ realm. An $M \times M$ field encloses these three stability regions.

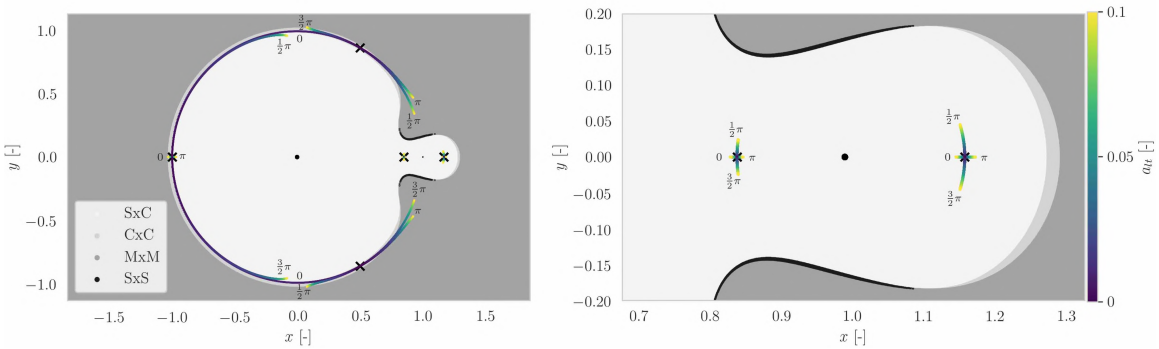

Figure 3. The a_{lt}-varying ZAC contours at four acceleration orientations $\alpha = [0, \frac{1}{2}\pi, \pi, \frac{3}{2}\pi]$ over the complete range of acceleration magnitude $a_{lt} \in [0, 0.1]$. The equilibria are plotted as black crosses whereas $P_{1,2}$ are shown as black circles.

Figure 2 reveals that a low-thrust acceleration vector can drastically change the location of the equilibrium solution as well as its stability mode. The largest displacements are observed at E_3 followed by the equilateral contours E_4 and E_5. This effect is so powerful that these three contours merge into a single C-shaped contour ($a_{lt} = 1.05 \cdot 10^{-2}$). Smaller displacements are observed at E_2 and the low-thrust acceleration has an even more limited effect at E_1. The varying effect of the low-thrust acceleration is directly attributed to the magnitude of the pseudo-potential at the specific location in the rotating frame. Furthermore, E_1 and E_2 remain in the $S \times C$ stability realm. Figure 3 underpins these conclusions and highlights how the displacement effect is proportional to the acceleration magnitude.

The stability portrait provides qualitative insight into the stability but fails to show how the magnitude of these stability components spatially evolve in the CR3BP-LT. Figure 4 provides such an insight for the saddle component.

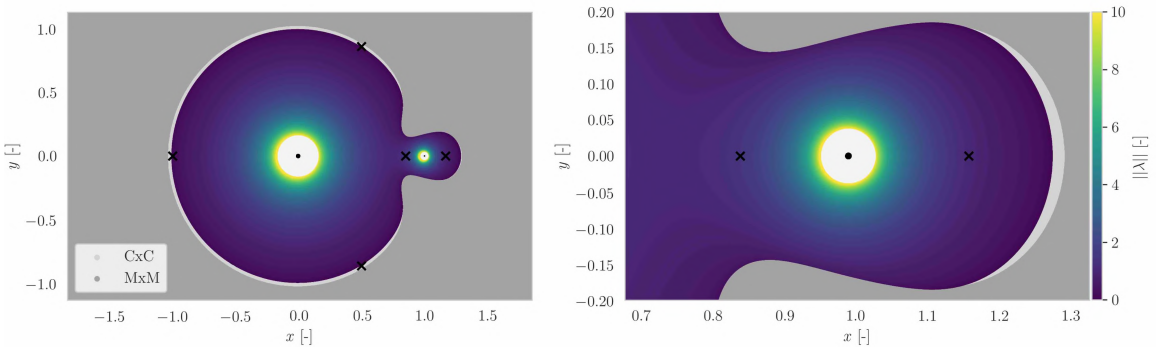

Figure 4. The magnitude of the eigenvalue related to the saddle component of the dynamics as a function of position in the rotating frame. The contour is computed for $||\lambda|| \leq 10$ for visualization reasons.

The saddle component of the dynamics is represented by the positive real eigenvalue of the eigensystem of Eq. 12. This saddle mode is associated with hyperbolic nature of the dynamics which give rise to the invariant manifolds.[15] A larger positive real eigenvalue is linked to a larger unwinding rate of the hyperbolic invariant manifolds,[17] which might provide opportunities for quicker low-energy transfer opportunities. Figure 4 shows that the hyperbolic unwinding behaviour increases when the equilibrium moves towards $P_{1,2}$ while it decreases towards zero in the neighbourhood of the $C \times C$ stability realm. These findings are confirmed by Figure 5 which shows the positive real eigenvalue magnitude as a function of the acceleration orientation at two distinct acceleration magnitudes.

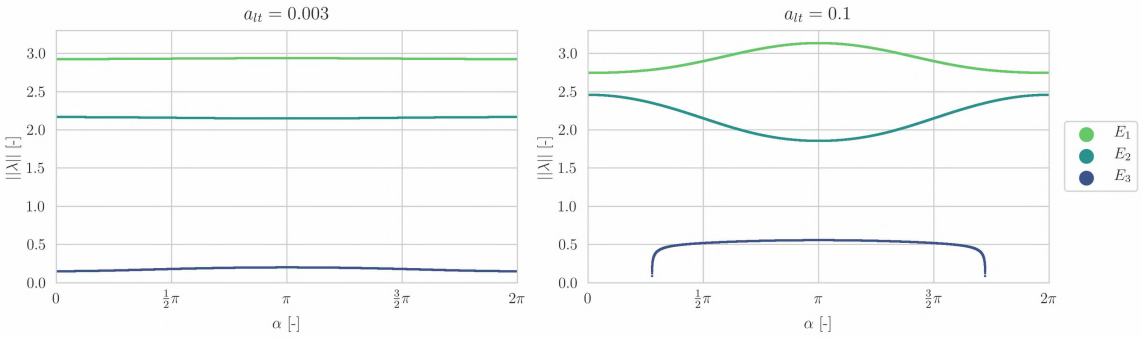

Figure 5. The magnitude of the eigenvalue related to the saddle component of the dynamics as a function of the thrust parameters.

The maximum hyperbolic unwinding behaviour of E_1 (E_2) occurs at at $\alpha = \pi$ rad (0 rad) since this specific orientation results in an equilibrium location closest to P_2. In an equivalent way, the maximum hyperbolic unwinding behaviour for E_3 the occurs at $\alpha = \pi$ rad since this corresponds to the equilibrium closest to P_1. At higher acceleration magnitudes, unwinding behaviour is not guaranteed at E_3 since parts of this contour are located in the $C \times C$ and $M \times M$ stability realm.

The final effect of a low-thrust acceleration on the equilibrium solutions concerns the change in Hamiltonian value. Figure 6 shows the integral of motion as a function of the acceleration orientation at two distinct acceleration magnitudes.

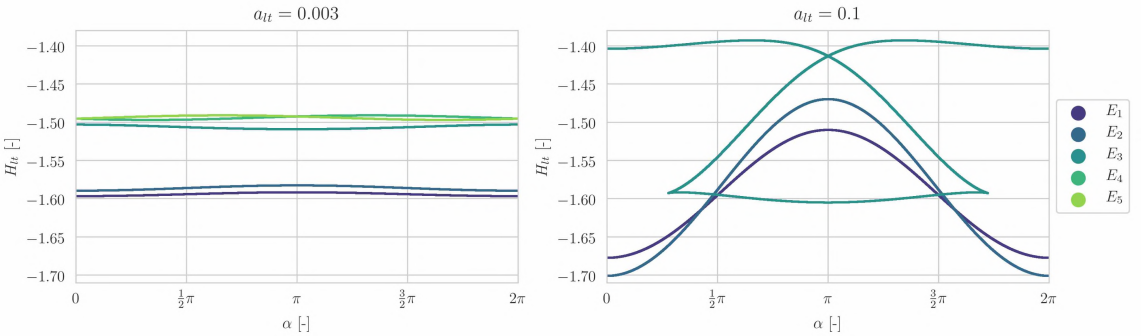

Figure 6. The evolution of the Hamiltonian over the equilibria contours for two distinct thrust magnitudes a_{lt} =[0.003,0.1].

These energy curves show the minimum Hamiltonian value that a periodic solution, which emanates from that specific equilibrium, can posses. Hence this plot allows to predict the existence of a_{lt}-varying α-varying families. Unsurprisingly, the change in Hamiltonian is proportional to the acceleration magnitude. Another interesting observation is the varying number of equilibrium solutions which can be attributed to the merge of E_3,E_4 and E_5.[11]

The low-thrust acceleration affects the equilibrium solutions in several ways. It can significantly alter the the position of an equilibrium and thereby qualitatively change its stability. Furthermore, the unwinding behaviour can be increased which may open up opportunities for faster transfers via invariant manifolds. The section is concluded with the notion that Figures (2-6) emphasize the existence of a symmetry in the CR3BP-LT. If an equilibrium exists at (x,y,a_{lt},α), another equilibrium exists at (x,$-y$,a_{lt},$-\alpha$).[11]

LOW-THRUST PLANAR PERIODIC SOLUTIONS

Periodic motion in the CR3BP has been the subject of extensive research which has resulted in a comprehensive understanding of the CR3BP periodic solution structure.[5] The CR3BP-LT periodic solution structure on the other hand has been barely investigated. Previous research shows that low-thrust periodic orbits (LTPO) exist[11] but the periodic solution structure of the CR3BP-LT is essentially unknown. This section provides an overview of the periodic solutions emanating from E_1 and E_2 in the CR3BP-LT, thereby investigating the effect of a low-thrust acceleration on planar periodic motion in the Earth-Moon system. An overview of low-thrust periodic solution structure is effectively achieved by analyzing families of periodic solutions. These families are a set of periodic solutions where points belonging to different family members constitute to a continuous curve in phase space.[18] Individual solutions of these families are uniquely defined by the three parameters H_{lt}, a_{lt}, and α. Along a periodic solution family, two of the three aforementioned variables remain constant while the other parameter, also referred to as the bifurcation parameter,[19] is different for each family member. This gives rise to three types of periodic solution families * which are analyzed in the remainder of this Section. First of all, the Hamiltonian-varying (H_{lt}-varying) families are investigated to get an initial understanding of the periodic solutions in the vicinity of E_1 and E_2. This is followed by analysis of acceleration-varying (a_{lt}-varying) families and orientation-varying (α-varying) families to explicitly characterize the effect of a low-thrust acceleration on the periodic motion. Before these families are investigated, the underlying methodology for the construction and characterization of these families is presented.

Construction and characterization of low-thrust periodic solution families

The three types of solution families are generated by employing numerical continuation procedures. The selected numerical continuation procedure depends on the family type (i.e. the varying parameter). H_{lt}-varying families are constructed via a pseudo-arclength numerical continuation[19] algorithm which shown in Eq. 13. The pseudo-arclength numerical continuation procedure ensures a consistent positional increment between two subsequent family members. These family members are indicated with $\mathbf{X}^n$ and $\mathbf{X}^{n+1}$ where n refers to the family member number (i.e. $\mathbf{X}^1$ is the first constructed member of the family). The consistent spacing is achieved by scaling the pseudo-arclength ρ relative to the positional increment between the initial states of two family members. The position coordinates of the initial state of a periodic solution are indicated with x_0^n and y_0^n. This

*In this research, a family type refers to the parameter that varies along the family rather than the type of periodic motion that is observed.

research adheres to positional increment of 10^{-4} between the initial state of two subsequent family members to achieve a near-continuous family of solutions.

$$\mathbf{X}^{n+2} = \mathbf{X}^{n+1} + \rho\left(\mathbf{X}^{n+1} - \mathbf{X}^{n}\right), \quad \rho = \frac{10^{-4}}{\sqrt{(x_0^{n+1} - x_0^n)^2 + (y_0^{n+1} - y_0^n)^2}} \tag{13}$$

The pseudo-arc length continuation procedure is initialized by two periodic seed solutions. These seed solutions are obtained via a two-step process. The first step concerns the construction of approximate periodic seed solutions via a Floquet controller.[20,21] During the second step, the approximate seed solutions are transformed into actual periodic seed solutions via a dual-stage multiple shooting procedure called the two-level targeter.[22,23] Each guess forwarded by the continuation procedure is solved using a 12$^{\text{th}}$ order Legendre-Gauss-Lobatto collocation method[24] augmented with Boor's method of mesh refinement for error control purposes.[25] The a_{lt}-varying and α-varying families are constructed viaa natural parameter continuation algorithm.[19] Natural parameter continuation requires a start-up solution which is directly obtained from the earlier computed H_{lt}-varying families. The guess for a new family member is created by slightly incrementing the bifurcation parameter, which is either a_{lt} or α depending on the family type. The aforementioned collocation method corrects the guess to a truly periodic solution.

Characterization of a periodic solution family is achieved in two distinct ways. First of all, a graphical projection is provided to show the spatial evolution of the family with respect to the bifurcation parameter. On the other hand, the stability of each family member is mapped with respect to the bifurcation parameter to detect bifurcations within the dynamical system. Bifurcations are qualitative changes in the dynamics of the system which help to identify topological equivalent regions in the phase space of the CR3BP-LT.[26] According to Floquet theory, the stability of a periodic solution can be investigated via the eigensystem of the monodromy matrix (M).[27] The monodromy matrix maps a state on the periodic solution with orbital period T at time t_i to a new state at time $t_i + T$. Hence, the monodromy matrix is a special case of the state transition matrix and can be obtained via numerical integration of the upper 6×6 block of A and the equations shown in Eq. 14.

$$M = \Phi(T, 0), \quad \dot{\Phi}(t_{i+1}, t_i) = A_{t_i}\Phi(t_{i+1}, t_i), \quad \Phi(t_i, t_i) = I \tag{14}$$

M adheres to a symplectic map structure since the CR3BP-LT is a Hamiltonian system.[6] This implies that if λ is an eigenvalue of M, λ^{-1} is also an eigenvalue of M. Hence, the six eigenvalues of M, also known as characteristic multipliers, occur in three reciprocal pairs. The values of these characteristic multipliers reveal the linear stability of the periodic solution. A pair of eigenvalues with modulus one indicates periodicity. On the other hand, A pair of eigenvalues with magnitude larger (smaller) than one indicates instability. More specifically, a real pair of eigenvalues with a magnitude greater and smaller than one indicates the existence of hyperbolic invariant manifolds.[6] The stability of an eigenvalue pair can be represented in the form of a stability index (ν_i) as shown in Eq. 15. $\nu_i > 1$ indicates instability and the magnitude of the stability index of related to the invariant manifolds (ν_1) is directly to the rate of hyperbolic unwinding behaviour.[17]

$$\nu_i = \frac{1}{2}\left(||\lambda_i|| + \frac{1}{||\lambda_i||}\right) \tag{15}$$

A change in the number of unstable eigenvalue pairs, referred to as the linear order of instability,[28] indicates the presence of a bifurcation. By providing a graphical projection, bifurcation overview, and the saddle stability index evolution of periodic solution families, the periodic solution structure of the CR3BP-LT can be characterized.

Hamiltonian-varying libration point orbit families

Analyzing H_{lt}-varying families emanating from E_1 and E_2 at different acceleration magnitudes and acceleration orientations provides an initial understanding of the CR3BP-LT periodic solution structure. The ballistic families emanating from L_1 and L_2 are presented first for comparison purposes. Low-thrust periodic solution families emanating from E_1 and E_2 are subsequently analyzed at three acceleration magnitudes ($a_{lt} = [0.01, 0.05, 0.1]$). At each acceleration magnitude, low-thrust periodic solution families are analyzed at six acceleration orientations ($\alpha = [0, \frac{1}{3}\pi, \frac{2}{3}\pi, \pi, \frac{4}{3}\pi, \frac{5}{3}\pi]$).

L_1 and L_2 ballistic families It is well known that the in-plane center modes of L_1 and L_2 give rise to the ballistic H-L families.[6] A graphical projection of these families can be found in Figure 7.

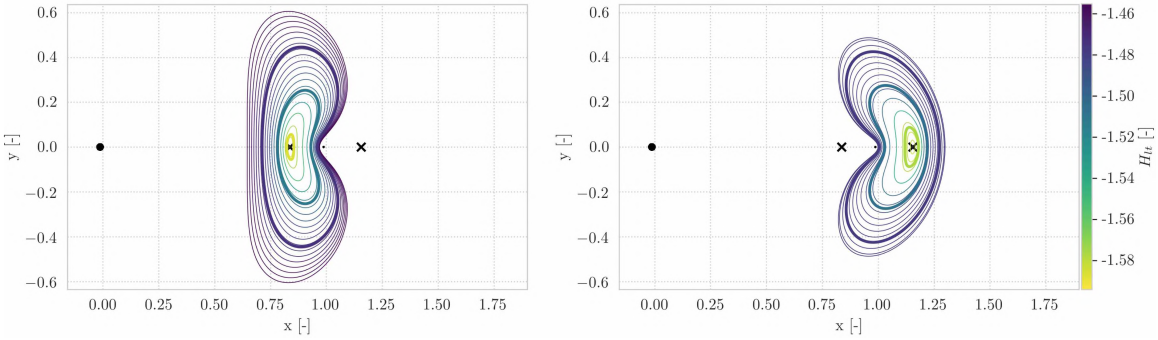

Figure 7. Graphical projection of the L_1 and L_2 H-L families. The ballistic L_1 family is shown on the left thewhereras L_2 H-L family is shown on right. P_1 and P_2 are denoted as black dots whereas the natural Lagrangian points are symbolized with black crosses. The color of the periodic solution indicates the Hamiltonian according to the colorbar depicted on the right. Each 50th member of the family is plotted.

The graphical projections show that the L_1 and L_2 ballistic H-L families differ in shape. The members of the L_2 family are heavily curved towards the Moon which can be attributed to the fact that the L_2 family is located to the right side of the Earth and Moon, resulting in a one-sided gravitational potential from the primaries. A bifurcation analysis of the H-L families at L_1 and L_2 is presented in Figure 8.

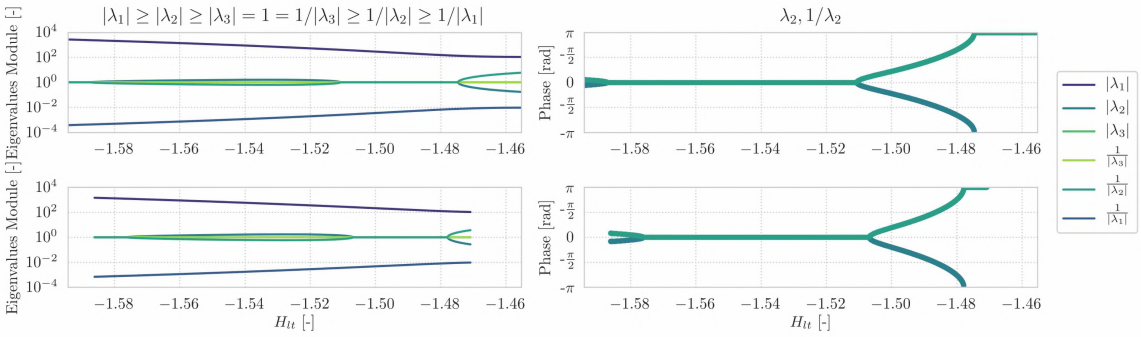

Figure 8. Bifurcation analysis of the ballistic L_1 and L_2 H-L families. The left plots display the characteristic multiplier moduli whereas the right plots present the phase of the eigenvalue related to the out-of-plane center subspace. The top plots relate to the L_1 H-L family whereas the bottom plots represent the L_2 H-L family.

The left plots of Figure 8 reveal the bifurcations by displaying the moduli of the three reciprocal eigenvalue pairs. The λ_1, $1/\lambda_1$ pair relates to the saddle component of the motion which give rise to the invariant manifolds. The λ_2, $1/\lambda_2$ pair denotes the out-of-plane center subspace whereas the λ_3, $1/\lambda_3$ pair relates to the in-plane center subspace from which the H-L family emanates. The left plots of Figure 8 show that three bifurcations occur in both families. The right plots of Figure 8 reveal that the first bifurcation of both families occurs when the λ_2, $1/\lambda_2$ eigenvalue pair leaves the unit circle at the positive x-axis. This behaviour is referred to as a tangent bifurcation and indicates the existence of a new family of solutions; the Halo family.[28] The second change in linear order of instability in both the L_1 and L_2 ballistic H-L families is also a tangent bifurcation.[28] This tangent bifurcation generates the axial family that connect the H-L families with the vertical Lyapunov (V-L) families at the respective Lagrangian point.[5] The third bifurcation in the L_1 and L_2 ballistic H-L families occurs when the λ_2, $1/\lambda_2$ leaves the unit circle at the negative x-axis. Such a phenomenon is interpreted as a period-doubling bifurcation and is related to periodic solutions with twice the period of the family they emanate from.[27] The discussion of the L_1 and L_2 ballistic H-L families is concluded with the analysis of the stability index of the unstable eigenvalue pair (ν_1) and the H_{lt} evolution as shown in Figure 9.

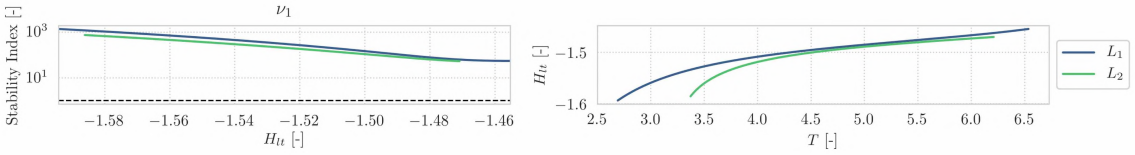

Figure 9. The evolution of ν_1 over the L_1 and L_2 ballistic H-L families is shown on the left. The evolution of H_{lt} as a function of T for both ballistic H-L families.

It can be observed that stability index of the eigenvalue pair related to the saddle subspace attains a maximum for periodic solutions situated closest the equilibrium point and decreases monotonically while the orbits grow in amplitude. Finally, The Hamiltonian and orbital period are minimal near the equilibria and increase monotonically over the families.

$a_{lt} = 0.01$ *families* The effect of a small low-thrust acceleration on the orbit geometry of LTPO's emanating from E_1 can be observed from Figure 10. At this acceleration magnitude, the characteristic H-L shape is maintained whenever the acceleration is parallel with the x-axis. However, distortions with respect to the ballistic H-L geometry occur when the acceleration orientation is not parallel with the x-axis. A lobe appears in the orbit geometry in either positive or negative y-direction, depending upon the acceleration orientation. Furthermore, families with acceleration orientation α and $-\alpha$ seem symmetric w.r.t to the x-axis which is expected because of the earlier mentioned symmetry.

The bifurcation diagrams of these H_{lt}-varying families are shown in Figure 11. It can be concluded that for $a_{lt} = 0.01$, the qualitative nature of the bifurcation diagrams do not change with respect to the bifurcation diagram of the ballistic L_1 family. This implies the existence of spatial low-thrust halo and axial families. Furthermore, the symmetry between families with acceleration orientation α and $-\alpha$ can be observed since the bifurcations of these families happen at identical Hamiltonians. Figure 12 shows the saddle subspace stability index of each family which reveals that the maximum unwinding behaviour can be found near the artificial equilibria. Furthermore, the Hamiltonian and orbital period increase monotonically over each family.

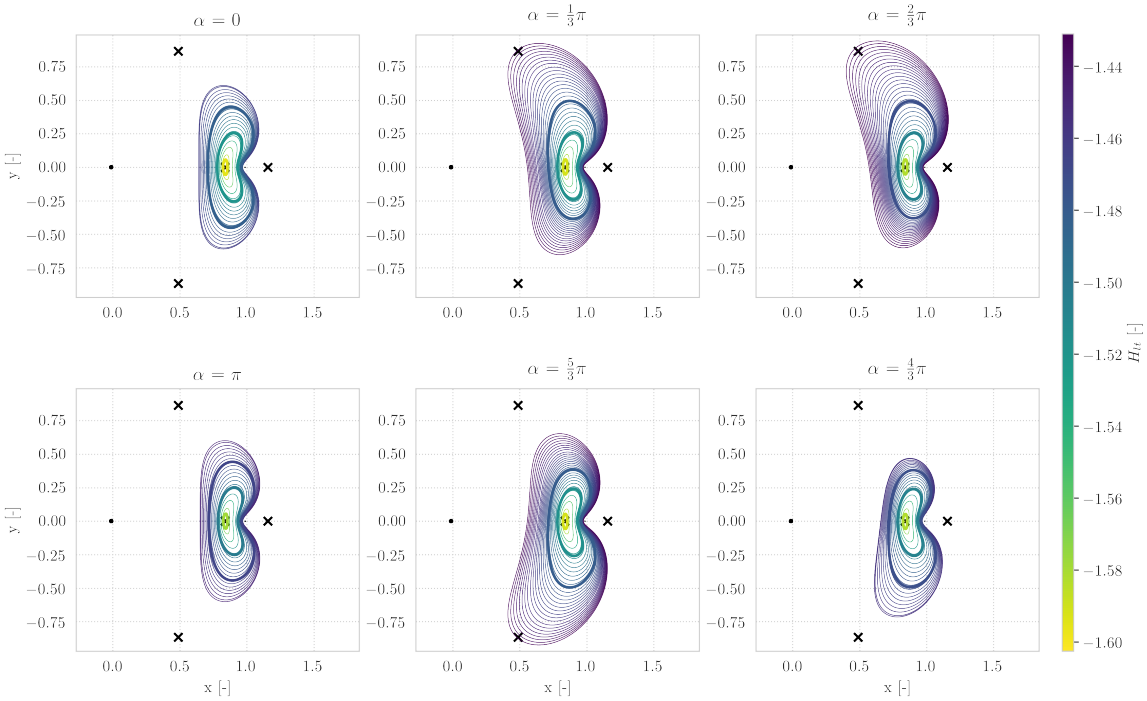

Figure 10. Six H_{lt}-varying families at $a_{lt} = 0.01$ for different α values in vicinity of E_1. The color of an LTPO corresponds to its Hamiltonian value according to the colorbar located on the right side. The family with $\alpha = \frac{4}{3}\pi$ is terminated earlier with respect to the $\alpha = \frac{2}{3}\pi$ family due to instabilities in the collocation algorithm.

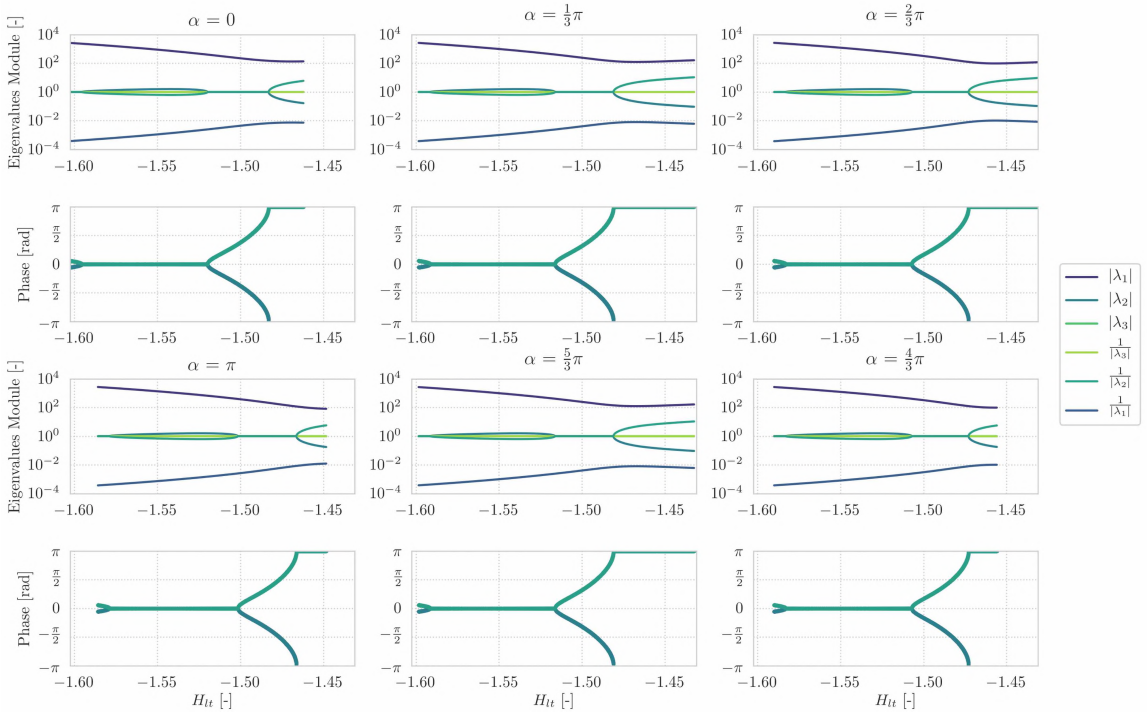

Figure 11. Bifurcation diagram of the six H_{lt}-varying families at $a_{lt} = 0.01$ for different α values in vicinity of E_1. The family with $\alpha = \frac{4}{3}\pi$ is terminated earlier with respect to $\alpha = \frac{2}{3}\pi$ due to instabilities in the collocation algorithm.

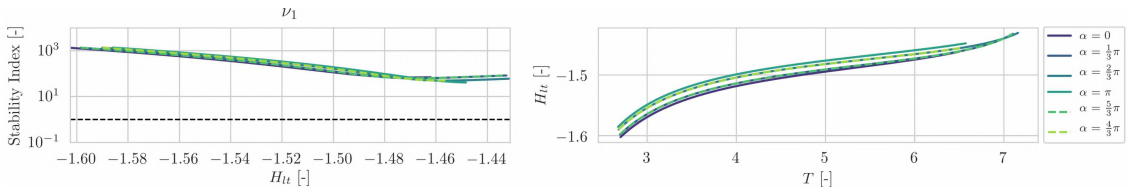

Figure 12. The evolution of ν_1 over the E_1, $a_{lt} = 0.01$, H_{lt}-varying families is shown on the left. The evolution of H_{lt} as a function of T is shown on the right.

Six H_{lt}-varying families with identical thrust parameters are constructed in vicinity of the E_2. The graphical projection of these families can be found in Figure 13, their bifurcation diagrams are shown in Figure 14 whereas the evolution of their saddle stability index and Hamiltonian is presented in Figure 15. Inspection of Figures 13-15 reveal that a small acceleration magnitude has an identical effect on families emanating from E_2 as on families that emanate from E_1. The geometry of the libration point orbit families is distorted by a lobe whose direction depends upon the orientation of the acceleration. The bifurcation diagram remains qualitatively identical implying that halo and axial libration point orbits exist in vicinity of E_2. The maximum unwinding behaviour is found near the artifical equilibria and the Hamiltonian and orbital period increase monotonically along these families.

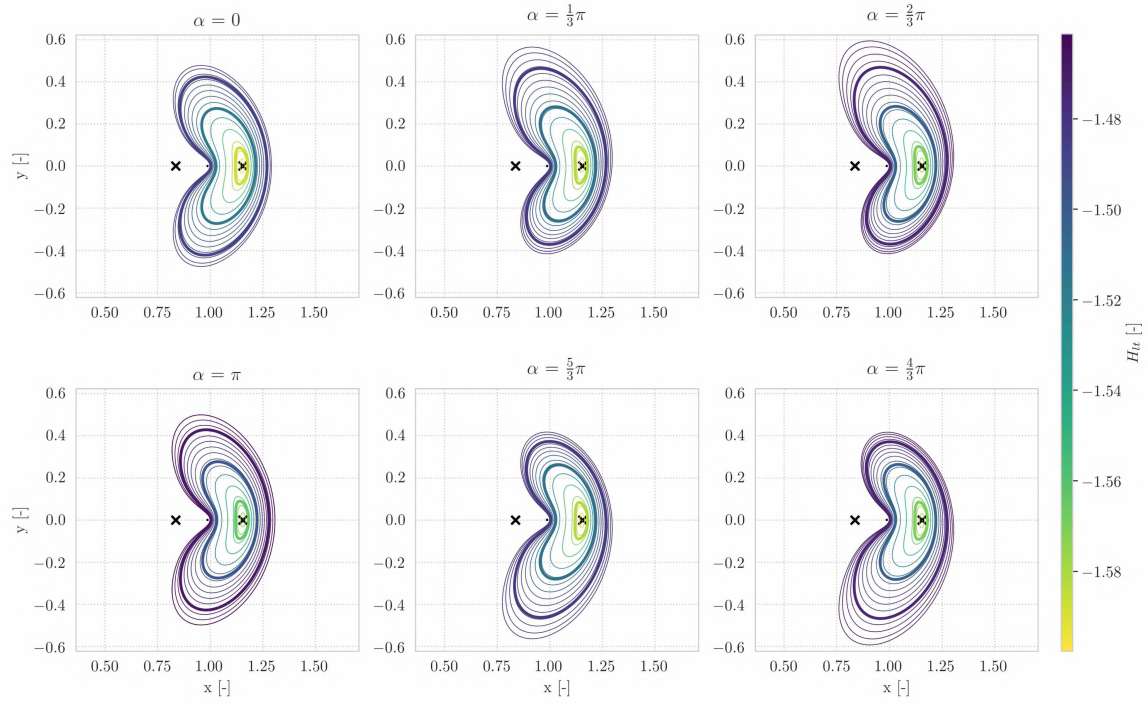

Figure 13. Six H_{lt}-varying families at $a_{lt} = 0.01$ for different α values in vicinity of E_2. The color of an LTPO corresponds to its Hamiltonian value according to the colorbar located on the right side.

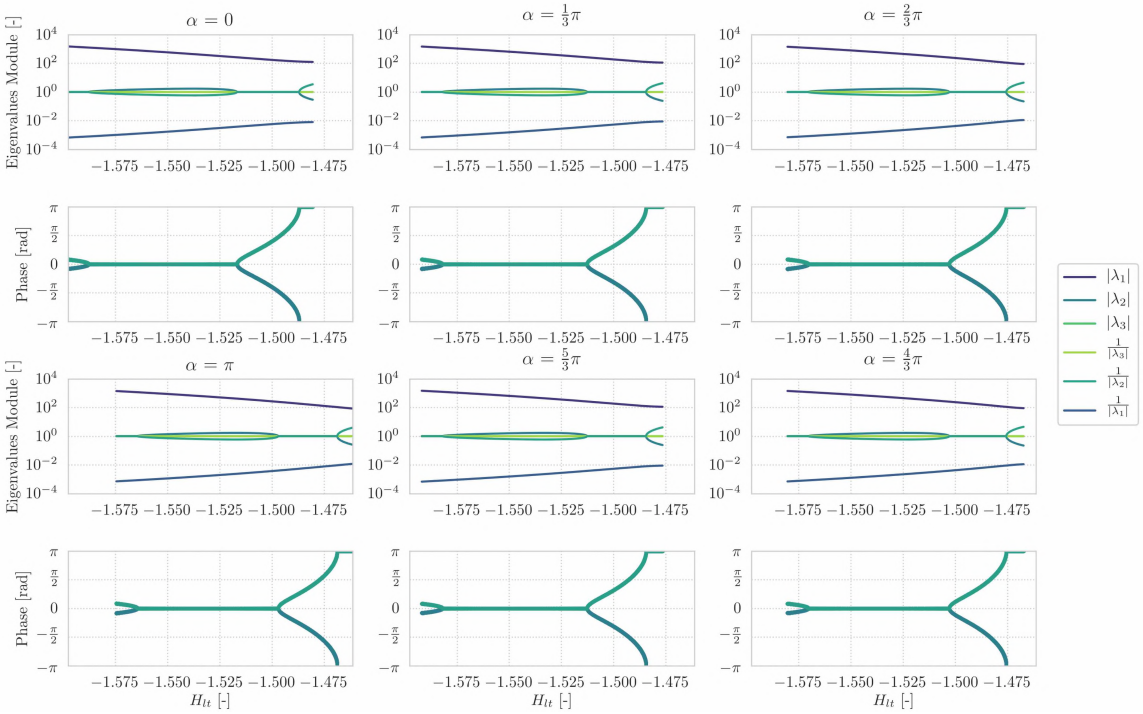

Figure 14. Bifurcation diagram of the six H_{lt}-varying families at $a_{lt} = 0.01$ for different α values in vicinity of E_2.

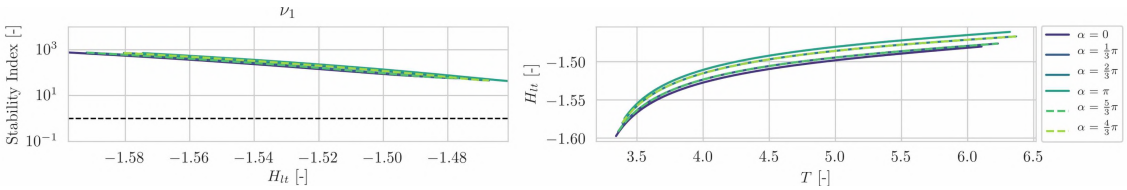

Figure 15. The evolution of ν_1 over the E_2, $a_{lt} = 0.01$, H_{lt}-varying families is shown on the left. The evolution of H_{lt} as a function of T is shown on the right.

$a_{lt} = 0.05$ *families* The effect of a medium low-thrust acceleration on the orbit geometry of periodic motion in vicinity of E_1 can be observed from Figure 16. While the acceleration is parallel with the x-axis, no clear differences can be observed with respect to the natural L_1 family in Figure 7. This cannot be said from the H_{lt}-varying families with an acceleration orientation that is not aligned with the x-axis. The geometry of these families is distorted in such a way that they take on an 'ear-like' shape. The lobe of the $\alpha = \frac{5}{3}\pi$ family even reaches twice as far in y-direction relative to the ballistic L_1 family. The bifurcation diagrams of these six H_{lt}-varying families, shown in Figure 17, reveal two interesting phenomena. First of all, the qualitative nature of the bifurcation behaviour remains identical with respect to the ballistic families for the $\alpha = [0, \frac{1}{3}\pi, \pi, \frac{5}{3}\pi]$ families. This suggests the existence of low-thrust axial and halo orbits. The existence of these spatial solutions is also suggested for the $\alpha = [\frac{2}{3}\pi, \frac{4}{3}\pi]$ families from the two tangent bifurcations but a period-doubling bifurcation is not observed here. Analysis of the saddle stability index, displayed in Figure 18, reveals that the maximum hyperbolic unwinding behaviour remains maximum near the equilibria but does not monotonically decrease for the $\alpha = [\frac{1}{3}\pi, \frac{5}{3}\pi]$ families. This figure also demonstrates that all six H_{lt}-varying families with $a_{lt} = 0.05$ in vicinity of E_1 increase monotonically in Hamiltonian and orbital period.

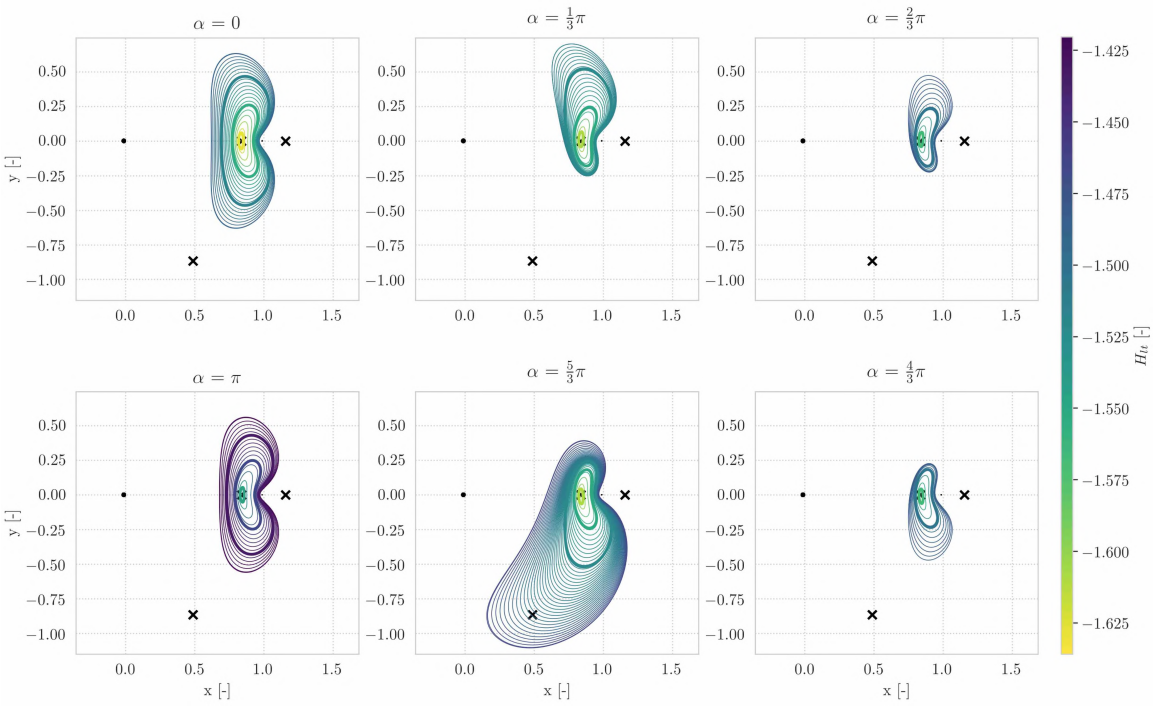

Figure 16. Six H_{lt}-varying families at $a_{lt} = 0.05$ for different α values in vicinity of E_1. The color of an LTPO corresponds to its Hamiltonian value according to the colorbar located on the right side. The family with $\alpha = \frac{1}{3}\pi$ is terminated earlier with respect to the $\alpha = \frac{5}{3}\pi$ family due to instabilities in the collocation algorithm.

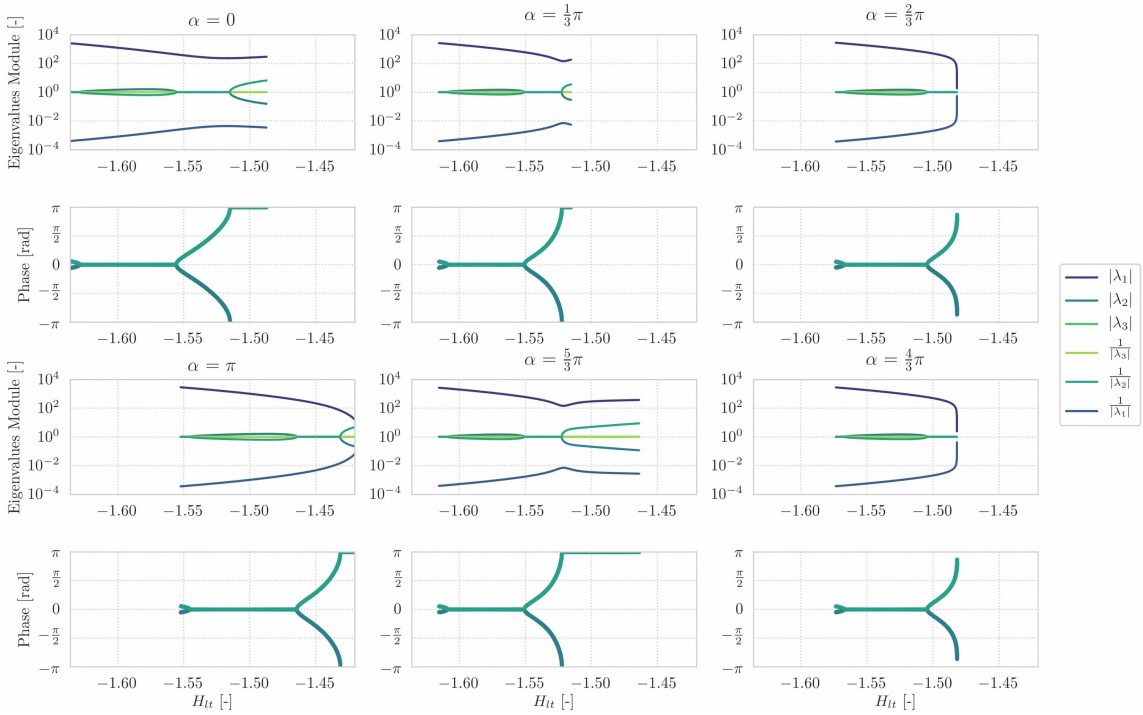

Figure 17. Bifurcation diagram of the six H_{lt}-varying families at $a_{lt} = 0.05$ for different α values in vicinity of E_2. The family with $\alpha = \frac{1}{3}\pi$ is terminated earlier with respect to $\alpha = \frac{5}{3}\pi$ due to instabilities in the collocation algorithm.

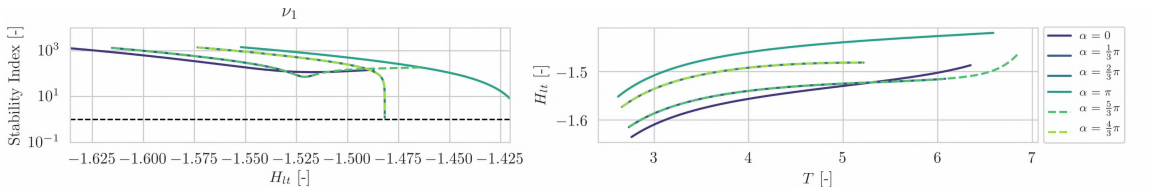

Figure 18. The evolution of ν_1 over the E_1, $a_{lt} = 0.05$, H_{lt}-varying families is shown on the left. The evolution of H_{lt} as a function of T is shown on the right.

Six H_{lt}-varying families with identical thrust parameters are constructed in vicinity of the E_2 contour. The graphical projection of these families can be found in Figure 19, corresponding bifurcation diagrams are shown in Figure 20 whereas evolution of the saddle stability index and Hamiltonian over these families is shown in Figure 21. Inspection of Figures 19-21 reveals that a medium low-thrust acceleration has a similar effect on H_{lt} families in vicinity of the E_2 contour as on periodic solutions emanating from the E_1 contour. As long as the acceleration vector remains parallel with the x-axis. The geometry of the low-thrust periodic solutions remains similar to the L_2 ballistic family. Off-axis acceleration orientations give rise to 'ear-shaped' families that curve around the Moon and even the ballistic L_1 Lagrangian point.

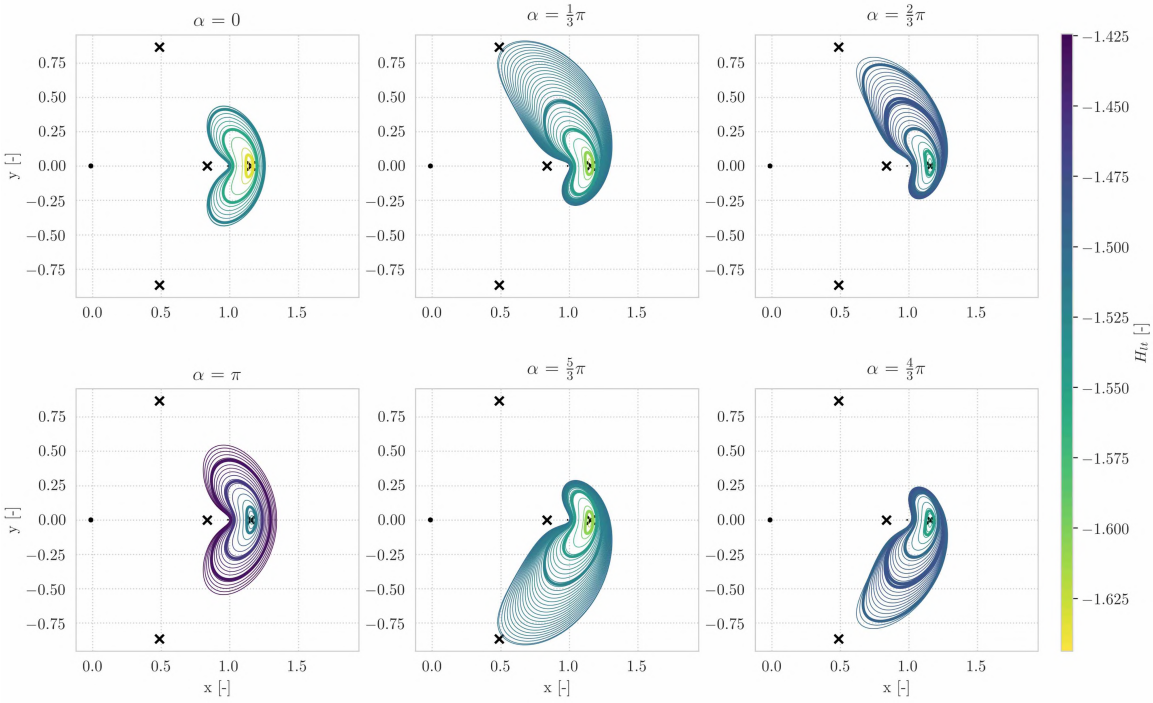

Figure 19. Six H_{lt}-varying families at $a_{lt} = 0.05$ for different α values in vicinity of E_2. The color of an LTPO corresponds to its Hamiltonian value according to the colorbar located on the right side.

The qualitative bifurcation behaviour of the $\alpha = [0, \frac{1}{3}\pi, \pi, \frac{5}{3}\pi]$ families remains identical to the ballistic L_2 family since two tangent bifurcations and one period-doubling bifurcation are observed in Figure 20. These bifurcations suggest the existence of low-thrust axial, halo, and double-period families for these acceleration orientations. The bifurcation behaviour of the $\alpha = [\frac{2}{3}\pi, \frac{4}{3}\pi]$ H_{lt}-varying families however is qualitatively different from the ballistic L_2 H-L family. Inspection of

their bifurcations diagrams reveal that these two families possess two tangent fold bifurcation after which the magnitude of all six characteristic multipliers goes to unity at the extremum of the family Hamiltonian. This indicates a cyclic-fold bifurcation and although it changes the linear order of instability it does not imply a new family of periodic solutions.[27] Besides these tangent and cyclic-fold bifurcations, three period-doubling bifurcations occurs towards the end of the families. The totality of these bifurcations imply that low-thrust halo, axial, and multiple double-period families bifurcate from the investigated families.

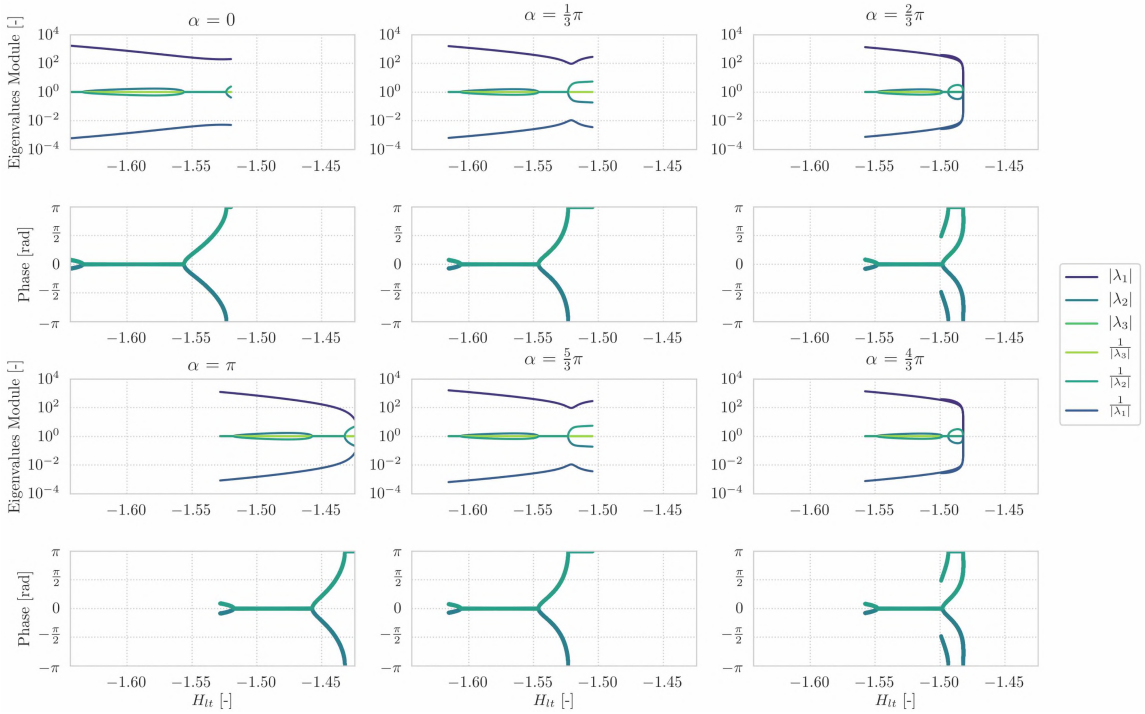

Figure 20. Bifurcation diagram of the six H_{lt}-varying families at $a_{lt} = 0.05$ for different α values in vicinity of E_2.

Figure 21 displays the evolution of the saddle stability index and Hamiltonian over the six E_2, $a_{lt} = 0.05$, H_{lt}-varying families. Inspection of this figure reveals that the hyperbolic unwinding behaviour remains maximum near the equilibria but does not monotonically decrease over the $\alpha = [\frac{1}{3}\pi, \frac{5}{3}\pi]$ families and even increases during the second half of the $\alpha = [\frac{2}{3}\pi, \frac{4}{3}\pi]$ families. The orbital period increases monotonically for all six families which can also be said for the Hamiltonian of the α $[\frac{1}{3}\pi, \frac{2}{3}\pi, \pi, \frac{4}{3}\pi, \frac{5}{3}\pi]$ families. An extremum in Hamiltonian ($H_{lt,max} = -1.482005956$) is encountered at the 1265$^{\text{th}}$ member of the α $[\frac{2}{3}\pi, \frac{4}{3}\pi]$ families.

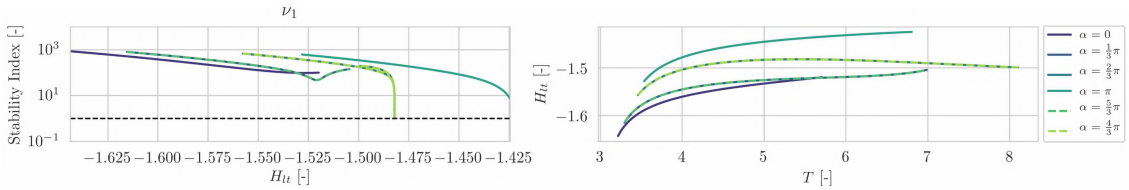

Figure 21. The evolution of ν_1 over the E_2, $a_{lt} = 0.05$, H_{lt}-varying families is shown on the left. The evolution of H_{lt} as a function of T is shown on the right.

$a_{lt} = 0.1$ *families* The effect of a large low-thrust acceleration on the orbit geometry of periodic solutions emanating from E_1 can be observed from Figure 22. Whereas the $\alpha = 0$ family has a similar geometry as the ballistic L_1 H-L family, this cannot be said for the $\alpha = \pi$ family. The orbits belonging to this family curve around the Moon in a similar fashion as the ballistic L_2 family. The geometry of the $\alpha = 0[\frac{1}{3}\pi, \frac{2}{3}\pi, \frac{4}{3}\pi, \frac{5}{3}\pi]$ family take on an 'ear-like' shape.

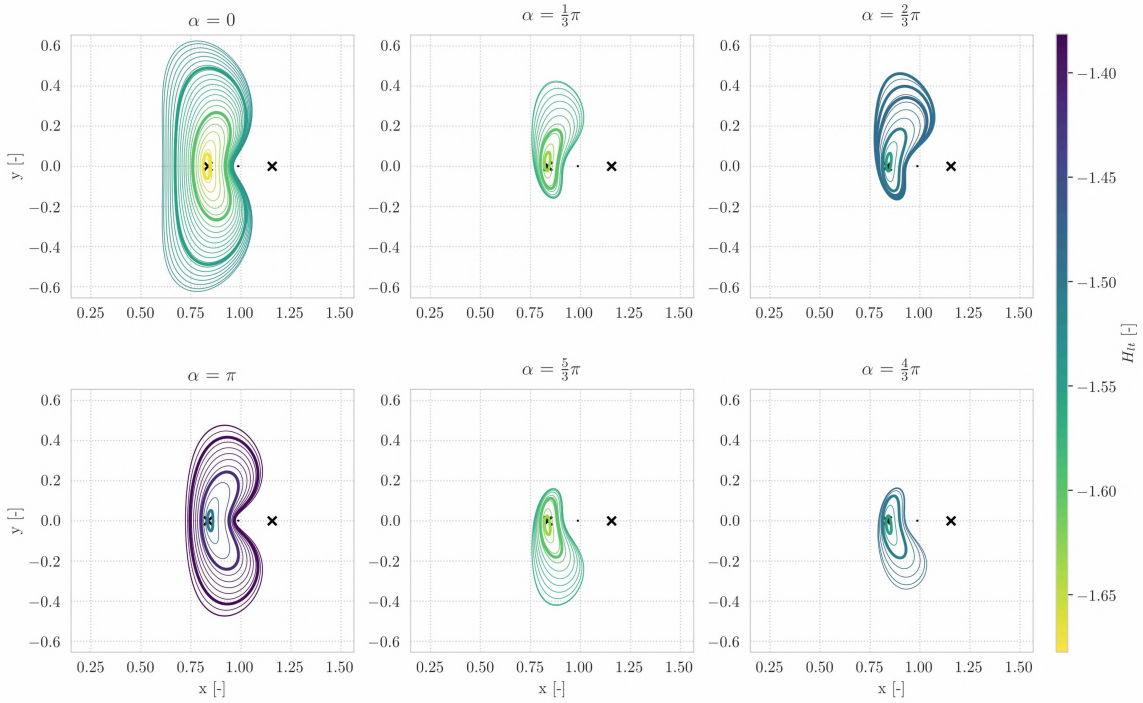

Figure 22. Six H_{lt}-varying families at $a_{lt} = 0.1$ for different α values in vicinity of E_1. The color of an LTPO corresponds to its Hamiltonian value according to the colorbar located on the right side. The family with $\alpha = \frac{4}{3}\pi$ is terminated earlier with respect to the $\alpha = \frac{2}{3}\pi$ family due to instabilities in the collocation algorithm.

The bifurcation diagrams of these families are presented in Figure 24. The bifurcation behaviour of the $\alpha = [0, \pi]$ families remains qualitatively identical to the ballistic L_1 H-L family. This cannot be said for families with off-axis acceleration orientations. The $\alpha = [\frac{1}{3}\pi, \frac{4}{3}\pi, \frac{5}{3}\pi]$ H_{lt}-varying families possess two tangent bifurcations before termination of the numerical continuation procedure. The $\alpha = \frac{2}{3}\pi$ H_{lt}-varying family however possesses two tangent bifurcations. one cyclic-fold bifurcation and three period-doubling bifurcation. The two tangent bifurcations that are present in each family implies the existence of low-thrust halo and axial orbits whereas the three period-doubling bifurcations suggest the existence multiple double-period families at $\alpha = \frac{2}{3}\pi$.

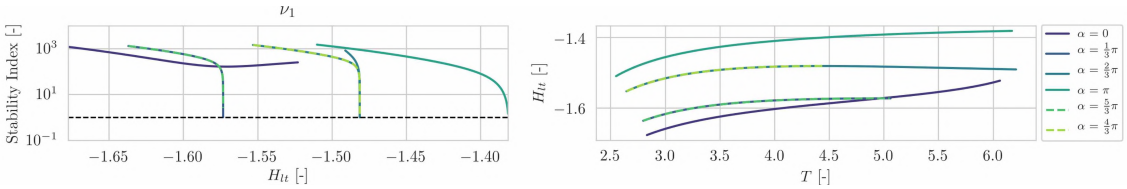

Figure 23. The evolution of ν_1 over the E_1, $a_{lt} = 0.10$, H_{lt}-varying families is shown on the left. The evolution of H_{lt} as a function of T is shown on the right.

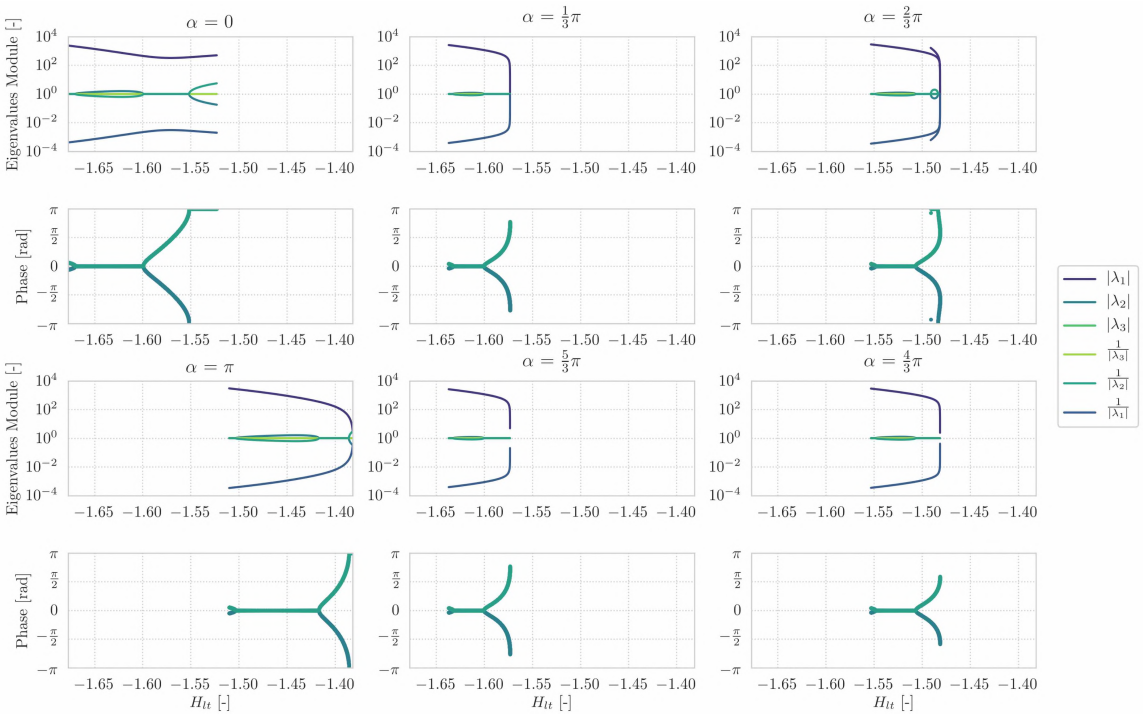

Figure 24. Bifurcation diagram of the six H_{lt}-varying families at $a_{lt} = 0.10$ for different α values in vicinity of E_1.

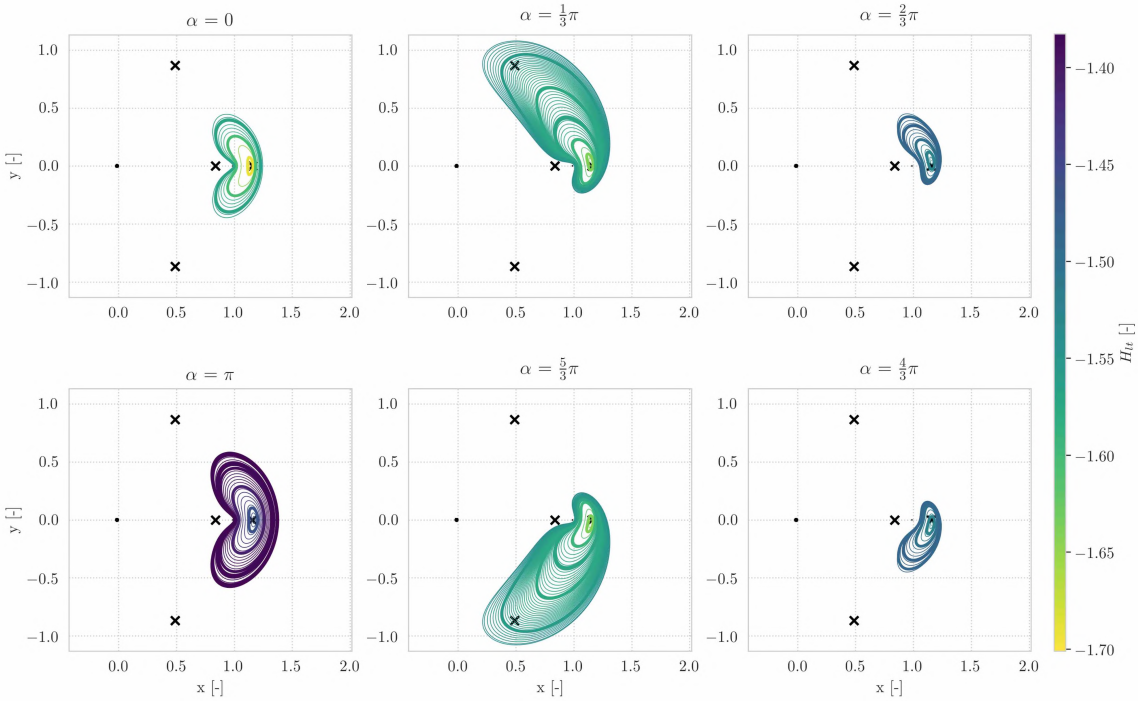

Figure 25. Six H_{lt}-varying families at $a_{lt} = 0.1$ for different α values in vicinity of E_2. The color of an LTPO corresponds to its Hamiltonian value according to the colorbar located on the right side.

Analysis of the saddle stability indices, shown in Figure 23, reveal that the unwinding behaviour is maximum near the equilibria at for all six families. ν_1 decreases monotonically over the family for each acceleration orientation apart from $\alpha = \frac{2}{3}\pi$ where an extremum in Hamiltonian occurs ($H_{lt,max} = -1.481275691$) is encountered at the 659^{th} member. The orbital period however increases monotonically over the six families.

The final families discussed in this section concern six E_2, H_{lt}-varying families with $a_{lt} = 0.1$ and varying acceleration orientations. The impact of this acceleration magnitude on the geometry of the periodic solution family can be observed in Figure 25. Similar to the previous discussed sets of periodic solution families, the families with an acceleration orientation parallel with the x-axis possess a similar geometry as the ballistic L_2 H-L family. This cannot be said for off-axis acceleration orientations which leads to 'ear-like' shaped families. These families curve well beyond the moon in case $\alpha = [\frac{1}{3}\pi, \frac{5}{3}\pi]$. The bifurcation diagrams of these families are presented in Figure 26.

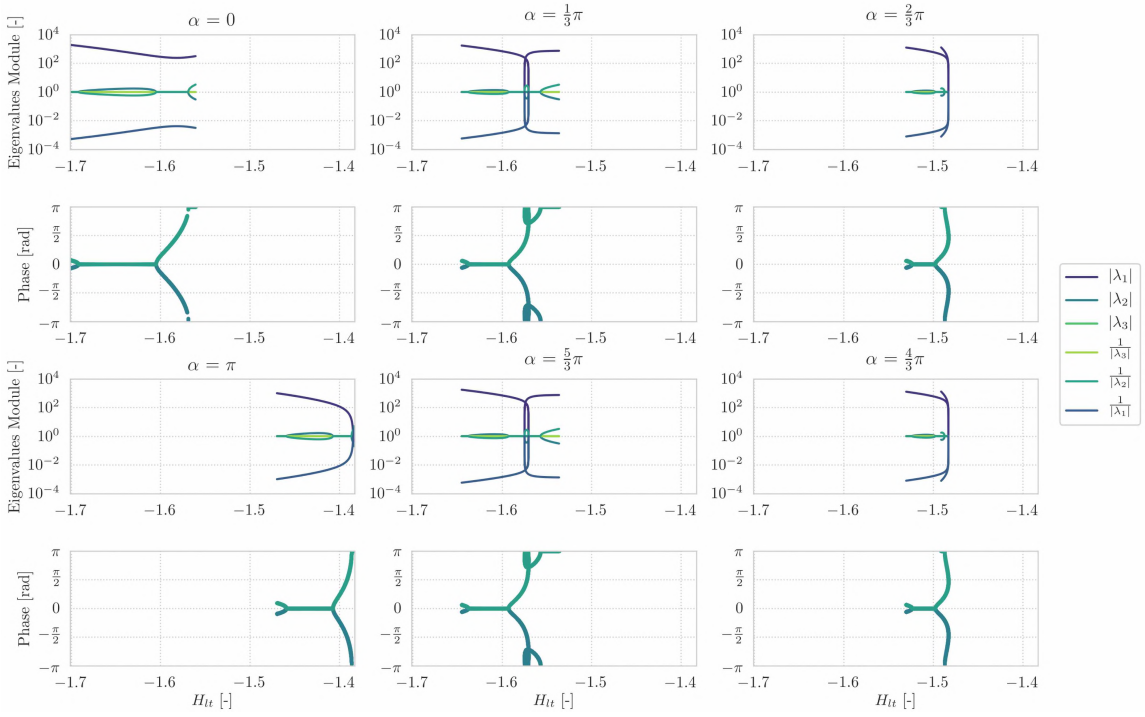

Figure 26. Bifurcation diagram of the six H_{lt}-varying families at $a_{lt} = 0.10$ for different α values that emanate from E_2. The family with $\alpha = \frac{2}{3}\pi$ is terminated earlier with respect to $\alpha = \frac{4}{3}\pi$ due to instabilities in the collocation algorithm.

The bifurcation behaviour of the $\alpha = [0, \pi]$ families remains qualitatively identical to the ballistic L_2 H-L family as these families possess two tangent bifurcations and one period-doubling bifurcation. A total of nine bifurcations occur along the $\alpha = [\frac{1}{3}\pi, \frac{5}{3}\pi]$ families. The first two bifurcations are tangent bifurcations which imply the existence of the halo and axial families at these acceleration orientations. The third bifurcation occurs at a local extremum and therefore classifies as a cyclic-fold bifurcation. The remaining five bifurcations are all period-doubling bifurcations apart from second-last bifurcation that classifies as a tangent bifurcation. Finally, five bifurcations appear at the $\alpha = [\frac{2}{3}\pi, \frac{4}{3}\pi]$ families which have are if the same type as the first five bifurcations of the $\alpha = [\frac{1}{3}\pi, \frac{5}{3}\pi]$ families.

The evolution of the saddle stability index and Hamiltonian over these six families can be found in Figure 27. It suggests that the maximum unwinding behaviour of the $\alpha = [0, \frac{1}{3}\pi, \pi, \frac{5}{3}\pi]$ family remains near the equilbria whereas the maximum unwinding behaviour of $\alpha = [\frac{2}{3}\pi, \frac{4}{3}\pi]$ occurs at the final member of the family. Two extrema in Hamiltonian are observed in the $\alpha = [\frac{1}{3}\pi, \frac{5}{3}\pi]$ whereas one extremum is present in the $\alpha = [\frac{2}{3}\pi, \frac{4}{3}\pi]$ families. These latter two families are the only H_{lt}-varying families that possess a local extremum in the orbital period.

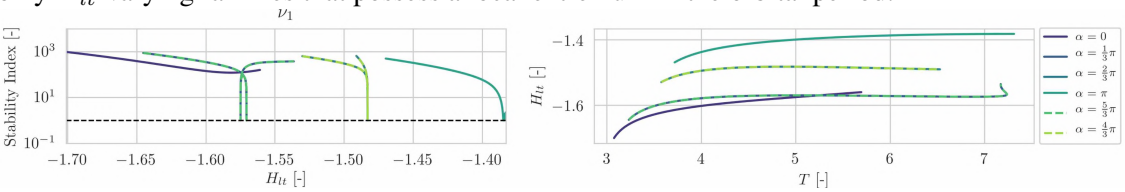

Figure 27. The evolution of ν_1 over the E_2, $a_{lt} = 0.10$, H_{lt}-varying families is shown on the left. The evolution of H_{lt} as a function of T is shown on the right.

This section investigated the geometry, bifurcations and hyperbolic unwinding behaviour of thirty-eight H_{lt}-varying families which provides the reader with an initial understanding of the periodic solution structure of the CR3BP-LT. The geometry of the low-thrust periodic solution family is heavily distorted with respect to the natural H-L geometry in case the low-thrust acceleration orientation is not parallel to the x-axis. An off-axis acceleration orientation also introduces numerous additional bifurcations of which the majority hints towards the existence of families with twice the orbital period they emanate from. Finally, the hyperbolic unwinding behaviour is also affected by the low-thrust acceleration. The maximum unwinding behaviour in vicinity of E_1 was found at the first member of the E_1, $a_{lt} = 0.1$, $\alpha = \pi$ family with a saddle stability index of $\nu_{1,max} = 1487$, which is approximately 11% higher compared to the maximum saddle stability index of the ballistic L_1 H-L family. The maximum unwinding behaviour in vicinity of E_2 was found at the first member of the E_1, $a_{lt} = 0.1$, $\alpha = 0$ family with a saddle stability index of $\nu_{1,max} = 1195$, which is 64% higher than the maximum saddle stability index of the ballistic L_2 H-L family.

Acceleration-varying libration point orbit families

While the H_{lt}-varying families provide an initial understanding of the CR3BP-LT, it remains difficult to characterize the effect of the low-thrust acceleration. To investigate the effect of a low-thrust acceleration magnitude, a_{lt}-varying families are investigated that in vicinity of the E_1 and E_2 contour for six different acceleration orientations $\alpha = [0, \frac{1}{3}\pi, \frac{2}{3}\pi, \pi, \frac{4}{3}\pi, \frac{5}{3}\pi]$. Every libration point orbit belonging to one of these twelve families has the same low-thrust Hamiltonian value ($H_{lt} = -1.525$). The graphical projections of the six a_{lt}-varying families in vicinity of the E_1 contour can be found in Figure 29 whereas the evolution of the saddle stability T over the families can be found in Figure 28.

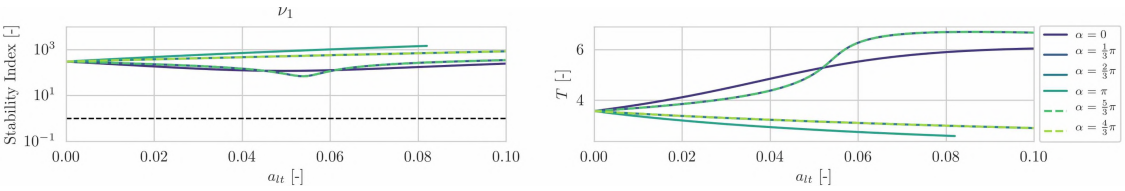

Figure 28. The evolution of ν_1 over the E_1, $H_{lt} = -1.525$, a_{lt}-varying families is shown on the left. The evolution of T as a function of a_{lt} is shown on the right.

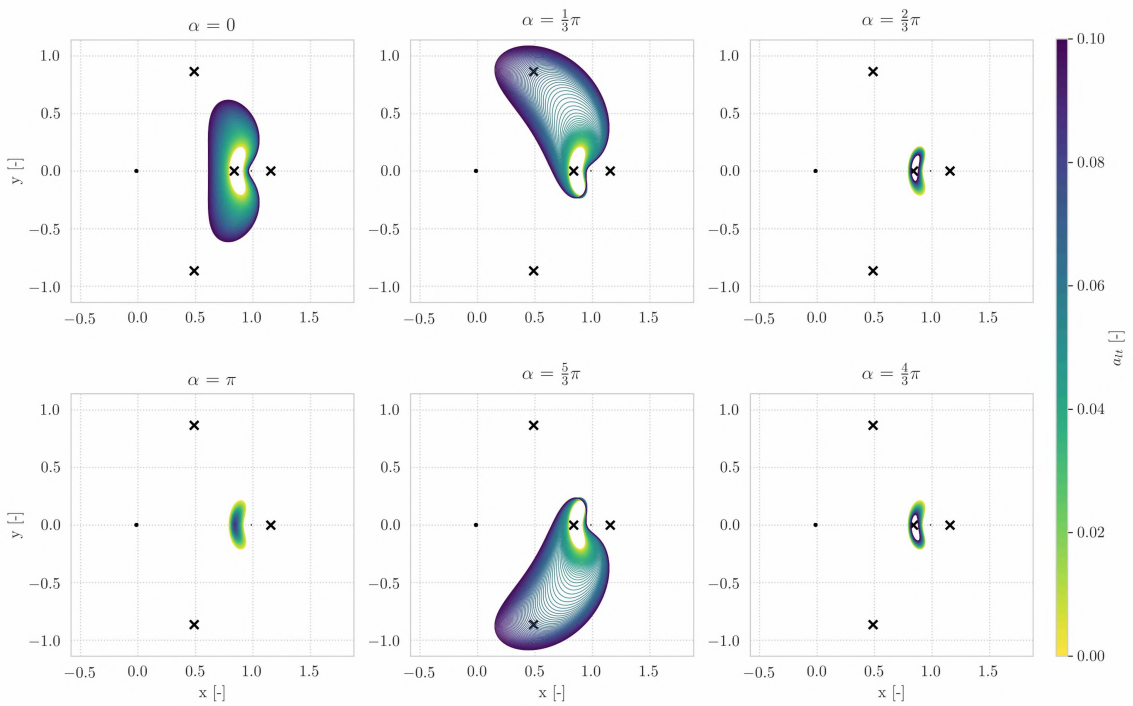

Figure 29. Six a_{lt}-varying families at $H_{lt} = -1.525$ for different α values in vicinity of E_1. The color of an LTPO corresponds to its acceleration magnitude according to the colorbar located on the right side.

The a_{lt}-varying families in Figure 29 reveal that the acceleration magnitude has various effects on the orbit geometry depending upon its orientation. The $\alpha = 0$ family shows that an increase in an acceleration magnitude orientated in the x-axis results in a larger low-thrust periodic solution. The opposite effect is observed for in with $\alpha = \pi$ family where an increase in acceleration results in a smaller low-thrust periodic solution. The α=[$\frac{1}{3}\pi$, $\frac{5}{3}\pi$] families show how the ballistic H-L orbit morphs into an 'ear-shaped' periodic solution with an increase in acceleration magnitude. These geometry distortions are not observed for α=[$\frac{2}{3}\pi$, $\frac{4}{3}\pi$] where an increase in acceleration magnitude leads to a slight deformation of the low-thrust periodic solutions. Inspection of the saddle stability indices in Figure 28 show that the rate of the hyperbolic unwinding behaviour monotonically increases with a growing acceleration magnitude for α = [$\frac{2}{3}\pi$, π, $\frac{4}{3}\pi$]. The saddle stability indices of the remaining families attain a first attain a local minimum before the hyperbolic unwinding behaviour increases. Depending upon the acceleration orientation, the orbital period monotonically increases or decreases with an increasing acceleration magnitude.

The a_{lt}-varying families in vicinity of the E_2 are investigated in the remainder of this section. Figure 31 shows graphical projections of theses six families whereas the evolution of the saddle stability index and orbital period can be found in Figure 30.

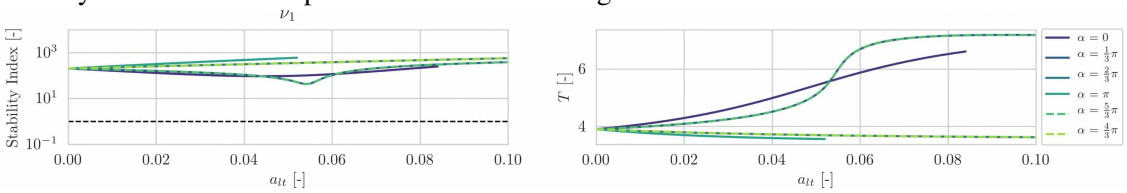

Figure 30. The evolution of ν_1 over the E_2, $H_{lt} = -1.525$, a_{lt}-varying families is shown on the left. The evolution of T as a function of a_{lt} is shown on the right.

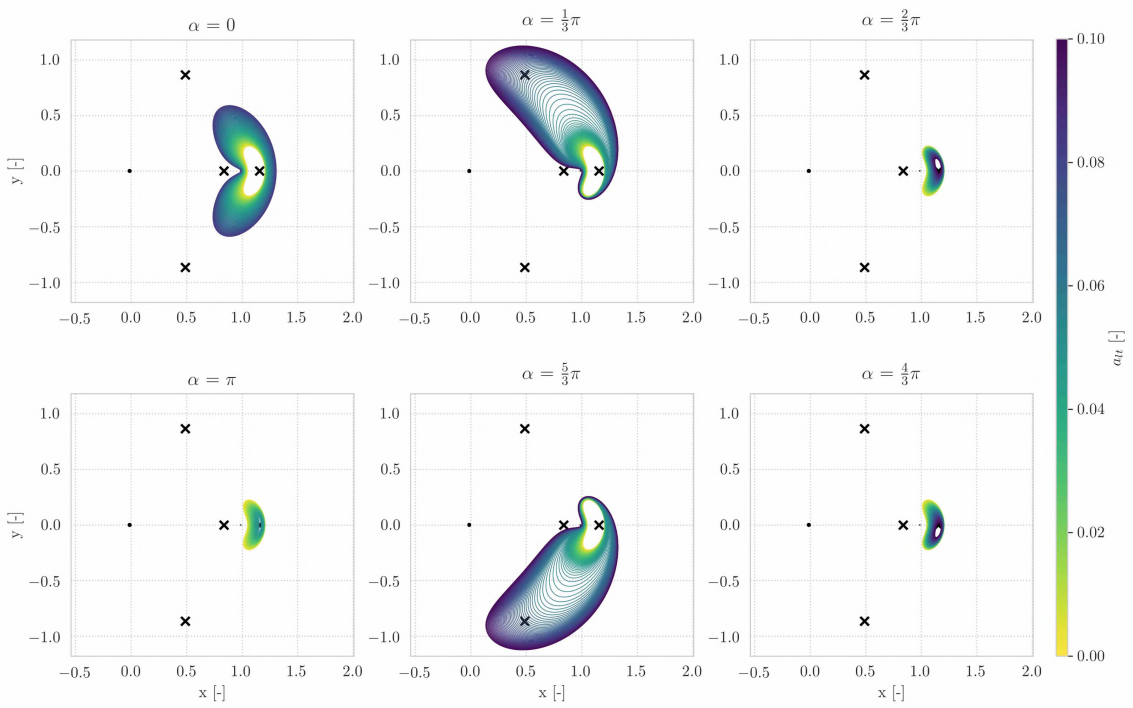

Figure 31. Six a_{lt}-varying families at $H_{lt} = -1.525$ for different α values in vicinity of E_2. The color of an LTPO corresponds to its acceleration magnitude according to the colorbar located on the right side.

Inspection of Figures 31 and 30 reveal the the acceleration magnitude has an identical effect on families emanating from the E_2 contour as families emanating from the E_1 contour.

Orientation-varying libration point orbit families

The H_{lt}-varying and a_{lt}-varying families show that the periodic solutions characteristics can widely vary due to a change in acceleration orientation. To characterize the effect of this parameter, α-varying families are constructed in vicinity of the E_1 and E_2 contour. Per contour, α-varying families are constructed at three distinct acceleration magnitudes ($a_{lt} = [0.01, 0.05, 0.10]$) and three low-thrust Hamiltonian values ($H_{lt} = [-1.55, -1.525, -1.50]$) which results in nine α-varying periodic solution families per contour. The geometries of the nine α-varying families in vicinity of the E_1 contour are shown in Figure 33 whereas the evolution of the saddle stability index and orbital period over these families is presented in Figure 32.

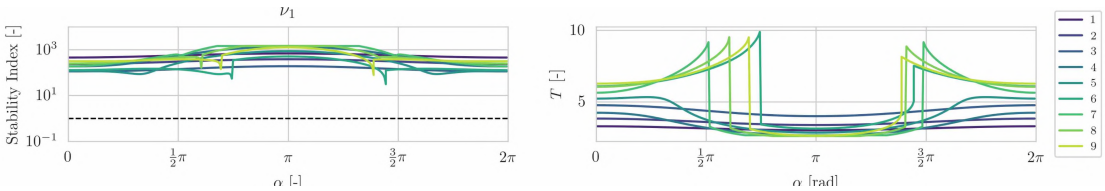

Figure 32. The evolution of ν_1 over the E_1, α-varying families is shown on the left. The evolution of T as a function of α is shown on the right.

The planar projections in Figure 33 show that the degree of geometry with respect to the ballistic L_1 H-L family depends upon the acceleration orientation. This effect even leads to the 'ear-shaped'

periodic solutions that curve beyond P_1. The bottom three subplots and the middle right subplot display asymmetric behaviour which are caused by instabilities of the collocation procedure and are not a feature of the dynamical model. These asymmetries are also clearly visible in Figure 32. However, it observed that the stability indices reaches a maximum at $\alpha = \pi$ or at the orientation closest to $\alpha = \pi$ for periodic solution families that do not exist over the complete domain of acceleration orientations ($\alpha \in [0, 2\pi]$).

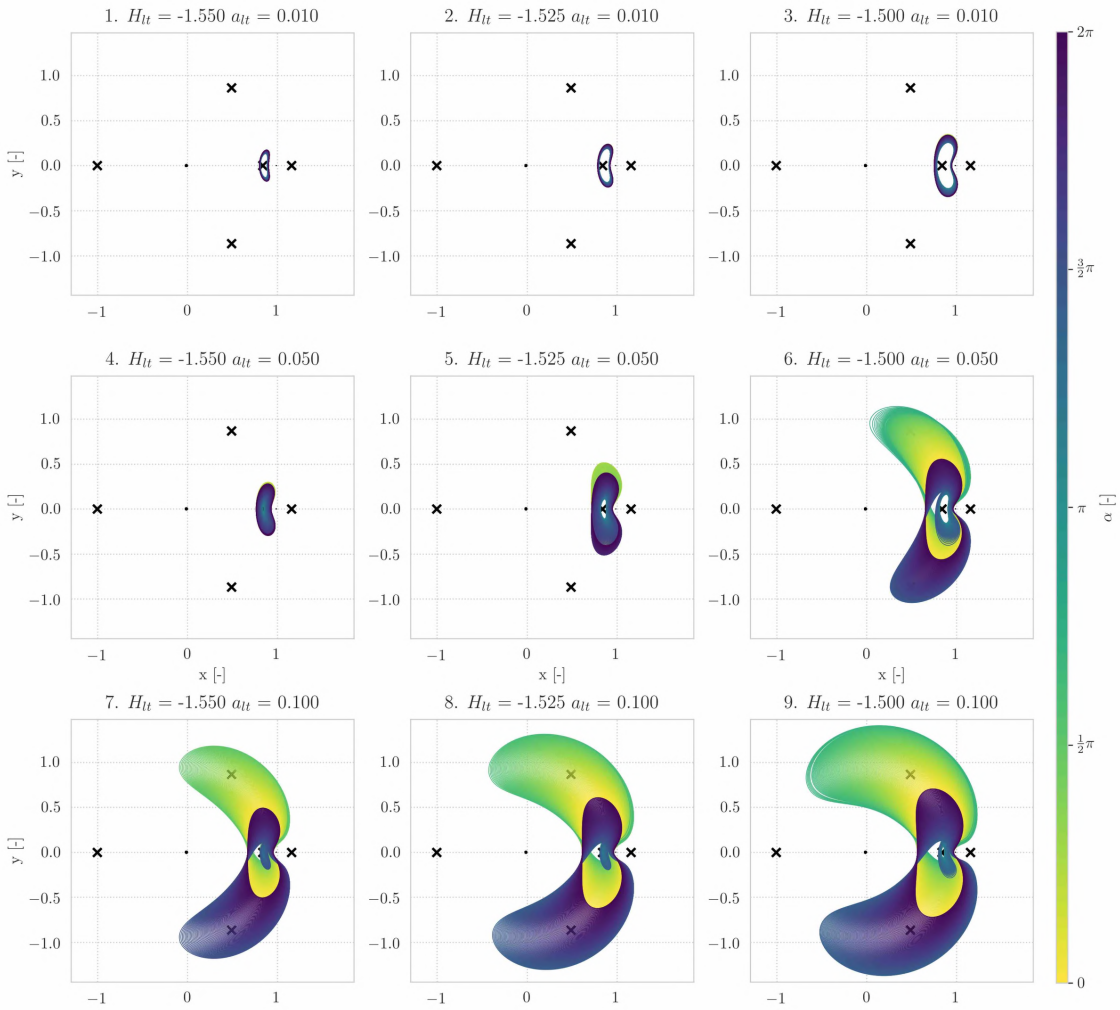

Figure 33. Nine α-varying families at different a_{lt} and H_{lt} values emanating from E_1. The color of an LTPO corresponds to its acceleration magnitude according to the colorbar provided on the right side of the Figure. The asymmetry observed in the middle right plot (6.) and bottom plot (7., 8., 9.) is caused by instabilities in the continuation procedure

Similar conclusions can be drawn from the analysis of the α-varying families in vicinity of the E_2 contour. Their planar projections, shown in Figure 34 reveal the existence of 'ear-shaped' LTPO which curve beyond the Earth. Inspection of their saddle stability indices, shown in Figure 35, reveal that the maximum unwinding behaviour of the α-varying families attain a maximum at $\alpha = \pi$ or at the orientation closest to $\alpha = \pi$ for periodic solution families that do not exist over the complete domain of acceleration orientations ($\alpha \in [0, 2\pi)$. It should be noted that asymmetries are also observed in α-varying families in vicinity of the E_2 contour which are caused by instabilities of the

collocation algorithm. Furthermore, the majority of the E_2-families could not be fully computed due to the earlier mentioned instabilities.

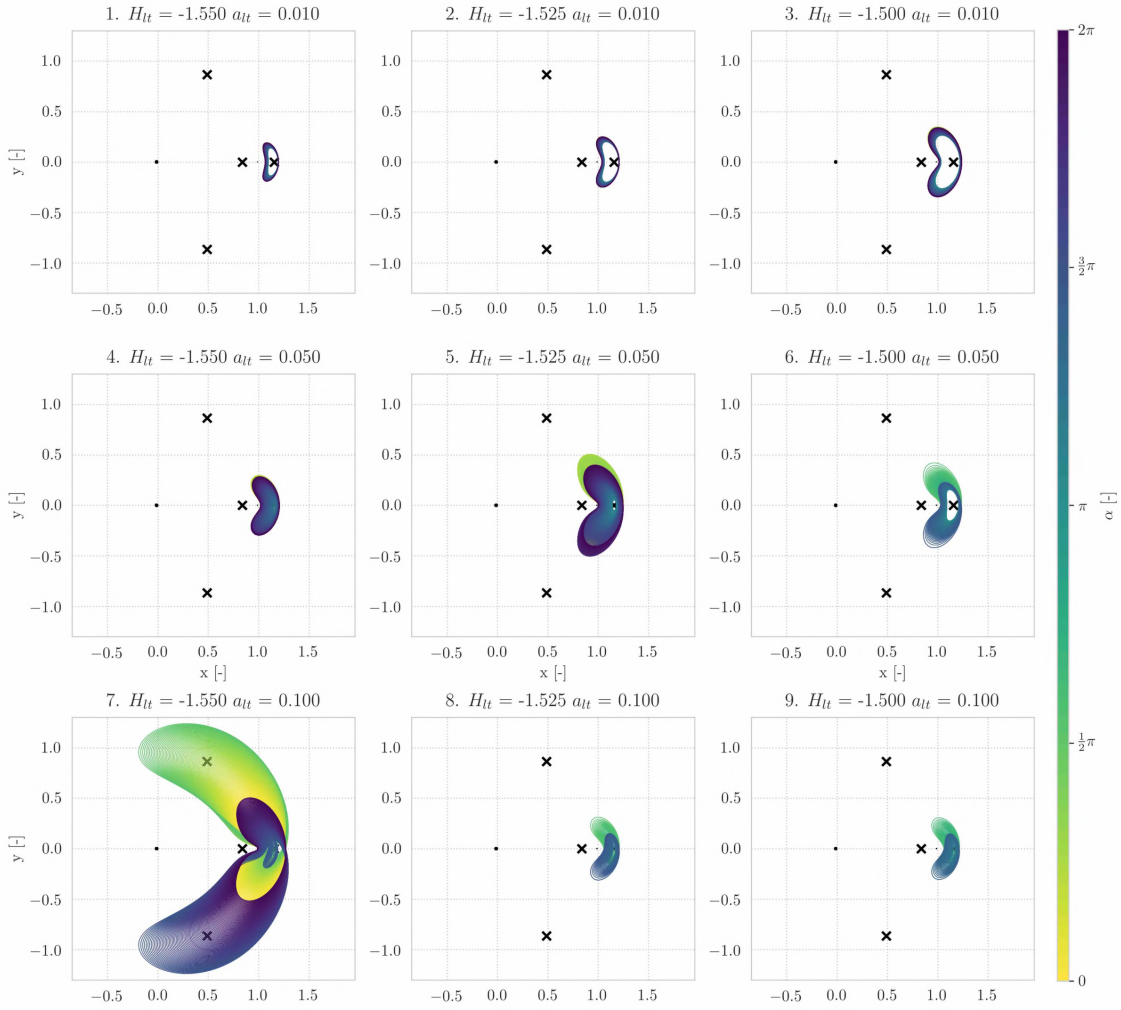

Figure 34. Nine α-varying families at different a_{lt} and H_{lt} values emanating from E_2. The color of an LTPO corresponds to its acceleration magnitude according to the colorbar provided on the right side of the Figure. The asymmetry observed in the bottom left plot (7.) is caused by instabilities in the continuation procedure

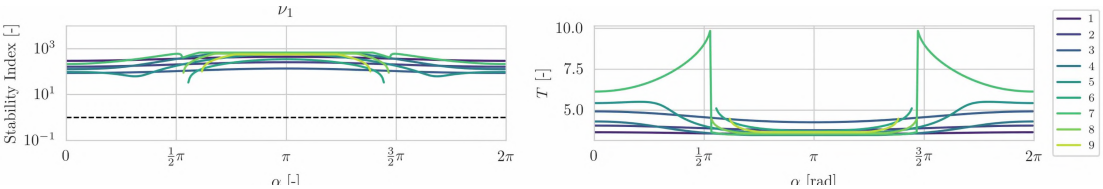

Figure 35. The evolution of ν_1 over the E_2, α-varying families is shown on the left. The evolution of T as a function of α is shown on the right.

CONCLUSIONS

This paper explores the effect of a constant low-thrust acceleration on the equilibria and horizontal Lyapunov orbits in the Earth-Moon CR3BP. These effects can be characterized by investigating the dynamics of a combined multi-body low-thrust model developed in previous work.[9–11]

The planar low-thrust equilibria, obtained via a multivariate relaxed Newton-Rapshon root-finder, show that the low-thrust acceleration can significantly shift the position of the natural Lagrangian points. These positional changes can lead to a qualitative change in the linear stability of the equilibria and increase (decrease) the rate of hyperbolic unwinding behaviour as the equilibria moves towards (away from) the primary and secondary body.

Families of low-thrust horizontal Lyapunov orbits are constructed in vicinity of L_1 and L_2 via numerical continuation methods that are driven by a 12^{th} order Legendre-Gauss-Lobatto collocation method. Employing the low-thrust Hamiltonian, acceleration magnitude, and acceleration orientation as bifurcation parameters give rise to three types of periodic solution families. Analysis of the geometry, bifurcations, and hyperbolic unwinding behaviour of these three family types allows characterization of the bifurcation parameters' effect on the ballistic horizontal Lyapunov families in an isolated fashion. Thirty-six low-thrust H_{lt}-varying families have been generated in vicinity of L_1 and L_2 for three distinct acceleration magnitudes and six acceleration orientations. Inspection of their geometry reveals that the ballistic horizontal Lyapunov shape is preserved while the acceleration orientation is aligned with the x-axis of the synodic frame whereas geometry distortions are observed whenever this is not the case. The degree of deformation is proportional to the low-thrust Hamiltonian and acceleration magnitude and can be so extreme that 'ear-shaped' low-thrust periodic solutions arise. Analysis of the bifurcation behaviour implies the existence of low-thrust halo and low-thrust axial periodic solution families for all H_{lt}-varying families. H_{lt}-varying families with $a_{lt} = 0.01$ show identical bifurcation behaviour with respect to the ballistic orbits but additional cyclic-fold and period-doubling bifurcations are observed at higher acceleration magnitudes. Inspection of the saddle stability indices of the H_{lt}-varying families reveal the existence of periodic solutions with a higher hyperbolic unwinding rate compared to the ballistic horizontal Lyapunov families. In vicinity of L_1 (L_2), an LTPO is identified with an hyperbolic unwinding rate that is 11% (64%) higher compared to the maximum hyperbolic unwinding rate of the ballistic L_1 (L_2) family. The invariant manifolds emanating from these orbits might provide the opportunity for more novel transfer solutions in the Earth-Moon system.

Analysis of the a_{lt}-varying families confirm that the degree of geometry distortion is proportional to the acceleration magnitude. A low-thrust acceleration in the direction of the positive x-axis is associated with an increase in amplitude while the opposite orientation is associated with a decrease in amplitude. These findings are confirmed by inspection of the α-varying families which emphasize that the degree of geometry distortion heavily depends upon the acceleration orientation. Inspection of the saddle stability indices of the a_{lt}-varying families reveal that the maximum rate of hyperbolic unwinding behaviour for a certain low-thrust Hamiltonian consistently occurs in the families with $\alpha = \pi$ rad. A similar conclusion can be drawn from the saddle stability indices of the α-varying families as the maximum rate of hyperbolic unwinding behaviour of a single α-varying family consistently occurs at the family member whose acceleration orientation is (closest to) $\alpha = \pi$ rad.

The families of low-thrust periodic solutions provided in this paper allow initial characterization of the effect of a constant low-thrust acceleration on horizontal Lyapunov orbits in the Earth-Moon CR3BP. The totality of presented periodic solution families scratch the surface of the low-thrust

periodic solution structure of the Earth-Moon CR3BP-LT. Improved numerical continuation algorithms are needed to further explore the largely unknown periodic solution of the CR3BP-LT.

NOTATION

α	In-plane angle of the low-thrust acceleration vector	(rad)
β	Out-of-plane angle of the low-thrust acceleration vector	(rad)
θ	In-plane rotation angle between inertial and synodic reference frame	(rad)
κ	Angle between positive x-axis of synodic frame and r_{13} vector	(rad)
λ	Eigenvalue	$(-)$
μ	Mass ratio parameter of the CR3BP(-LT)	$(-)$
ν	Stability index	
Φ	State transition matrix	$(-)$
Ω	Pseudo-potential	$(-)$
$\bar{A}$	State propagation matrix	$(-)$
$\bar{a}_{lt}$	Acceleration vector	$(-)$
a_{lt}	Dimensionless acceleration magnitude	$(-)$
C	Jacobi integral	$(-)$
E_i	Equilibria contour	$(-)$
F	Dimensional thrust force	(kN)
f	Dimensionless thrust force	(N)
g_0	Gravitational acceleration at sea level	(s)
H	Hamiltonian	$(-)$
$\bar{I}$	Identity matrix	$(-)$
I_{sp}	Specific impulse	(s)
L_i	Lagrangian point i of the CR3BP	$(-)$
l_*	Characteristic length of CR3BP(-LT)	(km)
M_i	Dimensional mass of body i	(kg)
m	Dimensionless mass of P_3	$(-)$
P_i	Body in the three-body problem	$(-)$
r_{ij}	Position vector from body i to body j	$(-)$
T	Orbital period	$(-)$
t_*	Characteristic time of the CR3BP(-LT)	(s)
$\bar{u}$	Acceleration orientation vector	$(-)$
V	Velocity magnitude in the rotating frame	$(-)$
x,y,z	synodic reference frame position coordinates	$(-)$
$\mathbb{X}$,$\mathbb{Y}$,$\mathbb{Z}$	Inertial reference frame position coordinates	$(-)$
$_{eq}$	Equilibrium	
$_{lt}$	Low-thrust	
$_{nat}$	Natural	
$_{x,y,z}$	Partial derivative with respect to the synodic position coordinates	
$\dot{}$	First time derivative	
$\ddot{}$	Second time derivative	

CR3BP	Circular restricted three-body problem
CR3BP-LT	Low-thrust circular restricted three-body problem
SPM	State propagation matrix
ZAC	Zero acceleration contour

APPENDIX A: LOW-THRUST PROPULSION SYSTEM CHARACTERISTICS

This research considers dimensionless thrust magnitudes $f \in [0.0, 0.1]$ since this is in line with the capabilities of current low-thrust propulsion technology as shown in Table 1.

Table 1. Overview of today's state of low-thrust propulsion technology.

Spacecraft	Propulsion type	$F\,(mN)$	$M_{3,0}\,(kg)$	$f\,(-)$	$I_{sp}\,(s)$	$\dot{m}\,(-)$
Deep Space[29]	Ion thruster	92.0	486	$6.95 \cdot 10^{-2}$	1900 - 3200	$2.61 \cdot 10^{-3}$
Hayabusa[30]	Ion thruster	72.0	510	$5.17 \cdot 10^{-2}$	2760 - 3000	$1.94 \cdot 10^{-3}$
Hayabusa 2[31]	Ion thruster	84.0	609	$1.73 \cdot 10^{-2}$	2400 - 2750	$1.90 \cdot 10^{-3}$
Dawn[32]	Ion thruster	92.7	1218	$2.79 \cdot 10^{-2}$	1740 - 3065	$1.04 \cdot 10^{-3}$
NEXT[33]	Ion thruster	236	1218	$7.10 \cdot 10^{-2}$	4190	$2.67 \cdot 10^{-3}$
Lunar Icecube[34]	Ion thruster	1.0	14	$2.62 \cdot 10^{-2}$	2500	$1.50 \cdot 10^{-4}$
SMART-I[35]	Ion thruster	70.0	350	$7.33 \cdot 10^{-2}$	1600	$2.75 \cdot 10^{-3}$
Sunjammer[36]	Solar sailing	8.0	32	$9.16 \cdot 10^{-2}$	not applicable	

Table 1 allows the reader to get an idea of the kind of propulsion systems involved in this study. Looking at the specific impulse column, it can be observed that some missions have a range of possible specific impulses whereas some missions have a fixed specific impulse. This can be adressed to the fact that some propulsion systems have throttling capability. This addendum is concluded with the notion that parts of Table 1 have been obtained from.[11]

APPENDIX B: SENSITIVITY ANALYSIS VARIABLE MASS

This research employs several assumptions that simplify the dynamics of the CR3BP-LT to ensure the existence of an integral of motion. Whereas the feasibility of a constant low-thrust force magnitude and orientation largely depend upon the selected electric propulsion system, a constant spacecraft mass cannot be realized as this type of propulsion generates thrust by expelling propellant at a high velocity. This Appendix tests the feasibility of $\dot{m} = 0$ by numerically verifying the original justification of this assumption.[11]

The reasoning behind the constant mass assumption is that if a varying spacecraft mass has a negligible effect on $\bar{a_{lt}}$, the low-thrust Hamiltonian can be reasonably assumed constant. The effect of a varying mass on $\bar{a_{lt}}$ can be investigated via the time derivative of $\bar{a_{lt}}$ which is shown in Eq (16).[11]

$$\dot{\bar{a}}_{lt} = -\frac{f\dot{m}}{m^2}\hat{u} = -a_{lt}^2 \frac{l_*}{I_{sp} g_0 t_*}\hat{u} \tag{16}$$

Previous literature[11] compares the derivative magnitude with the natural energy range of the CR3BP, defined as $\Delta H_{nat} = H_{nat}(L_5) - H_{nat}(L_1) \approx 0.100172$, to determine if $\bar{a}_{lt}$ and H_{lt} can be assumed constant. The third column of Table 2 provides a numerical example that shows that the derivative magnitude is 0.34% of the natural energy range when considering a low energy efficiency and high acceleration magnitude. Literature[11] considers this as enough proof to assume $\bar{a}_{lt}$ and H_{lt}

as constant quantities. This assertion is verified by simulating the trajectories of three satellites, situated on different low-thrust horizontal Lyapunov orbits, for one orbital period while assuming $\dot{m} > 0$. The first trajectory (test case 1) is the final member of the L_1 ($a_{lt} = 0.01$, $\alpha = 0$ rad) H_{lt}-varying family whereas the second (test case 2) and third (test case 3) trajectory are the final member of the L_1 ($a_{lt} = 0.05$, $\alpha = 0$) H_{lt}-varying family and E_1 ($a_{lt} = 0.10$, $\alpha = 0$) H_{lt}-varying family respectively. Table 2 shows the orbit characteristics, full-period state deviations, and ΔH_{lt} after one orbital revolution. Test case 3 is visualized in Figure 36.

Variable	Unit	Literature[11]	Test case 1	Test case 2	Test case 3
a_{lt}	[-]	0.07	0.01	0.05	0.1
α	[rad]	-	0	0	0
I_{sp}	[s]	1500	1500	1500	1500
$H_{lt_{start}}$	[-]	-	-1.462010	-1.487190	-1.522927
T	[-]	-	6.537957	6.347544	6.062807
$\Delta H_{lt_{family}}$	[-]	-	0.140525	0.148713	0.147015
$\Delta H_{lt_{nat}}$	[-]	0.100172	0.100172	0.100172	0.100172
$-a_{lt}^2 \frac{l_*}{I_{sp} g_0 t_*}$	[-]	$3.412839 \cdot 10^{-4}$	$6.964977 \cdot 10^{-6}$	$1.741244 \cdot 10^{-4}$	$6.964977 \cdot 10^{-4}$
$\|\|\Delta\bar{R}\|\|$	[-]	-	$4.653406 \cdot 10^{-3}$	$1.275210 \cdot 10^{-1}$	$4.706526 \cdot 10^{-1}$
$\|\|\Delta\bar{V}\|\|$	[-]	-	$2.276086 \cdot 10^{-3}$	$8.488162 \cdot 10^{-2}$	$3.726720 \cdot 10^{-1}$
$H_{lt_{period}}$	[-]	-	-1.462049	-1.488152	-1.526636
$-a_{lt}^2 \frac{l_*}{I_{sp} g_0 t_*} / \Delta H_{lt_{nat}}$	[%]	$3.4 \cdot 10^{-1}$	$7.0 \cdot 10^{-3}$	$1.7 \cdot 10^{-1}$	$6.9 \cdot 10^{-1}$
$\frac{\lvert H_{lt_{period}} - H_{lt_{start}} \rvert}{\Delta H_{lt_{nat}}}$	[%]	-	$3.8 \cdot 10^{-2}$	$9.6 \cdot 10^{-1}$	3.7
$\frac{\lvert H_{lt_{period}} - H_{lt_{start}} \rvert}{\Delta H_{lt_{family}}}$	[%]	-	$2.8 \cdot 10^{-2}$	$6.4 \cdot 10^{-1}$	2.5

Table 2. Verification of the constant mass assumption. The first five rows show the properties of the spacecraft and libration point orbit. The sixth and seventh column show the energy ranges of the H_{lt}-varying family and the CR3BP. The eight row shows the magnitude of acceleration time derivative. The full-period state discrepancies are presented in ninth and tenth row. The eleventh row shows the magnitude of acceleration time derivative as a percentage of the natural energy range. The final two rows express the low-thrust Hamiltonian deviation over one revolution as a percentage of the natural energy and periodic solution family energy range.

The results in Table 2 confirm that $\bar{a}_{lt}$ and H_{lt} can reasonably be considered as constant quantities since the Hamiltonian of a low-thrust libration point orbit only deviates 3.7% with respect to the natural energy range when assuming the highest possible acceleration magnitude and a low engine efficiency.

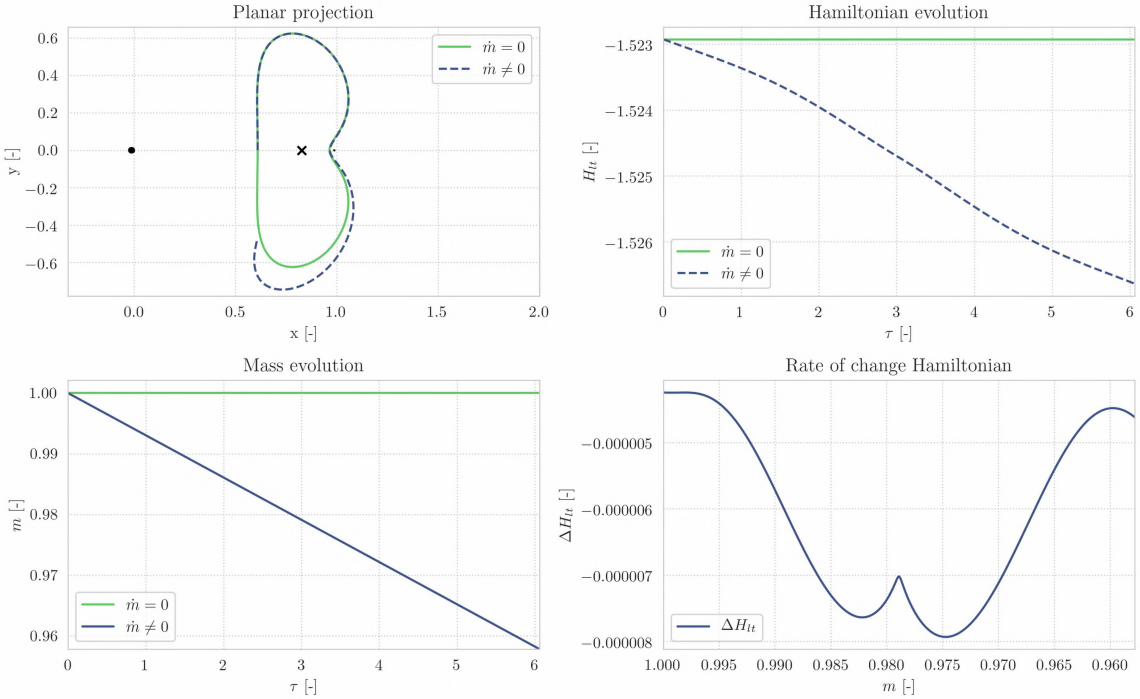

Figure 36. Propagation of a spacecraft with constant and varying mass ($I_{sp} = 1500$ s) situated on a L_1 ($a_{lt} = 0.01$, $\alpha = 0$ rad, $H_{lt} \approx -1.462010$) low-thrust Horizontal Lyapunov orbit. The upper left figure shows the trajectory whereas the upper right plot shows H_{lt} evolution as a function of time. The lower left plot shows the spacecraft mass as a function of time whereas the lower right plot presents the H_{lt} derivatve as a function of the spacecraft mass.

REFERENCES

[1] R. Bonnet and F.Felici, "Overview of the SOHO mission," *Advances in Space Research*, Vol. 20, No. 12, 1997. doi: https://doi.org/10.1016/S0273-1177(97)00894-6.

[2] J. Tauber, "The Planck mission," *Advances in Space Research*, Vol. 34, No. 3, 2004. doi: https://doi.org/10.1016/j.asr.2003.05.025.

[3] R. Whitley and R. Martinez, "Options for staging orbits in cislunar space," *IEEE Aerospace Conference*, 2016. doi: 10.1109/AERO.2016.7500635.

[4] M. Ozimek and K. H. D. Grebow, "Solar Sails and Lunar South Pole Coverage," *AIAA/AAS Astrodynamics Specialist Conference*, Honolulu, Hawaii, 2008. doi: https://doi.org/10.2514/6.2008-7080.

[5] E. Doedel, V. Romanov, R. Paffenroth, H. Keller, D. Dichmann, J. Gálan, and A. Vanderbauwhede, "Elemental periodic orbits associated with the libration points in the circular restricted 3-body problem," *International Journal of Bifurcation and Chaos*, Vol. 18, No. 7, 2011. - DOI: 10.1142/S0218127407018671.

[6] W. Koon, M. Lo, J. Marsden, and S. Ross, *Dynamical Systems, The Three-Body Problem and Space Mission Design*. New-York: Springer-Verlag, 2007. - ISBN: 978-0387495156.

[7] P. Verrier, T. Waters, and J. Sieber, "Evolution of the L1 Halo family in the radial solar sail CRTBP," *Celestial Mechanics and Dynamical Astronomy*, Vol. 120, No. 4, 2014. doi: 10.1007/s10569-014-9575-2.

[8] J. Heiligers, M. Macdonald, and J. Parker, "Extension of Earth-Moon libration point orbits with solar sail propulsion," *Astrophysics and Space Science*, Vol. 361, 2016. DOI: 10.1007/s10509-016-2783-3.

[9] A. Cox, K. Howell, and D. Folta, "Dynamical Structures in a Combined Low-Thrust Multi-Body Environment," *Advances in the Astronautical Sciences Series*, Vol. 162, 2017. ISBN: 978-0-87703-646-3.

[10] D. F. A. Cox, K. Howell, "Transit and Capture in the Planar Three-Body Problem Leveraging Low-Thrust Dynamical Structures," *AAS/AIAA Space Flight Mechanics Conference*, Honolulu Hawaii, jan 2019.

[11] A. Cox, K. Howell, and D. Folta, "Dynamical structures in a low-thrust, multi-body model with applications to trajectory design," *Celestial Mechanics and Dynamical Astronomy*, Vol. 131, feb 2019.

[12] V. Szebehely, *Theory of Orbits*. Academic Press, 1967. - ISBN: 978-0-12-395732-0.

[13] K. Kumar, Y. Abdulkadir, P. Barneveld, F. Belien, S. Billemont, E. Brandon, M. Dijkstra, D. Dirkx, F. Engelen, D. Gondelach, L. Ham, E. Heeren, E. Iorfida, E. Leloux, J. Melman, E. Mooij, P. Musegaas, R. Noomen, S. Persson, B. Romgens, A. Ronse, T. Secretin, B. Tong-Minh, and J. Vandamme, "Tudat: a modular and robust astrodynamics Toolbox.," *Fifth ICATT, International Conference on Astrodynamics Tools and Techniques*, 2012, pp. 1–8.

[14] E. Ott, *Chaos in Dynamical Systems*. Cambridge University Press, 1993. - ISBN: 978-0521010849.

[15] G. Gómez, W. Koon, M. Lo, J. Marsden, J. Masdemont, and S. Ross, "Connecting orbits and invariant manifolds in the spatial restricted three-body problem," *Nonlinearity*, Vol. 17, No. 5, 2004. DOI: https://doi.org/10.1088/0951-7715/17/5/002.

[16] C. Kelley, *Solving Nonlinear Equations with Newton's method*. Philadelphia: Society for Industrial and Applied Mathematics, 2003. - ISBN: 0-89871-546-6.

[17] E. Zimovan-Spreem, K. Howell, and D. Davis, "Near Rectilinear Halo Orbits and Their Application in Cis-Lunar Space," *3rd International Academy of Astronautics Conference on Dynamics and Control of Space Systems*, Moscow, Russia, 2017.

[18] C. Goudas, "Three-dimensional periodic orbits and their stability," *Icarus*, Vol. 2, 1963, pp. 1–18. doi: https://doi.org/10.1016/0019-1035(63)90003-4.

[19] D. Dichmann, E. Doedel, , and R. Paffenroth, "The Computation of Periodic Solutions of the 3-Body Using Numerical Continuation Software AUTO," *Libration Point Orbits and Applications*, 2002. ISBN: 978-981-238-361-1.

[20] K. Howell and T. Keeter, "Station-keeping strategies for libration point orbits—target point and Floquet mode approaches.," *Advances in the Astronautical Sciences*, Vol. 89, 1995, pp. 1377–1396.

[21] K. Howell and B. Marchand, "Natural and non-natural spacecraft formations near the L1 and L2 libration points in the Sun–Earth/Moon ephemeris system," *Dynamical Systems: An International Journal*, Vol. 201, mar 2005, pp. 149–173. - doi: https://doi.org/10.1080/14689360420002982 24.

[22] B. Marchand, K. Howell, and R. Wilson, "An Improved Corrections Process for Constrained Trajectory Design in the n-Body Problem," *Journal of Spacecraft and Rockets*, Vol. 44, No. 4, 2007. - eISSN: 1533-6794.

[23] K. Howell and H. Pernicka, "Numerical determination of Lissajous trajectories in the restricted three-body problem," *Celestial Mechanics and Dynamical Astronomy*, Vol. 41, No. 1, 1978, pp. 107–124. - ISSN: 0923-2958.

[24] A. Herman, *Improved collocation methods with application to direct trajectory optimization*. PhD thesis, University of Illinois at Urbana-Champaign, 1995.

[25] C. d. Boor, "Good Approximation by Splines with Variable Knots," *Spline Functions and Approximation Theory*, 1973. ISBN: 978-3-0348-5980-6.

[26] Y. Kuznetsov, *Elements of Applied Bifurcation Theory*. New-York: Springer-Verlag, 2004. ISBN 978-1-4757-3978-7.

[27] K. Howell and E. Campbell, "Three-dimensional Periodic Solutions that Bifurcate from Halo families in the Circular Restricted Three-Body Problem," *AIAA/AAS Astrodynamics Specialist Conference*, 1998.

[28] J. Howard and E. Mackay, "Linear stability of symplectic maps," *Journal of Mathematical Physics*, Vol. 28, 1987. - doi: https://doi.org/10.1063/1.527544.

[29] M. Rayman, P. Vargese, D. Lehman, and L. Livesay, "Results From The Deep Space 1 Technology Validation Mission," *Acta Astronautica*, Vol. 47, 2000, pp. 475–478. doi: https://doi.org/10.1016/S0094-5765(00)00087-4.

[30] H. Kuninaka, K. Nishiyama, Y. Shmimizy, I. Funaki, and H. Koizumi, "Hayabusa Asteroid Explorer Powered by Ion Engines on the Way to Earth," *The 31st International Electric Propulsion Conference*, 2009.

[31] K. Nishiyama, S. Hosoda, K. Ueno, and H. Kuninaka, "The Ion Engine System for Hayabusa2," *32nd International Electric Propulsion Conference,*, 2011.

[32] C. Russell and C. Raymond, *The Dawn Mission to Minor Planets 4 Vesta and 1 Ceres*. New York: Springer-Verlag, 2012. ISBN: 978-1-4614-4902-7.

[33] G. Schmidt, M. Patterson, and S. Benson, "The Nasa Evolutionary Xenon Thruster (NEXT): The Next Step For U.S. Deep Space Propulsion," *International Astronautical Congress*, 2008.

[34] N. Bosanac, A. Cox, K. Howell, and D. Folta, "Trajectory design for a cislunar CubeSat leveraging dynamical systems techniques: The Lunar IceCube mission," *Acta Astronautica*, Vol. 144, 2018. doi: https://doi.org/10.1016/j.actaastro.2017.12.025.

[35] R. Mackenzie, D. Salvador, and D. Miligan, "Orbit Determination of the SMART-1 Mission," *Proceedings of the 18th International Symposium on Space Flight Dynamics*, 2004.

[36] M. Macdonald, *Advances in Solar Sailing*. Berlin: Springer-Verlag, 2014. ISBN: 978-3-642-34906-5.

A

Physical constants and algorithm parameters

This adjunct presents all constants and parameters that have been used to produce the work in Chapter 1. Section A.1 discusses the constants that define the dynamics of the physical model while Section A.2 presents the settings of the algorithm responsible for the generation of the equilibria contours and libration point orbit (l.p.o) families. In case one wishes to reproduce the results in the TU Delft Astrodynamics Toolbox (TUDAT) development environment[12], the reader is advised to contact the author or thesis supervisor for a complete copy of the code[1]. Given that the reader wishes to reproduce the results outside the TUDAT environment, the remainder of this Chapter provides an exhaustive list of the constants and parameters used during this thesis project.

A.1. Physical constants

The low-thrust circular restricted three-body problem (CR3BP-LT) model is a combination of the natural circular restricted three-body problem (CR3BP) and a low-thrust force. The CR3BP is fully defined by the mass ratio parameter, which can be computed via Equation A.1.

$$\mu = \frac{\mu_{Moon}}{\mu_{Earth} + \mu_{Moon}} \tag{A.1}$$

The symbols on the right hand side denote the gravitational parameters of the primary and secondary body. The values of these parameters are listed in Table A.1.

Due to a presence of a low-thrust force in the CR3BP-LT, three additional physical constants are needed to fully parametrize the dynamical model. Two of these parameters are the characteristic length, (i.e. semi-major axis) and characteristic time (i.e. inverse of the system's mean motion). The latter follows directly from the former via Kepler's third law, shown below in Equation A.2.

$$t_* = \sqrt{\frac{l_*^3}{\mu_{Earth} + \mu_{Moon}}} \tag{A.2}$$

The final physical constant is the gravitational acceleration at sea-level. The values of these variables have been obtained directly from TUDAT and [25] and are listed in Table A.1. It should be emphasized that propulsion system characteristics of the spacecraft are also necessary to parametrize the CR3BP-LT model. These variables are regarded as mission-specific variables rather than fundamental physical constants of the CR3BP-LT model. An overview of the adopted propulsion system characteristics can be found in Chapter 1 of this report.

[1] S.H.F. Martens: shfmartens@gmail.com

Symbol	Description	Value		Unit
μ	Mass ratio parameter	1.2150581017337	$\cdot 10^{-2}$	[-]
μ_{Earth}	Earth gravitational parameter	3.986004418	$\cdot 10^{14}$	$[m^3 s^{-2}]$
μ_{Moon}	Moon gravitational parameter	4.9027988158612	$\cdot 10^{12}$	$[m^3 s^{-2}]$
l_*	Characteristic length	3.84400	$\cdot 10^5$	$[km]$
t_*	Characteristic time	4.354369171925	–	[days]
g_0	Gravitational acceleration at sea level	9.80665	–	$[m \cdot s^{-2}]$

Table A.1: Fundamental physical constants of the Earth-Moon CR3BP-LT model. All values have been directly adopted from TUDAT or [25].

A common approach to simplify analysis in multi-body models like the CR3BP-LT is nondimensionalization of the dynamics. A disadvantage of dimensionless variables is that their values are difficult to interpret. Table A.2 overcomes this problem by providing the relation between the dimensionless and dimensional values.

Symbol	Description	Value		Unit	Dimensionless Value
x	Position	3.84400	$\cdot 10^5$	$[km]$	1
t	Time	2.7359308403075	$\cdot 10^1$	[days]	2π
$\dot{x}$	Velocity	1.0245468537379	–	$[km \cdot s^{-1}]$	1

Table A.2: A representation of the dimensionless quantities of position, time, and velocity in the Earth-Moon CR3BP-LT.

The constants summarized in Table A.1 and A.2 fully establish CR3BP-LT dynamical model.

A.2. Algorithm settings for orbit generation

The results presented in Chapter 1 of this report have been obtained by employing techniques with specific settings. This section provides an exhaustive overview of the adopted settings of these numerical methods.

A.2.1. Integrator settings

The Runge-Kutta-Fehlberg 7(8) (RKF78) method is one of two numerical integration techniques that have been deployed in this thesis project. The RKF78 is an essential techniques in this work since it is employed in every step of l.p.o family construction process. An extensive discussion on the fundamentals of this technique can be found in Appendix B. TUDAT is equipped with a RKF78 integrator so the user is only concerned with selection of the integrator settings. Both the integrator settings and the integrator overshoot procedure are based on the work of [25] and can be found below in Table A.3. These settings have proven to allow the construction of l.p.o families in the CR3BP with near machine-precision.

Symbol	Value		Unit	Description
h_0	1.0	$\cdot 10^{-5}$	[-]	Initial stepsize
h_{min}	ϵ_m		[-]	Minimum stepsize
h_{max}	1.0	$\cdot 10^{-4}$	[-]	Maximum stepsize
ϵ_{abs}	1.0	$\cdot 10^{-24}$	[-]	Absolute error tolerance
ϵ_{rel}	ϵ_m	$\cdot 10^2$	[-]	Relative error tolerance
Overshoot procedure				
i	6.0 - 12.0		[-]	Step size control parameter
h_{min}	1.0	$\cdot 10^{-i}$	[-]	Minimum stepsize
h_{max}	1.0	$\cdot 10^{-i+1}$	[-]	Maximum stepsize

Table A.3: Parameter settings of the RKF7(8) used for trajectory propagation in CR3BP-LT. The settings have been obtained from [25].

In the Table above, ϵ_m denotes the machine epsilon. This variable is defined as the smallest quantity that can be added to number such that the machine interprets it as another number [2]. It's value is given below in Equation A.3.

$$\epsilon_m \approx 2.2204460492503 \cdot 10^{-16} \tag{A.3}$$

The other numerical integration method employed in this thesis project is the 12^{th} order Legendre-Gauss-Lobatto (LGL) collocation scheme. An extensive discussion on this method is provided in Appendix B. Contrary to the RK7(8) procedure, this method is built from scratch and the parameter settings, obtained via a trial-and-error procedure, are shown below in Table A.4.

Symbol	Value		Unit	Description
	5		[−]	Initial number of nodes
$e_{i_{max}}$	1.0	$\cdot 10^{-9}$	[−]	Maximum error tolerance per segment
Δe_i	1.0	$\cdot 10^{-12}$	[−]	Error equidistribution criterium

Table A.4: 12^{th} order Legendre-Gauss-Lobatto collocation methods parameter settings.

A.2.2. Settings for equilibria generation

The construction of the equilibria contours relies on a multivariate Newtown-Raphson (NR) root-finding method. An elaborate discussion on this method is provided in Appendix C. The settings of the root-finding procedure have been determined via a trial-and-error procedure resulting in robust performance as long as Equation A.4 is satisfied. The settings of the root-finding procedure can be found in Table A.5.

$$a_{lt} \leq 0.25 \tag{A.4}$$

Symbol	Value		Unit	Description
l	2.0	$\cdot 10^{-1}$	[−]	Relaxation parameter
	1.0	$\cdot 10^{5}$	[−]	Maximum number of univariate NR iterations
	8.0	$\cdot 10^{4}$	[−]	Maximum number of multivariate NR iterations
	1.0	$\cdot 10^{-13}$	[−]	Maximum potential deviation
$\Delta\alpha$	1.0	$\cdot 10^{-2}$	[°]	Step size angle contour
Δa_{lt}	1.0	$\cdot 10^{-5}$	[−]	Step size acceleration contour
	10		[−]	Save frequency
	0.1		[−]	Upper acceleration limit
$\lvert\alpha_{start} - \alpha\rvert$	$< 2\pi$		[rad]	Angle stopping condition

Table A.5: Settings of the Newton-Rapson multivariate root-finder employed for equilibria contour construction.

A.2.3. Settings for orbit generation

The l.p.o family construction process comprises a three-step approach as explained in Chapter 1 of this report. The first step concerns the generation of the approximate seed solutions via a Floquet targeter (FT). A detailed discussion and performance analysis of this technique is presented in Appendix C. The settings of the targeter algorithm have been determined via a trial-and-error procedure resulting in robust performance for in-plane amplitudes values far beyond the required amplitude of the seed solutions. An overview of these settings is provided below in Table A.6.

Symbol	Value		Unit	Description
A_x	1.0	$\cdot 10^{-5}$	[−]	Amplitude for first approximate solution
A_x	1.0	$\cdot 10^{-4}$	[−]	Amplitude for second approximate solution
	1.0	$\cdot 10^{-13}$	[−]	Numerical threshold for motion decomposition
	5.0	$\cdot 10^{-2}$	[−]	Time interval between two FT corrections
	1.0	$\cdot 10^{-6}$	[−]	Maximum eigenvalue deviation
	1000		[−]	Save frequency

Table A.6: Algorithm settings of the Floquet targeter used for computation of the approximate periodic solutions.

The second step in construction of l.p.o families concerns the refinement of the initial guess constructions via a multiple shooting approach known as the two-level targeter (TLT). An extensive discussion on the principles and performance of this method can be found in Appendix C. The values of the parameters involved in the TLT procedure are shown below in Table A.7.

Value		Unit	Description
5		[−]	Number of nodes
10		[−]	Maximum Number of TLT Cycles
1.0	$\cdot 10^{-12}$	[−]	Maximum position deviation
5.0	$\cdot 10^{-12}$	[−]	Maximum velocity deviation
1.0	$\cdot 10^{-12}$	[−]	Maximum period deviation
1000		[−]	Save frequency

Table A.7: Settings for the TLT algorithm employed for refinement of approximate seed solutions.

The numerical continuation procedure concerns the final step in the construction of the Hamiltonian-varying (H_{lt}-varying), acceleration-varying (a_{lt}-varying) and orientation-varying (α-varying) l.p.o families. The parameters of the continuation procedure are shown below in Table A.8 and have been established via a trial-and-error procedure.

Symbol	Value		Unit	Description
	5.0	$\cdot 10^{3}$	[−]	Maximum number of family members
	1.0	$\cdot 10^{-4}$	[−]	Pseudo-arclength H_{lt}-varying family
Δa_{lt}	1.0	$\cdot 10^{-2}$	[−]	Increment a_{lt}-varying family
$\Delta\alpha$	1.0		[°]	Increment α-varying family
κ	$[0.1, 0.2, \ldots, 1.0]$		[−]	Line search attenuation parameter
ϵ	1.0	$\cdot 10^{-10}$	[−]	Complex step increment
$\|\|\mathbf{F}\|\|$	1.0	$\cdot 10^{-12}$	[−]	Maximum defect vector magnitude
	5.0	$\cdot 10^{3}$	[−]	Maximum number of collocation iterations
	1.0	$\cdot 10^{-3}$	[−]	Maximum center eigenvalue deviation
	1.0	$\cdot 10^{-3}$	[−]	Maximum eigensystem determinant deviation
	1.0	$\cdot 10^{-5}$	[-]	Minimum spacing between family members at half-phase
	1.0	$\cdot 10^{-9}$	[-]	Maximum state component discrepancy at full-period

Table A.8: Settings for the numerical continuation procedure of the three types of periodic solution families.

The data in Tables A.1-A.8 comprise all constants and parameters employed during this thesis project and allow the reader to reproduce the results presented in Chapter 1 of this report.

B

Numerical integration

This Appendix provides a discussion on the techniques that are used for trajectory propagation in the CR3BP-LT. The propagation of trajectories requires one to find a solution to a set of differential equations subjected to various constraints [23]. In literature, this commonly referred to as a Boundary Value Problem (BVP). Numerical integrators are able to solve these systems of differential equations and two of them are adopted in this thesis project. The remainder of Appendix B presents the principles of both integrators. Section B.1 discusses the fundamentals of the RKF78 integrator while Section B.2 presents the principles of the 12^{th} order Legendre-Gauss-Lobatto collocation method.

B.1. Runge-Kutta Fehlberg 7(8) method

The RKF7(8) integrator belongs to the family of Runge-Kutta methods. These methods are widely used in the scientific community because of their simplicity and capability to straightforwardly control the truncation error [3]. The RKF7(8) integration procedure is a so-called explicit Runge-Kutta method since it uses the current state of the system to approximate the system's solution at another state. The principles of the RK78 method are illustrated on the basis of the system depicted in Equation B.1.

$$\dot{y} = f(x, y), \quad y(x_n) = Y_n, \quad x_{n+1} - x_n = h \tag{B.1}$$

The system's solution (y_n) is known at a particular location (x_n). Suppose one is interested in the solution at a new location x_{n+1} which is separated from x_{n-1} by a distance h, commonly referred to as the stepsize. Explicit Runge-Kutta methods compute the solution at the new location according to Equation B.2.

$$y_{n+1} = y_n + hF(x_n, y_n, h; f) \tag{B.2}$$

It can be observed from Equation B.2 that the core principle of Runge-Kutta methods is the approximation of the average slope over the specified increment. This is achieved by computing a weighted averages of slopes at different locations within the increment interval. The procedure for computing the weighted average slope is shown in Equations B.3-B.5 and involves a set of nodes (Z_j) with associated external weights (γ_j). The number of function evaluations per integration step (s) is referred to as stages. For an s-stage Runge-Kutta method, the location of the nodes and their respective weights are fixed on the increment interval.

$$F(x_n, y_n, h; f) = \sum_{j=1}^{s} \gamma_j Z_j \tag{B.3}$$

$$Z_1 = f(x_n, y_n) \tag{B.4}$$

$$Z_j = f(x + \alpha_j h, y + \sum_{i}^{j-1} \beta_{ij} Z_i) \quad j = 2, \ldots, s \tag{B.5}$$

For sake of accuracy, it is desirable that the local truncation error is constant for each step of the integration process. Embedded Runge-Kutta-Fehlberg methods provide an error estimate by comparing the computed solution of an Runge-Kutta method accurate up to order p with the solution obtained by a Runge-Kutta

method accurate up to order $p+1$. This error estimate can be obtained with little extra computation cost since the higher order method uses the same function evaluations as the lower order method. The RKF7(8) method belongs to this category of Runge-Kutta methods and the exact procedure can be described in a so-called Butcher tableau presented below in Table B.1.

	β_{ij}													
α_j	1	2	3	4	5	6	7	8	9	10	11	12	γ_j	$\hat{\gamma}_j$
0													41/840	0
2/27	2/27												0	0
1/9	1/36	1/12											0	0
1/6	1/24	0	1/8										0	0
5/12	5/12	0	-25/16	25/16									0	0
1/2	1/20	0	0	1/4	1/5								34/105	34/105
5/6	-25/108	0	0	125/108	-65/27	125/54							9/35	9/35
1/6	31/300	0	0	0	61/225	-2/9	13/900						9/35	9/35
2/3	2	0	0	-53/6	704/45	-107/9	67/90	3					9/280	9/280
1/3	-91/108	0	0	23/108	-976/135	311/54	-19/60	17/6	-1/12				9/280	9/280
1	2383/4100	0	0	-341/161	4496/1025	-301/82	2133/4100	45/82	45/164	18/4			41/840	0
0	3/205	0	0	0	0	-6/41	-3/205	-3/41	3/41	6/41	0		0	41/840
1	-1777/4100	0	0	-341/161	4496/1025	-289/82	2193/4100	51/82	33/164	12/41	0	1	0	41/840

Table B.1: The Butcher tableau of the RKF7(8) method as presented in [11]. External weights of the higher order are indicated by $\hat{y_j}$

The difference between the two solutions produced by the p^{th} and $(p+1)^{th}$ order method, provides an estimate of the truncation error ($e(h_i)$). The truncationerror estimate together with the error tolerance (ϵ_{tol}) allows adaption of the stepsize. The stepsize adaption procedure is outlined in Equation B.6 [28]. The largest of the absolute and relative error provides the error tolerance for the stepsize adaption procedure. The integration process is repeated with the new stepsize ($e^*(h_i)$) until the error criteria are satisfied. This procedure leads to a consistent truncation error over the complete integration process.

$$\begin{aligned} e(h_i) &= |\hat{y}_i - y_i| \\ h_i^* &= \sqrt[p+1]{\frac{\epsilon_{tol}}{e(h_i)}}] \cdot h_i \end{aligned} \tag{B.6}$$

The methodology outlined in Section B.1 establishes the numerical integration process that is leveraged in the approximation and refinement of the seed solutions for the l.p.o families as well as the verification of the periodic solutions.

B.2. 12th order Legendre-Gauss-Lobatto collocation method

The other numerical integration technique deployed in this thesis is the 12th order Legendre-Gauss-Lobatto collocation method. Subsection B.2.1 explains underlying process of collocation, while Subsection B.2.2 explains the methodology for error control.

B.2.1. Numerical integration through Gauss-Legendre-Lobatto quadrature

Collocation methods approximate the solution to an ordinary differential equation from a set of states via polynomial interpolation. For purpose of illustration, consider the system depicted in Equation B.7 [33]. This problem concerns the identification of a solution to an ordinary differential equation over the time interval $[t_{n-1}, t_n]$ separated by a time increment (h).

$$\begin{aligned} &\dot{y} = f(x,y), \text{ given a set of solutions } \quad y(t_1), y(t_2), \ldots, y(t_s) \\ &t_i = t_{n-1} + c_i h, \quad 0 \leq c_1 < c_2 < \cdots < c_s \leq 1 \end{aligned} \tag{B.7}$$

The goal of the collocation method is to find a polynomial ϕ up to a degree s which satisfies conditions listed below in Equation B.8. When these conditions are satisfied, the solution to the system in Equation B.7 is known on the entire segment $[t_{n-1}, t_n]$. The reliance of collocation methods on a reference trajectory show that collocation methods are implicit in nature [33].

$$\begin{aligned} \phi(t_{n-1}) &= y_{n-1} \\ \dot{\phi}(t_i) &= f(t_i, \phi(t_i)) \end{aligned} \tag{B.8}$$

All collocation methods discretize the reference trajectory into a set of n nodes, resulting in $n-1$ segments. At each segment, so-called interior points and defect points are added. The former, in conjunction with the segment bounds, is used for construction of the polynomial while the latter type allows one to check whether the constructed polynomial accurately approximates the dynamics of the reference trajectory. The number and distribution of the interior and defect points over a single segment is referred to as the node placement strategy which is unique per collocation method. This thesis project employs the 12th order Legendre-Gauss-Lobatto collocation method which places two interior points and three defect points at each segment. An illustration of the discretization procedure, together with the 12th order Legendre-Gauss-Lobatto node placement strategy is shown in Figure B.1.

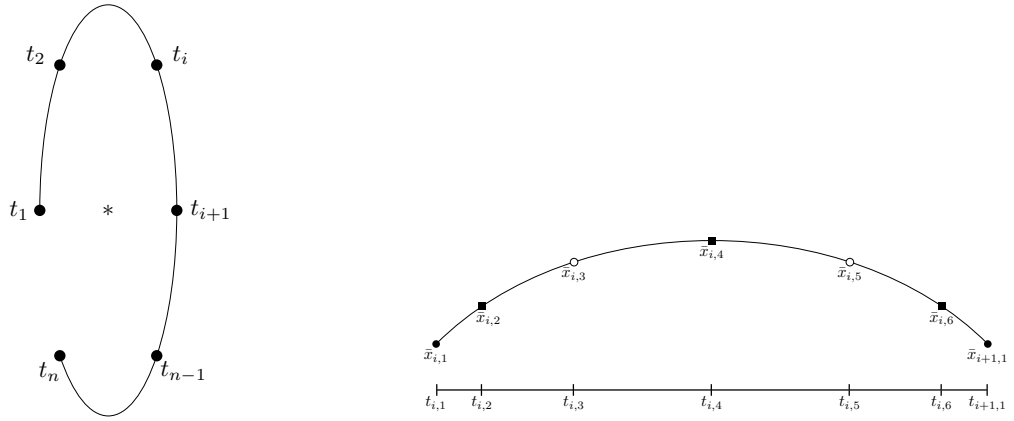

Figure B.1: The left figure shows the discretization of the trajectory into $n-1$ segments. The right picture shows how a seventh degree polynomial is constructed for a single segment. The bounds of the segment, denoted with black circles, together with the interior points, symbolized by white circles, are used to construct to the polynomial. The locations of the defect points are indicated by the black squares.

The node placement strategy is defined by the normalized time values of the collocation points. The normalized time values for the 12th order Legendre-Gauss-Lobatto collocation method can be found in Table B.2 [14].

node time symbol	normalized time symbol	normalized time value		node type
$t_{i,1}$	τ_1	0		node
$t_{i,2}$	τ_2	8.4888051860717	$\cdot 10^{-2}$	defect point
$t_{i,3}$	τ_3	2.65575603264643	$\cdot 10^{-1}$	interior point
$t_{i,4}$	τ_4	5.0	$\cdot 10^{-1}$	defect point
$t_{i,5}$	τ_5	7.34424396735357	$\cdot 10^{-1}$	interior point
$t_{i,6}$	τ_6	9.15111948139284	$\cdot 10^{-1}$	defect point
$t_{i+1,1}$	τ_7	1.0		node

Table B.2: The normalized time values characterizing the node placement starategy of the 12th order Legendre-Gauss-Lobatto collocation method. Values reproduced from [14].

Polynomial interpolation allows the computation of the solution on the entire segment interval via Equation B.9.

$$\bar{x}(\tau) = \mathbf{p}_i(\tau) = C_i \cdot \begin{bmatrix} 1 & \tau & \tau^2 & \tau^3 & \tau^4 & \tau^5 & \tau^6 & \tau^7 \end{bmatrix}^T \quad \text{on} \quad [t_i, t_{i+1}], \quad 0 \leq \tau \leq 1 \tag{B.9}$$

The piecewise polynomial is defined by the the coefficient matrix C_i, which depends upon a constant matrix ($\boldsymbol{B}$), shown in Equation B.11, the time duration of the segment (Δt), states $\bar{x}_i$ and field vector evaluation ($\bar{f}(\bar{x}_i)$). The coefficient matrix can be computed through Equation B.10.

$$C_i = \begin{bmatrix} \bar{x}_{i,1} & \bar{x}_{i,3} & \bar{x}_{i,5} & \bar{x}_{i+1,1} & \bar{x}'_{i,1} & \bar{x}'_{i,3} & \bar{x}'_{i,5} & \bar{x}'_{i+1,1} \end{bmatrix} \cdot B_i^{-1} \quad \text{where} \quad \bar{x}'_i = \Delta t_i \cdot \bar{f}(\bar{x}_i) \tag{B.10}$$

$$B_i = \begin{bmatrix} 1 & 1 & 1 & 1 & 0 & 0 & 0 & 0 \\ \tau_1 & \tau_3 & \tau_5 & \tau_7 & 1 & 1 & 1 & 1 \\ \tau_1^2 & \tau_3^2 & \tau_5^2 & \tau_7^2 & 2\tau_1 & 2\tau_3 & 2\tau_5 & 2\tau_7 \\ \tau_1^3 & \tau_3^3 & \tau_5^3 & \tau_7^3 & 3\tau_1^2 & 3\tau_3^2 & 3\tau_5^2 & 3\tau_2^7 \\ \tau_1^4 & \tau_3^4 & \tau_5^4 & \tau_7^4 & 4\tau_1^3 & 4\tau_3^3 & 4\tau_5^3 & 4\tau_7^3 \\ \tau_1^5 & \tau_3^5 & \tau_5^5 & \tau_7^5 & 5\tau_1^4 & 5\tau_3^4 & 5\tau_5^4 & 5\tau_7^4 \\ \tau_1^6 & \tau_3^6 & \tau_5^6 & \tau_7^6 & 6\tau_1^5 & 6\tau_3^5 & 6\tau_5^5 & 6\tau_7^5 \\ \tau_1^7 & \tau_3^7 & \tau_5^7 & \tau_7^7 & 7\tau_1^6 & 7\tau_3^6 & 7\tau_5^6 & 7\tau_7^6 \end{bmatrix} \tag{B.11}$$

Defect constraints are critical to obtain a polynomial that correctly approximates the dynamics over the entire interval. These constraints are computed at all three defect points according to Equations B.12-B.14.

$$\begin{aligned} \bar{\zeta}_{i,2} &= b_i^1 \bar{x}_{i,1} + b_{i,3}^1 \bar{x}_{i,3} + b_{i,5}^1 \bar{x}_{i,5} + b_{i+1,1}^1 \bar{x}_{i+1,1} \\ &\quad + \Delta t_i (w_{i,1}^1 \bar{f}_{i,1} + w_{i,2}^1 \bar{f}_{i,2} + w_{i,3}^1 \bar{f}_{i,3} + w_{i,5}^1 \bar{f}_{i,5} + w_{i+1,1}^1 \bar{f}_{i+1,1}) \end{aligned} \tag{B.12}$$

$$\begin{aligned} \bar{\zeta}_{i,4} &= b_i^c \bar{x}_{i,1} + b_{i,3}^c \bar{x}_{i,3} + b_{i,5}^c \bar{x}_{i,5} + b_{i+1,1}^c \bar{x}_{i+1,1} \\ &\quad + \Delta t_i (w_{i,1}^c \bar{f}_{i,1} + w_{i,3}^c \bar{f}_{i,3} + w_{i,4}^c \bar{f}_{i,4} + w_{i,5}^c \bar{f}_{i,5} + w_{i+1,1}^c \bar{f}_{i+1,1}) \end{aligned} \tag{B.13}$$

$$\begin{aligned} \bar{\zeta}_{i,6} &= b_i^6 \bar{x}_{i,1} + b_{i,3}^6 \bar{x}_{i,3} + b_{i,5}^6 \bar{x}_{i,5} + b_{i+1,1}^6 \bar{x}_{i+1,1} \\ &\quad + \Delta t_i (w_{i,1}^6 \bar{f}_{i,1} + w_{i,3}^6 \bar{f}_{i,3} + w_{i,5}^6 \bar{f}_{i,5} + w_{i,6}^6 \bar{f}_{i,6} + w_{i+1,1}^6 \bar{f}_{i+1,1}) \end{aligned} \tag{B.14}$$

The values for the constants b_i^j and w_i^j can be found below in Table B.3.

Parameter	Value		Parameter	Value	
b_i^1	+8.84260109348311	$\cdot 10^{-1}$	b_3^1	-8.23622559094327	$\cdot 10^{-1}$
b_5^1	-2.35465327970606	$\cdot 10^{-2}$	b_{i+1}^1	-3.70910174569208	$\cdot 10^{-2}$
b_i^c	+7.86488731947674	$\cdot 10^{-2}$	b_3^c	+8.00076026297266	$\cdot 10^{-1}$
b_5^c	-8.00076026297266	$\cdot 10^{-1}$	b_{i+1}^c	-7.86488731947674	$\cdot 10^{-2}$
b_i^6	+3.70910174569208	$\cdot 10^{-2}$	b_3^6	+2.35465327970606	$\cdot 10^{-2}$
b_5^6	+8.23622559094327	$\cdot 10^{-1}$	b_{i+1}^6	-8.84260109348311	$\cdot 10^{-1}$
$w_{i,1}^1$	+1.62213410652341	$\cdot 10^{-2}$	$w_{i,2}^1$	+1.38413023680783	$\cdot 10^{-1}$
$w_{i,3}^1$	+9.71662045547156	$\cdot 10^{-2}$	$w_{i,5}^1$	+1.85682012187242	$\cdot 10^{-2}$
$w_{i+1,1}^1$	+2.74945307600086	$\cdot 10^{-3}$	$w_{i,1}^c$	+4.83872966828888	$\cdot 10^{-3}$
$w_{i,3}^c$	+1.00138284831491	$\cdot 10^{-1}$	$w_{i,4}^c$	+2.43809523809524	$\cdot 10^{-1}$
$w_{i,5}^c$	+1.00138284831491	$\cdot 10^{-1}$	$w_{i+1,1}^c$	+4.83872966828888	$\cdot 10^{-3}$
$w_{i,1}^6$	+2.74945307600086	$\cdot 10^{-3}$	$w_{i,3}^6$	+1.85682012187242	$\cdot 10^{-2}$
$w_{i,5}^6$	+9.71662045547156	$\cdot 10^{-2}$	$w_{i,6}^6$	+1.38413023680783	$\cdot 10^{-1}$
$w_{i+1,1}^6$	+1.62213410652341	$\cdot 10^{-1}$			

Table B.3: An overview of the constants for the defect computation for the 12^{th} order Legendre-Gauss-Lobatto collocation method. Data is directly obtained from [14].

If the defect constraints do not meet the tolerance specified in Table A.4, The totality of nodes, interior points and defect points should be altered to improve the polynomial approximation of the dynamics. The procedure for this correction is presented in Section C.5.

B.2.2. Error control via Boor's method

A collocation problem solved via the methodology explained in Sections B.2.1 and C.5 does not necessarily satisfy the tolerances as specified in Table A.8. The root cause of the invalidity of such a solution is that the segment truncation error can vary widely over the mesh (i.e the totality of nodes representing the discretization of the trajectory). An ideal mesh equidistributes the truncation error over the segments and keeps the magnitude of this error within bounds as specified in Table A.8. This process is referred to as mesh refinement and is equivalent to the concept of stepsize control in explicit integration schemes [8]. The remainder of this

section explains the principles of Boor's method of mesh refinement [9]. This mesh refinement error method is favoured because no higher-order solution is required for error estimation which makes it a computationally efficient method. The following explanation is based on [8, 9, 14] unless stated otherwise.

The input for error control procedure is a discretized trajectory, proposed as a solution by the collocation procedure as outlined in Sections B.2.1 and C.5, with a mesh according to Equation B.15[8].

$$\Pi : t_1 < t_2 < \cdots < t_n \tag{B.15}$$

The error per segment, can be computed according to Equation B.16, where Δt_i denotes the time duration of the segment and ξ_i represents the eighth-order derivative of segment i.

$$\begin{aligned} e_i &= C\Delta t_i^8 \xi_i + \mathcal{O}(\Delta t_i^9), \quad i = 1, \ldots, n-1 \\ C &= 2.93579395141895 \cdot 10^{-9} \end{aligned} \tag{B.16}$$

The eighth-order derivative can be computed via a difference scheme, shown below in Equation B.17.

$$\xi i \approx \left\{ \begin{array}{cc} 2\max\left[\frac{|\mathbf{p}_1^7 - \mathbf{p}_2^7|}{\Delta t_1 + \Delta t_2}\right] & \text{on} \quad (t_1, t_2) \\ \max\left[\frac{|\mathbf{p}_{i-1}^7 - \mathbf{p}_i^7|}{\Delta t_{i-1} + \Delta t_i}\right] + \max\left[\frac{|\mathbf{p}_{i+1}^7 - \mathbf{p}_i^7|}{\Delta t_{i+1} + \Delta t_i}\right] & \text{on} \quad (t_i, t_{i+1}) \quad \text{for} \quad i = 2, \ldots, n-2 \\ 2\max\left[\frac{|\mathbf{p}_n^7 - \mathbf{p}_{n-1}^7|}{\Delta t_1 + \Delta t_2}\right] & \text{on} \quad (t_{n-1}, t_n) \end{array} \right] \tag{B.17}$$

The differencing scheme involves the seventh order derivatives $\boldsymbol{p}_i^7$ which can be computed using Equation B.18, where $\boldsymbol{b}$ denotes the final column of B_i^{-1}

$$\boldsymbol{p}_i^7 = 7! \begin{bmatrix} x_{i,1} & x_{i,3} & x_{i,5} & x_{i+1,1} & x'_{i,1} & x'_{i,3} & x'_{i,5} & x'_{i+1,1} \end{bmatrix} \frac{\boldsymbol{b}}{\Delta t_i^7} \tag{B.18}$$

The differencing scheme involves seventh-order derivatives $\boldsymbol{p}_i^7$ which can be computed using Equation B.18, where $\boldsymbol{b}$ denotes the final column of B_i^{-1}. The new mesh is then recomputed according to Equation B.19.

$$t_{i+1} = I^{-1}\left[\frac{iI(t_n)}{n-1}\right] \quad \text{for} \quad i = 1, \ldots, n-2 \tag{B.19}$$

The quantity $I(t)$ is defined in Equation B.20 and can be computed exactly since it is a piecewise linear function.

$$I(t) = \int_{t_1}^{t} \xi^{\frac{1}{8}}(s)\, ds \tag{B.20}$$

The states corresponding to the new mesh are computed via polynomial interpolation. The updated mesh is fed back into the collocation procedure and this procedure is repeated until the mesh satisfies the segment truncation error distribution tolerance and segment error magnitude criterium as specified in Table A.4. If the mesh satisfies the equidistribution criterium but does not meet segment truncation error magnitude tolerance the number of nodes is increased according to Equation B.21 [9].

$$n_{\text{new}} = \text{round}\left[n_{\text{old}}\left(\frac{10e_i}{\text{tol}}\right)^{\frac{1}{8}} + 5\right] \tag{B.21}$$

The new mesh with the updated number of nodes is subjected to the collocation and mesh refinement procedure until the error is equidistributed again. The totality of the collocation procedure and Boor's method of error control ensures that the solution adheres to the tolerances as specified in Table A.8.

This concludes the discussion on the numerical integration techniques employed during this thesis project. Recommendations for improving these techniques can be found in Chapter G.

This page is intentionally left blank.

C

Root-finding algorithms

Root-finding algorithms are the backbone of this thesis project. In conjunction with numerical integrators, these algorithms allow the construction of the equilibria contours and l.p.o families. This addendum provides an overview of all the root-finding algorithms employed during this thesis work. Section C.1 provides the reader with the principles of multivariate root-finding. The root-finder algorithm that computes the artificial equilibria is presented in Section C.2. Section C.3 discusses the targeting scheme that computes the approximate seed solutions. The refinement of these seed solutions is accomplished via the two-level targeter (TLT) which is explained in Section C.4. Finally, the algorithm that constructs the l.p.o families during the numerical continuation procedure is explained in Section C.5.

C.1. Multivariate Newton's method

The multivariate Newton's method is a numerical method which can solve a set of nonlinear equations subjected to multiple nonlinear constraints. It does so by finding the solution $\boldsymbol{X}$, commonly referred to as the design vector, such that the residual $\boldsymbol{F}$, commonly referred to as the defect vector, at this solution is zero. The mathematical formulation of this objective is shown below in Equation C.1 [24].

$$\boldsymbol{F}(\boldsymbol{X}) = 0 \tag{C.1}$$

The multivariate Newton's method is initialized with a seed solution, denoted by $\boldsymbol{X}_0$ with $\boldsymbol{F}(\boldsymbol{X}_0) > 0$. The solution to the system is found through an iterative process where $\boldsymbol{F}(\boldsymbol{X}_i) > \boldsymbol{F}(\boldsymbol{X}_{i+1}) > 0$. The design vector is updated throughout the iterative process until Equation C.1 is met. The required update can be computed from Equation C.2.

$$\boldsymbol{F} = D\boldsymbol{F}\Delta\boldsymbol{X}, \text{ where } \boldsymbol{X}_{i+1} = \boldsymbol{X}_i + \Delta\boldsymbol{X} \tag{C.2}$$

In the Equation above, $D(\boldsymbol{F})$ denotes the Jacobian of $\boldsymbol{X}$ with respect to $\boldsymbol{F}$. The Jacobian provides a relationship between the defect vector and design variables which allows one to find the required update to the current solution. For sake of clarity, the Jacobian is displayed in Equation C.3.

$$\boldsymbol{F} = \begin{bmatrix} \bar{f}_1 \\ \bar{f}_2 \\ \vdots \\ \bar{f}_k \end{bmatrix}, \quad \boldsymbol{X} = \begin{bmatrix} \bar{x}_1 \\ \bar{x}_2 \\ \vdots \\ \bar{x}_l \end{bmatrix}, \quad D\boldsymbol{F} = \frac{\partial \boldsymbol{F}}{\partial \boldsymbol{X}} = \begin{bmatrix} \frac{\partial \bar{x}_1}{\partial \bar{f}_1} & \frac{\partial \bar{x}_1}{\partial \bar{f}_2} & \cdots & \frac{\partial \bar{x}_1}{\partial \bar{f}_k} \\ \frac{\partial \bar{x}\bar{x}_2}{\partial \bar{f}_1} & \frac{\partial \bar{x}_2}{\partial \bar{f}_2} & \cdots & \frac{\partial \bar{x}_2}{\partial \bar{f}_k} \\ \vdots & \vdots & \ddots & \vdots \\ \frac{\partial \bar{x}_l}{\partial \bar{f}_1} & \frac{\partial \bar{x}_l}{\partial \bar{f}_2} & \cdots & \frac{\partial \bar{x}_l}{\partial \bar{f}_k} \end{bmatrix} \tag{C.3}$$

In case the number of unknowns equals the number of equations ($k = l$). The required update $\Delta\boldsymbol{X}$ can be computed via Equation C.4.

$$\Delta\boldsymbol{X} = -(D\boldsymbol{F})^{-1}\boldsymbol{F} \tag{C.4}$$

The number of unknowns will often exceed the number of equations ($k > l$). In that event, the update is computed via the Gauss-Newton algorithm, displayed below in Equation C.5 [6].

$$\Delta\boldsymbol{X} = -D\boldsymbol{F}^T\left(D\boldsymbol{F}D\boldsymbol{F}^T\right)^{-1}\boldsymbol{F} \tag{C.5}$$

The methodology presented in this Section provides the reader with the working principles of multivariate root-finding which is leveraged by all root-finders presented in the remainder of this Chapter.

C.2. Equilibria root-finding procedure

This section outlines the multivariate root-finding algorithm that computes the two types of artificial equilibria contours. The first type of equilibria contour has a fixed acceleration orientation while the acceleration magnitude varies over the curve. For this type of contour, the natural equilibria are employed as seed solutions. The design and defect vector for this procedure are listed in Equation C.6, whereas the partial derivatives of the Jacobian are presented in Equation C.7.

$$\boldsymbol{X} = \begin{bmatrix} x \\ y \end{bmatrix} \quad \boldsymbol{F} = \begin{bmatrix} f_1 \\ f_2 \end{bmatrix} = \begin{bmatrix} x\left(1 - \frac{1-\mu}{r_{13}^3} - \frac{\mu}{r_{23}^3}\right) + \mu\left(-\frac{1-\mu}{r_{13}^3} - \frac{\mu}{r_{23}^3}\right) + \frac{\mu}{r_{23}^3} + a_{lt}\cos(\alpha) \\ y\left(1 - \frac{1-\mu}{r_{13}^3} - \frac{\mu}{r_{23}^3}\right) + a_{lt}\sin(\alpha) \end{bmatrix} \tag{C.6}$$

$$\begin{aligned}
D\boldsymbol{F} &= \begin{bmatrix} \frac{\partial f_1}{\partial x} & \frac{\partial f_1}{\partial y} \\ \frac{\partial f_2}{\partial x} & \frac{\partial f_2}{\partial y} \end{bmatrix} = \begin{bmatrix} D\boldsymbol{F}_{11} & D\boldsymbol{F}_{12} \\ D\boldsymbol{F}_{21} & D\boldsymbol{F}_{22} \end{bmatrix} \\
D\boldsymbol{F}_{11} &= \left(1 - \frac{1-\mu}{r_{13}^3} - \frac{\mu}{r_{23}^3}\right) + (x+\mu)\left(3\frac{1-\mu}{r_{13}^5}(x+\mu) + 3\frac{\mu}{r_{23}^5}(x-1+\mu)\right) - 3\frac{\mu}{r_{23}^5}(x-1+\mu) \\
D\boldsymbol{F}_{12} &= (x+\mu)\left(3\frac{1-\mu}{r_{13}^5}y + 3\frac{\mu}{r_{23}^5}y\right) - 3\frac{\mu}{r_{23}^5}y \\
D\boldsymbol{F}_{21} &= y\left(3\frac{1-\mu}{r_{13}^5}(x+\mu) + 3\frac{\mu}{r_{23}^5}(x-1+\mu)\right) \\
D\boldsymbol{F}_{22} &= \left(1 - \frac{1-\mu}{r_{13}^3} - \frac{\mu}{r_{23}^3}\right) + y\left(3\frac{1-\mu}{r_{13}^5}y + 3\frac{\mu}{r_{23}^5}y\right)
\end{aligned} \tag{C.7}$$

The desired increment is computed according to Equation C.4. Correcting the solution in this way did not result in robust behaviour and led to the cyclic and sometimes divergent behaviour of the root-finder. Robust performance has been achieved by the introduction of a relaxation parameter (l), which attenuates the increment of the root-finding procedure [20]. Hence, the solution is updated according to Equation C.8.

$$\boldsymbol{X}_{i+1} = \boldsymbol{X}_i + l \cdot \Delta\boldsymbol{X} \tag{C.8}$$

When an equilibrium is found using the procedure listed in Equations C.6-C.8, the acceleration magnitude is increased and a new equilibrium is found via the root-finding procedure until acceleration magnitude exceeds an upper limit ($a_{lt_{,\max}} = 0.1$). The values for the acceleration increment and relaxation parameter can be found in Table A.5.

The second type of equilbria contour has fixed acceleration magnitude while the acceleration orientation varies over the contour. This contour is initialized from collinear equilibria with the desired acceleration magnitude. The seed solution(s) are found using the a relaxed version of the Newton-Raphson method, shown below in Equation C.9

$$x_1 = x_0 - l \cdot \frac{f(x_0)}{f'(x_0)} \tag{C.9}$$

In the Equation above, $f(x)$ equals f_1 of Equation C.6 while $f'(x)$ equals $D\boldsymbol{F}_{11}$ of Equation C.7. Th complete equilibria contours are achieved by incrementing the acceleration orientation in both a clockwise and counterclockwise fashion for each seed solution until the angle stopping condition is reached. This stopping condition is listed in Table A.5.

The procedure listed above provides robust performance while $a_{lt} \leq 0.25$. It worth noting that the equilibria contours start to merge if $a_{lt} > 0.25$ [1]. This merging phenomenon is likely the root cause for failure of the equilibria root-finding procedure. If one is interested in investigating the merging of these equilibria contours, the reader is referred to Chapter G for suggestions performance improvement of the equilibria root-finding procedure.

C.3. Floquet targeter

The approximate solutions of the first two members of H_{lt}-varying l.p.o families are constructed via a targeting scheme based on Floquet analysis [21]. The so-called Floquet targeter decomposes the spacecraft motion along the six stability components and determines a velocity correction to cancel out the unwanted components of motion. Section C.3.1 explains the fundamentals of the Floquet targeter and how the procedure is adapted to facilitate the construction of libration point orbits. The procedure of constructing approximate seed solutions is presented in Section C.3.2. This section is concluded with a performance analysis of the targeter scheme in Section C.3.3.

C.3.1. Velocity correction via Floquet analysis

To determine the required velocity correction at an arbitrary time, the Floquet controller should be provided with a periodic reference trajectory in the form of a monodromy matrix $M = \Phi(T,0)$ and an initial deviation with respect to this trajectory $\delta\bar{x}(t_0)$. The deviation at the time of interest is then easily obtained from Equation C.10.

$$\delta\bar{x}(t) = \Phi(t,0)\delta\bar{x}(t_0) \tag{C.10}$$

The Floquet controller decomposes this deviation into six states which indicate the deviation of spacecraft along each stability components with the help of Equation C.11.

$$\delta\bar{x}_t = \sum_{j=1}^{6} \delta\bar{x}_j = \sum_{j=1}^{6} \bar{g}_j(t)\bar{e}_j(t) \tag{C.11}$$

In the Equation above, $\bar{e}_i$ symbolizes the columns of the Floquet modal matrix $E(t)$ obtained from Equation C.13 whereas $\bar{g}_j$ represents the columns of matrix pertubation decomposition $G(t)$ shown in Equation C.12.

$$G(t) = E(t)^{-1}\delta\bar{x}(t) \tag{C.12}$$

The Floquet modal matrix depends upon the eigensystem of the reference trajectory J is a diagonal matrix which hold the complex characteristic exponents of the monodromy matrix. The eigenvectors related to these characteristic multipliers are stored in Matrix S

$$E(t) = \Phi(t,0)Se^{-Jt} \tag{C.13}$$

The motion decomposition matrix allows identification of the perturbation contributions of each stability component. Knowing these contributions allows determining of a velocity correction that cancels out the unwanted motion. The mathematical formulation of this problem is presented in Equation C.14 in which ι_j symbolises coefficients of the desired perturbation components.

$$\sum_{j=2,3,4} (1+\iota_j(t))\delta\bar{x}_j(t) = \sum_{j=1}^{6} \delta\bar{x}_j + \begin{bmatrix} 0_3 \\ \Delta\bar{V} \end{bmatrix} \tag{C.14}$$

The abovementioned procedure was originally designed for station keeping procedures in the vicinity of libration point orbits[21]. However, the procedure can be straightforwardly adapted for the construction of approximate periodic solutions. The reference trajectory is a stationary point rather than a periodic orbit. Since periodicity is not defined in a stationary point, The monodromy matrix of an equilibrium does not exist. However, the stability of an equilibrium point can be obtained from the eigensystem of the state propagation matrix (SPM). The deviation at any given time is simply obtained as the state difference between the equilibrium point and the current state of the spacecraft as displace in Equation C.15.

$$\delta\bar{x} = \bar{x}_{eq} - \bar{x} \tag{C.15}$$

It is evident that the deviation in Equation C.15 does not depend on time as opposed to Equation C.10. As a consequence, the Floquet modal matrix is a constant quantity and takes on the form as shown in Equation C.16

$$E = S \tag{C.16}$$

The Floquet targeter algorithm then boils down to Equation C.17.

$$\boldsymbol{X} = \begin{bmatrix} \iota_3 \\ \iota_4 \\ \dot{x} \\ \dot{y} \end{bmatrix}, \quad \boldsymbol{F} = \delta\bar{x}_1 + \delta\bar{x}_2 + \delta\bar{x}_5 + \delta\bar{x}_6,, \quad D\boldsymbol{F} = \begin{bmatrix} \delta\bar{x}_{3_r} & \delta\bar{x}_{4_r} & 0_2 \\ \delta\bar{x}_{3_v} & \delta\bar{x}_{4_v} & -I_2 \end{bmatrix} \tag{C.17}$$

The root-finding scheme ignores the out-of-plane stability components and out-of-plane state components to avoid an underdetermined system. In this way, the required velocity correction can be computed according to Equation C.4.

C.3.2. Construction of approximate periodic solutions

The root-finder algorithms presented in Sections C.4 and C.5 rely on a reference trajectory in the form of a set of nodes with associated times (i.e. a mesh). The approximate seed solutions are defined using an isochronous mesh as defined below in Equation C.18.

$$\Pi: \quad t_1 < \cdots < t_i < \cdots < t_n, \quad \text{for i = 2,...,n-1, where} \quad t_1 = 0, \; t_i = (i-1)\frac{t_n - t_1}{n-1} \; \text{and} \; t_n = T \tag{C.18}$$

The orbital period of the approximate periodic solution is unknown but Richardson's third-order method [31] provides an analytic expression for approximation of this period. This expression however, can only be used for libration point orbits that emanating from collinear equilibria. In this thesis project, an approximate orbital period is computed by propagating the initial state of a libration point orbit via a RK78 integration scheme until a full revolution has occurred. The initial state of this trajectory is determined in a two-way fashion. First, the initial position of the spacecraft is determined by offsetting it with respect to the equilibrium point according to Equation C.19. This positional offset provides an identical offset as Richardson's third-order method [31] in the case of natural l.p.o families but it extends well to libration point orbits emanating from artificial equilibria not located on the x-axis of the synodic reference frame.

$$\delta\bar{x}_{0_{\text{uncorrected}}} = \begin{bmatrix} A_x\cos(\theta) \\ A_x\sin(\theta) \\ 0 \\ 0 \\ 0 \\ 0 \end{bmatrix}, \quad \text{where} \quad \theta = \arctan2\left(y_{eq}, x_{eq} - (1.0-\mu)\right) \tag{C.19}$$

Secondly, the initial velocity of the spacecraft is computed according to the Floquet targeter specified in Equation C.17. The initial state is then computed via Equation C.20. The pseudocode for the aprroximation of the orbital period approximation is presented in Table C.1 .

$$\bar{x}_0 = \delta\bar{x}_{0_{\text{uncorrected}}} + \Delta\bar{V} \tag{C.20}$$

Pseudocode for orbital period approximation		
Input:	$\left(L_p, \bar{x}_0, \mu\right)$	
Output:	(T)	
1:	$\theta_0 \Leftarrow$ *ComputeOrbitAngle*$\left(\left(L_p, \bar{x}_0, \mu\right)\right)$	Equation C.19
2:	$\bar{x}_1, t_1 \Leftarrow$ *PropagateOrbit*$(\bar{x}_0, t_0)$	Section B.1
3:	$\theta_1 \Leftarrow$ *ComputeOrbitAngle*$\left(\left(L_p, \bar{x}_1, \mu\right)\right)$	Equation C.19
4:	**if** $\theta_1 - \theta_0 > 0$	
5:	$\quad\theta_{sign} = 1$	
6:	**else**	
7:	$\quad\theta_{sign} = -1$	
8:	$\theta_{change} = 0$	
9:	**while** $\theta_{change} < 2$	
10:	$\quad\bar{x}_i, t_i \Leftarrow$ *PropagateOrbit*$(\bar{x}_{i-1}, t_{i-1})$	Section B.1
11:	$\quad\theta_i \leftarrow$ *ComputeOrbitAngle*$\left(\left(L_p, \bar{x}_i, \mu\right)\right)$	Equation C.19
12:	$\quad\quad$**if** $(\theta_i - \theta_0)\cdot\theta_{sign} < 0$	
13:	$\quad\quad\quad\theta_{change}$++	
14:	$T = t_i$	

Table C.1: the subscript p refers to the equilibrium contour instead of the natural libration point. In the case that $p = 1$, the values of the orbit angle are rescaled to the [0,2π] domain to ensure proper functionality. The subscript i denotes a random state along the orbit and is not linked to the mesh as defined in Equation C.18.

With the orbital period known, the node times, as defined in Equation C.18, can be computed while their associated states can be approximated via explicit propagation. This completes the procedure for generation

of approximate periodic solutions. These start-up arcs serve as input for the two-level targeter algorithm which is described in Section C.4.

C.3.3. Effect of the velocity correction interval

The correction interval parameter of the Floquet targeter allows the user to exert control over the amount of velocity corrections that are performed during one orbital revolution. The effect of this parameter is analyzed in Figure C.1 which shows two sets of approximate periodic solutions. The sets of approximate periodic solutions have identical thrust parameters and in-plane amplitudes but differ in the amount of Floquet corrections which are applied during one orbital revolution. One family uses a correction interval $\Delta t = 50.0$ which means that no velocity corrections are applied during a single revolution. The other family uses a correction interval $\Delta t = 0.05$ resulting in a multitude of intermediate velocity corrections during a single revolution.

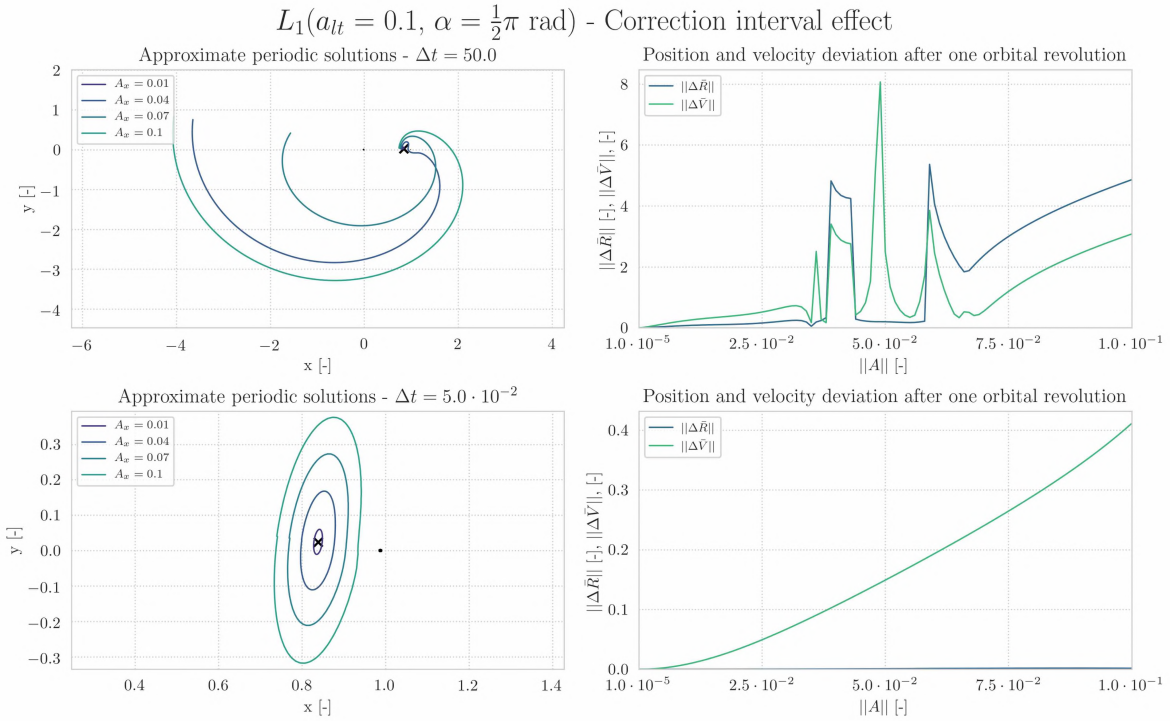

Figure C.1: Two families of approximate libration points generated by the floquet targeter with different correction intervals. The ΔV quantity in the bottom right plot symbolizes the totality of the velocity discrepancy at the full period and the intermediate velocity corrections. The maximum position discrepancy when using a $\Delta t = 5.0 \cdot 10^{-2}$ interval is $\Delta R = 1.9 \cdot 10^{-3}$

It can be observed from Figure C.1 that the intermediate corrections have a critical effect on the resulting trajectories. When no intermediate corrections are applied, the chaotic nature of the CR3BP-LT takes over resulting in unpredictable trajectories that do not come close to a periodic orbit. However, Trajectories remain bounded near the equilibrium when intermediate velocity corrections are applied. The deviation plots show that both the position and velocity discrepancy of the corrected trajectories are at least an order of magnitude smaller compared to the uncorrected trajectories for large amplitudes. Finally, it is worth noting that the corrected trajectories have an elliptical shape and do not posses the typical indent that is characteristic for the horizontal Lyapunov orbits.

C.4. Two-level targeter algorithm

A crucial step in the construction of the l.p.o families is the refinement of the approximate seed solutions to actual periodic orbits. Section C.4.1 explains the principles of this refinement procedure whereas the performance of the two-level targeter (TLT) is analysed in Section C.4.2. An extension to the TLT in the form of energy path constraints is discussed in Section C.4.3.

C.4.1. Two-level targeter correction scheme

As mentioned in Section C.3.2, the input into the TLT algorithm is a discretized trajectory in the form of n nodes with multiple state discontinuities. Each node is subjected to a set of constraints. A visualization of the input trajectory is shown below in Figure C.2.

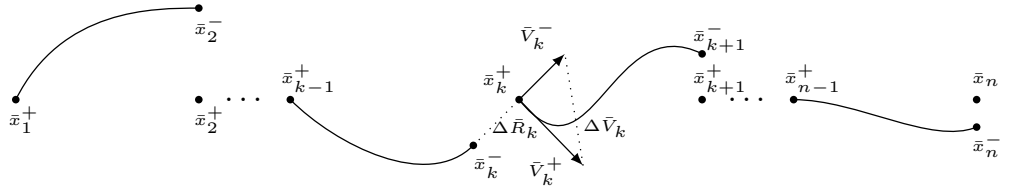

Figure C.2: A discretized trajectory with position and velocity continuous as shown at node k

The discretization transforms the BVP into $n-1$ two-point boundary value probblems (TPBVP). The TLT algorithm constructs a periodic trajectory by solving each TPBVP problem separately. The technique of subdividing a trajectory into smaller subintervals and solving them independently is better known as multiple shooting, which is a frequently adopted technique in the field spacecraft trajectory design [5]. The TLT owes its name to the two multiple shooting that make up the algorithm. These shooting schemes are referred to as the level-I corrector and the level-II corrector respectively.

Level-I corrector A multiple shooting scheme that alters the velocity of the nodes to generate a trajectory that is continuous in position.

Level-II corrector A multiple shooting scheme that alters the position and time of the nodes to construct a trajectory with smaller velocity discrepancies.

Both the level-I and level-II algorithm correct the state at a certain node based upon the state discontinuities at another node. The relationship between these deviations can be easily obtained from Equation C.21.

$$\delta\bar{x}(t_k) = \Phi(t_k, t_{k-1})\delta\bar{x}(t_{k-1}) \tag{C.21}$$

The deviations presented in the equation above are so-called contemporaneous deviations which do not consider deviations due to a change in node times. Since the Level-II corrector alters these times, non-contemporaneous deviation should be taken into account as well. This achieved via Equation C.22.

$$\delta\bar{x}' = \delta\bar{x}(t') = \delta\bar{x}(t) + \dot{\bar{x}}\delta t, \text{ where } \delta t = t - t' \tag{C.22}$$

The first term on the right hand side of Equation C.22 represents the contemporaneous deviation whereas the latter term represents the non-contemporaneous variation. Substituting Equation C.22 into C.21 results in the variational equation that serves as the basis for both levels of the TLT algorithm. This variational equation is shown below in Equation C.23.

$$(\delta\bar{x}'(t_k + \delta t_k) - \dot{\bar{x}}(t_k)\delta t_k) = \Phi(t_k, t_{k-1})(\delta\bar{x}'(t_{k-1} + \delta t_{k-1}) - \dot{\bar{x}}(t_{k-1})\delta t_{k-1}) \tag{C.23}$$

The partial derivatives of the state transition matrix (STM) are expressed below in Equation C.24 along with an abbreviated notation to avoid lengthy expressions later in this Section.

$$\Phi(t_k, t_{k-1}) = \begin{bmatrix} \frac{\partial x_k}{\partial x_{k-1}} & \frac{\partial x_k}{\partial y_{k-1}} & \frac{\partial x_k}{\partial z_{k-1}} & \frac{\partial x_k}{\partial \dot{x}_{k-1}} & \frac{\partial x_k}{\partial \dot{y}_{k-1}} & \frac{\partial x_k}{\partial \dot{z}_{k-1}} \\ \frac{\partial y_k}{\partial x_{k-1}} & \frac{\partial y_k}{\partial y_{k-1}} & \frac{\partial y_k}{\partial z_{k-1}} & \frac{\partial y_k}{\partial \dot{x}_{k-1}} & \frac{\partial y_k}{\partial \dot{y}_{k-1}} & \frac{\partial y_k}{\partial \dot{z}_{k-1}} \\ \frac{\partial z_k}{\partial x_{k-1}} & \frac{\partial z_k}{\partial y_{k-1}} & \frac{\partial z_k}{\partial z_{k-1}} & \frac{\partial z_k}{\partial \dot{x}_{k-1}} & \frac{\partial z_k}{\partial \dot{y}_{k-1}} & \frac{\partial z_k}{\partial \dot{z}_{k-1}} \\ \frac{\partial \dot{x}_k}{\partial x_{k-1}} & \frac{\partial \dot{x}_k}{\partial y_{k-1}} & \frac{\partial \dot{x}_k}{\partial z_{k-1}} & \frac{\partial \dot{x}_k}{\partial \dot{x}_{k-1}} & \frac{\partial \dot{x}_k}{\partial \dot{y}_{k-1}} & \frac{\partial \dot{x}_k}{\partial \dot{z}_{k-1}} \\ \frac{\partial \dot{y}_k}{\partial x_{k-1}} & \frac{\partial \dot{y}_k}{\partial y_{k-1}} & \frac{\partial \dot{y}_k}{\partial z_{k-1}} & \frac{\partial \dot{y}_k}{\partial \dot{x}_{k-1}} & \frac{\partial \dot{y}_k}{\partial \dot{y}_{k-1}} & \frac{\partial \dot{y}_k}{\partial \dot{z}_{k-1}} \\ \frac{\partial \dot{z}_k}{\partial x_{k-1}} & \frac{\partial \dot{z}_k}{\partial y_{k-1}} & \frac{\partial \dot{z}_k}{\partial z_{k-1}} & \frac{\partial \dot{z}_k}{\partial \dot{x}_{k-1}} & \frac{\partial \dot{z}_k}{\partial \dot{y}_{k-1}} & \frac{\partial \dot{z}_k}{\partial \dot{z}_{k-1}} \end{bmatrix} = \begin{bmatrix} A_{k,k-1} & B_{k,k-1} \\ C_{k,k-1} & D_{k,k-1} \end{bmatrix} \tag{C.24}$$

The remainder of this Section is dedicated to the explanation of both multiple shooting schemes. The discussion is based upon [4, 7, 22] unless stated otherwise.

Level-I corrector
The objective of the level-I corrector is to remove all position discrepancies. The root-finding scheme for a single segment of this trajectory is provided in Equation C.25.

$$\boldsymbol{X}_k = \begin{bmatrix} \dot{x}^+_{k-1} \\ \dot{y}^+_{k-1} \\ \dot{z}^+_{k-1} \end{bmatrix} = \bar{V}_k, \quad \boldsymbol{F}_k = \begin{bmatrix} x^+_k - x^-_k \\ y^+_k - y^-_k \\ z^+_k - z^-_k \end{bmatrix} = \Delta\bar{R}_k, \quad D\boldsymbol{F}_k = \begin{bmatrix} \frac{\partial x^+_k}{\partial \dot{x}_{k-1}} & \frac{\partial x^+_k}{\partial \dot{y}_{k-1}} & \frac{\partial x^+_k}{\partial \dot{z}_{k-1}} \\ \frac{\partial y^+_k}{\partial \dot{x}_{k-1}} & \frac{\partial y^+_k}{\partial \dot{y}_{k-1}} & \frac{\partial y^+_k}{\partial \dot{z}_{k-1}} \\ \frac{\partial z^+_k}{\partial \dot{x}_{k-1}} & \frac{\partial z^+_k}{\partial \dot{y}_{k-1}} & \frac{\partial z^+_k}{\partial \dot{z}_{k-1}} \end{bmatrix} = \bar{B}_{k,k-1} \tag{C.25}$$

The Level-1 corrector can simultaneously compute velocity corrections for each segment by merging the the $N-1$ root-finding algorithms into one large root-finding algorithm as shown in Equation C.26. The dimensions of the design vector and defect vector are identical and equal to $(3N \times 1)$. This results in a square Jacobian of dimensions $(3N \times 3N)$ meaning that correction can be computed via Equation C.4.

$$\boldsymbol{X} = \begin{bmatrix} \Delta\bar{V}_1 \\ \vdots \\ \Delta\bar{V}_{n-1} \end{bmatrix}, \quad \boldsymbol{F} = \begin{bmatrix} \Delta\bar{R}_1 \\ \vdots \\ \Delta\bar{R}_{n-1} \end{bmatrix}, \quad D\boldsymbol{F} = \begin{bmatrix} B_{2,1} & & \\ & \ddots & \\ & & B_{n,n-1} \end{bmatrix} \tag{C.26}$$

It is worth noting that [22] uses a different correction scheme than the correction scheme presented above. The difference being that the node times are allowed to vary. Both versions have been tested during this thesis project but no significant difference in performance was observed. The performance of the implemented Level-I corrector is analyzed in Section C.4.2.

Level-II corrector
The position-continuous trajectory arising from the level-I corrector serves as the input for the level-II corrector. The level-II scheme aims to provide an update to the position and times of the nodes such that another level-I correction will result in a trajectory with smaller velocity discrepancies. The root-finding scheme for single segment of the trajectory is presented below in Equation C.27.

$$\boldsymbol{X}_k = \begin{bmatrix} R_{k-1} \\ t_{k-1} \\ R_k \\ t_k \\ R_{k+1} \\ t_{k+1} \end{bmatrix}, \quad \boldsymbol{F}_k = \begin{bmatrix} \dot{x}^+_k - \dot{x}^-_k \\ \dot{y}^+_k - \dot{y}^-_k \\ \dot{z}^+_k - \dot{z}^-_k \end{bmatrix} = \Delta\bar{V}_k, \quad D\boldsymbol{F}_k = \begin{bmatrix} \frac{\partial \Delta\bar{V}_k}{\delta R_{k-1}} & \frac{\partial \Delta\bar{V}_k}{\delta t_{k-1}} & \frac{\partial \Delta\bar{V}_k}{\delta R_k} & \frac{\partial \Delta\bar{V}_k}{\delta t_k} & \frac{\partial \Delta\bar{V}_k}{\delta R_{k+1}} & \frac{\partial \Delta\bar{V}_k}{\delta t_{k+1}} \end{bmatrix} \tag{C.27}$$

The partial derivatives of the Jacobian in Equation C.27 can be obtained by relating the design variables to the defect variables. Such a relationship can be retrieved from a first-order expansion as shown in Equation C.28

$$\begin{aligned} \delta\bar{V}^-_k &= \frac{\partial \bar{V}^-_k}{\partial \bar{R}_{k-1}}\delta\bar{R}_{k-1} + \frac{\partial \bar{V}^-_k}{\partial t_{k-1}}\delta t_{k-1} + \frac{\partial \bar{V}^-_k}{\partial \bar{R}_k}\delta\bar{R}_k + \frac{\partial \bar{V}^-_k}{\partial t_k}\delta t_k \\ \delta\bar{V}^+_k &= \frac{\partial \bar{V}^+_k}{\partial \bar{R}_k}\delta\bar{R}_k + \frac{\partial \bar{V}^+_k}{\partial t_k}\delta t_k + \frac{\partial \bar{V}^+_k}{\partial \bar{R}_{k+1}}\delta\bar{R}_{k+1} + \frac{\partial \bar{V}^+_{k+1}}{\partial t_{k+1}}\delta t_{k+1} \end{aligned} \tag{C.28}$$

Leveraging this first-order expression, the elements of the Jacobian in Equation C.27 can be expressed in partial derivatives of velocity states with respected to the design vectors as shown in Table C.2.

Partial derivatives of the Jacobian of the level-II corrector

$\frac{\partial \Delta \bar{V}_k}{\partial \bar{R}_{k-1}} = -\frac{\partial \bar{V}_k^-}{\partial \bar{R}_{k-1}}$	$\frac{\partial \Delta \bar{V}_k}{\partial t_{k-1}} = -\frac{\partial \bar{V}_k^-}{\partial t_{k-1}}$	$\frac{\partial \Delta \bar{V}_k}{\partial \bar{R}_k} = \frac{\partial \bar{V}_k^+}{\partial \bar{R}_k} - \frac{\partial \bar{V}_k^-}{\partial \bar{R}_k}$
$\frac{\partial \Delta \bar{V}_k}{\partial t_k} = \frac{\partial \bar{V}_k^+}{\partial t_k} - \frac{\partial \bar{V}_k^-}{\partial t_k}$	$\frac{\partial \Delta \bar{V}_k}{\partial \bar{R}_{k+1}} = \frac{\partial \bar{V}_k^+}{\partial \bar{R}_{k+1}}$	$\frac{\partial \Delta \bar{V}_k}{\partial t_{k+1}} = \frac{\partial \bar{V}_k^+}{\partial t_{k+1}}$

Table C.2: Partial derivatives that form the Jacobian of the level-II corrector. The data in this Table is obtained from [4].

Expressions for the derivatives in Table C.2 can be obtained by considering the variational equations for segments $(k-1 \rightarrow k)$ and $(k+1 \rightarrow k)$. More specifically, a finite differencing method allows the formulation of these partial derivatives. For sake of clarity, the full expressions of these variational equations are shown below in Equation. C.29.

$$\begin{aligned}
\begin{bmatrix} (\delta \bar{R}_k')^- - \bar{V}_k^- \delta t_k^- \\ (\delta \bar{V}_k)^- - \bar{a}_k^- \delta t_k^- \end{bmatrix} &= \begin{bmatrix} A_{k-1,k} & B_{k-1,k} \\ C_{k-1,k} & D_{k-1,k} \end{bmatrix} \begin{bmatrix} (\delta \bar{R}_{k-1}')^+ - \bar{V}_{k-1}^+ \delta t_{k-1}^+ \\ (\delta \bar{V}_{k-1})^+ - \bar{a}_{k-1}^+ \delta t_{k-1}^+ \end{bmatrix} \\
\begin{bmatrix} (\delta \bar{R}_k')^+ - \bar{V}_k^+ \delta t_k^+ \\ (\delta \bar{V}_k)^+ - \bar{a}_k^+ \delta t_k^+ \end{bmatrix} &= \begin{bmatrix} A_{k,k+1} & B_{k,k+1} \\ C_{k,k+1} & D_{k,k+1} \end{bmatrix} \begin{bmatrix} (\delta \bar{R}_{k+1}')^- - \bar{V}_{k+1}^- \delta t_{k+1}^- \\ (\delta \bar{V}_{k+1})^- - \bar{a}_{k+1}^- \delta t_{k+1}^- \end{bmatrix}
\end{aligned} \tag{C.29}$$

The finite differencing approach is a well-known method in the field of engineering for the approximation of partial derivatives [36]. It allows the approximation of a change in the velocity state at node k due to a change in the design variables in a separate fashion. In the context of the level-II corrector, this boils down to nullifying the terms containing other design variables in the Equations of C.29. The results of the finite differencing procedure are presented below in Table C.3.

Partial derivatives of the velocity states at node k with respect to the design variables

$\frac{\partial \bar{V}_k^-}{\partial \bar{R}_{k-1}} = B_{k-1,k}^{-1}$	$\frac{\partial \bar{V}_k^-}{\partial t_{k-1}} = -B_{k-1,k}^{-1} \bar{V}_{k-1}^+$	$\frac{\partial \bar{V}_k^-}{\partial \bar{R}_k} = -B_{k-1,k}^{-1} \bar{A}_{k-1,k}$	$\frac{\partial \bar{V}_k^-}{\partial t_k} = \bar{a}_k^- - D_{k,k-1} B_{k,k-1}^{-1} \bar{V}_k^-$
$\frac{\partial \bar{V}_k^+}{\partial \bar{R}_k} = -B_{k+1,k}^{-1} A_{k+1,k}$	$\frac{\partial \bar{V}_k^+}{\partial t_k} = \bar{a}_k^+ - D_{k,k+1} B_{k,k+1}^{-1} \bar{V}_k^+$	$\frac{\partial \bar{V}_k^+}{\partial \bar{R}_{k+1}} = B_{k+1,k}^{-1}$	$\frac{\partial \bar{V}_k^+}{\partial t_{k+1}} = -B_{k+1,k} \bar{V}_{k+1}^-$

Table C.3: Expressions for the partial derivatives that form segment Jacobian of the level-II corrector. The data in this Table is obtained from [4].

The spatial and temporal correction of each node can be computed simultaneously by combining the defects into one vector and all partial derivatives into one matrix. This total root-finding scheme can be found below in Equations C.30 and C.31.

$$D\boldsymbol{F} = \begin{bmatrix}
\frac{\partial \Delta \bar{V}_2}{\delta \bar{R}_1} & \frac{\partial \Delta \bar{V}_2}{\delta t_1} & \frac{\partial \Delta \bar{V}_2}{\delta \bar{R}_2} & \frac{\partial \Delta \bar{V}_2}{\delta t_2} & \frac{\partial \Delta \bar{V}_2}{\delta \bar{R}_3} & \frac{\partial \Delta \bar{V}_2}{\delta t_3} & & & & \\
 & & \frac{\partial \Delta \bar{V}_2}{\delta \bar{R}_2} & \frac{\partial \Delta \bar{V}_3}{\delta t_2} & \frac{\partial \Delta \bar{V}_3}{\delta \bar{R}_3} & \frac{\partial \Delta \bar{V}_3}{\delta t_3} & \frac{\partial \Delta \bar{V}_3}{\delta \bar{R}_4} & \frac{\partial \Delta \bar{V}_3}{\delta t_4} & & \\
 & & & \ddots & \ddots & \ddots & \ddots & \ddots & \ddots & \\
 & & & & \frac{\partial \Delta \bar{V}_{N-1}}{\delta \bar{R}_{N-2}} & \frac{\partial \Delta \bar{V}_{N-1}}{\delta t_{N-2}} & \frac{\partial \Delta \bar{V}_{N-1}}{\delta \bar{R}_{N-1}} & \frac{\partial \Delta \bar{V}_{N-1}}{\delta t_{N-1}} & \frac{\partial \Delta \bar{V}_{N-1}}{\delta \bar{R}_N} & \frac{\partial \Delta \bar{V}_{N-1}}{\delta t_N}
\end{bmatrix} \tag{C.30}$$

$$\boldsymbol{X} = \begin{bmatrix} \bar{R}_1 \\ \bar{t}_1 \\ \vdots \\ \bar{R}_N \\ t_N \end{bmatrix}, \quad \boldsymbol{F} = \begin{bmatrix} \Delta \bar{V}_2 \\ \vdots \\ \Delta \bar{V}_{N-1} \end{bmatrix} \tag{C.31}$$

The level-II correction scheme as presented in Equations C.30 and C.31 provides a correction that reduces the velocity discontinuity at the interior nodes of the trajectory. The periodic nature of the libration point orbits also requires state continuity between the initial and terminal state of the discretized trajectory. Hence, the level-II corrector needs to be augmented with periodicity constraints. This constraint is denoted as η_k and can be found below in Equation C.32.

$$\eta_k = \begin{bmatrix} \bar{R}_1 - \bar{R}_n \\ \bar{V}_1^+ - \bar{V}_n^- \end{bmatrix} \tag{C.32}$$

The constraint above is used to construct the defect variable [4] which is defined in Equation C.33. Here, η_k^* is the desired value of the constraint. Defining the constraint in such away allows generalization of the

procedure to other types of constraints as will be shown in Section C.4.3. Regarding the periodicity constraint, it is obvious that $\eta_k^* = \bar{0}$.

$$\delta\eta_k = \eta_k^* - \eta_k \tag{C.33}$$

Similar to the derivation of the interior velocity continuity constraints, a first order Taylor series expansion provides a relationship between the constraints and design variables. This expansion is shown below in Equation C.34.

$$\begin{aligned}\delta\bar{\eta_k} = &\left(\frac{\partial\eta_k}{\partial\bar{R}_1} + \frac{\partial\eta_k}{\partial\bar{V}_1^+}\frac{\partial\bar{V}_1^+}{\partial\bar{R}_1}\right)\delta\bar{R}_1 + \left(\frac{\partial\eta_k}{\partial t_1} + \frac{\partial\eta_k}{\partial\bar{V}_1^+}\frac{\partial\bar{V}_1^+}{\partial t_1}\right)\delta t_1 + \left(\frac{\partial\eta_k}{\partial\bar{V}_1^+}\frac{\partial\bar{V}_1^+}{\partial\bar{R}_2}\right)\delta\bar{R}_2 + \left(\frac{\partial\eta_k}{\partial\bar{V}_1^+}\frac{\partial\bar{V}_1^+}{\partial t_2}\right)\delta t_2 \\ &+ \left(\frac{\partial\eta_k}{\partial\bar{V}_n^-}\frac{\partial\bar{V}_n^-}{\partial\bar{R}_{n-1}}\right)\delta\bar{R}_{n-1} + \left(\frac{\partial\eta_k}{\partial\bar{V}_n^-}\frac{\partial\bar{V}_n^-}{\partial t_{n-1}}\right)\delta t_{n-1} + \left(\frac{\partial\eta_k}{\partial\bar{R}_n} + \frac{\partial\eta_k}{\partial\bar{V}_n^-}\frac{\partial\bar{V}_n^-}{\partial\bar{R}_n}\right)\delta\bar{R}_n + \left(\frac{\partial\eta_k}{\partial t_n} + \frac{\partial\eta_k}{\partial\bar{V}_n^-}\frac{\partial\bar{V}_n^-}{\partial t_n}\right)\delta t_n\end{aligned} \tag{C.34}$$

A change in η_k with respect to $\bar{V}_1^+$, $\bar{R}_1$, $\bar{V}_n^-$ and $\bar{R}_n$ is obtained via basic differentiation. The result of these derivations are shown in C.35.[1]

$$\begin{aligned}\frac{\partial\eta_k}{\bar{R}_1}\begin{bmatrix}\bar{I}\\ \bar{0}\end{bmatrix} &= -\frac{\partial\eta_k}{\bar{R}_n} \\ \frac{\partial\eta_k}{\bar{V}_1^+}\begin{bmatrix}\bar{0}\\ \bar{I}\end{bmatrix} &= -\frac{\partial\eta_k}{\bar{V}_n^-}\end{aligned} \tag{C.35}$$

The eight partial derivatives $\frac{\partial\bar{V}_1^+}{\partial\bar{R}_1}$, $\frac{\partial\bar{V}_1^+}{\partial t_1}$, $\frac{\partial\bar{V}_1^+}{\partial\bar{R}_1}$, $\frac{\partial\bar{V}_1^+}{\partial t_2}$, $\frac{\partial\bar{V}_n^-}{\partial\bar{R}_{n-1}}$, $\frac{\partial\bar{V}_n^-}{\partial t_{n-1}}$, $\frac{\partial\bar{V}_n^-}{\partial\bar{R}_n}$ and $\frac{\partial\bar{V}_n^-}{\partial t_n}$ can be straightforwardly derived using Table C.3. The complete notation of the periodicity constraint can be found in Equation C.42[2].

$$\begin{aligned}\delta\bar{\eta_k} = &\begin{bmatrix}\bar{I}\\ -B_{21}^{-1}A_{21}\end{bmatrix}\delta\bar{R}_1 + \begin{bmatrix}\bar{0}\\ \bar{a}_1^+ - D_{12}B_{12}^{-1}\bar{V}_1^+\end{bmatrix}\delta t_1 + \begin{bmatrix}\bar{0}\\ B_{21}^{-1}\end{bmatrix}\delta\bar{R}_2 + \begin{bmatrix}\bar{0}\\ -\bar{B}_{21}\bar{V}_2^-\end{bmatrix}\delta t_2 \\ &+ \begin{bmatrix}\bar{0}\\ -B_{n-1,n}^{-1}\end{bmatrix}\delta\bar{R}_{n-1} + \begin{bmatrix}\bar{0}\\ B_{n-1,1}^{-1}\bar{V}_{n-1}^+\end{bmatrix}\delta t_{n-1} + \begin{bmatrix}-\bar{I}\\ B_{n,n-1}^{-1}A_{n,n-1}\end{bmatrix}\delta\bar{R}_n + \begin{bmatrix}\bar{0}\\ -\left(\bar{a}_n^- - D_{n,n-1}B_{n,n-1}^{-1}\bar{V}_n^-\right)\end{bmatrix}\delta t_n\end{aligned} \tag{C.36}$$

The complete level-II correction scheme with periodicity constraints is obtained by simply augmenting the Jacobian and defect vector of Equation C.37 with first order Taylor expansion of Equation C.42. The result is shown below in Equation C.37.

$$\begin{bmatrix}\boldsymbol{X}\\ \delta\eta_k\end{bmatrix} = \begin{bmatrix}D\boldsymbol{F}\\ \frac{\partial\eta_k}{\partial\boldsymbol{X}}\end{bmatrix}\boldsymbol{X} \tag{C.37}$$

The dimensions of the design and defect vector level-II corrector with periodicity constraints are $4n\times 1$ and $(3(n-1)+6)\times 1$ respectively. This results in a Jacobian of size $(3(n-1)+6)\times(4n)$. The inverse of this matrix can easily be solved with standard C++ operations due to the sparsity of the matrix. The sparsity is a direct consequence of the decoupling of the multiple shooting segments [4]. The performance of TLT algorithm is presented in Section C.4.2 whereas its veracity is discussed in Section F.3. It should stressed that TLT algorithm can be used to construct H_{lt}-varying l.p.o families. However, the root-finding scheme described in Section C.5 is preferred due to the lower computational cost and its ability to construct the a_{lt}-varying and α-varying l.p.o families.

[1] In [4], the partial derivatives of $\eta_k$with respect to $\bar{V}_1^+$ and $\bar{V}_N^-$ are incorrectly presented as $\frac{\partial\eta_k}{\partial\bar{V}_1^+} = \begin{bmatrix}\bar{I}\\ \bar{0}\end{bmatrix} = -\frac{\partial\eta_k}{\partial\bar{V}_n^-}$. When these partial derivatives were used, the TLT targeter did not converge.

[2] The sixth term contains the term V_n^+ which should be V_{n-1}^+ according to [4]. The TLT correction scheme could not find convergence when V_{n-1}^+ was used.

C.4.2. Two-level targeter performance analysis

The behaviour of the TLT correction procedure is defined by the tolerances (Table A.7), input trajectory and number of nodes. This section is dedicated to investigate the effect of the latter two on the algorithm's behaviour. Figure C.3 presents the performance of the algorithm for three different input trajectories over a wide variety of number of nodes used.

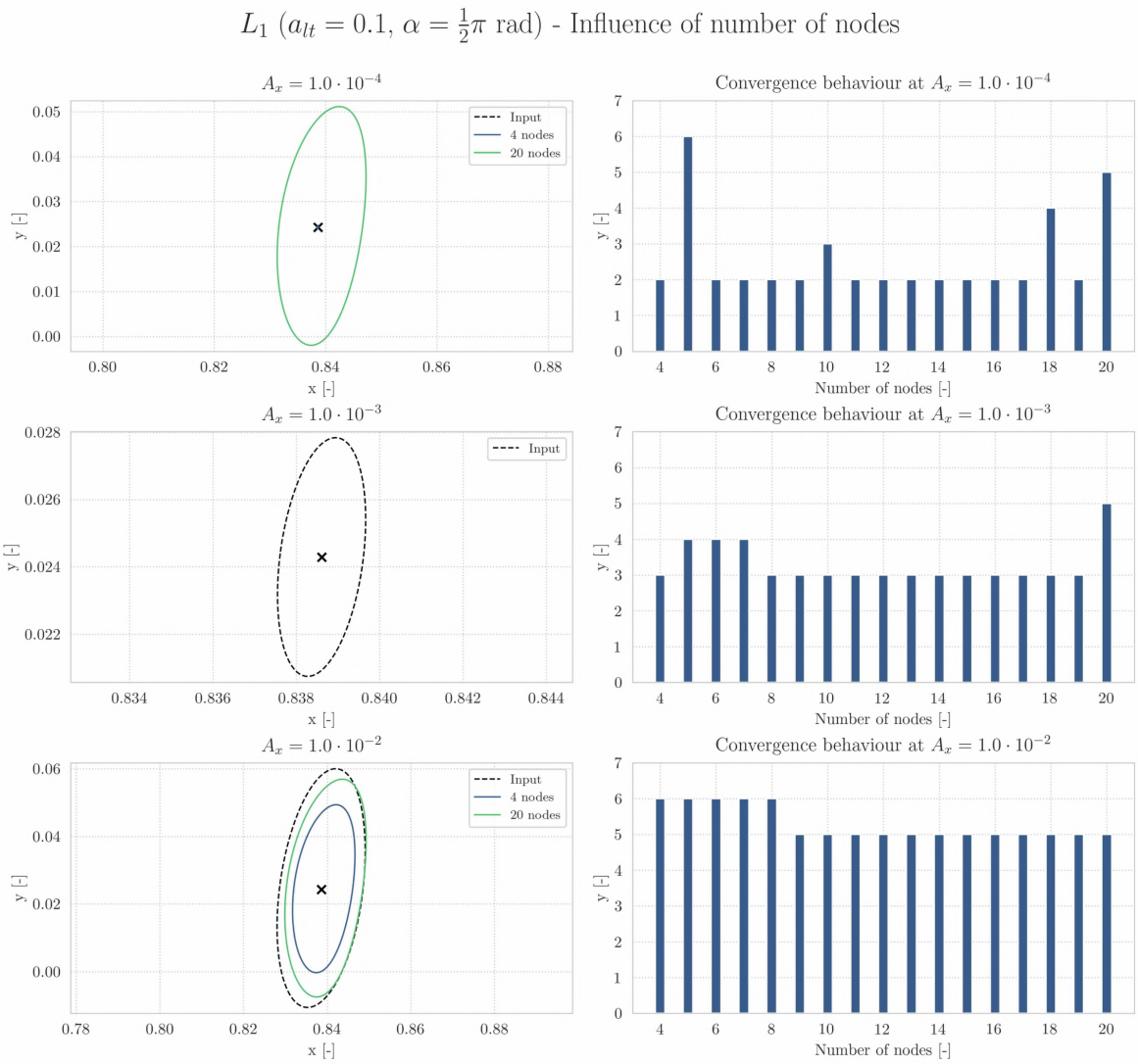

Figure C.3: Sensitivity analysis of TLT algorithm for different input trajectories amplitudes and number of nodes.

It can be concluded from Figure C.3 that the number of nodes has little effect on the converged solution for input trajectories with a small amplitude. This is not the case for libration point orbits with larger amplitudes since the shape of the converged solution heavily depends on the number of nodes used to discretize the input trajectory. A higher number of nodes corresponds to a periodic solution that has more similarities with the input trajectory.

An alternative way to ensure that the converged solution closely resembles the input trajectory is to fix the position of one of the nodes. Such an approach has been proposed for the construction of l.p.o families in the natural CR3BP [15]. However, it cannot be known a-priori at which positions periodic solutions exist. Hence the node states should remain variable. If the reader desires to use the TLT correction procedure for orbits with larger amplitudes, it is advised to carefully check if the periodic solution complies with the desired characteristics.

C.4.3. Hamiltonian path constraints

At the outset of the thesis project, the TLT algorithm was the preferred methodology for construction of l.p.o families. This idea was based on two observations. First of all, shooting algorithms in conjunction with a numerical continuation procedure have proven to be a robust method for the construction of l.p.o families in the natural CR3BP [25], elliptic restricted three-body problem [26] and even in non-ballistic versions of the CR3BP where the propulsive force is generated by a solar sail [17]. Secondly, literature concerning the two-level targeter state that it can be augmented with additional path constraints that depend on a combination of $\bar{R}_k$, $\bar{V}_k$and/or t_k [4]. A TLT algorithm with periodicity constraints and Hamiltonian path constraints is able to construct the $\alpha-$varying and a_{lt}-varying l.p.o families since periodic solutions with specific Hamiltonian values can be generated. The remainder of this section presents the efforts that have been undertaken to implement these path constraints and reports on the performance of the resulting TLT algorithm.

The derivation process of the Hamiltonian path constraint is identical to the derivation of the periodicity constraint in Section C.4.1. The constraint is defined below in Equation C.38. Although the thrust parameters influence the Hamiltonian of an orbit, it should be noted these are constant throughout the TLT correction process. Therefore, the constraint's only explicit dependencies are R_k and V_k^+.

$$\begin{aligned}\eta_k\left(\bar{R}_k,\bar{V}_k^+,a_{lt},\alpha\right) &= H_{lt} = H_{nat} - \bar{R}_k\cdot\bar{a}_{lt} = -\frac{1}{2}C - \langle\bar{R}_k\cdot\begin{bmatrix}a_{lt}\cos(\alpha) & a_{lt}\sin(\alpha) & 0\end{bmatrix}^T\rangle \\ &= -\frac{1}{2}(x_k^2+y_k^2) - \frac{1-\mu}{r_{13}} - \frac{\mu}{r_{23}} + \frac{1}{2}V_k^2 - \langle\bar{R}_k,\begin{bmatrix}a_{lt}\cos(\alpha) & a_{lt}\sin(\alpha) & 0\end{bmatrix}^T\rangle = \eta_k\left(\bar{R}_k,\bar{V}_k^+\right)\end{aligned} \tag{C.38}$$

Similar to the periodicity constraint described in Section C.4.1, the defect is computed as the difference between the desired Hamiltonian value, denoted as η_k^* and the current value of the Hamiltonian as shown in Equation C.39.

$$\delta\eta_k = \eta_k^* - \eta_k = H_{lt_k}^* - H_{lt_k} \tag{C.39}$$

The next step in deriving the Hamiltonian path constraint is relating the design variables to the constraint variables via a first order Taylor expansion. This expansion is shown below in Equation C.40.

$$\delta\eta_k = \left(\frac{\partial\eta_k}{\partial\bar{R}_k} + \frac{\partial\eta_k}{\partial\bar{V}_k^+}\frac{\partial\bar{V}_k^+}{\partial\bar{R}_k}\right)\delta\bar{R}_k + \left(\frac{\partial\eta_k}{\partial\bar{t}_k} + \frac{\partial\eta_k}{\partial\bar{V}_k^+}\frac{\partial\bar{V}_k^+}{\partial\bar{t}_k}\right)\delta t_k + \left(\frac{\partial\eta_k}{\partial+\bar{V}_k^+}\frac{\partial\bar{V}_k^+}{\partial\bar{R}_{k+1}}\right)\delta\bar{R}_{k+1} + \left(\frac{\partial\eta_k}{\partial\bar{V}_k^+}\frac{\partial\bar{V}_k^+}{\partial\bar{t}_{k+1}}\right)\delta t_{k+1} \tag{C.40}$$

The partial derivatives in the aforementioned Taylor series expansion can be obtained from Table C.3, except from $\frac{\partial\eta_k}{\partial\bar{R}_k}$ and $\frac{\partial\eta_k}{\partial\bar{R}_k}$ which are shown below in Equation C.41.

$$\frac{\partial\eta_k}{\partial\bar{R}_k} = \begin{bmatrix}\frac{\partial\eta_k}{\partial x}\\ \frac{\partial H_{lt}}{\partial y}\\ \frac{\partial\eta_k}{\partial z}\end{bmatrix}^T = \begin{bmatrix}-x+\frac{1-\mu}{r_{13}^3}(x+\mu)+\frac{\mu}{r_{23}^3}(x-1+\mu)-a_{lt}\cos(\alpha)\\ -y+\frac{1-\mu}{r_{13}^3}y+\frac{\mu}{r_{23}^3}y-a_{lt}\sin(\alpha)\\ \frac{1-\mu}{r_{13}^3}z+\frac{\mu}{r_{23}^3}z\end{bmatrix}^T, \quad \frac{\partial\eta_k}{\partial\bar{V}_k^+} = \begin{bmatrix}\frac{\partial\eta_k}{\partial\dot{x}}\\ \frac{\partial\eta_k}{\partial\dot{y}}\\ \frac{\partial\eta_k}{\partial\dot{z}}\end{bmatrix}^T = \begin{bmatrix}\dot{x}\\ \dot{y}\\ \dot{z}\end{bmatrix}^T \tag{C.41}$$

The full version of the periodicity constraint is defined below in Equation C.42.

$$\begin{aligned}\delta\eta_k = &\left(\begin{bmatrix}-x+\frac{1-\mu}{r_{13}^3}(x+\mu)+\frac{\mu}{r_{23}^3}(x-1+\mu)-a_{lt}\cos(\alpha)\\ -y+\frac{1-\mu}{r_{13}^3}y+\frac{\mu}{r_{23}^3}y-a_{lt}\sin(\alpha)\\ \frac{1-\mu}{r_{13}^3}z+\frac{\mu}{r_{23}^3}z\end{bmatrix}^T - \begin{bmatrix}\dot{x}\\ \dot{y}\\ \dot{z}\end{bmatrix}^T\cdot B_{k+1,k}^{-1}A_{k+1,k}\right)\delta\bar{R}_k \\ &+\left(\begin{bmatrix}\dot{x}\\ \dot{y}\\ \dot{z}\end{bmatrix}^T\cdot\left(\bar{a}_k^+ - D_{k,k+1}B_{k,k+1}^{-1}\bar{V}_k^+\right)\right)\delta t_k + \left(\begin{bmatrix}\dot{x}\\ \dot{y}\\ \dot{z}\end{bmatrix}^T\cdot B_{k+1,k}^{-1}\right)\bar{R}_{k+1} + \left(-\begin{bmatrix}\dot{x}\\ \dot{y}\\ \dot{z}\end{bmatrix}^T\cdot B_{k+1,k}\bar{V}_{k+1}^-\right)\delta t_{k+1}\end{aligned} \tag{C.42}$$

The performance of this constraint is evaluated via a simple test case. The objective is to find a natural L_1 H-L orbit with a specific Hamiltonian value. The input to the TLT targeter consists of a periodic libration

L_1 ($a_{lt} = 0.0$, $\alpha = 0.0$, $H_{lt} = -1.594170243726332$), $n = 10$

	Seed solution		Input deviations		TLT result	
$\|\|\Delta\bar{R}\|\|$	5.5476770323909	$\cdot 10^{14}$	5.5476770323909	$\cdot 10^{14}$	3.53674153196	$\cdot 10^{-10}$
$\|\|\Delta\bar{V}\|\|$	1.5003029806242	$\cdot 10^{12}$	1.5003029806242	$\cdot 10^{12}$	8.27673925667	$\cdot 10^{-11}$
$\|\Delta H_{lt}\|$	0.0000000000000		-1.000000000000	$\cdot 10^{-6}$	1.80496935643	$\cdot 10^{-7}$

Table C.4: Evaluation of the Hamiltonian path constraints. It should be stressed that the TLT result was obtained in 30 iterations after which the TLT process was manually terminated since the algorithm showed cyclic behaviour. 10 nodes were used during the TLT correction process.

point orbit with a Hamiltonian that differs slightly from the desired Hamiltonian value ($\Delta H_{lt} = 1.0 \cdot 10^{-6}$). The Hamiltonian path constraint is enforced at the initial node of the trajectory which leads to the results as presented in Table C.4.

The results of the test case show that the Hamiltonian path constraint does not provide the TLT corrector with the ability to find periodic orbits of a desired Hamiltonian. Although the position and velocity discrepancies approach the tolerances as specified in Table A.7, the Hamiltonian of the resulting trajectory does not come close to the desired value. It should be stressed that the state and Hamiltonian discrepancies with the same order of magnitude were already obtained after the third iteration of the TLT algorithm. However the algorithm did not improve in subsequent iterations and therefore the correction process was killed after 30 iterations. A possible cause for the non-convergence is the nonlinear relationship between the Hamiltonian constraints and the design variables which makes the problem difficult to solve [5]. The inability of the TLT algorithm to refine orbits to a desired Hamiltonian solution creates the need for another correction methodology that can correct orbits to the desired Hamiltonian value. This algorithm is presented in Section C.5.

C.5. Collocation root-finding scheme

The section discusses the root-finding schemes that, in conjunction with numerical continuation algorithms, generate the three types of l.p.o families. Subsection C.5.1 presents the root-finder algorithm for one segment whereas C.5.2 discusses additional constraints. The totality of this section with the matter discussed in Section B.2.1 is commonly referred to as the 12^{th} order Legendre-Gauss-Lobatto collocation method.

C.5.1. General collocation root-finding scheme

The design vector, defect vector and Jacobian of the root-finding scheme for a single segment can be found below in Equation C.43. Please note that the computation of the design and defect vector are discussed in Section B.2.1.

$$\boldsymbol{X}_i = \begin{bmatrix} \bar{x}_{i,1} \\ t_{i,1} \\ \bar{x}_{i,3} \\ \bar{x}_{i,5} \\ \bar{x}_{i+1,1} \\ t_{i+1,1} \end{bmatrix}, \quad \boldsymbol{F}_i = \begin{bmatrix} \bar{\zeta}_{i,2} \\ \bar{\zeta}_{i,4} \\ \bar{\zeta}_{i,6} \end{bmatrix}, \quad D\boldsymbol{F}_i = \begin{bmatrix} \frac{\partial\bar{\zeta}_{i,2}}{\partial\bar{x}_{i,1}} & \frac{\partial\bar{\zeta}_{i,2}}{\partial t_{i,1}} & \frac{\partial\bar{\zeta}_{i,2}}{\partial\bar{x}_{i,3}} & \frac{\partial\bar{\zeta}_{i,2}}{\partial\bar{x}_{i,5}} & \frac{\partial\bar{\zeta}_{i,2}}{\partial\bar{x}_{i+1,1}} & \frac{\partial\bar{\zeta}_{i,2}}{\partial t_{i+1,1}} \\ \frac{\partial\bar{\zeta}_{i,4}}{\partial\bar{x}_{i,1}} & \frac{\partial\bar{\zeta}_{i,4}}{\partial\bar{x}_{i+1,1}} & \frac{\partial\bar{\zeta}_{i,4}}{\partial t_{i,1}} & \frac{\partial\bar{\zeta}_{i,4}}{\partial\bar{x}_{i,3}} & \frac{\partial\bar{\zeta}_{i,4}}{\partial\bar{x}_{i,5}} & \frac{\partial\bar{\zeta}_{i,4}}{\partial t_{i+1,1}} \\ \frac{\partial\bar{\zeta}_{i,6}}{\partial\bar{x}_{i,1}} & \frac{\partial\bar{\zeta}_{i,6}}{\partial t_{i,1}} & \frac{\partial\bar{\zeta}_{i,6}}{\partial\bar{x}_{i,3}} & \frac{\partial\bar{\zeta}_{i,6}}{\partial\bar{x}_{i,5}} & \frac{\partial\bar{\zeta}_{i,6}}{\partial\bar{x}_{i+1,1}} & \frac{\partial\bar{\zeta}_{i,6}}{\partial t_{i+1,1}} \end{bmatrix} \tag{C.43}$$

Similar to the TLT corrector, the multivariate root finding scheme can compute the required correction for the complete mesh at once by collecting the design vectors, defect vectors and Jacobian of each segments and merge them into a single design vector, defect vector and Jacobian according to Equation C.44.

$$\boldsymbol{X} = \begin{bmatrix} \boldsymbol{X}_1 \\ \vdots \\ \boldsymbol{X}_{n-1} \end{bmatrix}, \quad \boldsymbol{F} = \begin{bmatrix} \boldsymbol{F} \\ \vdots \\ \boldsymbol{F}_{n-1} \end{bmatrix} \tag{C.44}$$

$$D\boldsymbol{F} = \begin{bmatrix} \frac{\partial\boldsymbol{F}_1}{\partial\bar{x}_{1,1}} & \frac{\partial\boldsymbol{F}_1}{\partial t_{1,1}} & \frac{\partial\boldsymbol{F}_1}{\partial\bar{x}_{1,3}} & \frac{\partial\boldsymbol{F}_1}{\partial\bar{x}_{1,5}} & \frac{\partial\boldsymbol{F}_1}{\partial\bar{x}_{2,1}} & \frac{\partial\boldsymbol{F}_1}{\partial t_{2,1}} & & & & & & \\ & & & & \frac{\partial\boldsymbol{F}_2}{\partial\bar{x}_{2,1}} & \frac{\partial\boldsymbol{F}_2}{\partial t_{2,1}} & \frac{\partial\boldsymbol{F}_2}{\partial\bar{x}_{2,3}} & \frac{\partial\boldsymbol{F}_2}{\partial\bar{x}_{2,5}} & \frac{\partial\boldsymbol{F}_2}{\partial\bar{x}_{3,1}} & \frac{\partial\boldsymbol{F}_2}{\partial t_{3,1}} & & \\ & & & & & & & & \ddots & \ddots & \ddots & \\ & & & & & & & & \frac{\partial\boldsymbol{F}_{n-1}}{\partial\bar{x}_{n-1,1}} & \frac{\partial\boldsymbol{F}_{n-1}}{\partial t_{n-1,1}} & \frac{\partial\boldsymbol{F}_{n-1}}{\partial\bar{x}_{n-1,3}} & \frac{\partial\boldsymbol{F}_{n-1}}{\partial\bar{x}_{n-1,5}} & \frac{\partial\boldsymbol{F}_{n-1}}{\partial\bar{x}_{n,1}} & \frac{\partial\boldsymbol{F}_{n-1}}{\partial t_{n,1}} \end{bmatrix} \tag{C.45}$$

The partial derivatives that form the Jacobian in Equation C.43 are approximated via the complex step method [18]. This technique computes the partial derivative of the defect vector $\boldsymbol{F}$ with respect to a single design variable $\boldsymbol{X}_{kj}$ by re-evaluation of the defect vector with a modified version of the design variable of interest according to $\boldsymbol{X}_{kj_{\text{complex}}} = \boldsymbol{X}_{kj} + \sigma i$. The partial derivative with respect to $\boldsymbol{X}_{kj}$ is then obtained via Equation C.46.

$$\frac{\partial \boldsymbol{F}}{\partial \boldsymbol{X}_{kj}} \approx \frac{\text{Im}\left(\boldsymbol{F}\left(\boldsymbol{X}_{kj_{\text{complex}}}\right)\right)}{\sigma} \tag{C.46}$$

The complex step method avoids the need for manual derivation of partial derivatives, which is inherent to the finite difference approach as described in Section C.4.1. Furthermore, the quadratic convergence of the complex step method is preserved as long as $\epsilon < 10^{-8}$, resulting in a derivative estimation of $\mathcal{O}(10^{-16})$. At these tiny increments, finite-difference approaches experience substractive cancellation errors and produce unreliable estimates [19].

The existing solution is updated via a line search procedure which finds a correction step by reducing the computed correction step with an attenuation factor k according to Equation C.47.

$$\boldsymbol{X}^{n+1} = \boldsymbol{X}^{n} + \kappa \Delta X^{n} \tag{C.47}$$

The attenuation factor that provides a correction step resulting the defect vector with the smallest euclidian norm is selected as the new solution. The range of values used for parameter κ can be found in Table A.8.

C.5.2. Additional constraints

Various types of constraints are necessary to enable the collocation algorithm to compute l.p.o families. Regardless of the family that is being generated, the size of the Jacobian for a trajectory consisting of n nodes will be $((18(n-1)+7) \times (19(n-1)+7))$. The remainder of this section is dedicated to the explanation of these constraints.

Periodicity constraint

Periodicity is of the solution is enforced through an equality constraint in the form of the state discrepancy between the initial state. The dimensions of the resulting constraints are $(6 \times (19(n-1)+7))$, where only the first and final seven columns contain non-zero entries, as shown below in Equation C.48.

$$\boldsymbol{F}_{\text{periodicity}} = \left[\delta\left(\bar{x}_{1,1} - \bar{x}_{n,1}\right)\right], \quad D\boldsymbol{F}_{\text{periodicity}} = \begin{bmatrix} \frac{\partial \bar{x}_{1,1} - \bar{x}_{n,1}}{\partial \bar{x_{1,1}}} & \frac{\partial \bar{x}_{1,1} - \bar{x}_{n,1}}{\partial t_{1,1}} & \bar{0} & \dots & \bar{0} & \frac{\partial \bar{x}_{1,1} - \bar{x}_{n,1}}{\partial \bar{x_{n,1}}} & \frac{\partial \bar{x}_{1,1} - \bar{x}_{n,1}}{\partial t_{n,1}} \end{bmatrix} \tag{C.48}$$

Phase constraint for H_{lt}-varying families

The spacing of the members of the H_{lt}-varying l.p.o families is determined via pseudo-archlength continuation procedure. To ensure consistent spacing between subsequent family members, it is necessary that the phase drift between orbit members is minimized. Literature suggests the use of a Poincaré phase condition in the form of Equation C.49 [10]. It comprises the inner product of the state increment between the family members $\bar{x}^{n-1}$ and $\bar{x}^{n-1}$ between their initial states and the state derivative of $\bar{x}^{n}$.

$$\delta\phi = \langle \bar{x}^{n}_{1,1} - \bar{x}^{n-1}_{1,1}, \dot{x}^{n-1}_{1,1} \rangle \tag{C.49}$$

The disadvantage of the Poincaré phase condition is that the phase error grows during the numerical continuation procedure [10]. Hence, this thesis project introduces two adaptions to decrease the phase drift over the l.p.o family. First of all, the state increment over the complete family becomes constant. It is defined as the state discrepancy between the initial state of the first family member and the equilibrium point. Secondly, the initial node state derivative of the already computed member $x^{n-1}_{1,1}$ is replaced by the initial node state derivative of the to be computed member $\dot{x}^{n}_{1,1}$. The resulting constraint is shown below in Equation C.50.

$$\delta\phi = k \cdot \frac{(\bar{x}^{1}_{1,1} - \bar{x}_{eq})^{T} \dot{x}^{n}_{1,1}}{||(\bar{x}^{1}_{1,1} - \bar{x}_{eq})^{T} \dot{x}^{n}_{1,1}||} \tag{C.50}$$

It can be observed that the resulting phase constraint is normalized and multiplied by an amplification factor k. This modification allows the user to control the constraint magnitude and thereby the sensitivity of the

collocation procedure to phase constraint. The value of k has been determined through a trial and error procedure and can be found in Table A.8. The phase constraint is implemented in the root-finding scheme via Equation C.51.

$$\boldsymbol{F}_{\text{phase}} = \left[\delta\phi\right], \;\; D\boldsymbol{F}_{\text{phase}} = \left[\begin{array}{cccc} \frac{\partial\phi}{\partial x_{1,1}^{\bar{1}}} & \frac{\partial\delta\phi}{\partial t_{1,1}} & \bar{0} \quad \ldots & \bar{0} \end{array}\right] \tag{C.51}$$

Hamiltonian constraint for a_{lt}-varying and α-varying families

The members of a single a_{lt}-varying and α-varying families should have an identical Hamiltonian. This is achieved through an equality constraint at the first node of the trajectory in the form of the discrepancy between the desired Hamiltonian and the actual value of the Hamiltonian of the first node. The dimensions of the resulting constraints are $(1 \times (19(n-1)+7))$, where only the first seven columns contain non-zero partial derivatives, as shown below in Equation C.52.

$$\boldsymbol{F}_{\text{Hamiltonian}} = \left[H_{lt}^{*} - H_{lt_{1,1}}\right], \;\; D\boldsymbol{F}_{\text{Hamiltonian}} = \left[\begin{array}{cccc} \frac{\partial H_{lt}^{*} - H_{lt_{1,1}}}{\partial x_{1,1}^{\bar{1}}} & \frac{\partial H_{lt}^{*} - H_{lt_{1,1}}}{\partial t_{1,1}} & \bar{0} \quad \ldots & \bar{0} \end{array}\right] \tag{C.52}$$

D

Extended analysis of acceleration-varying families

In Chapter 1 of this report, twelve a_{lt}-varying families at $H_{lt} = -1.525$ are presented for different acceleration orientation at E_1 and E_2. More a_{lt}-varying families have been constructed at other Hamiltonian values ($H_{lt} = [-1.55, -1.50]$) but these are not included in Chapter 1 for sake of conciseness. The remainder of this Appendix D is dedicated to analyzing these a_{lt}-varying families for reasons of completeness. Section D.1 discusses the a_{lt}-varying families with $H_{lt} = -1.55$ whereas Section D.2 presents the a_{lt}-varying families with $H_{lt} = -1.50$.

D.1. Acceleration-varying families at low-thrust Hamiltonian of -1.55

Figure D.1 shows a planar projection of six a_{lt}-varying families emanating from the E_1 contour whereas Figure D.2 presents the evolution of their saddle stability index as well as the evolution of their orbital period.

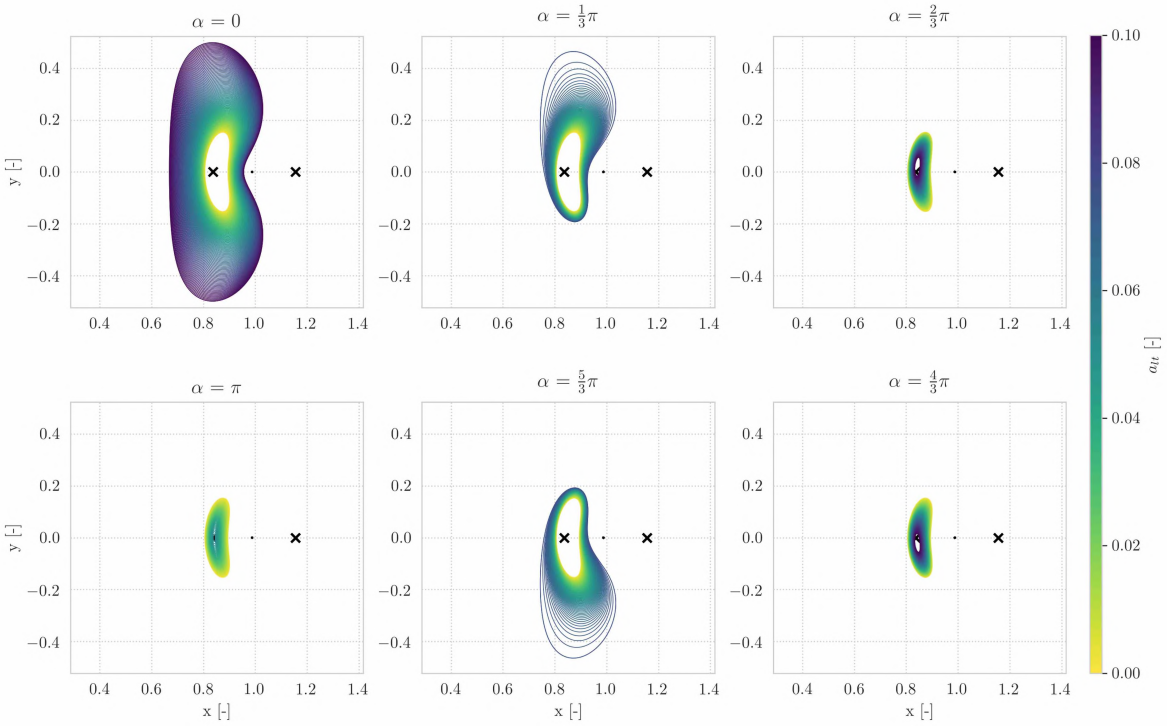

Figure D.1: Six a_{lt}-varying families at $H_{lt} = -1.55$ for different α values in vicinity of E_2. The color of an l.p.o corresponds to its acceleration magnitude according to the colorbar located on the right side.

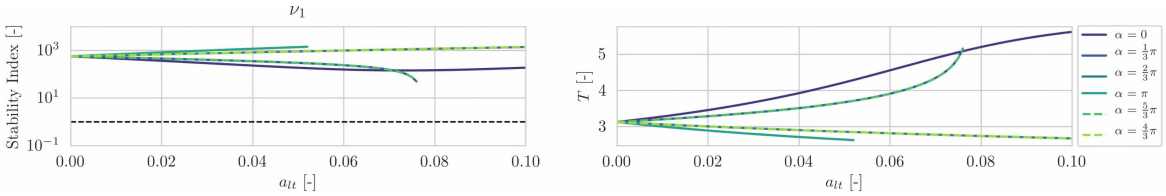

Figure D.2: The evolution of ν_1 over the E_1, $H_{lt} = -1.55$, a_{lt}-varying families is shown on the left. The evolution of T as a function of a_{lt} is shown on the right.

The planar projections support the conclusions provided in Chapter 1. These conclusions state that a growing acceleration orientation enlarges (shrinks) the orbit size in case of positive (negative) collinear acceleration and distorts the orbit geometry into 'ear-shaped' solutions for non-collinear acceleration orientations. The evolution of the stability indices in Figure D.2 support a different conclusion than presented in Chapter 1. Figure D.2 shows that an increase in acceleration orientation either monotonically decreases or increases the saddle stability index, apart from the $\alpha = 0$ family. Another interesting observation is that the orbital period evolves in an opposite way compared to the saddle stability indices.

These analyses are repeated for a_{lt}-varying families emanating from E_2. Figure D.3 shows a planar projection of six a_{lt}-varying families emanating from the E_2 contour whereas Figure D.4 presents the evolution of their saddle stability index as well as the evolution of their orbital period.

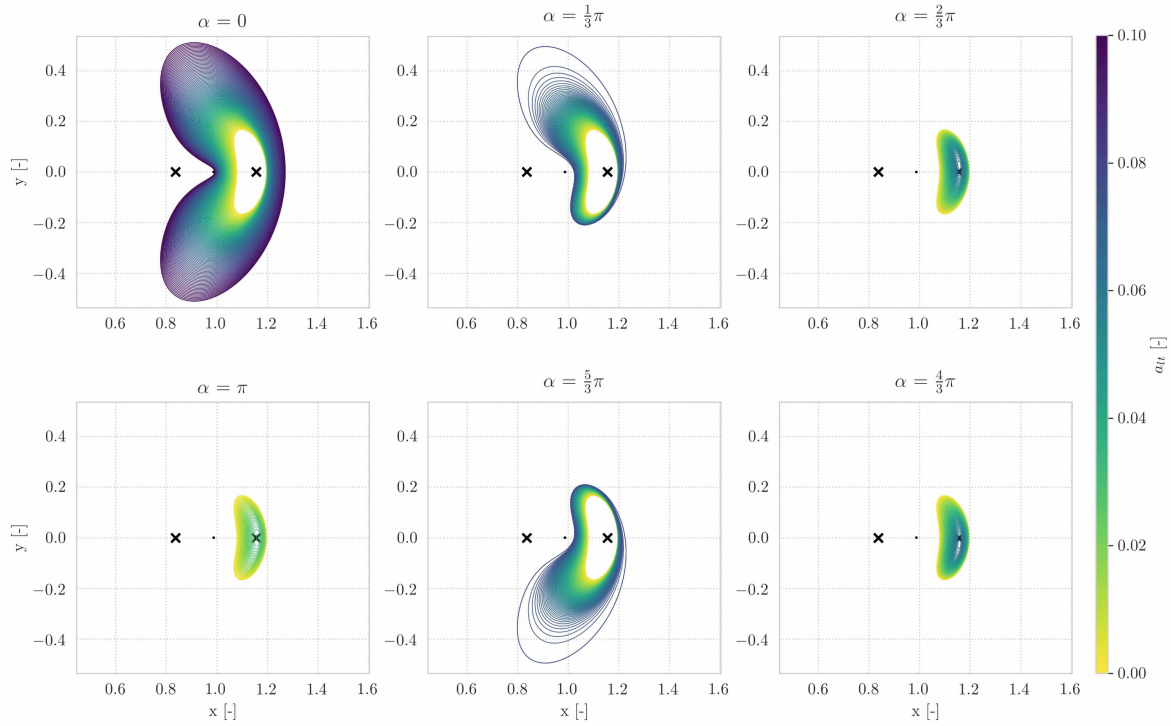

Figure D.3: Six a_{lt}-varying families at $H_{lt} = -1.55$ for different α values in vicinity of E_2. The colour of an l.p.o corresponds to its acceleration magnitude according to the colorbar located on the right side.

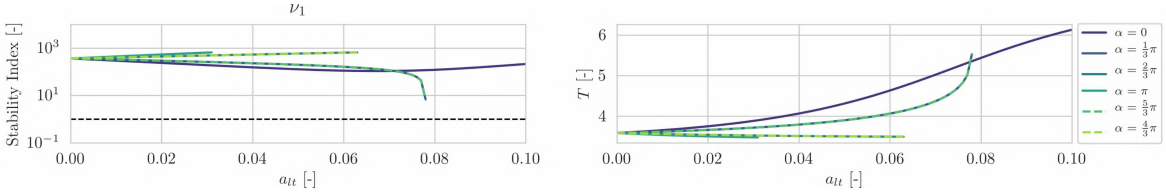

Figure D.4: The evolution of ν_1 over the E_2, $H_{lt} = -1.55$, a_{lt}-varying families is shown on the left. The evolution of T as a function of a_{lt} is shown on the right.

Figures D.3 and D.4 show that the acceleration magnitude has the same effect on the geometry, saddle stability index and orbital period of the E_2 a_{lt}-varying families as on the a_{lt}-varying families arising from E_1.

D.2. Acceleration-varying families at a low-thrust Hamiltonian of -1.50

Figure D.5 shows a planar projection of six a_{lt}-varying families emanating from the E_1 contour whereas Figure D.6 presents the evolution of their saddle stability index as well as the evolution of their orbital period.

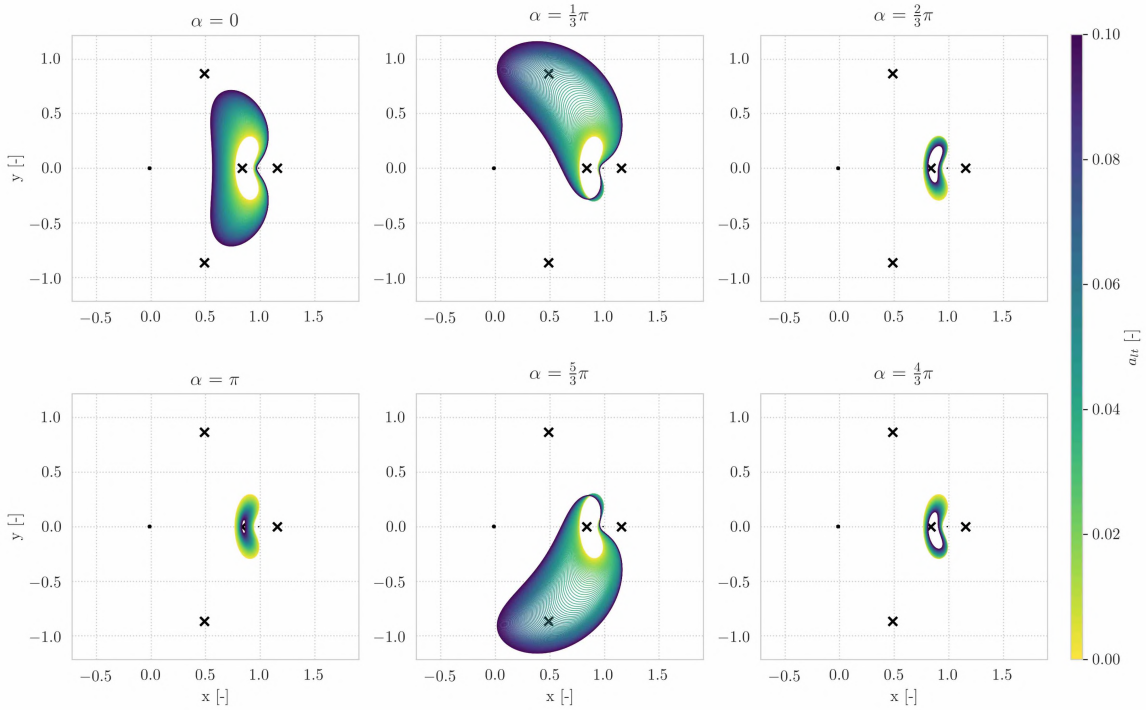

Figure D.5: Six a_{lt}-varying families at $H_{lt} = -1.50$ for different α values in vicinity of E_1. The color of an l.p.o corresponds to its acceleration magnitude according to the colorbar located on the right side.

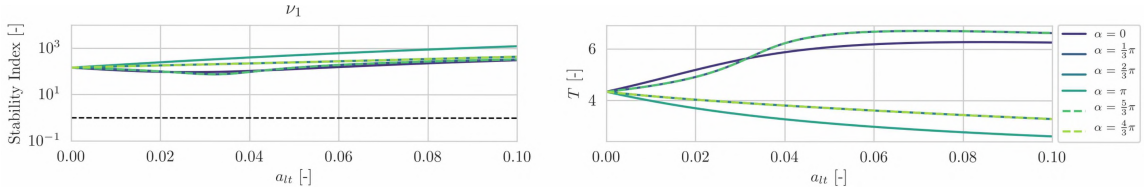

Figure D.6: The evolution of ν_1 over the E_1, $H_{lt} = -1.50$, a_{lt}-varying families is shown on the left. The evolution of T as a function of a_{lt} is shown on the right.

The planar projections in Figure D.5 support the conclusions provided in Chapter 1. These conclusions state that an increase in acceleration orientation can enlarge (shrink) the orbit size in case of positive (negative) collinear acceleration and distort the orbit geometry into 'ear-shaped' solutions for non-collinear acceleration orientation. The evolution of the stability indices in Figure D.6 also support the conclusions drawn in Chapter 1 and previous the Section. It can be observed that an increase in acceleration orientation monotonically increases the saddle stability index when $H_{lt} = -1.50$, apart from the $\alpha = [0, \frac{1}{3}\pi, \frac{5}{3}\pi]$ families. Furthermore, it can be observed that the orbital period evolves in an opposite way compared to the saddle stability indices. The a_{lt}-varying families emanating from E_2 support these conclusions as well. The graphical projections of the E_2 a_{lt}-varying families can be found in Figure D.7 whereas the evolution of the saddle stability indices and orbital periods are provided in Figure D.8. These two figures complete the analysis of the a_{lt}-varying families.

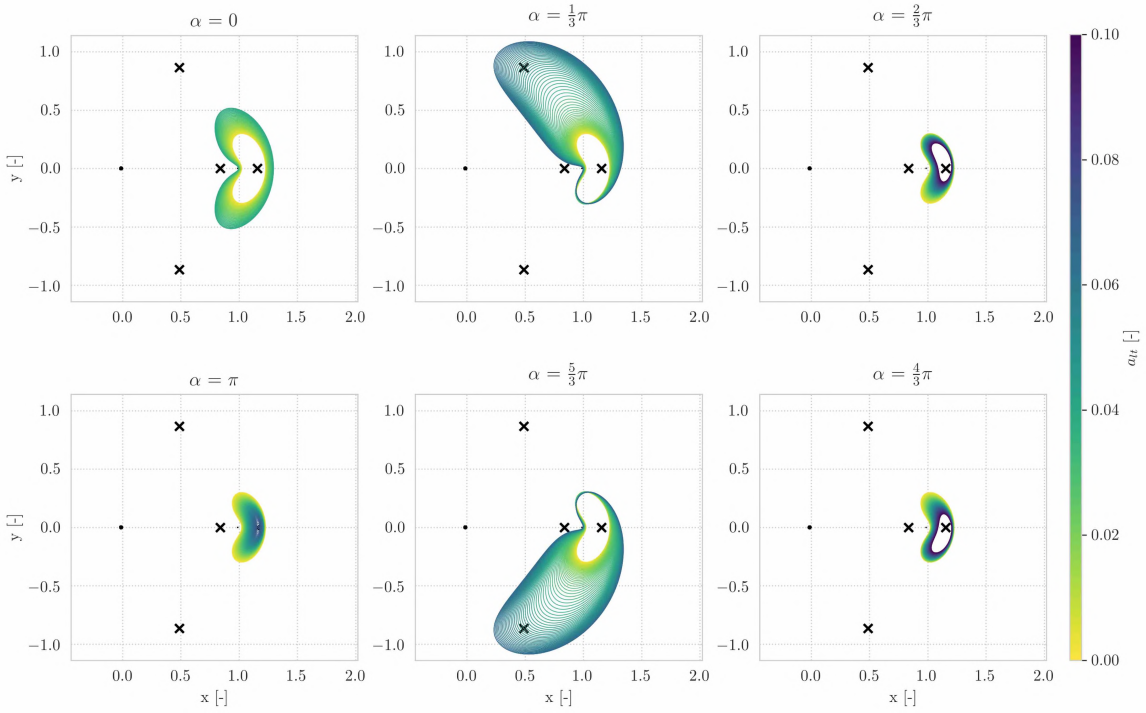

Figure D.7: Six a_{lt}-varying families at $H_{lt} = -1.50$ for different α values in vicinity of E_2. The color of an l.p.o corresponds to its acceleration magnitude according to the colorbar located on the right side.

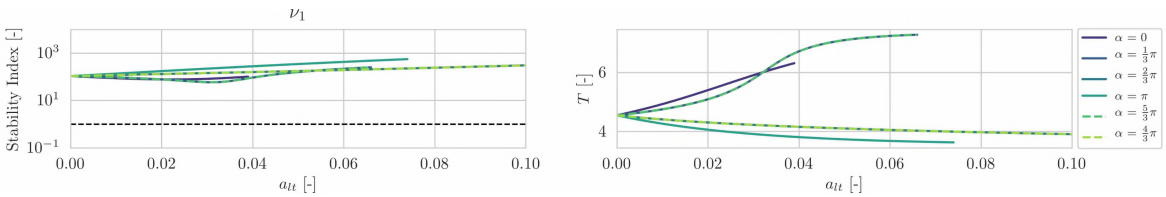

Figure D.8: The evolution of ν_1 over the E_2, $H_{lt} = -1.50$, a_{lt}-varying families is shown on the left. The evolution of T as a function of a_{lt} is shown on the right.

E

Quantitative results overview

Chapter 1 and Appendix D contain several quantitative assertions which are not clearly observable from the Figures present in these Chapters. The goal of this section is to substantiate these claims by providing a quantitative overview of characteristics of both the equilibria contours and periodic solution families. Section E.1 presents the equilibria contour characteristics while Sections E.2,E.3 and E.4 discuss the characteristics of the H_{lt}-varying, a_{lt}-varying and α-varying families respectively.

E.1. Low-thrust equilibrium solutions

The low-thrust equilibria are studied in Chapter 1 via analysis of its position, Hamiltonian and eigenvalue related to the unstable subspace. Table E.2 presents the extrema of these variables for the $\alpha-$varying equilibria contour at $a_{lt} = 0.1$. The characteristics of the natural Lagrangian points are shown in Table E.1 for reference purposes.

Variable	L_1	L_2	L_3	L_4	L_5
x	0.836915148369	1.1557821477825	-1.005072643897	0.487854418983	0.487854418983
y	0.000000000000	0.000000000000	0.000000000000	0.866034064038	-0.866034064038
λ	2.932055876779	2.158674362159	0.177875325621	-	-
H_{lt}	-1.594170537701	-1.586080212362	-1.506073573046	-1.493998527801	-1.493998527801

Table E.1: Characteristics of the CR3BP equilibrium solutions. λ denotes the eigenvalue related to the saddle subspace.

Variable	E_1	E_2	E_3
x_{min}	0.827608726610	1.143236632185	-1.039291188287
x_{max}	0.845328433899	1.170499045727	0.948146945706
y_{min}	0.024529061495	-0.047042953312	-1.031812984559
y_{max}	-0.024529061495	0.047042953312	1.031812984559
λ_{min}	2.745942677592	1.856372716147	0.089124730775
λ_{max}	3.135841405289	2.459287202304	0.557456692346
$H_{lt,min}$	-1.677404319667	-1.701008408830	-1.604961223715
$H_{lt,max}$	-1.510051094876	-1.469793025395	-1.392875936337

Table E.2: Characteristics of the α-varying equilibria contour at $a_{lt} = 0.1$. These properties involve the minimum and maximum position,Hamiltonian and dominant eigenvalue related to the saddle subspace.

E.2. Hamiltonian-varying families

A multitude of H_{lt}-varying families has been generated during this thesis project. The characteristics of these families are presented below in Table E.3. These characteristics include the number of orbits (N) in the family and the extrema of the Hamiltonian, orbital period and hyperbolic unwinding behaviour rate per family. The family members at which these extrema occur are provided in superscript. Besides these characteristics, the bifurcations occurring in a single family are defined by stating the member (Me) at which a bifurcation occurs along with the change in order of instability (OI). Specification of the bifurcation type (Type), which is either

Tangent Bifurcation (T-B), Period-Doubling (P-D) or Cyclic-Fold (C-F) together with the Hamiltonian value at which they occur fully define the bifurcation behaviour of a family.

Family				Bifurcation behaviour						
E_i	a_{lt}	α	N	OI	Me	Type	$H_{lt_{\text{bif}}}$	H_{lt} range	T range	ν_1 range
L_1	0.00	0	1898	I → II	127	T-B	-1.587131685972	-1.594170243723^{1} -1.455227124540^{1898}	2.691581656261^{1} 6.537957262589^{1898}	1337.7^{1} 53.7^{1888}
				II → I	545	T-B	-1.510627491172			
				I → II	1232	P-D	-1.474609611856			
L_2	0.00	0	1440	I → II	253	T-B	-1.576017966662	-1.586080211259^{1} -1.470838424172^{1440}	3.373258092264^{1} 6.211633967258^{1440}	726.8^{1} 52.5^{1440}
				II → I	644	T-B	-1.506802366126			
				I → II	1191	P-D	-1.477844290086			
L_1	0.01	0	1939	I → II	130	T-B	-1.595379944034	-1.602534960129^{1} -1.462009914700^{1938}	2.705787709739^{1} 6.499910706631^{1939}	1323.1^{1} 67.3^{1702}
				II → I	558	T-B	-1.519718995775			
				I → II	1259	P-D	-1.482933044552			
L_1	0.01	$\frac{1}{3}\pi$	3000	I → II	128	T-B	-1.591327226597	-1.591873692006^{1} -1.476534133883^{3000}	2.698985760709^{1} 7.102833648051^{3000}	1330.0^{1} 62.3^{1814}
				II → I	545	T-B	-1.516244859768			
				I → II	1274	P-D	-1.481012979867			
L_1	0.01	$\frac{2}{3}\pi$	3000	I → II	126	T-B	-1.582959708307	-1.589993539486^{1} -1.448265450575^{1857}	2.684769667025^{1} 7.161039053478^{3000}	1345.3^{1} 49.1^{1999}
				II → I	533	T-B	-1.507044344097			
				I → II	1247	P-D	-1.472851211016			
L_1	0.01	π	1858	I → II	125	T-B	-1.578761182010	-1.585796673777^{1} -1.448265450575^{1858}	2.677378562633^{1} 6.575905566807^{1858}	1352.4^{1} 40.5^{1858}
				II → I	532	T-B	-1.501487136680			
				I → II	1205	P-D	-1.466191776357			
L_1	0.01	$\frac{4}{3}\pi$	2038	I → II	126	T-B	-1.582959584247	-1.589993539484^{1} -1.455866621202^{2038}	2.677378562633^{1} 6.575905566807^{1858}	1345.3^{1} 49.1^{1999}
				II → I	553	T-B	-1.507044715495			
				I → II	1247	P-D	-1.472851297376			
L_1	0.01	$\frac{5}{3}\pi$	3000	I → II	128	T-B	-1.591327107766	-1.598362818423^{1} -1.432477077350^{3000}	2.698985760716^{1} 7.102836662653^{3000}	1330.0^{1} 62.3^{1814}
				II → I	545	T-B	-1.516244640995			
				I → II	1274	P-D	-1.481012923014			
L_2	0.01	0	1364	I → II	237	T-B	-1.587624895773	-1.597630183786^{1} -1.480458348793^{1364}	3.341566996283^{1} 6.107393027090^{3000}	750.6^{1} 62.3^{1363}
				II → I	611	T-B	-1.516718364461			
				I → II	149	P-D	-1.486959298629			
L_2	0.01	$\frac{1}{3}\pi$	1484	I → II	240	T-B	-1.581892566913	-1.591873692006^{1} -1.476534133883^{1484}	3.357569231525^{1} 6.230640019901^{1483}	738.9^{1} 56.3^{1484}
				II → I	622	T-B	-1.512605435535			
				I → II	1174	P-D	-1.484420421819			
L_2	0.01	$\frac{2}{3}\pi$	1583	I → II	248	T-B	-1.570199462219	-1.580317368709^{1} -1.467219992942^{1583}	3.389529156994^{1} 6.368002583197^{1583}	715.1^{1} 44.9^{1583}
				II → I	642	T-B	-1.502852851866			
				I → II	1211	P-D	-1.475502524684			
L_2	0.01	π	1501	I → II	252	T-B	-1.564336329171	-1.574516471279^{1} -1.461282912082^{1501}	3.405442828917^{1} 6.322031591006^{1501}	703.1^{1} 42.5^{1500}
				II → I	658	T-B	-1.496983113191			
				I → II	1215	P-D	-1.468723798407			
L_2	0.01	$\frac{4}{3}\pi$	1583	I → II	248	T-B	-1.570199480946	-1.580317368709^{1} -1.467219795463^{1583}	3.389529156817^{1} 6.368019369489^{1583}	715.1^{1} 44.9^{1583}
				II → I	642	T-B	-1.502852069664			
				I → II	1211	P-D	-1.475502275274			
L_2	0.01	$\frac{5}{3}\pi$	1484	I → II	240	T-B	-1.581892620441	-1.591873692006^{1} -1.476534131310^{1484}	3.357569231434^{1} 6.230640211391^{1484}	738.9^{1} 56.3^{1484}
				II → I	622	T-B	-1.512605414373			
				I → II	1174	P-D	-1.484420419112			
L_1	0.05	0	2114	I → II	139	T-B	-1.628666470803	-1.635903489984^{1} -1.487190282472^{2114}	2.762547367512^{1} 6.347544478985^{2114}	1265.2^{1} 114.8^{1317}
				II → I	609	T-B	-1.555701732880			
				I → II	1376	P-D	-1.514931886986			
L_1	0.05	$\frac{1}{3}\pi$	2102	I → II	128	T-B	-1.608790672486	-1.615299356089^{1} -1.515292637373^{2102}	2.735243439561^{1} 6.078723161132^{2102}	1308.4^{1} 71.5 ^{1482}
				II → I	471	T-B	-1.550650408588			
				I → II	1341	P-D	-1.522298526451			
L_1	0.05	$\frac{2}{3}\pi$	1097	I → II	118	T-B	-1.566967967973	-1.573438410103^{1} -1.481731615213^{1097}	2.662854000472^{1} 5.215265956783^{1097}	1381.9^{1} 1.2 ^{1097}
				II → I	424	T-B	-1.504286336700			

L_1	0.05	π	1616	I → II	116	T-B	-1.545349079168	-1.552215639155^{1} -1.420338951864^{1616}	2.620683501984^{1} 6.586998048961^{1616}	1411.8^{1} 7.9 ^{1616}
				II → I	481	T-B	-1.464305486592			
				I → II	1104	P-D	-1.431376314540			
L_1	0.05	$\frac{4}{3}\pi$	1097	I → II	118	T-B	-1.566967440708	-1.573438410097^{1} -1.481731663114^{1097}	2.662854000353^{1} 5.213407659519^{1097}	1381.9^{1} 1.4 ^{1097}
				II → I	424	T-B	-1.504286214386			
L_1	0.05	$\frac{5}{3}\pi$	4023	I → II	128	T-B	-1.608790279609	-1.615299356084^{1} -1.463706323153^{4023}	2.735243439440^{1} 6.848460792790^{4023}	1308.4^{1} 71.5 ^{1482}
				II → I	471	T-B	-1.550649993159			
				I → II	1341	P-D	-1.522298495545			
L_2	0.05	0	1109	I → II	211	T-B	-1.633937104194	-1.643699625989^{1} -1.519792342150^{1109}	3.219570834641^{1} 5.714019662870^{1109}	846.7^{1} 95.6 ^{937}
				II → I	517	T-B	-1.556032081390			
				I → II	1015	P-D	-1.523429301657			
L_2	0.05	$\frac{1}{3}\pi$	3038	I → II	221	T-B	-1.606075307705	-1.615328081021^{1} -1.504483473431^{3038}	3.299381592529^{1} 6.989038029065^{3038}	792.4^{1} 46.6 ^{1437}
				II → I	535	T-B	-1.546099631383			
				I → II	1151	P-D	-1.523287719992			
L_2	0.05	$\frac{2}{3}\pi$	2465	I → II	255	T-B	-1.548206547685	-1.557605785592^{1} -1.482005956353^{1265}	3.462040675034^{1} 8.102618857627^{2465}	673.3^{1} 1.0 ^{1266}
				II → I	629	T-B	-1.497993846942			
				I → 0	1266	C-F	-1.482005957509			
				0 → I	1277	P-D	-1.482008183610			
				I → II	1362	P-D	-1.482152122822			
				II → I	2305	P-D	-1.493633812747			
L_2	0.05	π	1789	I → II	242	T-B	-1.517721259775	-1.528121601483^{1} -1.424422731445^{1789}	3.539273423919^{1} 6.805384196096^{1789}	609.7^{1} 7.2 ^{1789}
				II → I	752	T-B	-1.457276785819			
				I → II	1343	P-D	-1.432171258093			
L_2	0.05	$\frac{4}{3}\pi$	2465	I → II	255	T-B	-1.548206316982	-1.557605785592^{1} -1.482005956311^{1265}	3.462040675106^{1} 8.102650133739^{2465}	673.3^{1} 1.0 ^{1266}
				II → I	629	T-B	-1.497993624051			
				I → 0	1266	C-F	-1.482005957557			
				0 → I	1277	P-D	-1.482008184640			
				I → II	1362	P-D	-1.482152130639			
				II → I	2305	P-D	-1.493633875187			
L_2	0.05	$\frac{5}{3}\pi$	3038	I → II	221	T-B	-1.606075553625	-1.615328081022^{1} -1.504483800573^{3038}	3.299381592529^{1} 6.989038029065^{3038}	792.4^{1} 46.6 ^{1437}
				II → I	535	T-B	-1.546101085825			
				I → II	1151	P-D	-1.523287901842			
L_1	0.10	0	2168	I → II	152	T-B	-1.669942040687	-1.677404083560^{1} -1.522927333320^{2168}	2.832973779640^{1} 6.062806853410^{2168}	1195.1^{1} 163.2 ^{1137}
				II → I	676	T-B	-1.599363160136			
				I → II	1544	P-D	-1.551679481714			
L_1	0.10	$\frac{1}{3}\pi$	1018	I → II	114	T-B	-1.632321869922	-1.636875201208^{1} -1.573162949308^{1018}	2.799032663228^{1} 5.061850543120^{1018}	1294.9^{1} 1.0 ^{1018}
				II → I	339	T-B	-1.600447087399			
L_1	0.10	$\frac{2}{3}\pi$	947	I → II	99	T-B	-1.548341123295	-1.553061063199^{1} -1.481275690618^{659}	2.645611803359^{1} 6.209508129725^{947}	1441.1^{1} 1.0 ^{659}
				II → I	297	T-B	-1.506675678442			
				I → 0	659	C-F	-1.481275717243			
				0 → I	661	P-D	-1.481276343384			
				I → II	813	P-D	-1.483385202767			
				II → I	946	P-D	-1.490997327610			
L_1	0.10	π	1210	I → II	106	T-B	-1.503326358770	-1.510050725211^{1} -1.381539521799^{1210}	2.550380070168^{1} 6.172596299591^{1210}	1486.9^{1} 1.4 ^{1210}
				II → I	415	T-B	-1.416820162272			
				I → II	916	P-D	-1.385549149138			
L_1	0.10	$\frac{4}{3}\pi$	659	I → II	99	T-B	-1.548339738565	-1.553061063187^{0} -1.481275689579^{659}	2.645611803170^{1} 4.441184225369^{659}	1441.1^{1} 1.4 ^{659}
				II → I	297	T-B	-1.506672652333			
L_1	0.10	$\frac{5}{3}\pi$	1014	I → II	114	T-B	-1.632321045167	-1.636875201199^{0} -1.573163201882^{1013}	2.799032662956^{1} 5.052558988979^{1014}	1294.9^{1} 2.6 ^{1014}
				II → I	339	T-B	-1.600445578392			
L_2	0.10	0	1000	I → II	182	T-B	-1.691702004715	-1.701008243733^{1} -1.560772516307^{1000}	3.077238027380^{1} 5.694800008875^{1000}	967.4^{1} 120.4 ^{627}
				II → I	401	T-B	-1.604890150188			
				I → II	827	P-D	-1.568950027379			

				I → II	190	T-B	-1.637709361660		
				II → I	422	T-B	-1.592804071586		
				I → 0	966	C-F	-1.570479376834		
				0 → I	973	P-D	-1.570480485213	-1.645177476356[1]	3.233262389575[1]
L_2	0.10	$\frac{1}{3}\pi$	4450	I → II	1008	P-D	-1.570514780452	-1.536285315023[4500]	7.236676547926[3028]
				II → I	1942	P-D	-1.574864562848		
				I → 0	1948	P-D	-1.574865435036		
				0 → I	1955	T-B	-1.574865741211		
				I → II	3737	P-D	-1.557066278025		
				I → II	238	T-B	-1.523476564602		
				II → I	520	T-B	-1.497633780034		
				I → 0	929	C-F	-1.482899373508	-1.530106194844[1]	3.578028913259[1]
L_2	0.10	$\frac{2}{3}\pi$	1278	0 → I	932	P-D	-1.482899910330	-1.482899373508[929]	6.527464529521[1278]
				I → II	1210	P-D	-1.487231349121		
				I → II	330	T-B	-1.459199384025		
				II → I	867	T-B	-1.407251797015		
				I → II	1498	P-D	-1.386382553565	-1.469792954215[1]	3.718678830228[1]
L_2	0.10	π	2037	II → I	1629	T-B	-1.384751919567	-1.382736177347[2035]	7.311805076634[2037]
				I → II	1698	P-D	-1.384105703933		
				II → I	1970	P-D	-1.382785759706		
				I → II	238	T-B	-1.523477507825		
				II → I	520	T-B	-1.497634654480		
				I → 0	929	C-F	-1.482899373396	-1.530106194845[1]	3.578028913085[1]
L_2	0.10	$\frac{4}{3}\pi$	1278	0 → I	932	P-D	-1.482899906931	-1.482899373396[929]	6.527238199053[1278]
				I → II	1210	P-D	-1.487230995314		
				I → II	190	T-B	-1.637708250609		
				II → I	422	T-B	-1.592805054171		
				I → 0	966	C-F	-1.570479376767		
				0 → I	973	P-D	-1.570480483551	-1.645177476357[1]	3.233262389265[1]
L_2	0.10	$\frac{5}{3}\pi$	4450	I → II	1008	P-D	-1.570514772557	-1.536285405817[4500]	7.236676547752[3028]
				II → I	1942	P-D	-1.570514772557		
				I → 0	1948	P-D	-1.574865434552		
				0 → I	1955	T-B	-1.574865741264		
				I → II	3737	P-D	-1.557066325982		

Table E.3: An overview of the key characteristics of H_{lt}-varying families. These characteristics include the number of family members, bifurcation behaviour and extrema of the Hamiltonian, orbital period and hyperbolic unwinding behaviour. All variables are dimensionless apart from the angle which is shown in radians.

The bifurcation diagrams in Chapter 1 of this report reveal the bifurcation behaviour by plotting the module of all six eigenvalues along with the phase of the out-of-plane center subspace (λ_2 and $\frac{1}{\lambda_2}$) as a function of the bifurcation parameter. This allows full specification of the bifurcations as long as the stability of the saddle subspace eigenvalue pair (λ_1 and $\frac{1}{\lambda_1}$) remains unchanged. However, The stability saddle subspace eigenvalue pair did change for eight of the 38 H_{lt}-varying families which are listed below:

- L_2 ($a_{lt} = 0.05$, $\alpha = \frac{2}{3}\pi$ and $\frac{4}{3}\pi$)
- L_1 ($a_{lt} = 0.10$, $\alpha = \frac{2}{3}\pi$)
- L_2 ($a_{lt} = 0.10$, $\alpha = \frac{1}{3}\pi$ and $\frac{5}{3}\pi$)
- L_2 ($a_{lt} = 0.10$, $\alpha = \pi$)
- L_2 ($a_{lt} = 0.10$, $\alpha = \frac{2}{3}\pi$ and $\frac{4}{3}\pi$)

The bifurcations occurring in these eight families have been determined by manually inspecting the values, phase and stability indices[1] of the three eigenvalue pairs. The remainder of this section shows how these variables change along the eight families to remove any ambiguity regarding the documented bifurcation behaviour in Chapter 1 and Table E.3.

[1] The minimum value of the stability index is +1 as its the average of an absolute valued reciprocal eigenvalue pair. This observation coincides with work from renowned scientists [37] but opposes previous student work [25, 26]. Inspection of Langemeijer's source code [25] revealed that the absolute value operator was omitted in computation of the stability index.

L_2(a_{lt} = 0.05, $\alpha = \frac{2}{3}\pi$ and $\alpha = \frac{4}{3}\pi$)

The evolution of the eigenvalues and stability indices along the L_2 ($a_{lt} = 0.05$, $\alpha = \frac{2}{3}\pi$) H_{lt}-varying family can be observed below in Figure E.1.

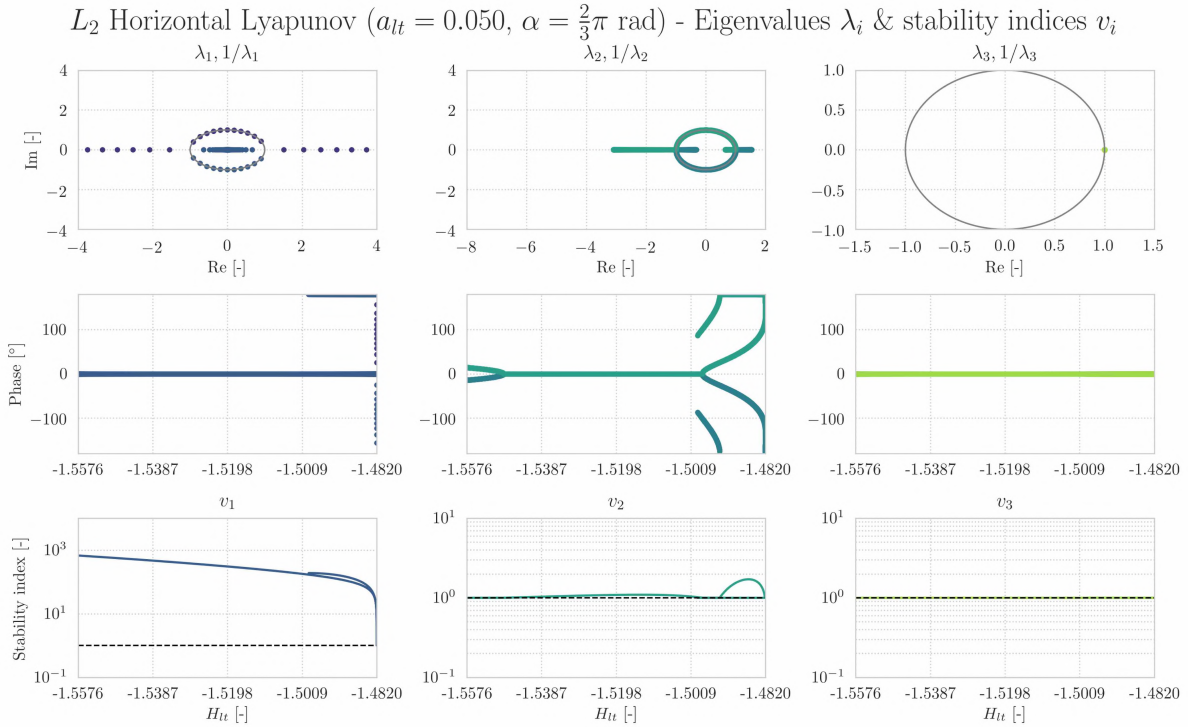

Figure E.1: Stability analysis of the L_2 ($a_{lt} = 0.05$, $\alpha = \frac{2}{3}\pi$) H_{lt}-varying family. The upper rows shows the magnitude of the eigenvalue pairs whereas the middle row shows their phase as a function of H_{lt}. From left to right, the bottom row shows the stability indices related to the saddle subspace, out-of-plane center subspace and in-plane center subspace respectively.

Table E.3 states that six bifurcations are present in this specific family. Inspection of Figure E.1 confirms that the first two bifurcations are tangent bifurcations since the phase of the out-of-plane center subspace eigenvalue pair leaves and rejoins the unit circle. The third bifurcation is caused by the saddle eigenvalue pair which joins the unit circle at +1. This change in order of instability is a cyclic-fold rather than a tangent bifurcation as it occurs at an extremum of the Hamiltonian. The fourth bifurcation occurs when the saddle eigenvalue pair leaves the unit circle at −1 which gives rise to a period-doubling bifurcation. The final two bifurcations are also period-doubling bifurcations caused by the out-of-plane center subspace eigenvalue pair that leaves and rejoins the unit circle at −1. The stability analysis of the the evolution of the eigenvalues and stability indices along the L_2 ($a_{lt} = 0.05$, $\alpha = \frac{4}{3}\pi$) H_{lt}-varying family is identical to Figure E.1 and has been omitted from this report for sake of conciseness.

L_1($a_{lt} = 0.1$, $\alpha = \frac{2}{3}\pi$)

The evolution of the eigenvalues and stability indices along the L_1 ($a_{lt} = 0.10$, $\alpha = \frac{2}{3}\pi$) H_{lt}-varying family can be observed below in Figure E.2.

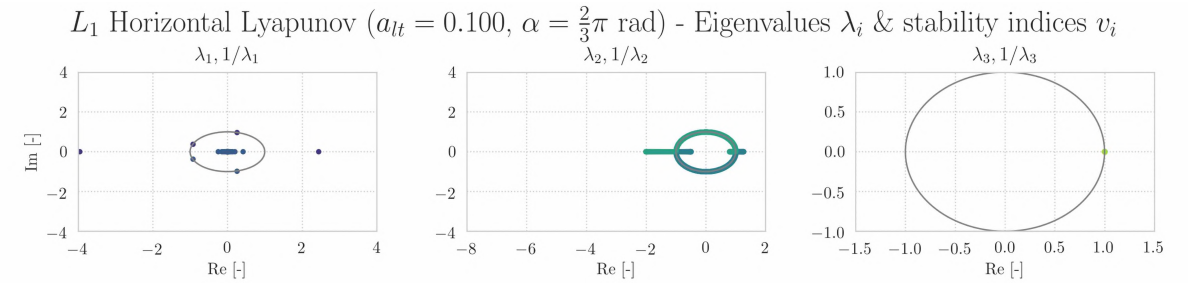

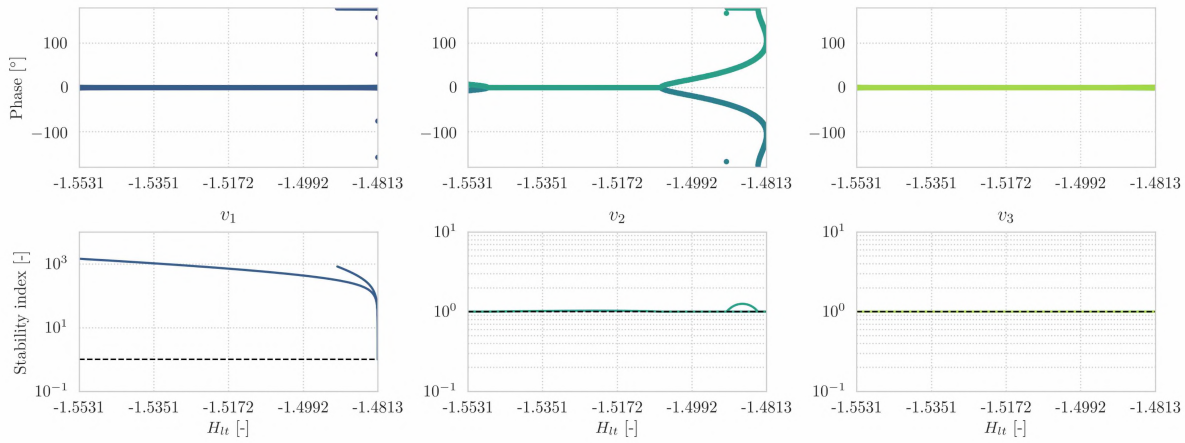

Figure E.2: Stability analysis of the L_1 ($a_{lt} = 0.10$, $\alpha = \frac{2}{3}\pi$) H_{lt}-varying family. The upper rows shows the magnitude of the eigenvalue pairs whereas the middle row shows their phase as a function of H_{lt}. From left to right, the bottom row shows the stability indices related to the saddle subspace, out-of-plane center subspace and in-plane center subspace respectively.

Table E.3 states that five bifurcations are present in this specific family. Inspection of Figure E.2 confirms that the first two bifurcations are tangent bifurcations since the out-of-plane center subspace eigenvalue pair leaves and rejoins the unit circle. The third bifurcation is caused by the saddle eigenvalue pair which joins the unit circle at +1. This change in order of instability is a cyclic-fold rather than a tangent bifurcation as it occurs at an extremum of the Hamiltonian. The fourth bifurcation occurs when the saddle eigenvalue pair leaves the unit circle at −1 which gives rise to a period-doubling bifurcation. The final two bifurcations are also period-doubling bifurcations caused by the out-of-plane center subspace eigenvalue pair that leaves and rejoins the unit circle at −1.

L_2 ($a_{lt} = 0.05$, $\alpha = \frac{1}{3}\pi$ and $\alpha = \frac{5}{3}\pi$)

The evolution of the eigenvalues and stability indices along the L_2 ($a_{lt} = 0.10$, $\alpha = \frac{1}{3}\pi$) H_{lt}-varying family can be observed below in Figure E.3.

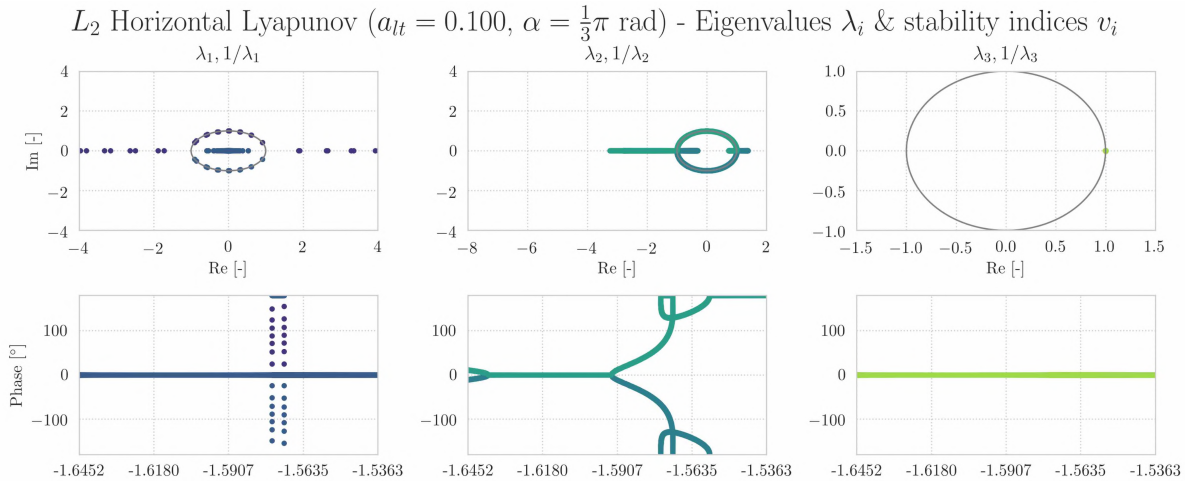

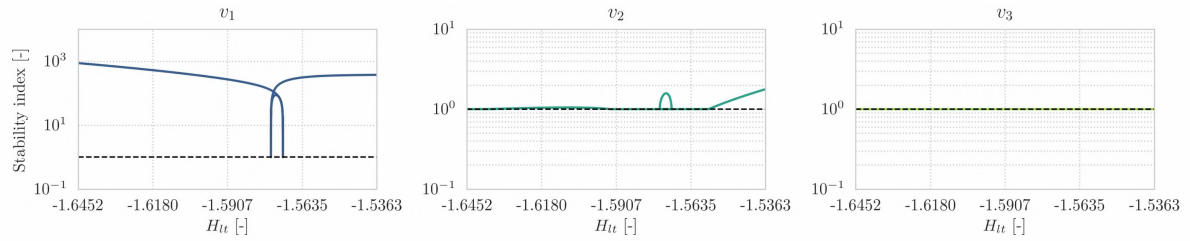

Figure E.3: Stability analysis of the L_2 ($a_{lt} = 0.10$, $\alpha = \frac{1}{3}\pi$) H_{lt}-varying family. The upper rows shows the magnitude of the eigenvalue pairs whereas the middle row shows their phase as a function of H_{lt}. From left to right, the bottom row shows the stability indices related to the saddle subspace, out-of-plane center subspace and in-plane center subspace respectively.

Table E.3 states that nine bifurcations are present in this specific family. Inspection of Figure E.3 confirms that the first two bifurcations are tangent bifurcations since the out-of-plane center subspace eigenvalue pair leaves and rejoins the unit circle. The third bifurcation is caused by the saddle eigenvalue pair which joins the unit circle at +1. This change in order of instability is a cyclic-fold rather than a tangent bifurcation as it occurs at an extremum of the Hamiltonian. The fourth and fifth bifurcation occur when the saddle eigenvalue pair followed by the out-of-plane center eigenvalue pair leave the unit circle at −1, resulting in two period-doubling bifurcations. The sixth and seventh change in order of linear instability are also period-doubling bifurcations as the two eigenvalue pairs rejoin the unit circle at −1. The eighth bifurcation is a tangent bifurcation which happens when the saddle eigenvalue pair leaves the unit circle at +1. The final bifurcation is a period-doubling bifurcation as the out-of-plane center eigenvalue pair leaves the unit circle at −1. The stability analysis of the the evolution of the eigenvalues and stability indices along the L_2 ($a_{lt} = 0.10$, $\alpha = \frac{5}{3}\pi$) H_{lt}-varying family is identical to Figure E.3 and has been omitted from this report for sake of conciseness.

L_2($a_{lt} = 0.1$, $\alpha = \frac{2}{3}\pi$ and $\alpha = \frac{4}{3}\pi$)

The evolution of the eigenvalues and stability indices along the L_2 ($a_{lt} = 0.10$, $\alpha = \frac{2}{3}\pi$) H_{lt}-varying family can be observed below in Figure E.4.

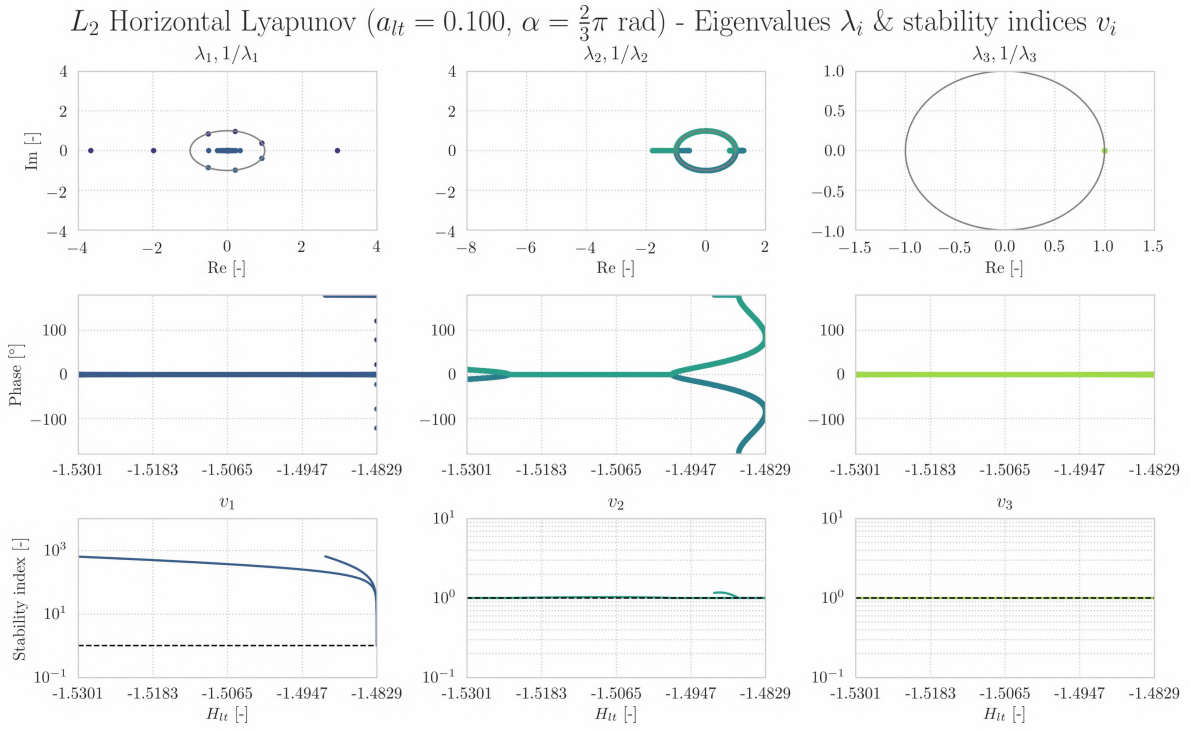

Figure E.4: Stability analysis of the L_2 ($a_{lt} = 0.10$, $\alpha = \frac{2}{3}\pi$) H_{lt}-varying family. The upper rows shows the magnitude of the eigenvalue pairs whereas the middle row shows their phase as a function of H_{lt}. From left to right, the bottom row shows the stability indices related to the saddle subspace, out-of-plane center subspace and in-plane center subspace respectively.

Table E.3 states that five bifurcations are present in this specific family. Inspection of Figure E.4 confirms that the first two bifurcations are tangent bifurcations since the out-of-plane center subspace eigenvalue pair leaves and rejoins the unit circle. The third bifurcation is caused by the saddle eigenvalue pair which joins the unit circle at +1. This change in order of instability is a cyclic-fold rather than a tangent bifurcation as it occurs at an extremum of the Hamiltonian. The fourth bifurcation occurs when the saddle eigenvalue pair leaves the unit circle at −1 which gives rise to a period-doubling bifurcation. The final bifurcation is also period-doubling bifurcations caused by the out-of-plane center eigenvalue pair leavin the unit circle at −1. The stability analysis of the evolution of the eigenvalues and stability indices along the L_2 ($a_{lt} = 0.10$, $\alpha = \frac{4}{3}\pi$) H_{lt}-varying family is identical to Figure E.4 and has been omitted from this report for sake of conciseness.

L_2($a_{lt} = 0.1$, $\alpha = \pi$)
The evolution of the eigenvalues and stability indices along the L_2 ($a_{lt} = 0.10$, $\alpha = \pi$) H_{lt}-varying family can be observed below in Figure E.5.

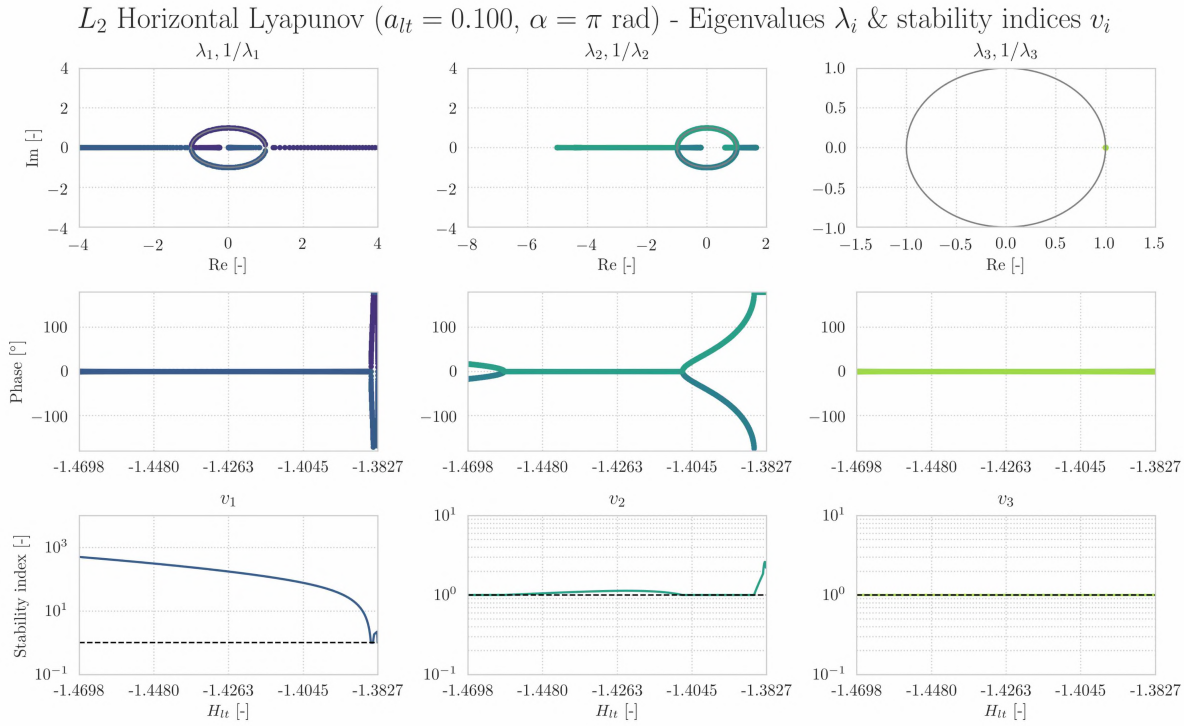

Figure E.5: Stability analysis of the L_2 ($a_{lt} = 0.10$, $\alpha = \pi$) H_{lt}-varying family. The upper rows shows the magnitude of the eigenvalue pairs whereas the middle row shows their phase as a function of H_{lt}. From left to right, the bottom row shows the stability indices related to the saddle subspace, out-of-plane center subspace and in-plane center subspace respectively.

Table E.3 states that six bifurcations are present in this specific family. Inspection of Figure E.5 confirms that the first two bifurcations are tangent bifurcations since the out-of-plane center subspace eigenvalue pair leaves and rejoins the unit circle. The third bifurcation is a period-doubling bifurcation caused by the out-of-plane center eigenvalue pair which leaves the unit circle at −1. The fourth bifurcations is caused by the saddle eigenvalue pair which joins the unit circle at +1 giving rise to a tangent bifurcation. The final two bifurcations are also caused by the saddle eigenvalue pair as it leaves and rejoins the unit circle at −1. Hence these bifurcations are period-doubling bifurcations.

E.3. Acceleration-varying families

The characteristics of the a_{lt}-varying families are presented in an similar way as the H_{lt}-varying families in Section E.2. The only difference being that the a_{lt} range of the family is presented instead of the H_{lt} range since it is the bifurcation parameter of this family type. The characteristics of the a_{lt}-varying families can be found in Table E.4.

Family				Bifurcation behaviour						
E_i	H_{lt}	α	N	OI	Me	Type	$a_{lt_{\text{bif}}}$	a_{lt} range	T range	ν_1 range
L_1	−1.550	0	101	II → I	45	T-B	0.044	0.000^{1}	3.123750902666^{1}	556.0^{1}
				I → II	99	P-D	0.098	0.100^{101}	5.621647753697^{101}	141.8^{74}
L_1	−1.550	$\frac{1}{3}\pi$	77	II → I	51	T-B	0.050	0.000^{1}	3.123750902666^{1}	556.0^{1}
								0.076^{77}	5.156177821610^{77}	49.1^{77}
L_1	−1.550	$\frac{2}{3}\pi$	101	II → I	97	T-B	0.096	0.000^{1}	2.667445460384^{101}	1365.8^{101}
								0.076^{77}	3.123750902666^{0}	556.0^{1}
L_1	−1.550	π	53	II → I	46	T-B	0.045	0.000^{1}	2.621231031409^{53}	1402.0^{53}
								0.052^{53}	3.123750902666^{1}	556.0^{0}
L_1	−1.550	$\frac{4}{3}\pi$	101	II → I	97	T-B	0.096	0.000^{1}	2.667445460384^{101}	1365.8^{101}
								0.076^{77}	3.123750902666^{0}	556.0^{1}
L_1	−1.550	$\frac{5}{3}\pi$	77	II → I	51	T-B	0.050	0.000^{1}	3.123750902666^{1}	556.0^{1}
								0.076^{77}	5.156177821609^{77}	49.1^{77}
L_2	−1.550	0	101	II → I	45	T-B	0.044	0.000^{1}	3.583795054267^{1}	360.2^{1}
				I → II	81	P-D	0.080	0.100^{101}	6.132330574703^{101}	106.7^{77}
L_2	−1.550	$\frac{1}{3}\pi$	79	II → I	56	T-B	0.055	0.000^{1}	3.583795054267^{1}	360.2^{1}
				I → II	79	P-D	0.078	0.078^{79}	5.525275511698^{79}	6.7^{78}
L_2	−1.550	$\frac{2}{3}\pi$	64	II → I	48	T-B	0.047	0.000^{1}	3.490615013276^{64}	656.9^{64}
								0.063^{64}	3.583795054267^{1}	360.2^{1}
L_2	−1.550	π	32	II → I	24	T-B	0.023	0.000^{1}	3.475493645283^{32}	651.5^{32}
								0.031^{32}	3.583795054267^{1}	360.2^{1}
L_2	−1.550	$\frac{4}{3}\pi$	64	II → I	48	T-B	0.047	0.000^{1}	3.490615013275^{64}	656.9^{64}
								0.063^{64}	3.583795054267^{1}	360.2^{1}
L_2	−1.550	$\frac{5}{3}\pi$	79	II → I	56	T-B	0.055	0.000^{1}	3.583795054267^{1}	360.2^{1}
				I → II	79	P-D	0.078	0.078^{79}	5.525275511669^{79}	6.7^{78}
L_1	−1.525	0	101	II → I	17	T-B	0.016	0.000^{1}	3.565417899804^{1}	300.5^{1}
				I → II	65	P-D	0.064	0.100^{101}	6.038622665072^{101}	118.1^{50}
L_1	−1.525	$\frac{1}{3}\pi$	101	II → I	23	T-B	0.022	0.000^{1}	3.565417899804^{1}	346.7^{101}
				I → II	54	P-D	0.053	0.100^{101}	6.697816402987^{87}	68.7^{55}
L_1	−1.525	$\frac{2}{3}\pi$	101	II		-	-	-	0.000^{1}	2.892552556355^{101}	840.5^{101}
								0.100^{101}	3.565417899804^{0}	300.5^{1}
L_2	−1.525	π	83	II → I	77	T-B	0.076	0.000^{1}	2.577090826652^{83}	651.5^{32}
								0.082^{83}	3.565417899804^{1}	360.2^{1}
L_1	−1.525	$\frac{4}{3}\pi$	101	II		-	-	-	0.000^{1}	2.892552556355^{101}	840.5^{101}
								0.100^{101}	3.565417899804^{0}	300.5^{1}
L_1	−1.525	$\frac{5}{3}\pi$	101	II → I	23	T-B	0.022	0.000^{1}	3.565417899804^{1}	346.7^{101}
				I → II	54	P-D	0.053	0.100^{101}	6.697816402987^{87}	68.7^{55}
L_2	−1.525	0	85	II → I	20	T-B	0.019	0.000^{1}	3.893439278124^{1}	247.1^{84}
				I → II	53	P-D	0.052	0.084^{85}	6.609936968758^{84}	93.2^{48}
L_2	−1.525	$\frac{1}{3}\pi$	101	II → I	28	T-B	0.027	0.000^{1}	3.893439278124^{1}	382.5^{101}
				I → II	53	P-D	0.052	0.100^{101}	7.191263338808^{95}	42.3^{55}
L_2	−1.525	$\frac{2}{3}\pi$	101	II → I	98	T-B	0.097	0.000^{1}	3.612698367901^{101}	568.9^{101}
								0.100^{101}	3.893439278124^{1}	203.1^{1}
L_2	−1.525	π	53	II → I	46	T-B	0.045	0.000^{1}	3.550057521667^{53}	596.1^{53}
								0.052^{53}	3.893439278124^{1}	203.1^{1}
L_2	−1.525	$\frac{4}{3}\pi$	101	II → I	98	T-B	0.097	0.000^{1}	3.612698367901^{101}	568.9^{101}
								0.100^{101}	3.893439278124^{1}	203.1^{1}
L_2	−1.525	$\frac{5}{3}\pi$	101	II → I	28	T-B	0.027	0.000^{1}	3.893439278124^{1}	382.5^{101}
				I → II	53	P-D	0.052	0.100^{101}	7.191263338809^{95}	42.3^{55}
L_1	−1.500	0	101	II → I	32	T-B	0.031	0.000^{1}	4.335079769635^{1}	312.9^{100}
								0.100^{101}	6.278534335832^{86}	92.9^{26}
L_1	−1.500	$\frac{1}{3}\pi$	101	I → II	31	T-B	0.030	0.000^{1}	4.335079769636^{1}	336.3^{100}
								0.100^{101}	6.709708849920^{73}	75.4^{33}
L_1	−1.500	$\frac{2}{3}\pi$	101	I		-	-	-	0.000^{1}	3.285404209897^{101}	441.0^{101}
								0.100^{101}	4.335079769636^{0}	143.8^{1}

L_1	-1.500	π	101	I → II	13	T-B	0.012	0.000^{1} 0.100^{101}	2.610808484840^{101} 4.335079769636^{1}	1253.0^{101} 143.8^{1}
L_1	-1.500	$\frac{4}{3}\pi$	101	I	-	-	-	0.000^{1} 0.100^{101}	3.285404209898^{101} 4.335079769636^{0}	441.0^{101} 143.8^{1}
L_1	-1.500	$\frac{5}{3}\pi$	101	I → II	31	T-B	0.030	0.000^{1} 0.100^{101}	4.335079769636^{1} 6.709708849920^{73}	336.3^{100} 75.4^{33}
L_2	-1.500	0	40	I → II	26	T-B	0.025	0.000^{1} 0.039^{40}	4.542999724001^{1} 6.314061641933^{40}	106.3^{1} 76.7^{22}
L_2	-1.500	$\frac{1}{3}\pi$	67	I → II	28	T-B	0.027	0.000^{1} 0.066^{67}	4.542999724000^{1} 7.280094134109^{67}	249.2^{67} 58.2^{31}
L_2	-1.500	$\frac{2}{3}\pi$	101	I → II	24	T-B	0.023	0.000^{1} 0.100^{101}	3.902464774388^{101} 4.542999724000^{1}	302.5^{100} 106.3^{1}
L_2	-1.500	π	75	I → II II → I	8 67	T-B T-B	0.007 0.066	0.000^{1} 0.074^{75}	3.6245657993^{75} 4.542999724000^{1}	553.3^{75} 106.3^{1}
L_2	-1.500	$\frac{4}{3}\pi$	101	I → II	24	T-B	0.023	0.000^{1} 0.100^{101}	3.902464774388^{101} 4.542999724000^{1}	302.5^{100} 106.3^{1}
L_2	-1.500	$\frac{5}{3}\pi$	67	I → II	28	T-B	0.027	0.000^{1} 0.066^{67}	4.542999724000^{1} 7.280094134109^{67}	249.2^{67} 58.2^{31}

Table E.4: An overview of the key characteristics of a_{lt}-varying families. These characteristics include the number of family members, bifurcation behaviour and range of the acceleration magnitude, orbital period and hyperldlic unwinding behaviour. All variables are dimensionless apart from the angle which is shown in radians.

E.4. Orientation-varying families

The characteristics of the α-varying families are presented in an similar way as the two other family types presented in Sections E.2 and E.3. The only difference being that the α range of the family is presented instead of the H_{lt} or a_{lt} domain since it is the bifurcation parameter of this family type. The characteristics of the α-varying families can be found in Table E.5.

Family				Bifurcation behaviour						
E_i	a_{lt}	H_{lt}	N	OI	Me	Type	α_{bif}	α range	T range	ν_1 range
L_1	0.01	-1.550	360	I	-	-	-	$[0.0^{1}, 359.0^{360}]$	2.996039048368^{181} 3.274197020998^{1}	678.3^{181} 450.6^{1}
L_1	0.01	-1.525	360	II	-	-	-	$[0.0^{1}, 359.0^{360}]$	3.361571234121^{181} 3.812684720807^{1}	379.8^{181} 235.3^{1}
L_1	0.01	-1.500	360	II	-	-	-	$[0.0^{1}, 359.0^{360}]$	3.982295048464^{181} 4.747987299041^{1}	112.4^{181} 188.7^{1}
L_2	0.01	-1.550	360	I	-	-	-	$[0.0^{1}, 359.0^{360}]$	3.774611374213^{181} 4.058051784401^{1}	440.3^{181} 292.2^{1}
L_2	0.01	-1.525	360	II	-	-	-	$[0.0^{1}, 359.0^{360}]$	3.774611374213^{181} 4.058051784401^{1}	254.4^{181} 161.5^{1}
L_2	0.01	-1.500	360	I → II II → I	140 223	T-B T-B	139.0 222.0	$[0.0^{1}, 359.0^{360}]$	4.259693007789^{181} 4.923847377346^{1}	134.4^{181} 86.4^{1}
L_1	0.05	-1.550	360	II → I I → II II → I I → II	63 155 208 300	T-B T-B T-B T-B	62.0 154.0 207.0 299.0	$[0.0^{1}, 359.0^{360}]$	2.634915062987^{181} 4.221543764930^{1}	1359.1^{181} 184.3^{1}
L_1	0.05	-1.525	360	I → II II → I	99 264	T-B T-B	98.0 263.0	$[0.0^{1}, 359.0^{360}]$	2.827514995243^{181} 5.318177675332^{41}	856.1^{181} 85.1^{302}
L_1	0.05	-1.500	360	I → II II → I I → II II → I	96 124 237 268	P-D T-B T-B P-D	95.0 123.0 236.0 267.0	$[0.0^{1}, 359.0^{360}]$	3.109902476676^{181} 9.887662172813^{134}	500.2^{181} 31.0^{260}

L_2	0.05	−1.550	259	II → I	53	T-B	52.0		
				I → II	120	T-B	119.0	$[0.0^{1}, 129.0^{130}]$	3.482678917992^{259}	656.7^{259}
				II → I	142	T-B	242.0	$[231.0^{131}, 359.0^{259}]$	4.310716269762^{130}	126.6^{130}
				I → II	209	T-B	309.0			
L_2	0.05	−1.525	360	I → II	16	P-D	15.0			
				II → I	56	P-D	55.0			
				I → II	92	T-B	91.0			
				II → I	154	T-B	153.0	$[0.0^{1}, 359.0^{360}]$	3.554712961880^{180}	574.7^{181}
				I → II	207	T-B	206.0		5.507825353936^{323}	61.6^{305}
				II → I	270	T-B	269.0			
				I → II	306	P-D	305.0			
				II → I	346	P-D	345.0			
L_2	0.05	−1.500	161	I → II	19	T-B	118.0	$[100.0^{1}, 260.0^{161}]$	3.727493620628^{81}	342.7^{81}
				II → I	145	T-B	243.0		5.112035199537^{161}	33.2^{1}
L_1	0.10	−1.550	247	II → I	70	P-D	69.0			
				I → II	99	T-B	98.0			
				II → I	121	T-B	120.0	$[0.0^{1}, 123.0^{124}]$	2.643556604309^{124}	1432.0^{124}
				I → II	128	T-B	242.0	$[237.0^{125}, 359.0^{247}]$	9.166995135348^{93}	185.7^{1}
				II → I	149	T-B	263.0			
				I → II	178	P-D	291.0			
L_1	0.10	−1.525	291	II → I	69	P-D	118.0			
				I → II	82	T-B	81.0			
				II → I	111	T-B	110.0	$[0.0^{1}, 145.0^{146}]$	2.589415277041^{146}	1455.3^{146}
				I → II	141	T-B	140.0	$[215.0^{147}, 359.0^{291}]$	9.517163714780^{110}	161.5^{110}
				II → I	182	T-B	250.0			
				I → II	212	P-D	280.0			
L_1	0.10	−1.500	360	II → I	95	P-D	94.0			
				I → II	125	T-B	124.0	$[0.0^{1}, 359.0^{360}]$	2.610808484840^{181}	1252.9^{181}
				II → I	237	T-B	236.0		9.504294020205^{125}	78.1^{251}
				I → II	267	P-D	266.0			
L_2	0.10	−1.550	219	II → I	64	P-D	63.0			
				I → II	89	T-B	88.0			
				II → I	108	T-B	107.0	$[0.0^{1}, 109.0^{110}]$	3.522504113637^{110}	669.1^{110}
				I → II	115	P-D	246.0	$[251.0^{110}, 359.0^{219}]$	9.831729889375^{125}	211.6^{1}
				II → I	134	T-B	227.0			
				I → II	159	P-D	202.0			
L_2	0.10	−1.525	54	I → II	11	T-B	106.0			
				II → I	25	T-B	120.0	$[96.0^{1}, 122.0^{27}]$	3.598043439816^{27}	604.1^{27}
				I → II	30	T-B	240.0	$[238.0^{28}, 264.0^{54}]$	4.471732102814^{0}	88.6^{1}
				II → I	44	T-B	254.0			
L_2	0.10	−1.500	57	I → II	9	T-B	119.0			
				II → I	24	T-B	134.0	$[111.0^{1}, 138.0^{28}]$	3.661058724039^{28}	554.0^{28}
				I → II	34	T-B	227.0	$[222.0^{29}, 249.0^{57}]$	4.478621636207^{57}	100.6^{1}
				II → I	50	T-B	252.0			

Table E.5: An overview of the key characteristics of α-varying families. These characteristics include the number of family members, bifurcation behaviour and range of the acceleration orientation, orbital period and hyperbolic unwinding behaviour. All variables are dimensionless apart from the acceleration orientation which is shown in degrees.

This page is intentionally left blank.

F

Verification and validation

The totality of techniques presented in Appendices A, B and C enable the numerical approximation of equilibria contours and l.p.o families. This Addendum establishes the veracity of these dynamical structures via verification and validation of the techniques presented in Appendices A-C. Section F.1 presents the verification procedure for the root-finding algorithms used for construction of equilibria contours. The veracity of the Floquet targeter is discussed in Section F.3 whereas the correctness of the collocation method is presented in Section F.4. The veracity of the continuation procedure and resulting periodic solution families is discussed in Section F.5.

F.1. Equilibria contour verification

The equilibria contours comprise a set positions where a stationary spacecraft experiences a net zero acceleration. Each equilibrium location is calculated via the root-finding algorithm presented in Section C.2. The performance of this root-finder is verified by inspecting whether the defect vector of each solution satisfies the tolerances as specified in Table A.8.

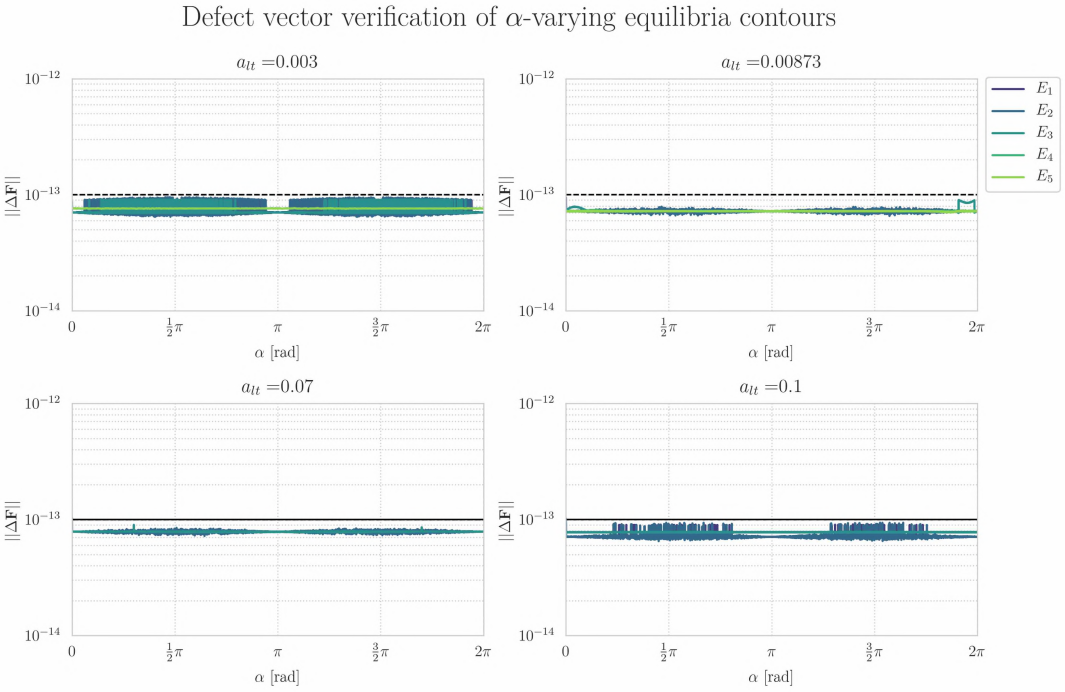

Figure F.1: Each subfigure shows the modulus of the defect vector of the complete equilibria contour at a specified acceleration.

It can be concluded from Figure F.1 that the root-finding algorithm performs as expected since the defect vector of each solution adheres to the defect tolerances.

While Figure F.1 confirms a correct implementation of the multivariate root-finding technique. It does not prove that the positions produced by the algorithm are equilibria. According to [35], a spacecraft that is exactly positioned at a Lagrangian point without any velocity, will forever stay at this Lagrangian point. Validation of the algorithm' solutions are obtained by explicit propagation for half a synodic period. The state deviations with respect to the equilibrium point after propagation are shown below in Figure F.2.

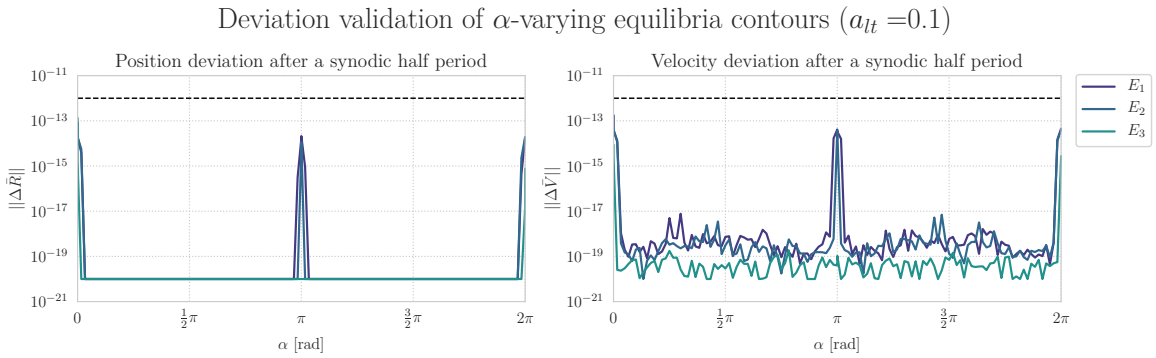

Figure F.2: The left Figure shows the position discrepancy whereas the right Figure shows the velocity discrepancy after propagation for a synodic half-period. The black dotted line indicates a threshold for machine noise. All deviation smaller than $10 \cdot 1.0^{-20}$ have been set to $1.0 \cdot 10^{-20}$ for visualization purposes.

The data in Figure F.2 shows that the position and velocity discrepancy are negligible after propgation of a synodic half-period. These deviations are the result of the errors associated with the explicit propagation procedure and a near-perfect computation of the equilibrium position via the root-finding algorithm of Section C.2. It is interesting to see that the deviations of the seed solutions are considerably larger compared to the deviations of other equilibria on the contour. A possible explanation for this phenomenon is that the seed solutions are computed via the univariate Newton-Raphson method instead of a multivariate root-finding method.

Figure F.1 proves a robust performance of the root-finding algorithm over the complete range of acceleration magnitudes whereas Figure F.2 confirms that the solutions generated by the algorithm are in fact libration points of the CR3BP-LT. These two Figures provide confidence in the veracity of the equilibria contours.

F.2. Floquet targeter verification

The veracity of the Floquet targeter is established by investigating how the state discrepancies of the seed solutions evolve as a function of the in-plane amplitudes and thrust parameters. These errors should evolve smoothly since the CR3BP-LT is a smooth system. The amplitude range is determined by the maximum amplitude offset as specified in Section A.6. Furthermore, rhe state discrepancies are investigated for all possible values of thrust orientations and the complete range of investigated thrust acceleration as specified in Chapter 1 of this report. The evolution of the state discrepancies due to a change in the three aforementioned variables. can be found in Figures F.3-F.5.

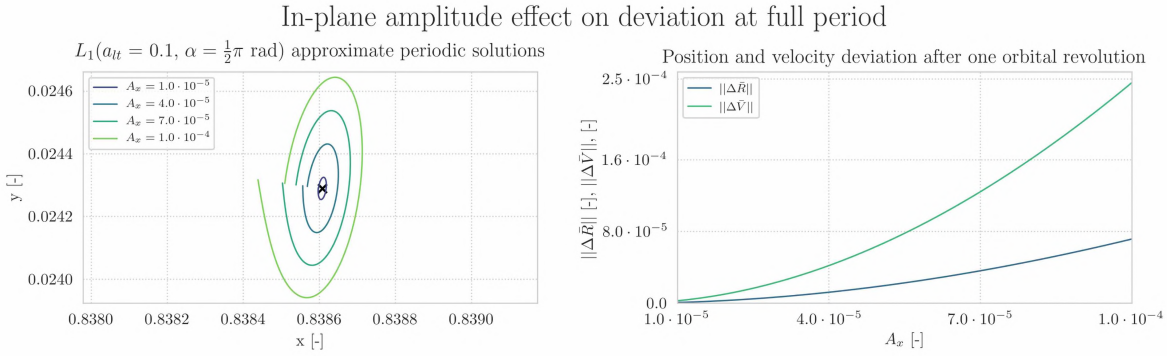

Figure F.3: Evolution of the approximate periodic solution state discrepancies due to a change in in-plane amplitude.

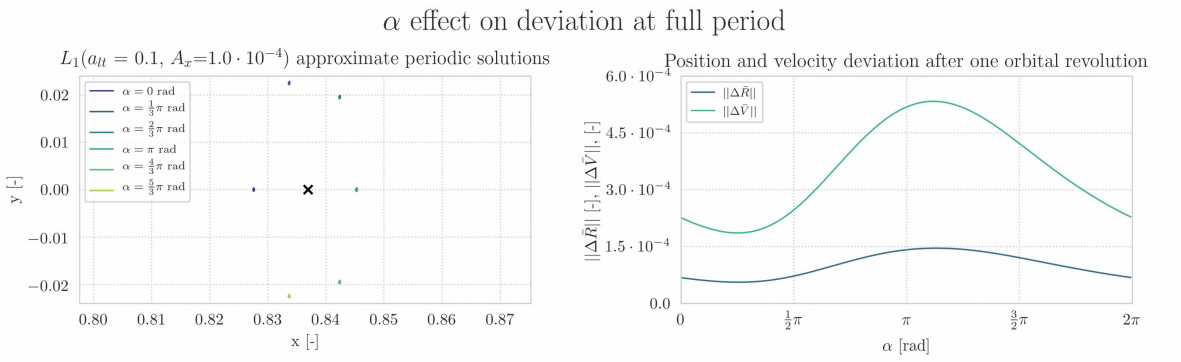

Figure F.4: Evolution of the approximate periodic solution state discrepancies due to a change in acceleration orientation.

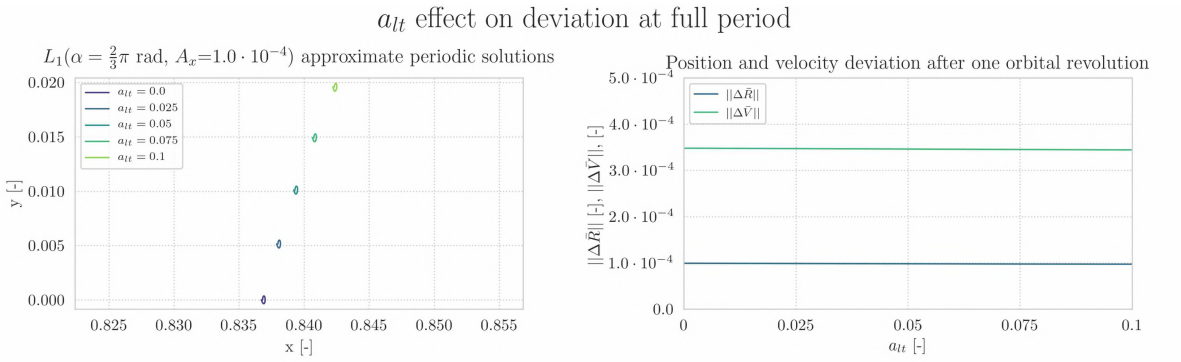

Figure F.5: Evolution of the approximate periodic solution state discrepancies due to a change in acceleration magnitude.

Figure F.3 show that the state discprencies of the approximate seed solutions smoothly evolve over the range of in-plane amplitudes as specified in Table A.6. Hence a robust performance of the Floquet targeter algorithm is proved within this range of in-plane amplitudes. Figures F.4 and F.5 show that the state discrepancies smoothly evolve as a function of the thrust parameters. The validation of the Floquet targeter is accomplished by comparing its performance against Richardson third order method [31]. Richardson's approximation is a widely used methodology for computation of approximate libration point orbits in the CR3BP [31]. A comparison between the two methods is provided below in Table F.1. A natural L_1 H-L orbit is selected as a test case. The in-plane amplitude is set equal to the maximum in-plane amplitude specified in Table A.6.

State	Floquet targeter		Richardson's method		Difference	
x	8.368151483688	$\cdot 10^{-1}$	8.368151483689	$\cdot 10^{-1}$	-1.0	$\cdot 10^{-12}$
y	1.2246467991474	$\cdot 10^{-20}$	0.0		-1.2246467991474	$\cdot 10^{-20}$
z	0.0		0.0		0.0	
$\dot{x}$	0.0		0.0		0.0	
$\dot{y}$	8.3722730179494	$\cdot 10^{-4}$	8.3784707256357	$\cdot 10^{-4}$	-6.197707686299	$\cdot 10^{-7}$
$\dot{z}$	0.0		0.0		0.0	
T	2.6915797202527		2.6915816604254		-1.940172699832488	$\cdot 10^{-6}$

Table F.1: Initial states for a natural H-L orbit around L_1 with an in-plane amplitude $A_x = 1.0 \cdot 10^{-4}$. It can be observed that the two methods provide a near-identical position but the methods provide a different starting velocity and estimation of the orbital period. The data regarding Richardson's method has been obtained from [25].

It can be concluded from Table F.1 that the positional difference between the two methods is in the range of machine noise. It can also be observed that there are significant differences between the Floquet targeter and Richardson's third order method in terms of velocity and orbital period. Both differences are attributed to the different order of the methods. The Floquet targeter determines a velocity correction based upon a first order linearization of the dynamics whereas Richardson's method cancels out secular components of the dynamics up to the third order.

The totality of Figures F.3- F.5 and Table F.1 prove the correctness of the Floquet targeter scheme as described in Section C.4.

F.3. Two-level targeter verification

The TLT algorithm is verified by correcting an approximate solution around an artificial equilibrium in vicinity of L_1. The low-thrust orientation acceleration of the seed solution is set to its maximum value ($a_{lt} = 0.1$) with an orientation perpendicular to the x-axis of the synodic reference frame ($\alpha = \frac{1}{2}\pi$). Furthermore, an in-plane amplitude is chosen that is almost two orders of magnitude larger than maximum in-plane amplitude specified in Table A.6. These settings result in a test case which tests the full functionality of the TLT algorithm. The behaviour of the TLT algorithm during the correction procedure of this orbit is shown below in Figure F.6.

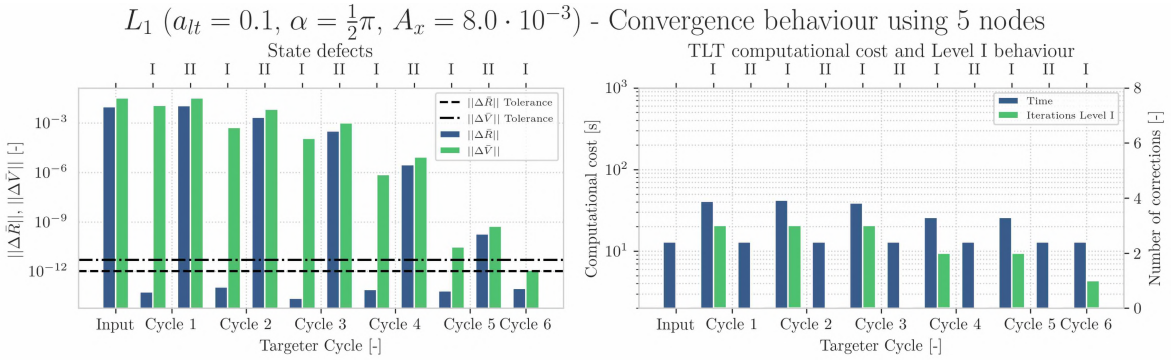

Figure F.6: The left Figure shows the convergence behaviour of the TLT procedure. The right Figure shows the computational cost of the TLT and the number of iterations required for the Level-I corrector needs to produce a position-continous trajectory.

Figure F.6 shows that the algorithm exhibits monotone convergence and converges in six iterations. Furthermore, it confirms the findings of [4] which state that the corrections provided by the level-II correction procedure should result in a smaller velocity discontinuities once the solution is reconverged with the level-I correction process. A visualization of the process presented in Figure F.6 is shown below in Figures F.7-F.9.

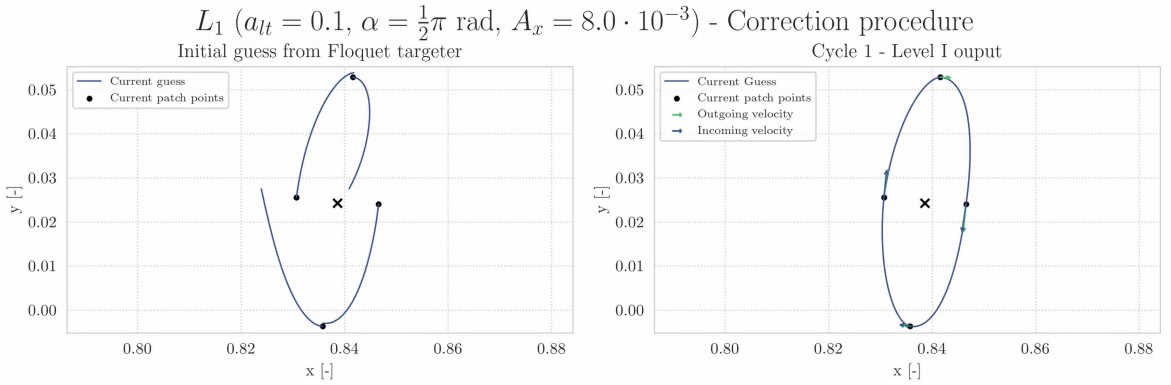

Figure F.7: The input trajectory of the TLT trajectory and the trajectory forwarded by the level-I corrector of cycle 1

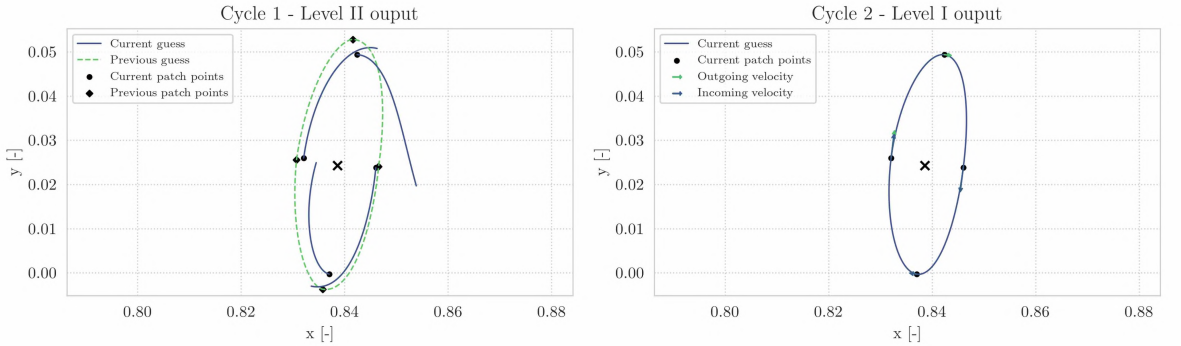

Figure F.8: The result of the TLT cycle 1, level-II corrector cycle 2, level-I corrector.

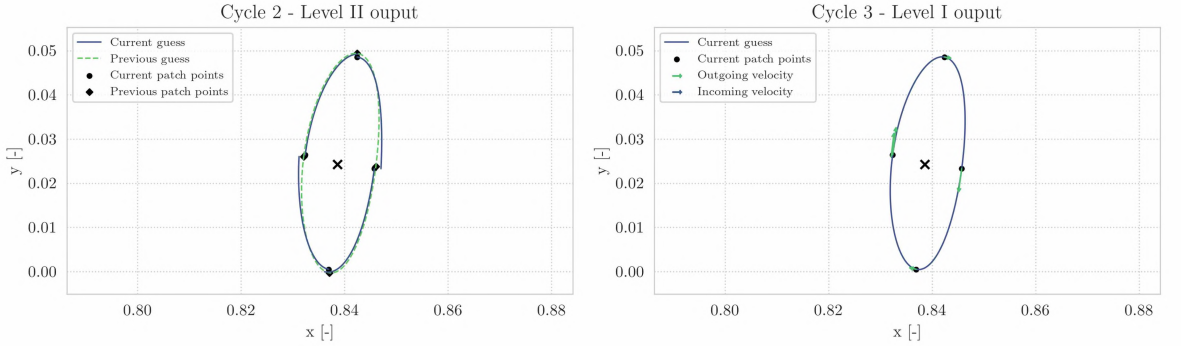

Figure F.9: The result of the TLT cycle 2, level-II corrector cycle 3, level-I corrector.

Figures F.7-F.9 do not show the complete process depicted in Figure F.6 since the corrections of the final three cycles cannot be observed with the naked eye.

The TLT correction procedure is validated by propagating the initial states of the input trajectory and corrected trajectory for their estimated orbital periods. Table F.2 provides an overview of the full-period deviations after one orbital revolution together with the characteristic multiplier related to the in-plane center subspace.

	Approximate seed solution		Refined seed solution	
$\|\|\Delta\bar{R}\|\|$	3.8290618036382	$\cdot 10^{-1}$	4.2363516820387	$\cdot 10^{-11}$
$\|\|\Delta\bar{V}\|\|$	0.82710696039002	$\cdot 10^{-1}$	1.2258327370445	$\cdot 10^{-10}$
$\|\| 1-\|\|\lambda_3\|\| \|\|$	1.5983036872667	$\cdot 10^{-1}$	1.9085844016331	$\cdot 10^{-12}$
$\|\| 1-\det(M) \|\|$	-4.4061911896875	$\cdot 10^{-9}$	-1.1124317467193	$\cdot 10^{-8}$

Table F.2: The full period state discrepancies of the input and corrected trajectory. Furthermore, the error in characteristic multiplier related to the in-plane center subspace is displayed for both trajectories.

Table F.2 shows that the TLT is able to produce an initial state and estimate an orbital period that belong to a periodic libration point orbit emanating from a noncollinear low-thrust equilibrium.

F.4. Collocation method verification

The veracity of the collocation procedure is established by computing the L_1 ($a_{lt} = 0.05$, $\alpha = 0.0$ rad, $H_{lt} = -1.525$) orbit from a ballistic seed solution L_1 ($a_{lt} = 0.0$, $\alpha = 0.0$ rad, $H_{lt} = -1.525$). In case the collocation procedure succeeds, it confirms its capability to produce libration point orbits with a desired Hamiltonian. This is an essential capability to compute the a_{lt}- and α-varying l.p.o families. The input orbit of the collocation procedure is obtained by providing an acceleration increment ($\Delta a_{lt} = 0.05$) to each node of the ballistic seed orbit. The ballistic, input and converged orbit are depicted in Figure F.10 while their full period deviations and monodromy eigensystem are presented in Table F.3.

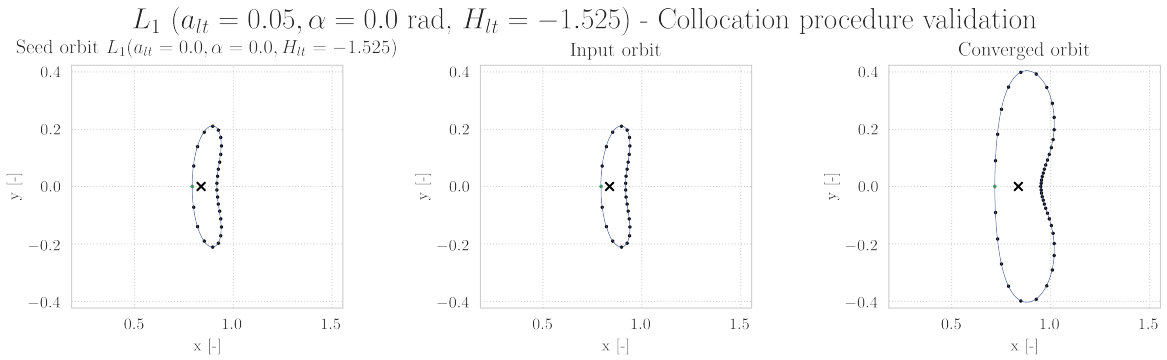

Figure F.10: A visualization of the seed orbit, input trajectory and converged solution of the collocation procedure. The totality of the dots form the mesh of the algorithm whereas the green dot indicates the initial state.

It should be stressed that the center subfigure in Figure F.10 is nowhere close to a periodic solution, although it could be interpreted as such from visual inspection.The periodicity of an orbit can be checked by investigating the state deviations and eigensystem properties. Such an analysis is presented below in Table F.3.

Method	Variable	Seed orbit	Input orbit	Converged orbit
Collocation	$\|\|\Delta \boldsymbol{F}\|\|$	$4.3230053967504 \cdot 10^{-13}$	$4.6386010389410 \cdot 10^{-2}$	$3.5152358156095 \cdot 10^{-13}$
	Δe_i	$2.7869117126167 \cdot 10^{-13}$	$1.38974793094065 \cdot 10^{-4}$	$3.6751022289658 \cdot 10^{-13}$
	$\max(e_i)$	$4.6724900286984 \cdot 10^{-10}$	$1.42080133528164 \cdot 10^{-4}$	$1.8799082394172 \cdot 10^{-13}$
	nodes	26	26	43
TLT defects	$\|\|\Delta \bar{R}\|\|$	$1.6005337645492 \cdot 10^{-12}$	$4.4031766961721 \cdot 10^{-3}$	$5.6570955097312 \cdot 10^{-12}$
	$\|\|\Delta \bar{V}\|\|$	$2.9338554376173 \cdot 10^{-12}$	$4.1270508152016 \cdot 10^{-2}$	$5.7516248616859 \cdot 10^{-12}$
	$\|\|\Delta H_{lt}\|\|$	$4.4381578877015 \cdot 10^{-13}$	$2.2776414277751 \cdot 10^{-1}$	$5.3794955767292 \cdot 10^{-12}$
Explicit propagation	$\|\|\Delta \bar{R}\|\|$	$7.5734759633996 \cdot 10^{-12}$	1.3671995113793	$6.2045150719090 \cdot 10^{-11}$
	$\|\|\Delta \bar{V}\|\|$	$2.1321116993244 \cdot 10^{-11}$	1.7345934861397	$2.0004908897853 \cdot 10^{-11}$
	$\|\|\Delta H_{lt}\|\|$	$9.3258734068512 \cdot 10^{-15}$	$3.9657409547945 \cdot 10^{-2}$	$7.5495165674510 \cdot 10^{-15}$
	$\|\| 1 - \|\|\lambda_3\|\| \|\|$	$9.8530295034038 \cdot 10^{-11}$	$4.9451492555471 \cdot 10^{-1}$	$5.5449405624963 \cdot 10^{-5}$
	$\|\|1 - \det(M)\|\|$	$4.36806768533415 \cdot 10^{-9}$	$3.6865976937861 \cdot 10^{-10}$	$5.2271951211935 \cdot 10^{-12}$

Table F.3: Validation of the collocation procedure by benchmarking comparing full period state deviations and monodromy eigensystem characteristics to the TLT and explicit propagation.

The top four rows of Table F.3 show whether the converged solution adheres to the collocation tolerances as specified in Table A.4. The middle three rows provide a consistency check with the TLT by computing the TLT defect vector. Finally, the bottom five rows present the state deviations and eigensystem properties of the orbits after explicit propagation of the initial state for estimated orbital period.

Several conclusions can be drawn from Table F.3. First of all, the collocation procedure described in Section C.5 satisfies the constraints specified in Table A.4 despite significant state discrepancies in the input trajectory. Secondly, the TLT defect vector resulting from the mesh of the converged orbit nearly satisfies with the criteria as specified in Table A.7. The similarity between the state deviations of both methods establish confidence in a correct implementation of the collocation procedure and an appropriate selection of the tolerances as specified in Table A.4. Thirdly, inspection of the state deviations and eigensystem properties after explicit propagation reveal that the collocation procedure is able to produce an initial state and orbital period that belong to a periodic solution. Finally, it can be concluded that the collocation procedure can refine periodic solutions to a desired Hamiltonian, contrary to the TLT targeter as specified in Secion C.4.3.

The converged solution in Figure F.10 shows a peculiar spacing of the nodes over the interval. The mesh is the result of the mesh refinement methodology as explained in Section B.2.2. This error control method is crucial in obtaining a periodic solution that satisfies the tolerances as specified in A.8. Tthe mesh refinement process associated with the transformation of the input orbit to the converged orbit as described Figure F.10

and Table F.3 is visualized via a collection of bar charts in Figure F.11. The error distribution of single mesh is represented using a bar chart where the width of each bar represents the time duration of the segment and the bar's height indicates the segment error.

Figure F.11: The mesh refinement procedure associated with the collocation procedure as described in Figure F.10 and Table F.3.

Figure F.11 suggests a correct implementation of Boor's method for error control [9] since the mesh refinement procedure distributes the errors more equally with each iteration and the number of nodes is increased once the equidistributed mesh does not meet the error tolerance as specified in Table A.4.

The totality of Figure F.10, Table F.3 and Figure F.11 establish confidence in a proper implementation of the collocation procedure as explained in Section C.5.

F.5. Libration point orbit families verification

The final Section of this addendum discusses the veracity of the l.p.o families as presented in Chapter 1 and Appendices D and E. The veracity of the l.p.o families are established per type of family. Section F.5.1 presents the veracity of the H_{lt}-varying families. The correctness of the a_{lt}-varying families is discussed in Section F.5.2 whereas the authenticity of the α-varying families is discussed in Section F.5.3. Each Section provides an overview of the termination causes for the numerical continuation procedure associated with construction of an l.p.o family. An exhaustive list of the encountered termination causes is provided in Table F.4.

Label	Termination root cause
A	Full-period position discrepancy exceeds threshold.
B	Full-period velocity discrepancy exceeds threshold.
C	Increment at half-period below threshold.
D^n	Maximum number (n) of family members reached.
E	Termination due to reversing of continuation direction.
F	Periodic eigenvalue deviation exceeds threshold.
G	Acceleration of a_{lt}-varying family exceeds upper limit.
H	Orbit Hamiltonian smaller than Hamiltonian of associated equilibrium.
I	Instability in collocation procedure.
J	Full revolution of α-varying family reached.

Table F.4: An overview of the termination causes of the numerical continuation procedure responsible for the construction of l.p.o families.

An instability in the collocation procedure refers to the phenomenon where a node at t_{i+1} is corrected to a time earlier than node t_i. This results in a mesh where a part of the trajectory travels back in time. This phenomenon results in a unsolvable collocation problem which triggers the numerical model to terminate the numerical continuation procedure.

Besides an understanding of the termination causes, the veracity of a single l.p.o family is established via four analyses. First of all, it is checked whether each family member satisfies the tolerances as specified in Tables A.4 and A.8. Secondly, the monodromy eigensystem of each family member is investigated to check whether it adheres to the structure of a symplectic map. Thirdly, the evolution of H_{lt}, a_{lt} and α are investigated to see if a family evolves along the H_{lt}, a_{lt} or α solution branch respectively. Finally, a symmetry shooting analysis evaluates the degree of symmetry between the shooting condition of two families (H_{lt}- and a_{lt}-varying) or within one family (α-varying) to investigate the root cause of observed asymmetries. The aforementioned four analyses are shown for a subset of all constructed l.p.o families for sake of conciseness.

F.5.1. Hamiltonian-varying families

A multitude of H_{lt}-varying families is presented in Chapter 1 and their veracity is discussed in this Section. The termination cause of each numerical continuation procedure associated with construction of a H_{lt}-varying family is presented in Table F.5.

	E_1						E_2					
α [rad]	0	$\frac{1}{3}\pi$	$\frac{2}{3}\pi$	π	$\frac{4}{3}\pi$	$\frac{5}{3}\pi$	0	$\frac{1}{3}\pi$	$\frac{2}{3}\pi$	π	$\frac{4}{3}\pi$	$\frac{5}{3}\pi$
$a_{lt} = 0.00$	C	-	-	-	-	-	E	-	-	-	-	-
$a_{lt} = 0.01$	C	D^{3000}	D^{3000}	C	A	D^{3000}	I	I	I	I	I	I
$a_{lt} = 0.05$	C	B	F	C	F	I	I	I	I	I	I	I
$a_{lt} = 0.10$	C	F	I	E	F	I	D^{1000}	I	I	I	I	D^{4500}

Table F.5: An overview of the termination causes of the numerical continuation procedures associated with H_{lt}-varying families. The termination cause of some H_{lt}-varying families is underlined, meaning that proof of their veracity is provided later in this Section

Several reasons for termination are observed from Table F.5. Most families with a collinear acceleration orientation are terminated because the spacing between two subsequent family members at the half-period falls below the threshold specified in Table A.4. Some families have been terminated after reaching a specified number of family members. This constraint has been imposed to keep the computational cost of a H_{lt}-varying family bounded to a maximum of ten days. However, the majority of continuation procedures have been terminated because of instabilities in the collocation algorithm which are attributed to the variable node times of the collocation root-finding scheme. The remainder of this Section discusses the veracity of the H_{lt}-varying families whose termination code in Table F.5 is underlined.

L_1 ($a_{lt} = 0.0$, $\alpha = 0$ rad) H_{lt}-varying family

The periodicity of each member of the natural L_1 family is verified in Figure F.12. This Figure shows that the collocation procedure produces a converged solution with an equidistributed truncation error. The initial state of the resulting solution is explicitly propagated for the estimated orbital period which confirms the periodicity of the family members and a correct implementation of the collocation procedure. The full-period state discrepancy of the first orbits exceeds the thresholds of Table A.8 but termination is intentionally suppressed since the performance of the collocation procedure improves afterwards.

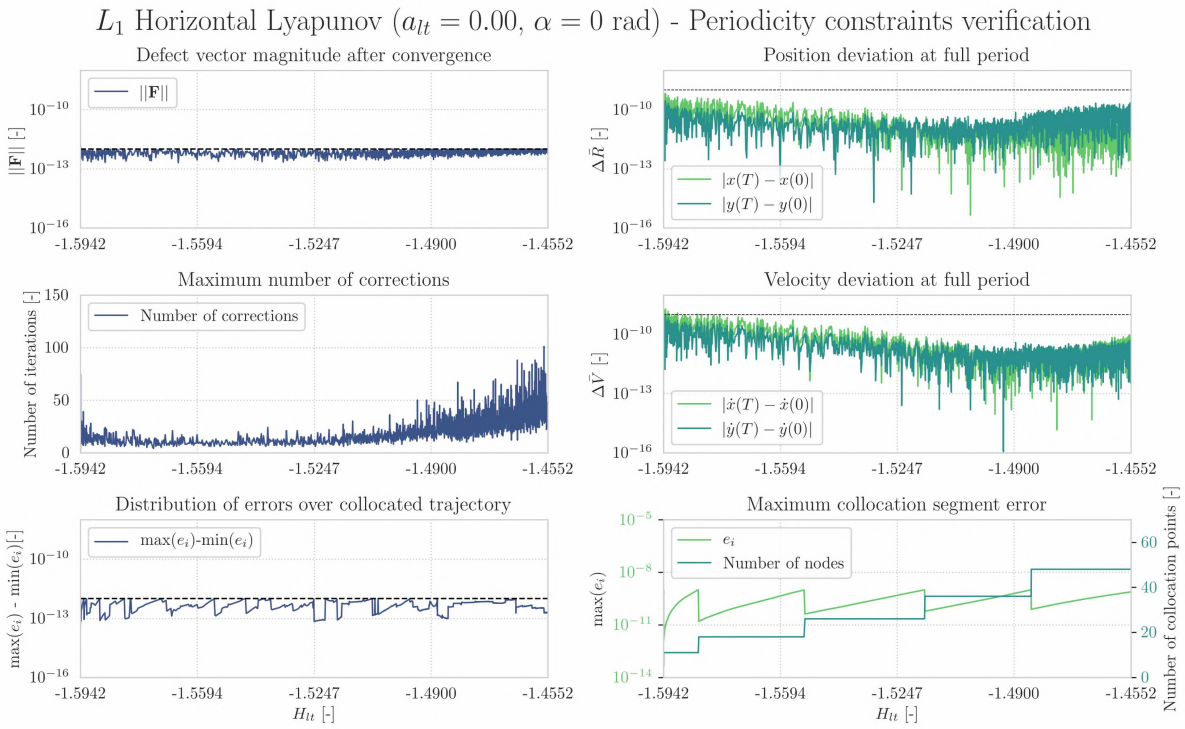

Figure F.12: Periodicity verification of the L_1 (a_{lt} = 0.0, α = 0 rad) family. The three left subfigures and the bottom right subfigure demonstrate the characteristics of the collocation method whereas the upper and middle right subfigure show the full-period state discrepancy of the solution. These discrepancies are obtained via explicit propagation of the initial state forwarded by the collocation procedure.

According to Floquet theory [34], The eigensystem of the monodromy matrix of a periodic solution adheres to the structure of a symplectic map. Among others, the determinant of a symplectic map is equal to one and its eigenvalues occur in reciprocal pairs. Furthermore, a periodic solution requires at least one eigenvalue pair with $|\lambda| = 1$. Figure F.13 demonstrates that these properties are satisfied for each member of the ballistic L_1 family.

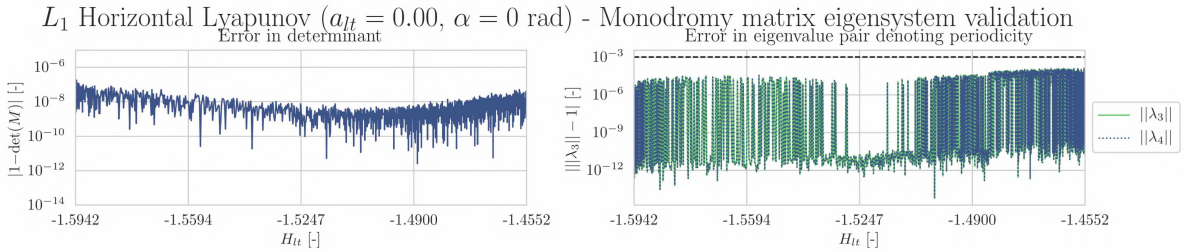

Figure F.13: Monodromy matrix eigensystem validation of the L_1 (a_{lt} = 0.0, α = 0 rad) family. The left subfigure shows the deviation of the monodromy matrix determinant whereas the right subfigure demonstrates the deviation of the eigenvalue representing the in-plane center subspace.

Figure F.14 demonstrates that the Hamiltonian varies over the ballistic L_1 family while both thrust parameters are constant. Furthermore, the phase constraint is also satisfied over the complete family.

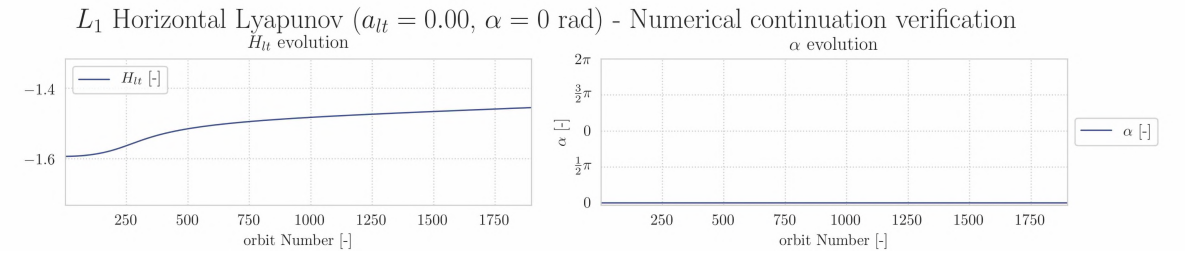

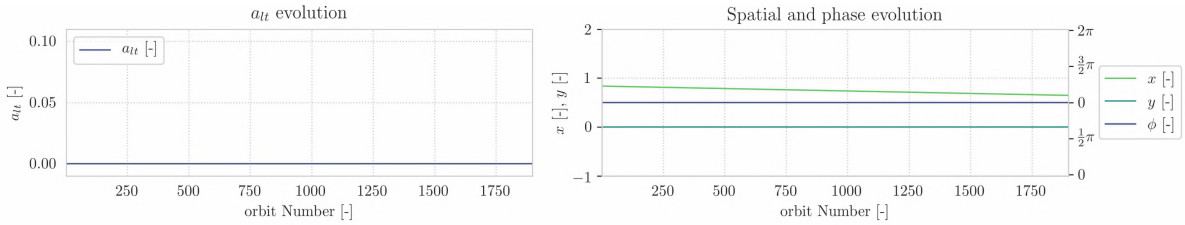

Figure F.14: Numerical continuation verification of the L_1 (a_{lt} = 0.0, α = 0 rad) family. The top subfigures and bottom left subfigure show the evolution of H_{lt}, a_{lt} and α. The bottom right subfigure shows the spatial evolution and phase drift of the initial condition along the family.

Figure F.15 confirms a consistent spacing between the initial state of two consecutive members of the solution family. The bottom left subfigure shows that the positional increment between two consecutive members does not meet the threshold in Table A.8 resulting in termination of the continuation procedure.

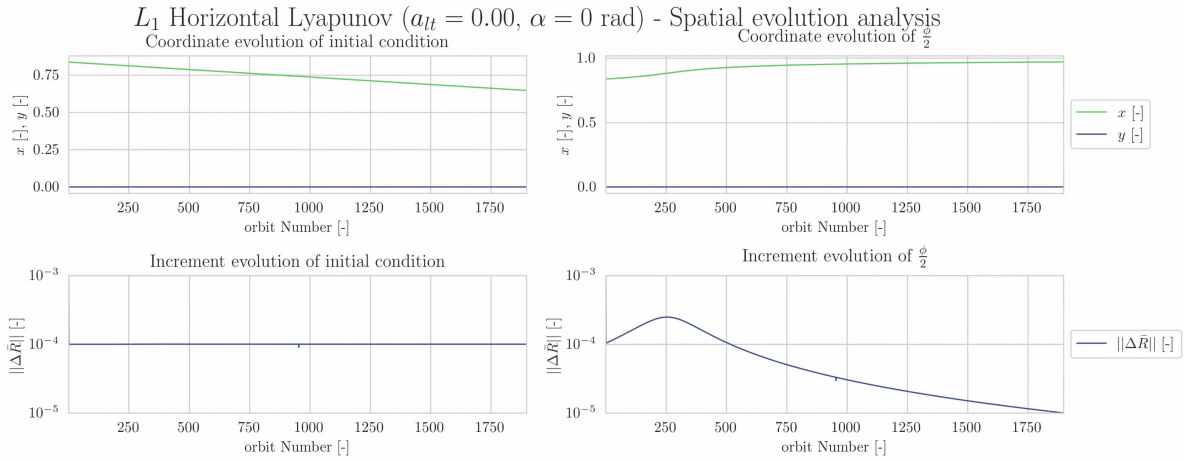

Figure F.15: Spatial evolution of the L_1 (a_{lt} = 0.0, α = 0 rad) family. The two top subfigures show the spatial evolution of the initial condition and half-period state. The bottom two subfigures show the positional increment between the initial and half-period state between two subsequent family members.

L_2 (a_{lt} = 0.0, α = 0.0 rad) H_{lt}-varying family

The periodicity of each member of the natural L_2 family is verified in Figure F.16. This Figure shows that the collocation procedure generates a converged solution with an equidistributed truncation error. The initial state of the resulting solution is explicitly propagated for the estimated orbital period which confirms the periodicity of the family members and a correct implementation of the collocation procedure.

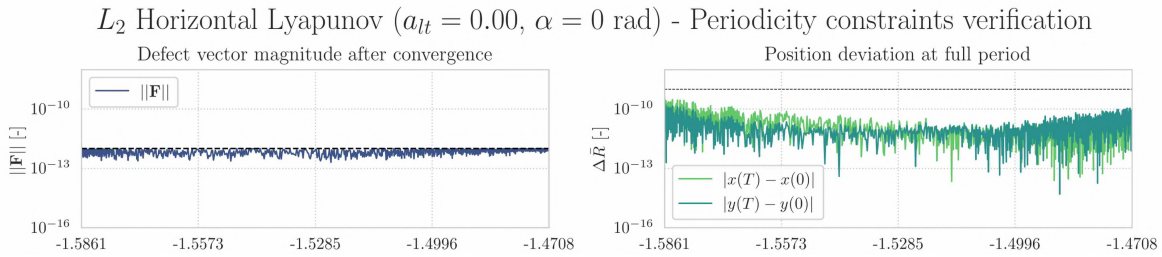

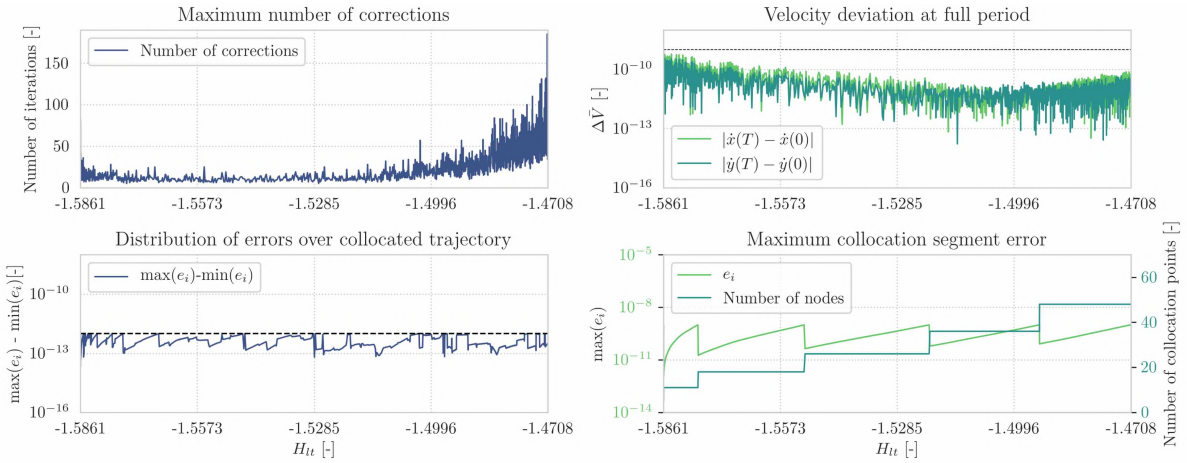

Figure F.16: Periodicity verification of the L_2 (a_{lt} = 0.0, α = 0 rad) family. The three left subfigures and the bottom right subfigure demonstrate the characteristics of the collocation method whereas the upper and middle right subfigure show the full-period state discrepancy of the solution. These discrepancies are obtained via explicit propagation of the initial state forwarded by the collocation procedure.

Characteristics of the monodromy eigensystem of each member of the ballistic L_2 family are shown in Figure F.17. It can be concluded that the monodromy eigensystem of each family member adheres to the structure of a symplectic map.

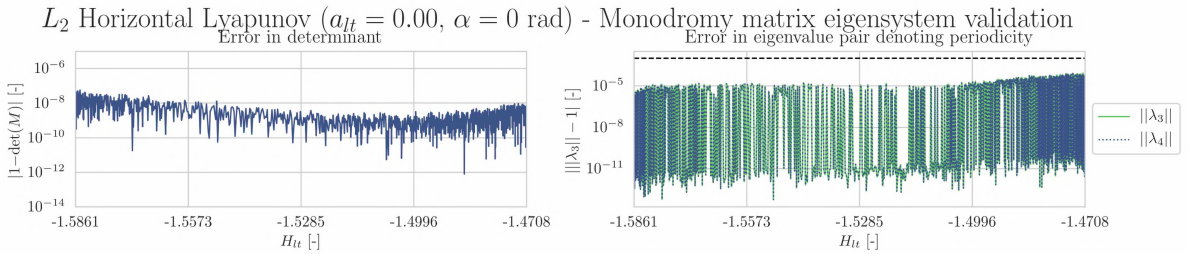

Figure F.17: Monodromy matrix eigensystem validation of the L_2 (a_{lt} = 0.0, α = 0 rad) family. The left subfigure shows the deviation of the monodromy matrix determinant whereas the right subfigure demonstrates the deviation of the eigenvalue representing the in-plane center subspace.

Figure F.18 proves that the ballistic family is a H_{lt}-varying family since its thrust parameters are constant. Next to that it can be observed that the pseudo-arclength continuation provides a constant spacing between the family members and the phase constraint is also satisfied over the complete family.

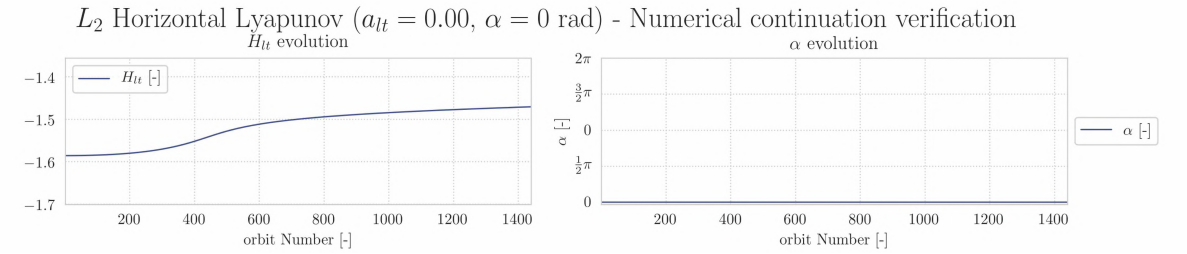

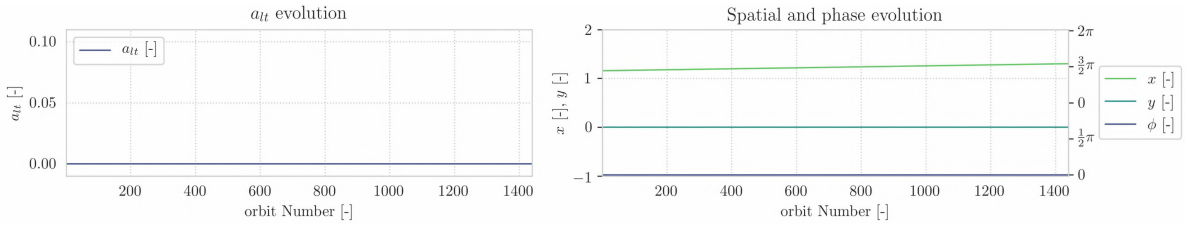

Figure F.18: Numerical continuation verification of the L_2 (a_{lt} = 0.0, α = 0 rad) family. The top subfigures and bottom left subfigure demonstrate that the l.p.o family unfolds along the Hamiltonian branch. The bottom right subfigure shows the spatial evolution and phase drift of the initial condition along the family.

L_1 ($a_{lt} = 0.01$, $\alpha = \frac{2}{3}\pi$ rad) H_{lt}-varying family

The periodicity of the members that form the $L_1(a_{lt} = 0.01,\ \alpha = \frac{2}{3}\pi$ rad) family are established in Figure F.19. This Figure shows that the collocation procedure produces a converged solution with an equidistributed truncation error. The initial state of the resulting solution is explicitly propagated for the estimated orbital period which confirms the periodicity of the family members and a correct implementation of the collocation procedure. The full-period state discrepancy of the first orbits exceeds the thresholds of Table A.8. but termination is intentionally suppressed since the performance of the collocation procedure improves afterwards. It can also be observed that the error distribution does not always meet the equidistribution threshold but this does not result in a member with a state discrepancy that violates the periodicity constraints.

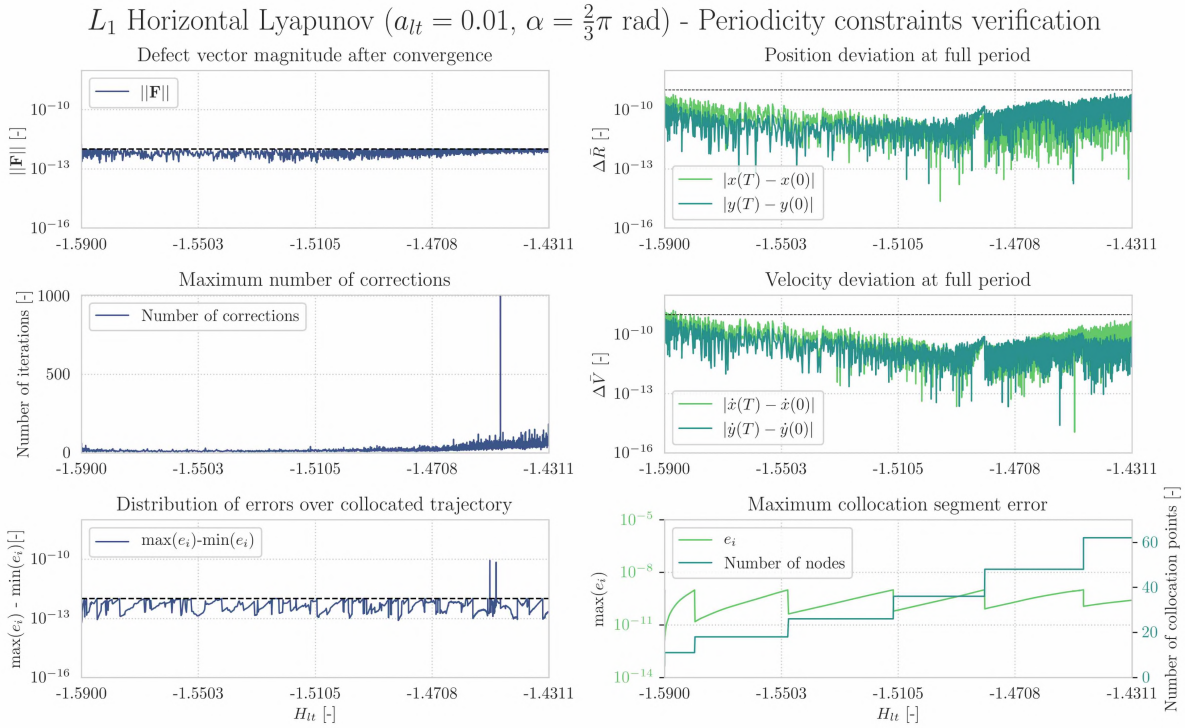

Figure F.19: Periodicity verification of the L_1 ($a_{lt} = 0.01$, $\alpha = \frac{2}{3}\pi$ rad) family. The three left subfigures and the bottom right subfigure demonstrate the characteristics of the collocation method whereas the upper and middle right subfigure show the full-period state discrepancy of the solution. These discrepancies are obtained via explicit propagation of the initial state forwarded by the collocation procedure.

Characteristics of the monodromy eigensystem of each member of the L_1 ($a_{lt} = 0.01$, $\alpha = \frac{2}{3}\pi$ rad) family are shown in Figure F.20. It can be concluded that the monodromy eigensystem of each family member adheres to the structure of a symplectic map.

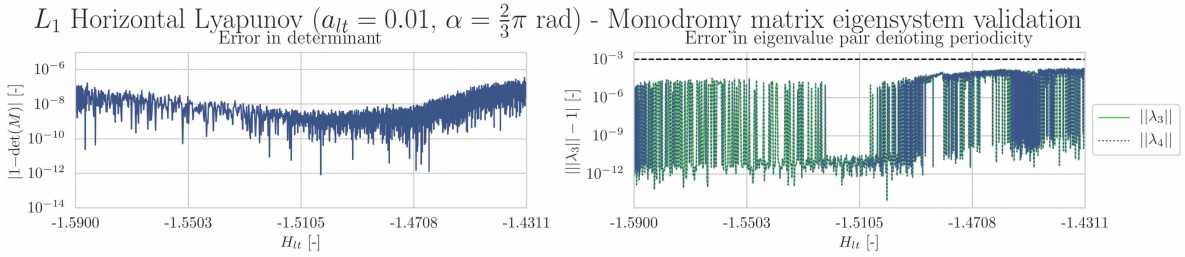

Figure F.20: Monodromy matrix eigensystem validation of the L_1 ($a_{lt} = 0.01$, $\alpha = \frac{2}{3}\pi$ rad) family. The left subfigure shows the deviation of the monodromy matrix determinant whereas the right subfigure demonstrates the deviation of the eigenvalue representing the in-plane center subspace.

Figure F.21 proves that the L_1 ($a_{lt} = 0.01$, $\alpha = \frac{2}{3}\pi$ rad) family is a H_{lt}-varying family since its thrust parameters are constant. Next to that it can be observed that the pseudo-arclength continuation provides a constant spacing between the family members. The phase constraint is satisfied for the majority of the family apart from the final members of the family where a slight phase shift is observed.

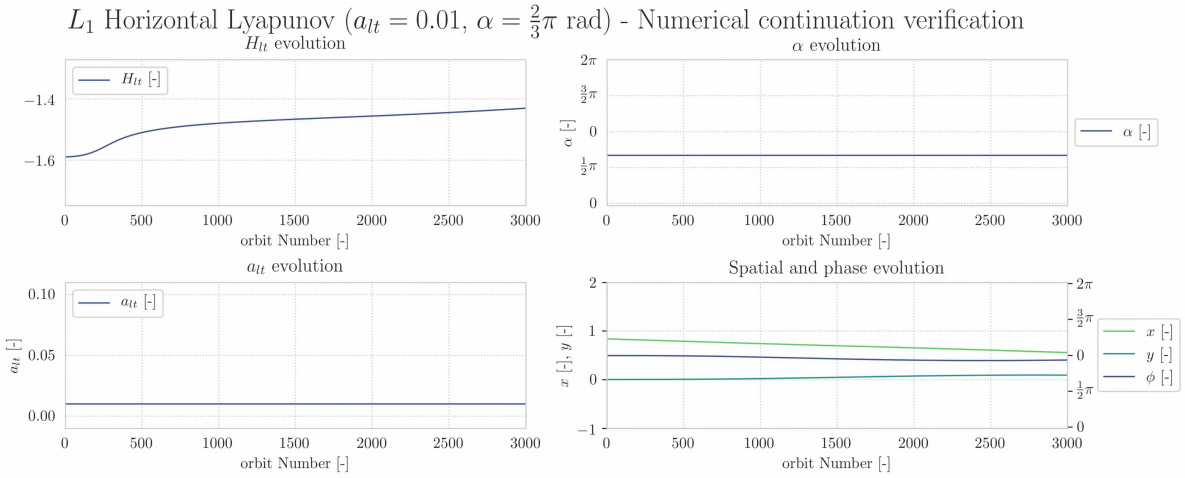

Figure F.21: Numerical continuation verification of the L_1 ($a_{lt} = 0.01$, $\alpha = \frac{2}{3}\pi$ rad) family. The top subfigures and bottom left subfigure demonstrate that the l.p.o family unfolds along the Hamiltonian branch. The bottom right subfigure demonstrates that pseudo-archlength continuation results in a constant spacing between family members and the phase constraint is satisfied over the complete family. The bottom right subfigure shows the spatial evolution and phase drift of the initial condition along the family.

The symmetry shooting analysis that investigates the root cause between different termination points of the L_1 ($a_{lt} = 0.01$, $\alpha = \frac{2}{3}\pi$ rad and $\alpha = \frac{4}{3}\pi$ rad) families is presented in the next paragraph.

L_1 ($a_{lt} = 0.01$, $\alpha = \frac{4}{3}\pi$ rad) H_{lt}-varying family

The periodicity of the members that form the L_1($a_{lt} = 0.01$, $\alpha = \frac{4}{3}\pi$ rad) family are established in Figure F.22. This Figure shows that the collocation procedure produces a converged solution with an equidistributed truncation error. The initial state of the resulting solution is explicitly propagated for the estimated orbital period which confirms the periodicity of the family members and a correct implementation of the collocation procedure. The full-period state discrepancy of the first orbits exceeds the thresholds of Table A.8. but termination is intentionally suppressed since the performance of the collocation procedure improves afterwards. At the end of the family generation procedure, the numerical continuation algorithm is terminated since the final member exceeds the position discrepancy threshold at full-period.

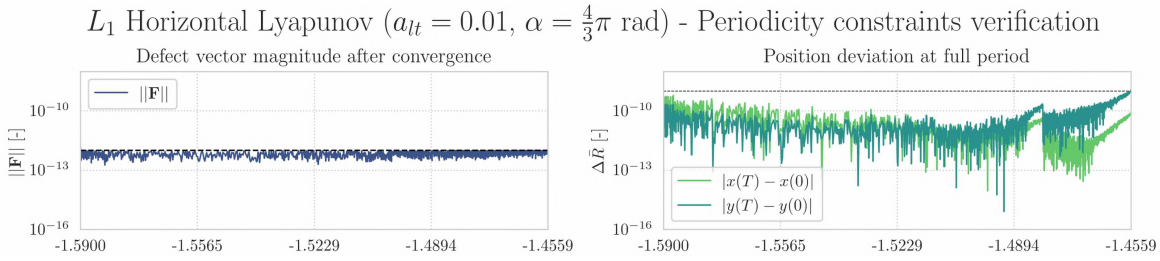

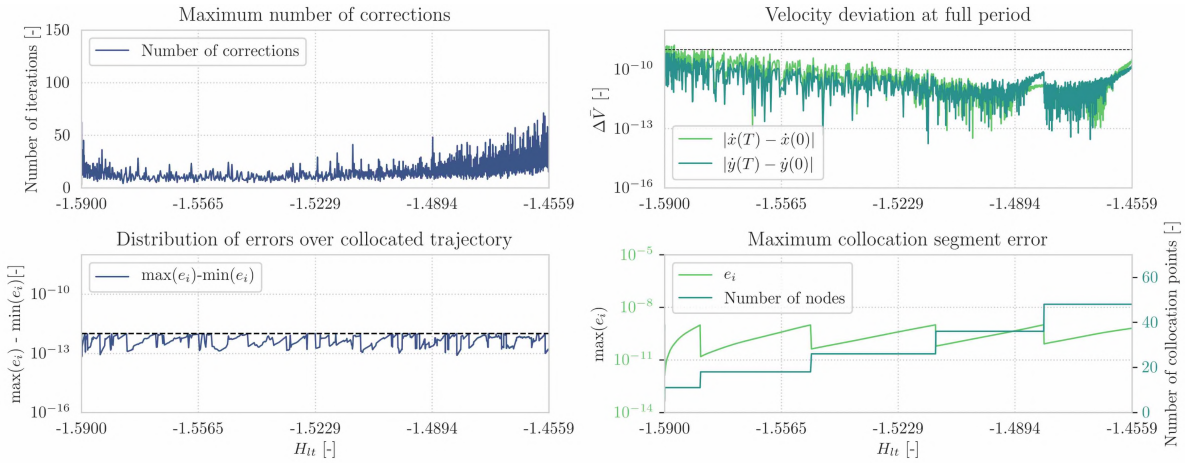

Figure F.22: Periodicity verification of the L_1 ($a_{lt} = 0.01$, $\alpha = \frac{4}{3}\pi$ rad) family. The three left subfigures and the bottom right subfigure demonstrate the characteristics of the collocation method whereas the upper and middle right subfigure show the full-period state discrepancy of the solution. These discrepancies are obtained via explicit propagation of the initial state forwarded by the collocation procedure.

Characteristics of the monodromy eigensystem of each member of the L_1 ($a_{lt} = 0.01$, $\alpha = \frac{4}{3}\pi$ rad) family are shown in Figure F.23. It can be concluded that the monodromy eigensystem of each family member adheres to the structure of a symplectic map.

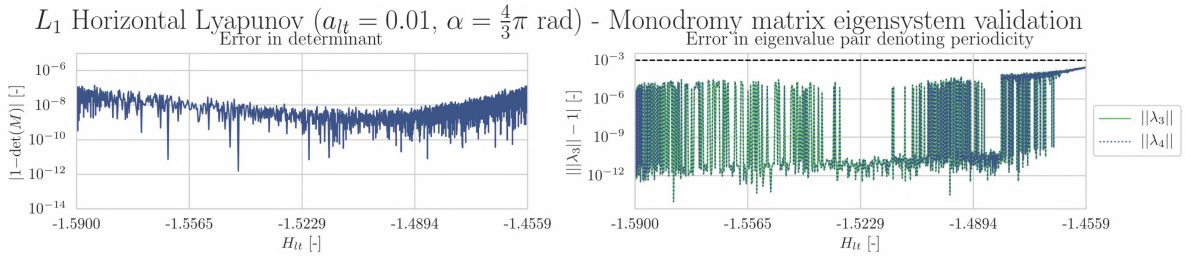

Figure F.23: Monodromy matrix eigensystem validation of the L_1 ($a_{lt} = 0.01$, $\alpha = \frac{4}{3}\pi$ rad) family. The left subfigure shows the deviation of the monodromy matrix determinant whereas the right subfigure demonstrates the deviation of the eigenvalue representing the in-plane center subspace.

Figure F.24 proves that the L_1 ($a_{lt} = 0.01$, $\alpha = \frac{4}{3}\pi$ rad) family is a H_{lt}-varying family since its thrust parameters are constant. Next to that it can be observed that the pseudo-arclength continuation provides a constant spacing between the family members. The phase constraint is satisfied for the majority of the family apart from the final members of the family where a slight phase shift is observed. The phase shift is in the opposite direction as the shift observed at the end of the L_1 ($a_{lt} = 0.01$, $\alpha = \frac{2}{3}\pi$ rad) family.

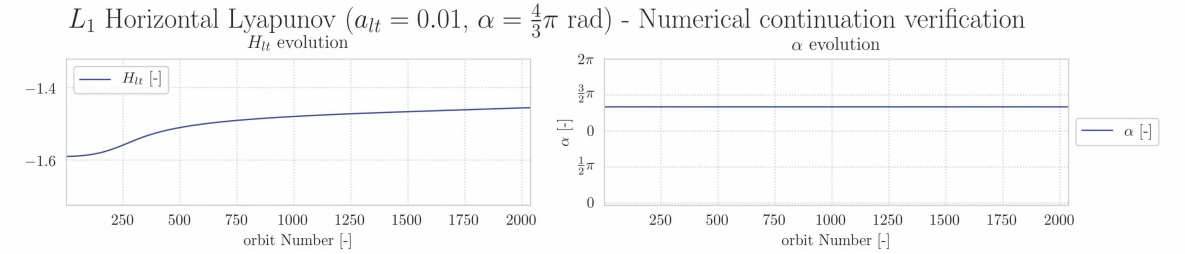

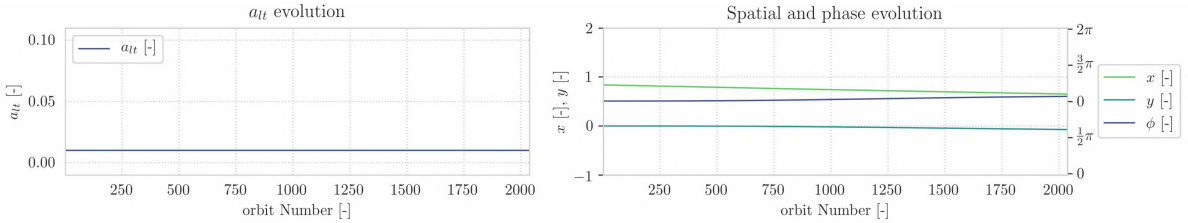

Figure F.24: Numerical continuation verification of the L_1 ($a_{lt} = 0.01$, $\alpha = \frac{4}{3}\pi$ rad) family. The top subfigures and bottom left subfigure demonstrate that the l.p.o family unfolds along the Hamiltonian branch. The bottom right subfigure shows the spatial evolution and phase drift of the initial condition along the family.

It is expected that the numerical continuation procedure of the L_1 ($a_{lt} = 0.01$, $\alpha = \frac{2}{3}\pi$ rad) and L_1 ($a_{lt} = 0.01$, $\alpha = \frac{4}{3}\pi$ rad) family would terminate after the same number of members because of the symmetry in the CR3BP-LT. Since this is not the case, a symmetry analysis between the shooting conditions of both families is shown below in Figure F.25.

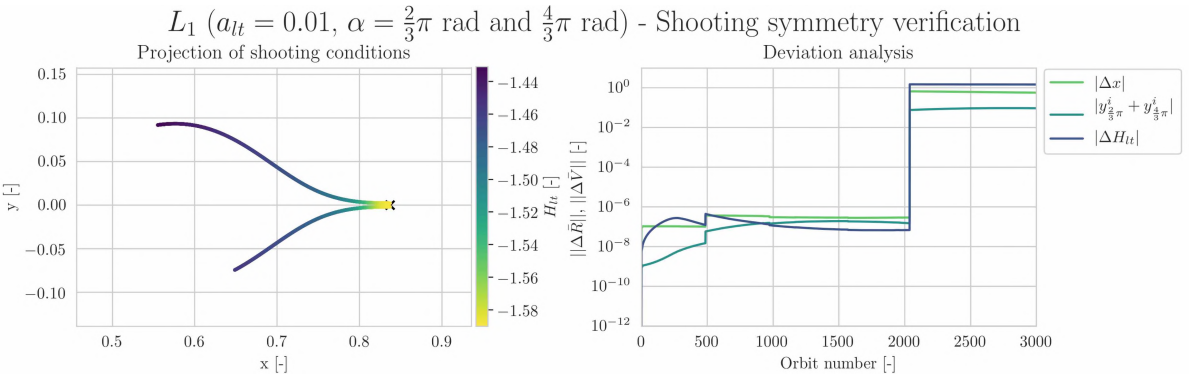

Figure F.25: Shooting symmetry analysis of the L_1 ($a_{lt} = 0.01$, $\alpha = \frac{2}{3}\pi$ and $\frac{4}{3}\pi$ rad) families. The left subfigure shows the evolution of the spatial conditions of both families. The upper branch shows the $\alpha = \frac{2}{3}\pi$ family whereas the lower branch denotes the $\alpha = \frac{4}{3}\pi$ family. The right subfigure shows the symmetry between the initial conditions of the family members.

Figure F.25 reveals that the degree of symmetry between the initial conditions of both families remains constant until the preliminary termination of the L_1 ($a_{lt} = 0.01$, $\alpha = \frac{4}{3}\pi$ rad) family. Therefore, it is unlikely that the phase drift is the cause for the different termination points of the two families. This discrepancy is explained by the fact that collocation procedure responsible for generation of the final member of the $\alpha = \frac{4}{3}\pi$ family uses an insufficient number of nodes.

L_1 ($a_{lt} = 0.05$, $\alpha = \frac{1}{3}\pi$ rad) H_{lt}-varying family

The periodicity of the members that form the L_1($a_{lt} = 0.05$, $\alpha = \frac{1}{3}\pi$ rad) family are established in Figure F.26. This Figure show that the collocation procedure produces a converged solution with an equidistributed truncation error. The initial state of the resulting solution is explicitly propagated for the estimated orbital period which confirms the periodicity of the family members and a correct implementation of the collocation procedure. The full-period state discrepancy of the first orbits exceeds the thresholds of Table A.8. but termination is intentionally suppressed since the performance of the collocation procedure improves afterwards. At the end of the family generation procedure, the continuation procedure is terminated since the final member exceeds the velocity discrepancy threshold at full-period.

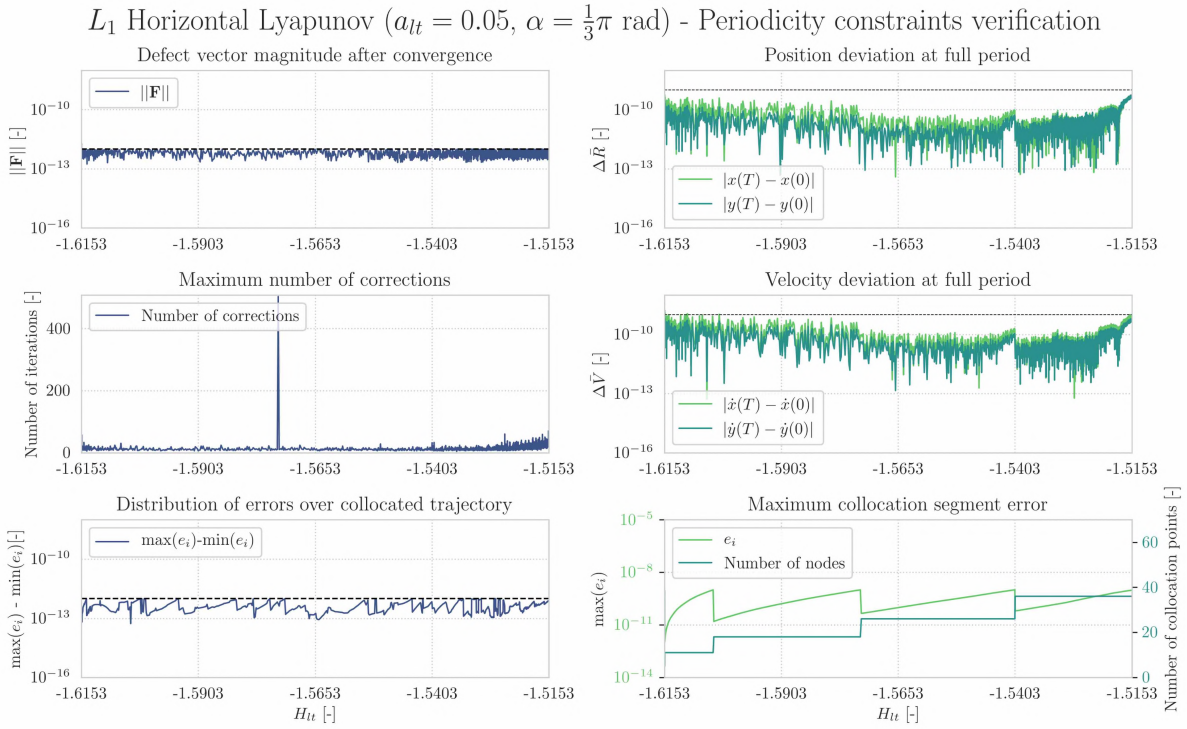

Figure F.26: Periodicity verification of the L_1 ($a_{lt} = 0.05$, $\alpha = \frac{1}{3}\pi$ rad) family. The three left subfigures and the bottom right subfigure demonstrate the characteristics of the collocation method whereas the upper and middle right subfigure show the full-period state discrepancy of the solution. These discrepancies are obtained via explicit propagation of the initial state forwarded by the collocation procedure.

Characteristics of the monodromy eigensystem of each member of the L_1 ($a_{lt} = 0.05$, $\alpha = \frac{1}{3}\pi$ rad) family are shown in Figure F.27. It can be concluded that the monodromy eigensystem of each family member adheres to the structure of a symplectic map.

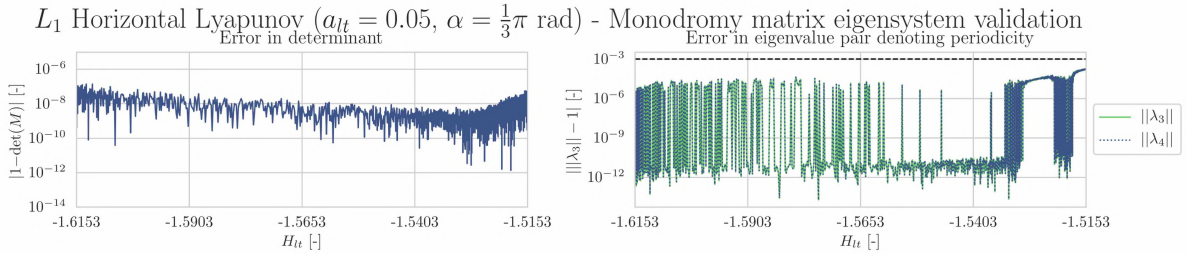

Figure F.27: Monodromy matrix eigensystem validation of the L_1 ($a_{lt} = 0.05$, $\alpha = \frac{1}{3}\pi$ rad) family. The left subfigure shows the deviation of the monodromy matrix determinant whereas the right subfigure demonstrates the deviation of the eigenvalue representing the in-plane center subspace.

Figure F.28 proves that the L_1 ($a_{lt} = 0.05$, $\alpha = \frac{1}{3}\pi$ rad) family is a H_{lt}-varying family since its thrust parameters are constant. Next to that it can be observed that the pseudo-arclength continuation provides a constant spacing between the family members. The phase constraint is satisfied for the first half of the family but drifts during the final half of the continuation procedure.

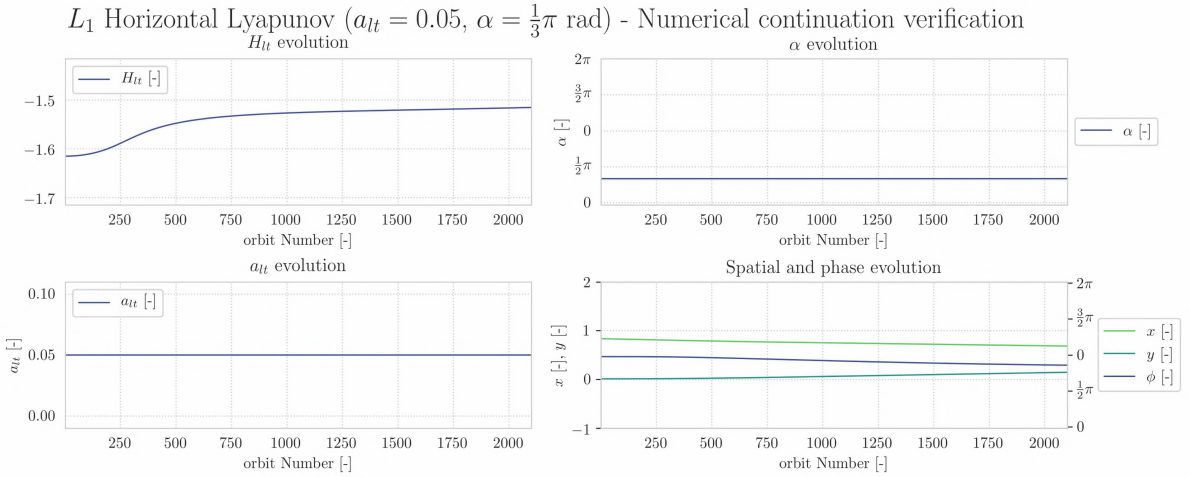

Figure F.28: Numerical continuation verification of the L_1 ($a_{lt} = 0.05$, $\alpha = \frac{1}{3}\pi$ rad) family. The top subfigures and bottom left subfigure demonstrate that the l.p.o family unfolds along the Hamiltonian branch. The bottom right subfigure shows the spatial evolution and phase drift of the initial condition along the family

The symmetry shooting analysis that investigates the root cause between different termination points of the L_1 ($a_{lt} = 0.05$, $\alpha = \frac{1}{3}\pi$ rad and $\alpha = \frac{5}{3}\pi$ rad) families is presented in the next paragraph.

L_1 ($a_{lt} = 0.05$, $\alpha = \frac{5}{3}\pi$ rad) H_{lt}-varying family

The periodicity of the members that form the $L_1(a_{lt} = 0.05,\ \alpha = \frac{5}{3}\pi$ rad) family are established in Figure F.29. This Figure shows that the collocation procedure produces a converged solution with an equidistributed truncation error. The initial state of the resulting solution is explicitly propagated for the estimated orbital period which confirms the periodicity of the family members and a correct implementation of the collocation procedure. The full-period state discrepancy of the first orbits exceeds the thresholds of Table A.8. but termination is intentionally suppressed since the performance of the collocation procedure improves afterwards until the end of the family where the members just meet the periodicity criteria.

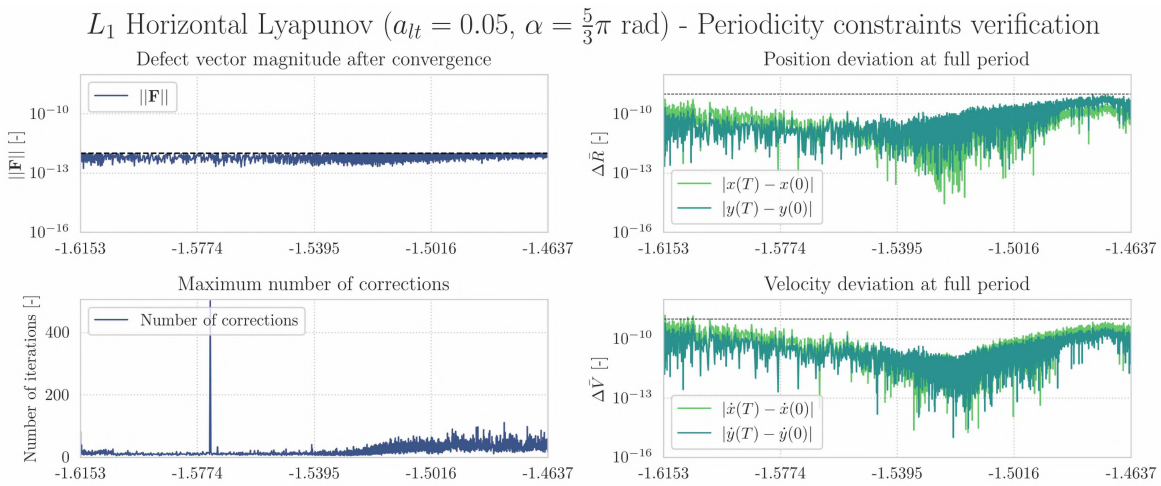

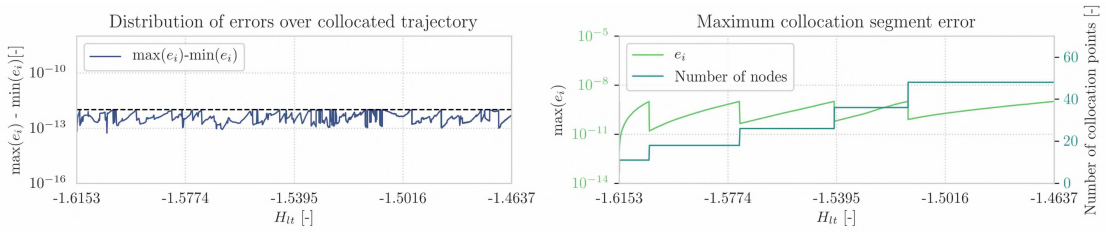

Figure F.29: Periodicity verification of the L_1 ($a_{lt} = 0.05$, $\alpha = \frac{5}{3}\pi$ rad) family. The three left subfigures and the bottom right subfigure demonstrate the characteristics of the collocation method whereas the upper and middle right subfigure show the full-period state discrepancy of the solution. These discrepancies are obtained via explicit propagation of the initial state forwarded by the collocation procedure.

Characteristics of the monodromy eigensystem of each member of the L_1 ($a_{lt} = 0.05$, $\alpha = \frac{5}{3}\pi$ rad) family are shown in Figure F.30. It can be concluded that the monodromy eigensystem of each family member adheres to the structure of a symplectic map.

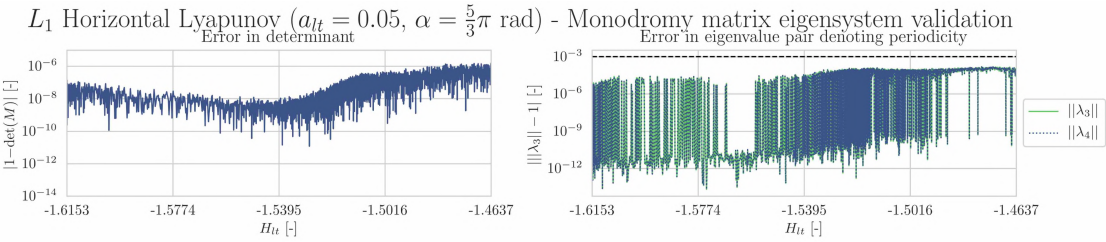

Figure F.30: Monodromy matrix eigensystem validation of the L_1 ($a_{lt} = 0.05$, $\alpha = \frac{5}{3}\pi$ rad) family. The left subfigure shows the deviation of the monodromy matrix determinant whereas the right subfigure demonstrates the deviation of the eigenvalue representing the in-plane center subspace.

Figure F.31 proves that the L_1 ($a_{lt} = 0.05$, $\alpha = \frac{5}{3}\pi$ rad) family is a H_{lt}-varying family since its thrust parameters are constant. The phase constraint is satisfied for the beginning of the family but drifts significantly throughout the family.

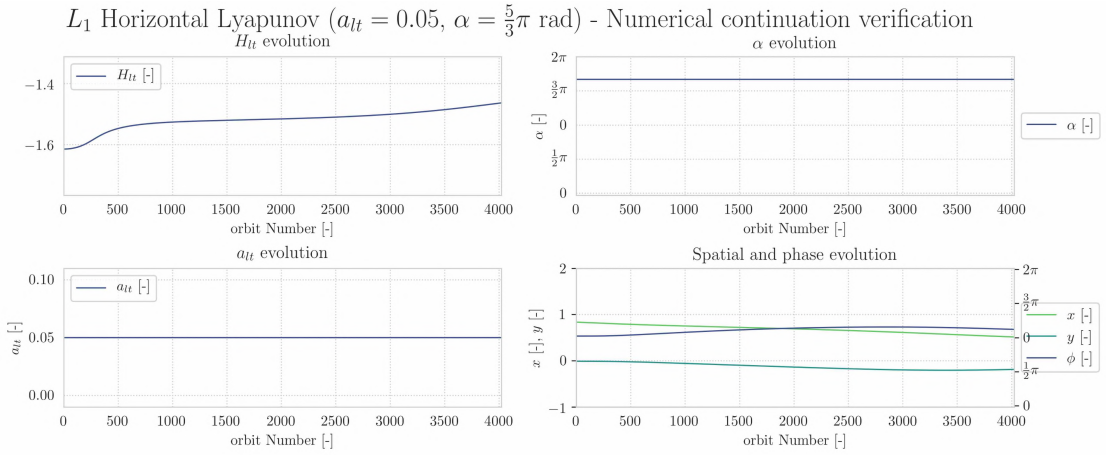

Figure F.31: Numerical continuation verification of the L_1 ($a_{lt} = 0.05$, $\alpha = \frac{5}{3}\pi$ rad) family. The top subfigures and bottom left subfigure demonstrate that the l.p.o family unfolds along the Hamiltonian branch. The bottom right subfigure shows the spatial evolution and phase drift of the initial condition along the family

It is expected that the numerical continuation procedure of the L_1 ($a_{lt} = 0.05$, $\alpha = \frac{1}{3}\pi$ rad) and L_1 ($a_{lt} = 0.05$, $\alpha = \frac{5}{3}\pi$ rad) family would terminate after the same number of members because of the symmetry in the CR3BP-LT. Since this is not the case, a symmetry analysis between the shooting conditions of both families is shown below in Figure F.32.

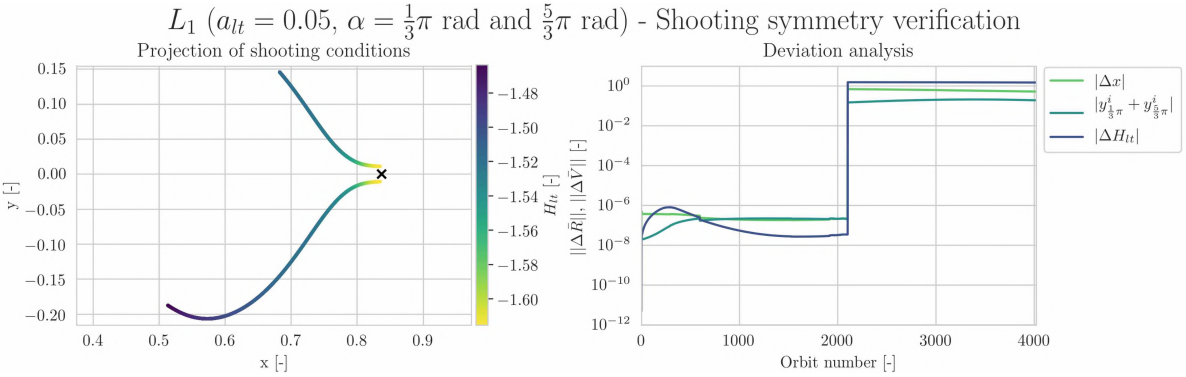

Figure F.32: Shooting symmetry analysis of the L_1 ($a_{lt} = 0.05$, $\alpha = \frac{1}{3}\pi$ and $\frac{5}{3}\pi$ rad) families. The left subfigure shows the evolution of the spatial conditions of both families. The upper branch shows the $\alpha = \frac{2}{3}\pi$ family whereas the lower branch denotes the $\alpha = \frac{4}{3}\pi$ family. The right subfigure shows the symmetry between the initial conditions of the family members.

Figure F.32 reveals that the degree of symmetry between the initial conditions of both families remains constant until the preliminary termination of the L_1 ($a_{lt} = 0.05$, $\alpha = \frac{1}{3}\pi$ rad) family. Therefore, it is unlikely that the phase drift is the cause for the different termination points of the two families. This discrepancy is explained by the fact that collocation procedure responsible for generation of the final member of the $\alpha = \frac{1}{3}\pi$ family uses an insufficient number of nodes.

L_1 ($a_{lt} = 0.10$, $\alpha = \frac{2}{3}\pi$ rad) H_{lt}-varying family

The periodicity of the members that form the $L_1(a_{lt} = 0.10,\ \alpha = \frac{2}{3}\pi$ rad) family are established in Figure F.33. This Figure shows that the collocation procedure produces a converged solution with an equidistributed truncation error. The initial state of the resulting solution is explicitly propagated for the estimated orbital period which confirms the periodicity of the family members and a correct implementation of the collocation procedure. All family members adhere to the periodicity threshold listed in Table A.8. The family is ultimately terminated due to an instability in the collocation procedure. The equidistribution threshold of the truncation error is not satisfied for all members of the family but this does not lead to violation of the periodicity thresholds.

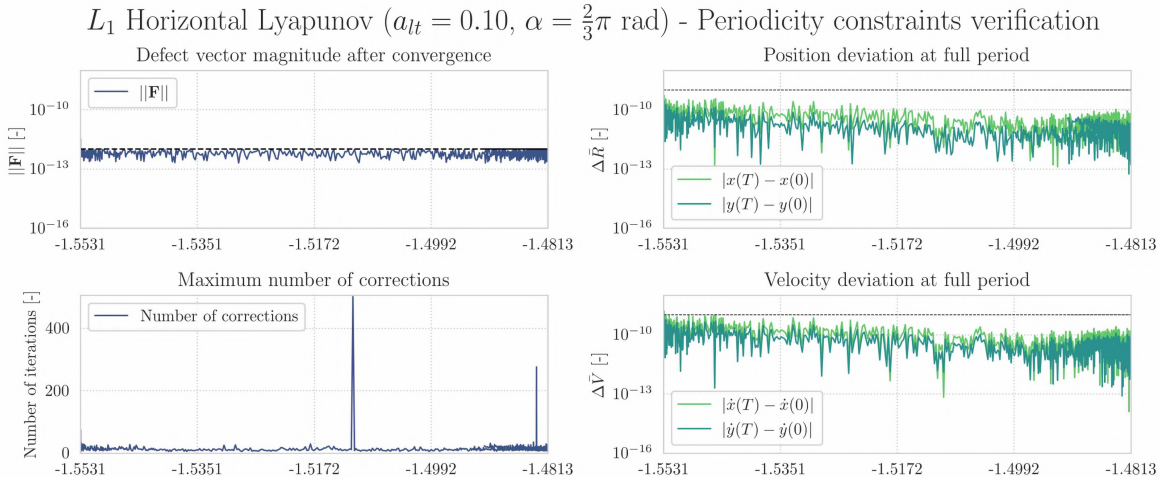

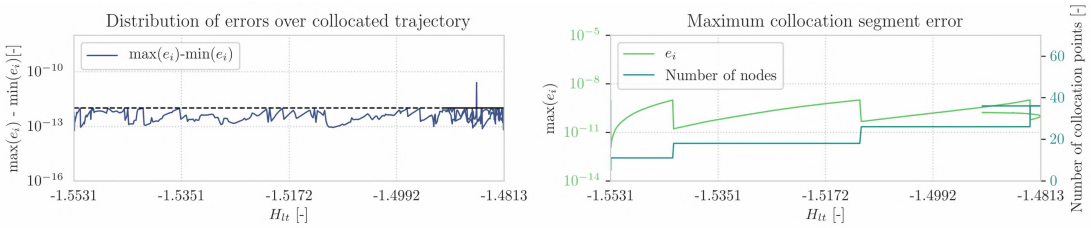

Figure F.33: Periodicity verification of the L_1 ($a_{lt} = 0.10$, $\alpha = \frac{2}{3}\pi$ rad) family. The three left subfigures and the bottom right subfigure demonstrate the characteristics of the collocation method whereas the upper and middle right subfigure show the full-period state discrepancy of the solution. These discrepancies are obtained via explicit propagation of the initial state forwarded by the collocation procedure.

Characteristics of the monodromy eigensystem of each member of the L_1 ($a_{lt} = 0.10$, $\alpha = \frac{2}{3}\pi$ rad) family are shown in Figure F.34. It can be concluded that the monodromy eigensystem of each family member adheres to the structure of a symplectic map.

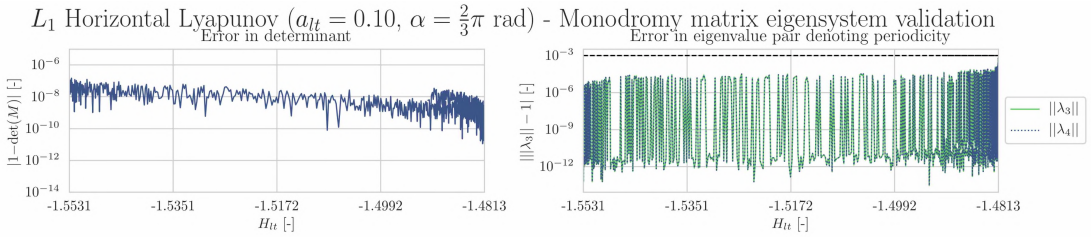

Figure F.34: Monodromy matrix eigensystem validation of the L_1 ($a_{lt} = 0.10$, $\alpha = \frac{2}{3}\pi$ rad) family. The left subfigure shows the deviation of the monodromy matrix determinant whereas the right subfigure demonstrates the deviation of the eigenvalue representing the in-plane center subspace.

Figure F.35 proves that the L_1 ($a_{lt} = 0.10$, $\alpha = \frac{2}{3}\pi$ rad) family is a H_{lt}-varying family since its thrust parameters are constant. The phase constraint is satisfied for the beginning of the family but drifts significantly throughout the family.

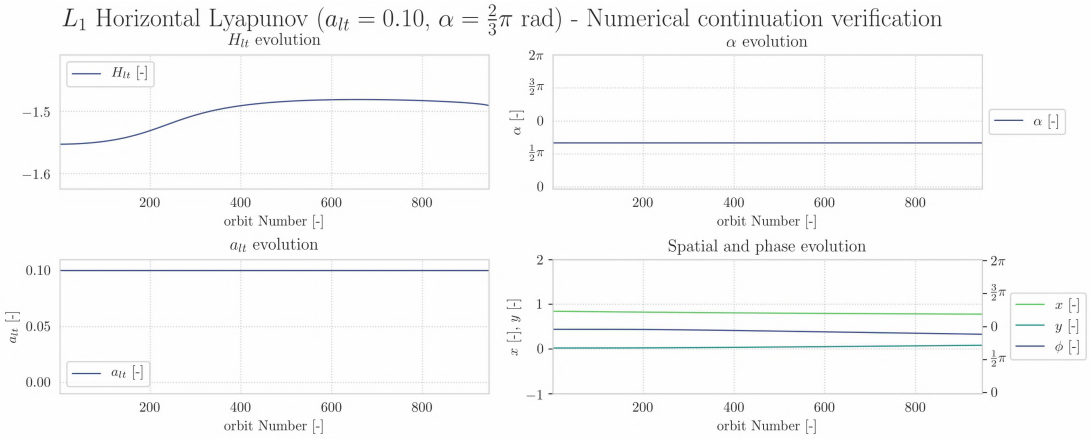

Figure F.35: Numerical continuation verification of the L_1 ($a_{lt} = 0.10$, $\alpha = \frac{2}{3}\pi$ rad) family. The top subfigures and bottom left subfigure demonstrate that the l.p.o family unfolds along the Hamiltonian branch. The bottom right subfigure shows the spatial evolution and phase drift of the initial condition along the family.

The symmetry shooting analysis that investigates the root cause between different termination points of the L_1 ($a_{lt} = 0.10$, $\alpha = \frac{2}{3}\pi$ rad and $\alpha = \frac{4}{3}\pi$ rad) families is presented in the next paragraph.

L_1 ($a_{lt} = 0.10$, $\alpha = \frac{4}{3}\pi$ rad) H_{lt}-varying family

The periodicity of the members that form L_1($a_{lt} = 0.10$, $\alpha = \frac{4}{3}\pi$ rad) family are established in Figure F.36. This Figure shows that the collocation procedure produces a converged solution with an equidistributed truncation error. The initial state of the resulting solution is explicitly propagated for the estimated orbital period which confirms the periodicity of the family members and a correct implementation of the collocation procedure. All family members adhere to the periodicity threshold and equidistribution criterium listed in Table A.8.

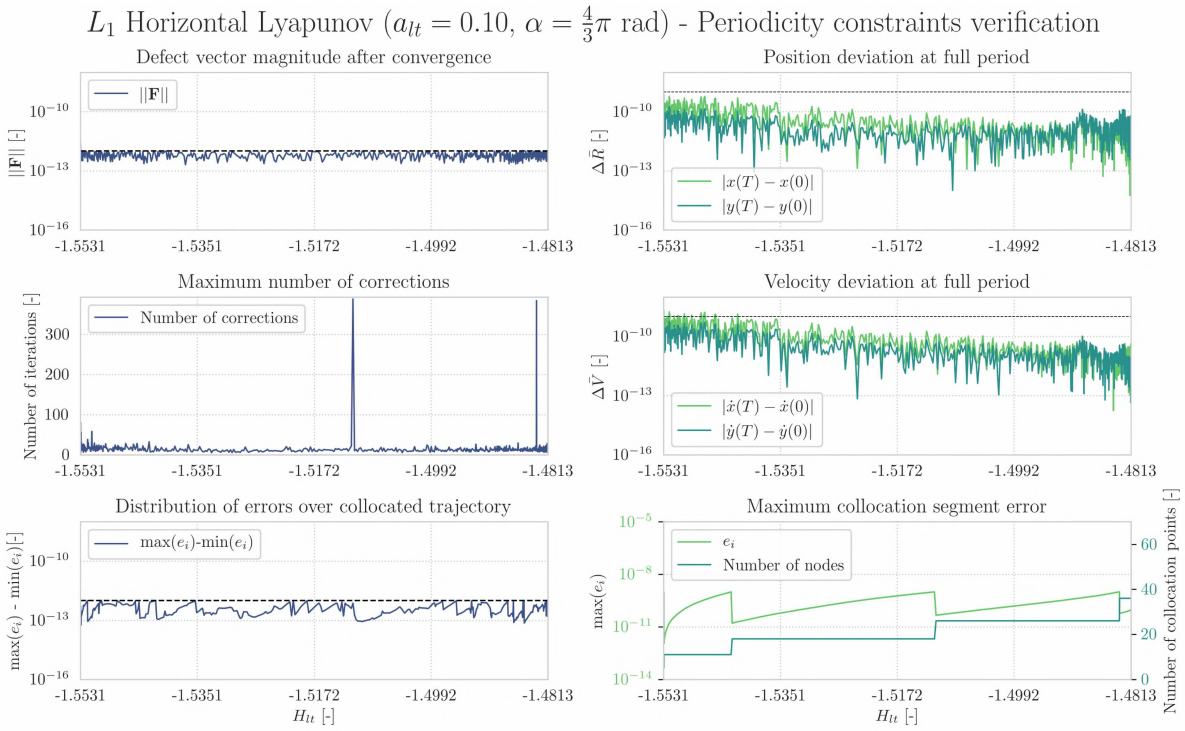

Figure F.36: Periodicity verification of the L_1 ($a_{lt} = 0.10$, $\alpha = \frac{2}{3}\pi$ rad) family. The three left subfigures and the bottom right subfigure demonstrate the characteristics of the collocation method whereas the upper and middle right subfigure show the full-period state discrepancy of the solution. These discrepancies are obtained via explicit propagation of the initial state forwarded by the collocation procedure.

Characteristics of the monodromy eigensystem of each member of the L_1 ($a_{lt} = 0.10$, $\alpha = \frac{4}{3}\pi$ rad) family are shown in Figure F.37. It can be concluded that the monodromy eigensystem of each family member adheres to the structure of a symplectic map.

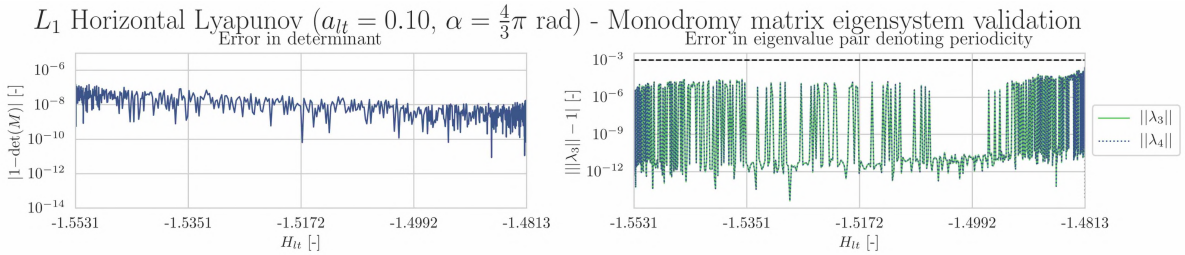

Figure F.37: Monodromy matrix eigensystem validation of the L_1 ($a_{lt} = 0.10$, $\alpha = \frac{4}{3}\pi$ rad) family. The left subfigure shows the deviation of the monodromy matrix determinant whereas the right subfigure demonstrates the deviation of the eigenvalue representing the in-plane center subspace.

Figure F.38 proves that the L_1 ($a_{lt} = 0.10$, $\alpha = \frac{4}{3}\pi$ rad) family is a H_{lt}-varying family since its thrust parameters are constant. The phase constraint is satisfied for the first half of the family but shifts slightly during the second half of the family.

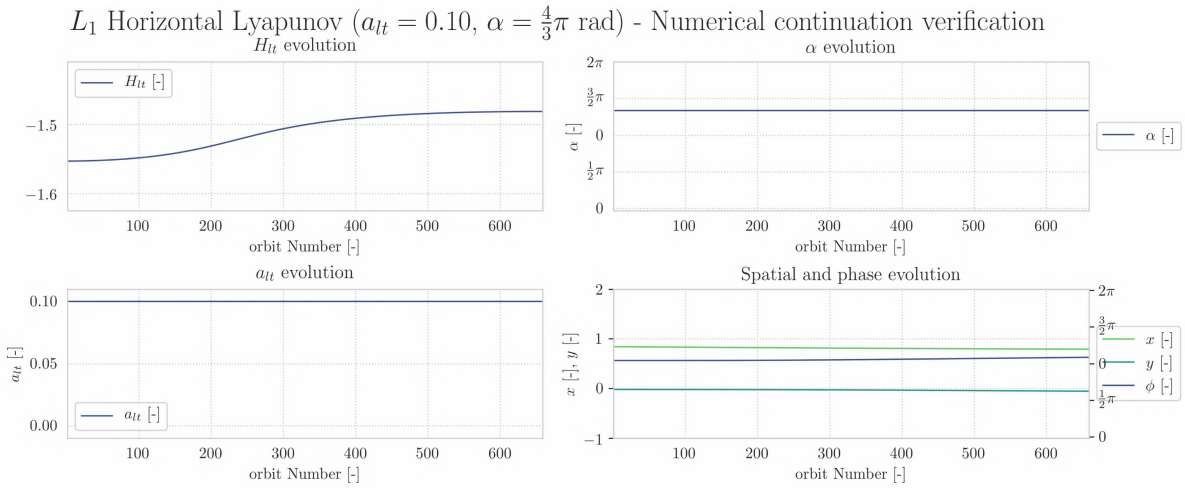

Figure F.38: Numerical continuation verification of the L_1 ($a_{lt} = 0.10$, $\alpha = \frac{4}{3}\pi$ rad) family. The top subfigures and bottom left subfigure demonstrate that the l.p.o family unfolds along the Hamiltonian branch. The bottom right subfigure shows the spatial evolution and phase drift of the initial condition along the family.

It is expected that the numerical continuation procedure of the L_1 ($a_{lt} = 0.10$, $\alpha = \frac{2}{3}\pi$ rad)and L_1 ($a_{lt} = 0.10$, $\alpha = \frac{4}{3}\pi$ rad) family would terminate after the same number of members because of the symmetry in the CR3BP-LT. Since this is not the case, a symmetry analysis between the shooting conditions of both families is shown below in Figure F.39.

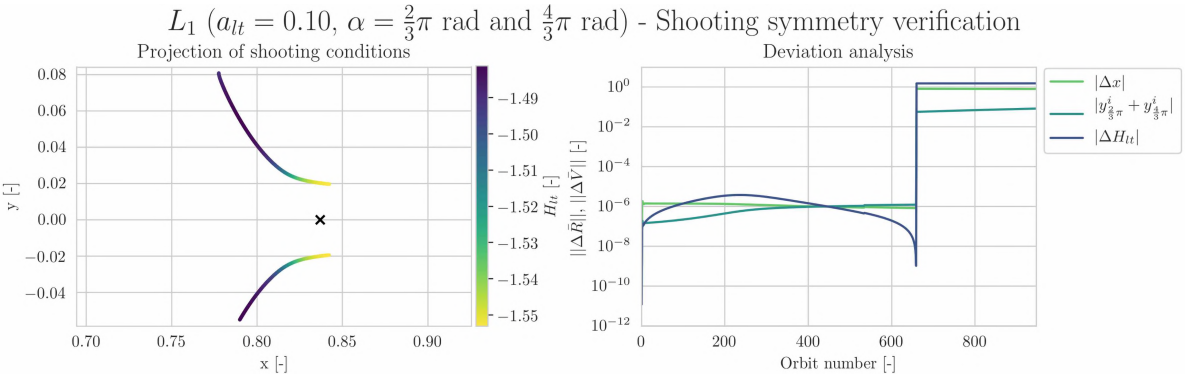

Figure F.39: Shooting symmetry analysis of the L_1 ($a_{lt} = 0.10$, $\alpha = \frac{2}{3}\pi$ and $\frac{4}{3}\pi$ rad) families. The left subfigure shows the evolution of the spatial conditions of both families. The upper branch shows the $\alpha = \frac{2}{3}\pi$ family whereas the lower branch denotes the $\alpha = \frac{4}{3}\pi$ family. The right subfigure shows the symmetry between the initial conditions of the family members.

Figure F.39 reveals that the degree of symmetry between the initial conditions of both families remains constant until the preliminary termination of the L_1 ($a_{lt} = 0.10$, $\alpha = \frac{4}{3}\pi$) family. Therefore, it is unlikely that the phase drift is the cause for the different termination points of the two families. This discrepancy can be attributed to the instability of the collocation procedure due to the variable nodes times.

L_2 ($a_{lt} = 0.10$, $\alpha = \frac{1}{3}\pi$ rad) H_{lt}-varying family

the periodicity of the members that form the L_2($a_{lt} = 0.10$, $\alpha = \frac{1}{3}\pi$ rad) family are established in Figure F.40. This Figure shows that the collocation procedure produces a converged solution with an equidistributed truncation error. The initial state of the resulting solution is explicitly propagated for the estimated orbital period which confirms the periodicity of the family members and a correct implementation of the collocation procedure. All family members adhere to the periodicity threshold despite the fact that some members do not adhere to the equidistribution criterium listed in Table A.8.

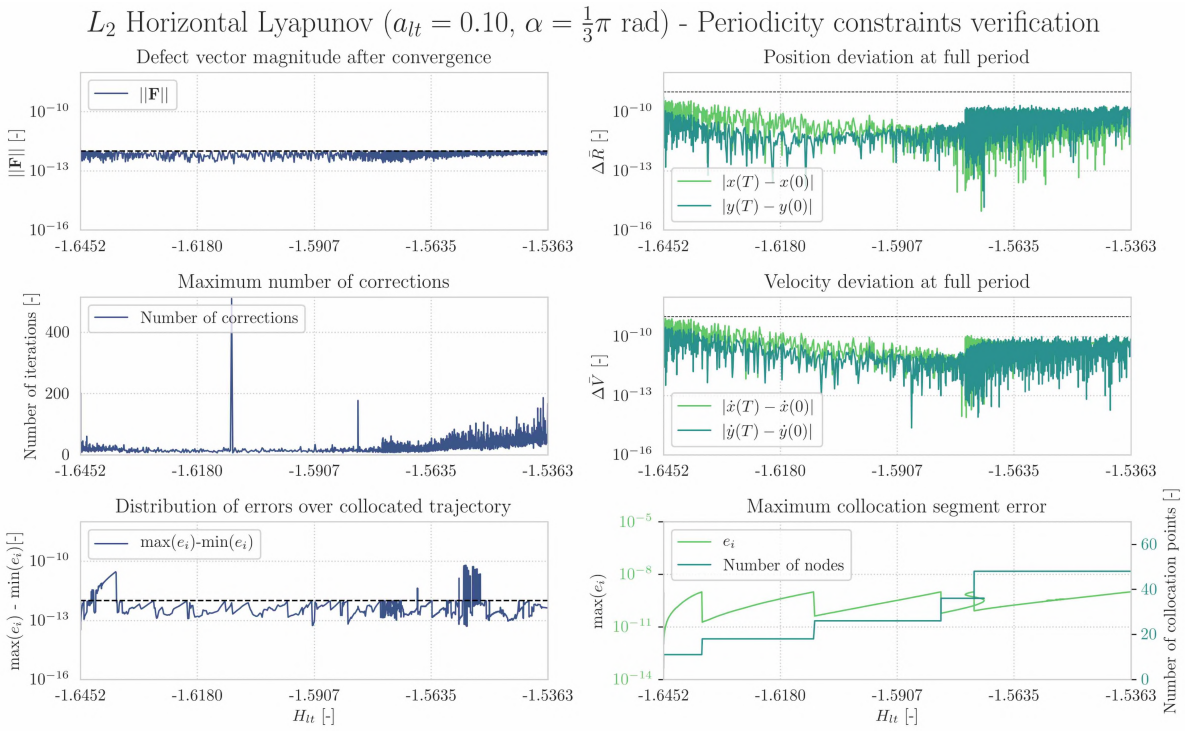

Figure F.40: Periodicity verification of the L_2 ($a_{lt} = 0.10$, $\alpha = \frac{1}{3}\pi$ rad) family. The three left subfigures and the bottom right subfigure demonstrate the characteristics of the collocation method whereas the upper and middle right subfigure show the full-period state discrepancy of the solution. These discrepancies are obtained via explicit propagation of the initial state forwarded by the collocation procedure.

Characteristics of the monodromy eigensystem of each member of the L_2 ($a_{lt} = 0.10$, $\alpha = \frac{1}{3}\pi$ rad) family are shown in Figure F.41. It can be concluded that the monodromy eigensystem of each family member adheres to the structure of a symplectic map although the eigenvalue pair related to the in-plane center subspace is nearly violated at the end of the family.

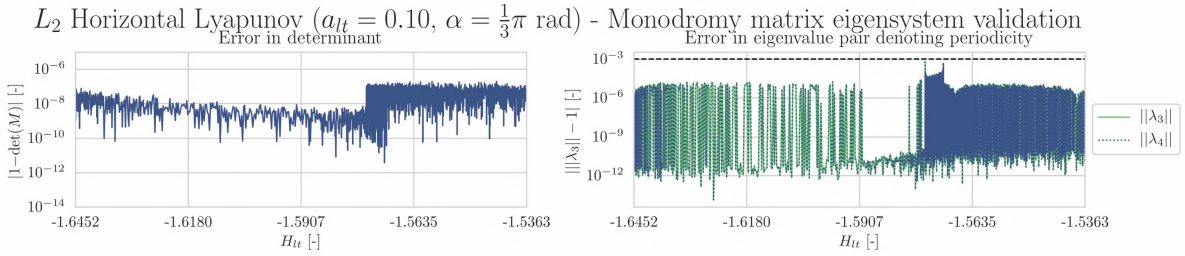

Figure F.41: Monodromy matrix eigensystem validation of the L_2 ($a_{lt} = 0.10$, $\alpha = \frac{1}{3}\pi$ rad) family. The left subfigure shows the deviation of the monodromy matrix determinant whereas the right subfigure demonstrates the deviation of the eigenvalue representing the in-plane center subspace.

Figure F.42 proves that the L_2 ($a_{lt} = 0.10$, $\alpha = \frac{1}{3}\pi$ rad) family is a H_{lt}-varying family since its thrust parameters are constant. A phase shift is observed throughout the family which does not affect the periodicity of the family members.

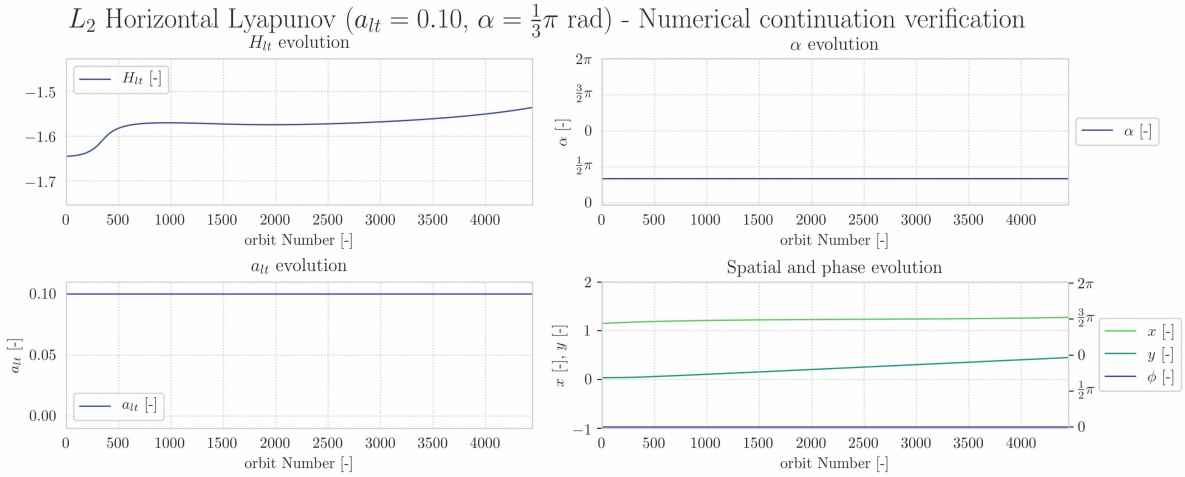

Figure F.42: Numerical continuation verification of the L_2 ($a_{lt} = 0.10$, $\alpha = \frac{2}{3}\pi$ rad) family. The top subfigures and bottom left subfigure demonstrate that the l.p.o family unfolds along the Hamiltonian branch. The bottom right subfigure shows the spatial evolution and phase drift of the initial condition along the family.

The symmetry shooting analysis that investigates the root cause between different termination points of the L_2 ($a_{lt} = 0.10$, $\alpha = \frac{1}{3}\pi$ rad and $\alpha = \frac{5}{3}\pi$ rad) families is presented in the next paragraph.

L_2 ($a_{lt} = 0.10$, $\alpha = \frac{5}{3}\pi$ rad) H_{lt}-varying family

the periodicity of the members that form the $L_2(a_{lt} = 0.10, \alpha = \frac{5}{3}\pi$ rad) family are established in Figure F.43. This Figure shows that the collocation procedure produces a converged solution with an equidistributed truncation error. The initial state of the resulting solution is explicitly propagated for the estimated orbital period which confirms the periodicity of the family members and a correct implementation of the collocation procedure. All family members adhere to the periodicity threshold despite the fact that some members do not adhere to the equidistribution criterium listed in Table A.8.

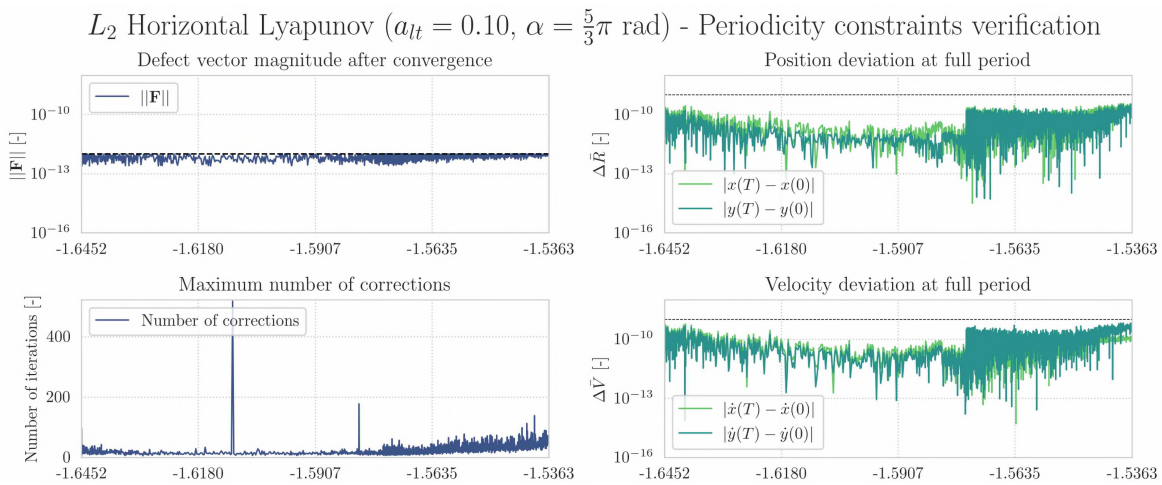

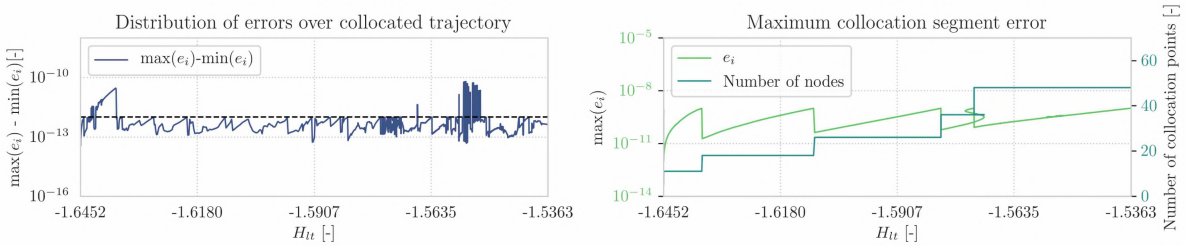

Figure F.43: Periodicity verification of the L_2 ($a_{lt} = 0.10$, $\alpha = \frac{5}{3}\pi$ rad) family. The three left subfigures and the bottom right subfigure demonstrate the characteristics of the collocation method whereas the upper and middle right subfigure show the full-period state discrepancy of the solution. These discrepancies are obtained via explicit propagation of the initial state forwarded by the collocation procedure.

Characteristics of the monodromy eigensystem of each member of the L_2 ($a_{lt} = 0.10$, $\alpha = \frac{5}{3}\pi$ rad) family are shown in Figure F.44. It can be concluded that the monodromy eigensystem of each family member adheres to the structure of a symplectic map apart from the final member who's eigenvalue pair related to the planar center subspace violates the threshold listed in Table A.4. This violation leads to the termination of the continuation procedure.

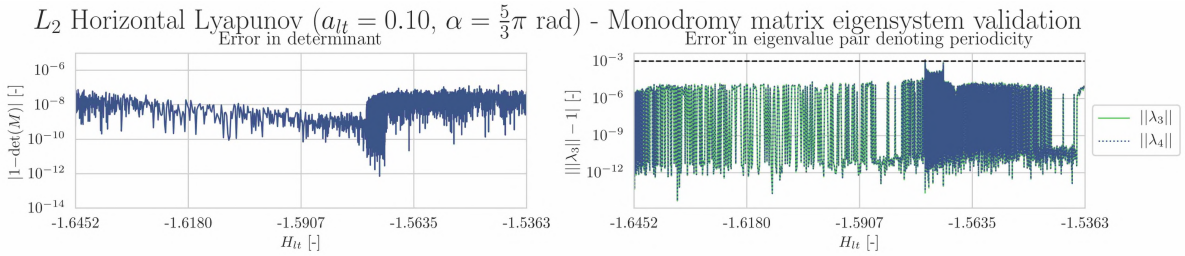

Figure F.44: Monodromy matrix eigensystem validation of the L_2 ($a_{lt} = 0.10$, $\alpha = \frac{5}{3}\pi$ rad) family. The left subfigure shows the deviation of the monodromy matrix determinant whereas the right subfigure demonstrates the deviation of the eigenvalue representing the in-plane center subspace.

Figure F.45 proves that the L_2 ($a_{lt} = 0.10$, $\alpha = \frac{5}{3}\pi$ rad) family is a H_{lt}-varying family since its thrust parameters are constant. No phase shift is observed throughout the family.

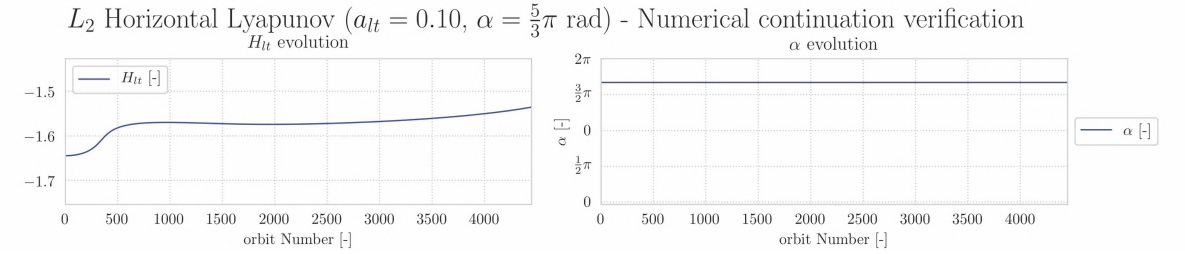

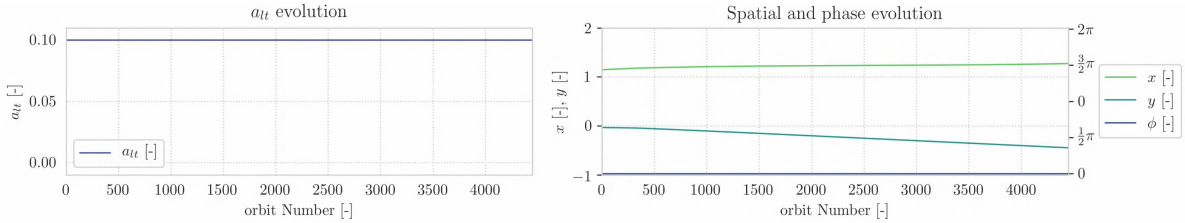

Figure F.45: Numerical continuation verification of the L_2 ($a_{lt} = 0.10$, $\alpha = \frac{5}{3}\pi$ rad) family. The top subfigures and bottom left subfigure demonstrate that the l.p.o family unfolds along the Hamiltonian branch. The bottom right subfigure shows the spatial evolution and phase drift of the initial condition along the family.

It is expected that the numerical continuation procedure of the L_2 ($a_{lt} = 010$, $\alpha = \frac{1}{3}\pi$ rad) and L_2 ($a_{lt} = 0.10$, $\alpha = \frac{5}{3}\pi$) family would terminate after the same number of members because of the symmetry in the CR3BP-LT. Since this is not the case, a symmetry analysis between the shooting conditions of both families is shown below in Figure F.46.

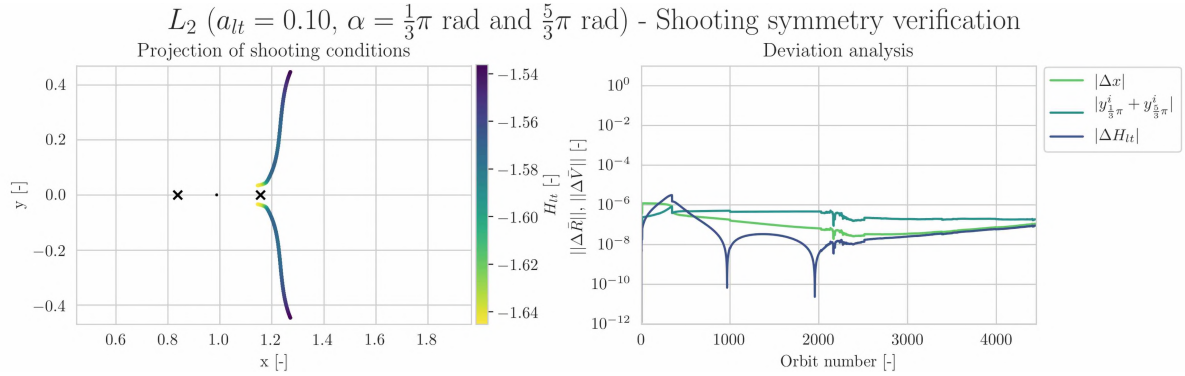

Figure F.46: Shooting symmetry analysis of the L_2 ($a_{lt} = 0.10$, $\alpha = \frac{1}{3}\pi$ and $\frac{5}{3}\pi$ rad) families. The left subfigure shows the evolution of the spatial conditions of both families. The upper branch shows the $\alpha = \frac{1}{3}\pi$ family whereas the lower branch denotes the $\alpha = \frac{5}{3}\pi$ family. The right subfigure shows the symmetry between the initial conditions of the family members.

Figure F.39 reveals that the degree of symmetry between the initial conditions of both families slightly decreases over the numerical continuation procedures. The imperfections in degree of symmetry can be attributed to the truncation errors associated with the implicit integration technique described in Appendix B.2.1.

F.5.2. Acceleration-varying families

A total of thirty-six a_{lt}-varying families have been presented in Chapter 1 and Appendix D. The veracity of these families is discussed in this Section. The termination cause of each numerical continuation procedure associated with construction of an a_{lt}-varying family is presented in Table F.6.

	E_1						E_2					
α [rad]	0	$\frac{1}{3}\pi$	$\frac{2}{3}\pi$	π	$\frac{4}{3}\pi$	$\frac{5}{3}\pi$	0	$\frac{1}{3}\pi$	$\frac{2}{3}\pi$	π	$\frac{4}{3}\pi$	$\frac{5}{3}\pi$
$H_{lt} = -1.55$	G	I	G	H	G	I	G	I	H	H	H	I
$H_{lt} = -1.525$	G	G	G	H	G	G	D^{85}	G	G	H	G	G
$H_{lt} = -1.50$	G	G	G	G	G	G	D^{40}	I	G	G	G	I

Table F.6: An overview of the termination causes of the numerical continuation procedures associated with a_{lt}-varying families. The termination cause of some a_{lt}-varying families is underlined, meaning that proof of their veracity is provided later in this Section.

Table F.6 reveals that the continuation procedures associated with generation of the a_{lt}-varying families are terminated due to four different reasons. Most numerical continuation procedures are terminated because the periodic solutions over the complete range of acceleration magnitudes ($0 \leq a_{lt} \leq 0.1$) have been computed. Six continuation procedures were terminated before orbits for the complete range of acceleration

magnitudes were computed since these solutions do not exist. Two continuation procedures have been intentionally terminated before computation of the complete family since the computational cost exceeded the time constraints of this thesis project. The remaining six continuation procedures were terminated due to an instability in the collocation algorithm associated with the numerical continuation procedure. The veracity of these six families will be discussed in the remainder of this Section.

L_1 ($H_{lt} = -1.55$, $\alpha = \frac{1}{3}\pi$ rad) a_{lt}-varying family

The periodicity of the members that form the $L_1(H_{lt} = -1.55,\ \alpha = \frac{1}{3}\pi$ rad) family are established in Figure F.47. This Figure shows that the collocation procedure produces a converged solution with an equidistributed truncation error. The initial state of the resulting solution is explicitly propagated for the estimated orbital period which confirms the periodicity of the family members and a correct implementation of the collocation procedure. All family members adhere to the periodicity criteria listed in Table A.8.

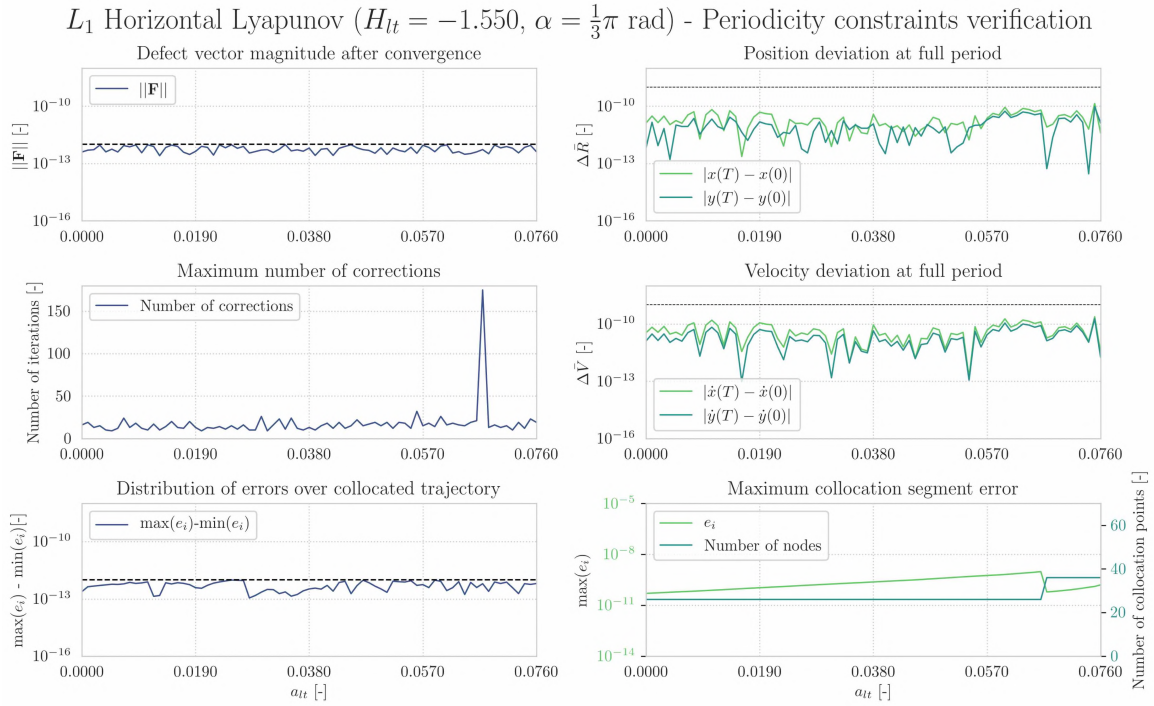

Figure F.47: Periodicity verification of the L_1 ($H_{lt} = -1.55$, $\alpha = \frac{1}{3}\pi$ rad) family. The three left subfigures and the bottom right subfigure demonstrate the characteristics of the collocation method whereas the upper and middle right subfigure show the full-period state discrepancy of the solution. These discrepancies are obtained via explicit propagation of the initial state forwarded by the collocation procedure.

Characteristics of the monodromy eigensystem of each member of the L_1 ($H_{lt} = -1.55$, $\alpha = \frac{1}{3}\pi$ rad) family are shown in Figure F.48. It can be concluded that the monodromy eigensystem of each family member adheres to the structure of a symplectic map.

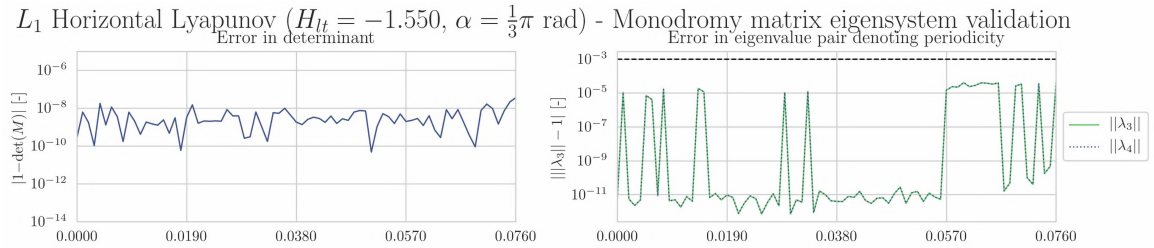

Figure F.48: Monodromy matrix eigensystem validation of the L_1 ($H_{lt} = -1.55$, $\alpha = \frac{1}{3}\pi$ rad) family. The left subfigure shows the deviation of the monodromy matrix determinant whereas the right subfigure demonstrates the deviation of the eigenvalue representing the in-plane center subspace.

Figure F.49 proves that the L_1 ($H_{lt} = -1.55$, $\alpha = \frac{1}{3}\pi$ rad) family is an a_{lt}-varying family since the Hamiltonian and acceleration orientation are constant.

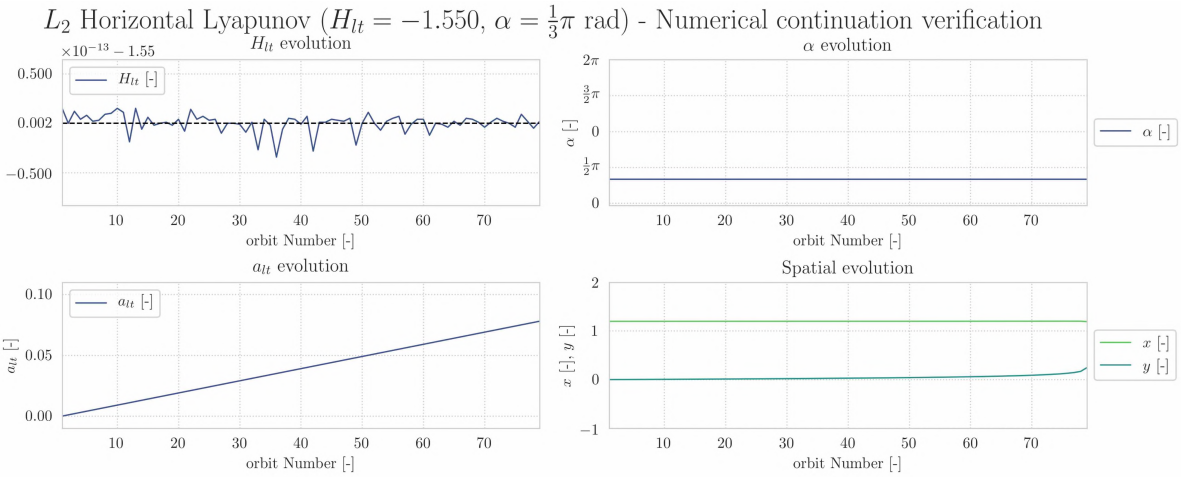

Figure F.49: Numerical continuation verification of the L_1 ($H_{lt} = -1.55$, $\alpha = \frac{1}{3}\pi$ rad) family. The top subfigures and bottom left subfigure demonstrate that the l.p.o family unfolds along the acceleration branch. The bottom right subfigure shows the spatial evolution of the initial condition along the family.

The symmetry shooting analysis that investigates the root cause between different termination points of the L_2 ($H_{lt} = -1.55$, $\alpha = \frac{1}{3}\pi$ rad and $\alpha = \frac{5}{3}\pi$ rad) families is presented in the next paragraph.

L_1 ($H_{lt} = -1.55$, $\alpha = \frac{5}{3}\pi$ rad) a_{lt}-varying family

The periodicity of the members that form the L_1($H_{lt} = -1.55$, $\alpha = \frac{5}{3}\pi$ rad) family are established in Figure F.50. This Figure shows that the collocation procedure produces a converged solution with an equidistributed truncation error. The initial state of the resulting solution is explicitly propagated for the estimated orbital period which confirms the periodicity of the family members and a correct implementation of the collocation procedure. All family members adhere to the periodicity criteria listed in Table A.8.

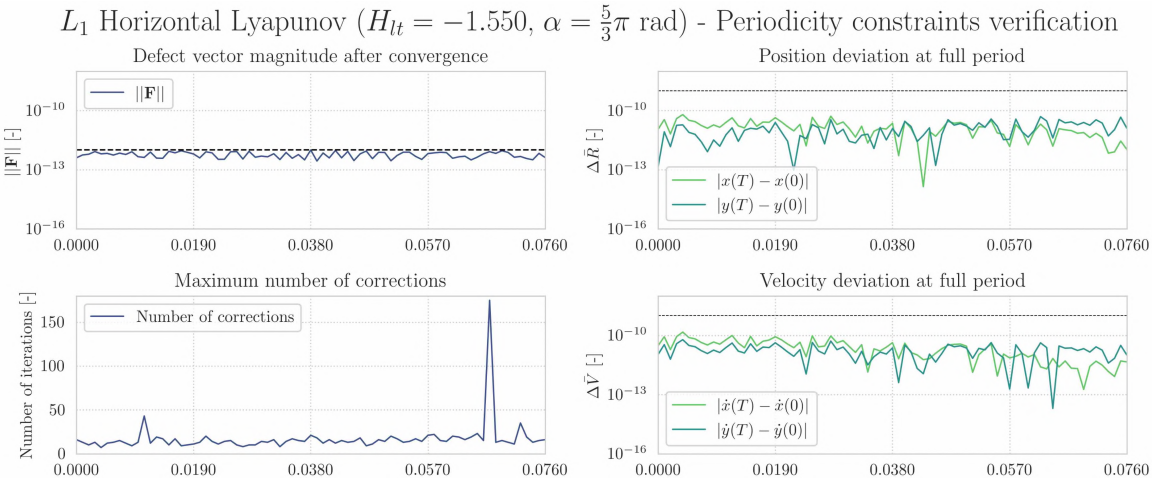

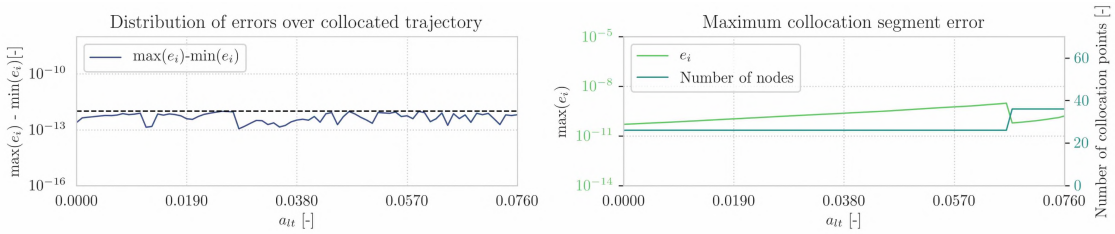

Figure F.50: Periodicity verification of the L_1 ($H_{lt} = -1.55$, $\alpha = \frac{5}{3}\pi$ rad) family. The three left subfigures and the bottom right subfigure demonstrate the characteristics of the collocation method whereas the upper and middle right subfigure show the full-period state discrepancy of the solution. These discrepancies are obtained via explicit propagation of the initial state forwarded by the collocation procedure.

Characteristics of the monodromy eigensystem of each member of the L_1 ($H_{lt} = -1.55$, $\alpha = \frac{5}{3}\pi$ rad) family are shown in Figure F.51. It can be concluded that the monodromy eigensystem of each family member adheres to the structure of a symplectic map.

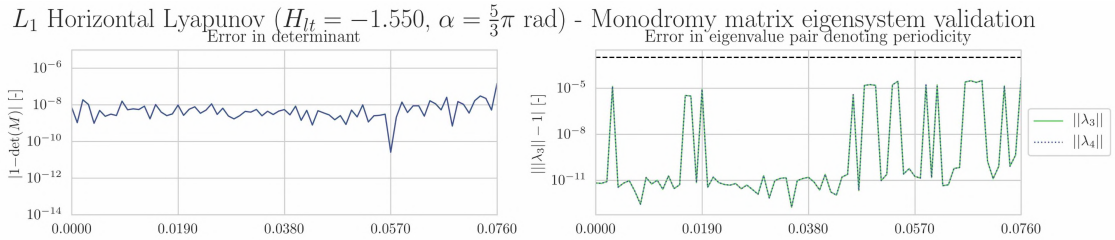

Figure F.51: Monodromy matrix eigensystem validation of the L_1 ($H_{lt} = -1.55$, $\alpha = \frac{5}{3}\pi$ rad) family. The left subfigure shows the deviation of the monodromy matrix determinant whereas the right subfigure demonstrates the deviation of the eigenvalue representing the in-plane center subspace.

Figure F.52 proves that the L_1 ($H_{lt} = -1.55$, $\alpha = \frac{5}{3}\pi$ rad) family is an a_{lt}-varying family since the Hamiltonian and acceleration orientation are constant.

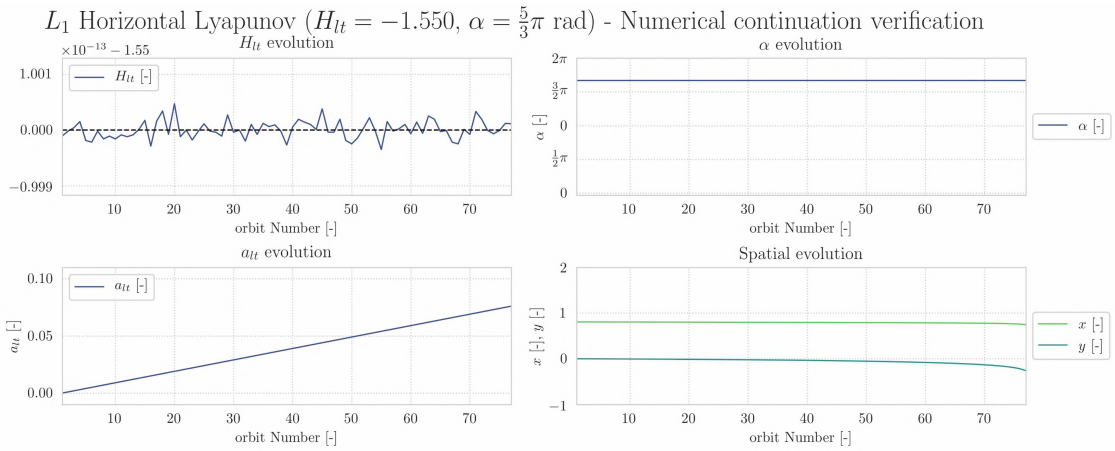

Figure F.52: Numerical continuation verification of the L_1 ($H_{lt} = -1.55$, $\alpha = \frac{5}{3}\pi$ rad) family. The top subfigures and bottom left subfigure demonstrate that the l.p.o family unfolds along the acceleration branch. The bottom right subfigure shows the spatial evolution of the initial condition along the family.

The verification of the L_1 ($H_{lt} = -1.55$, $\alpha = \frac{1}{3}\pi$ rad) and L_1 ($H_{lt} = -1.55$, $\alpha = \frac{5}{3}\pi$ rad) family is wrapped up by evaluating the degree of symmetry between their shooting conditions. This analysis can be found in Figure F.53.

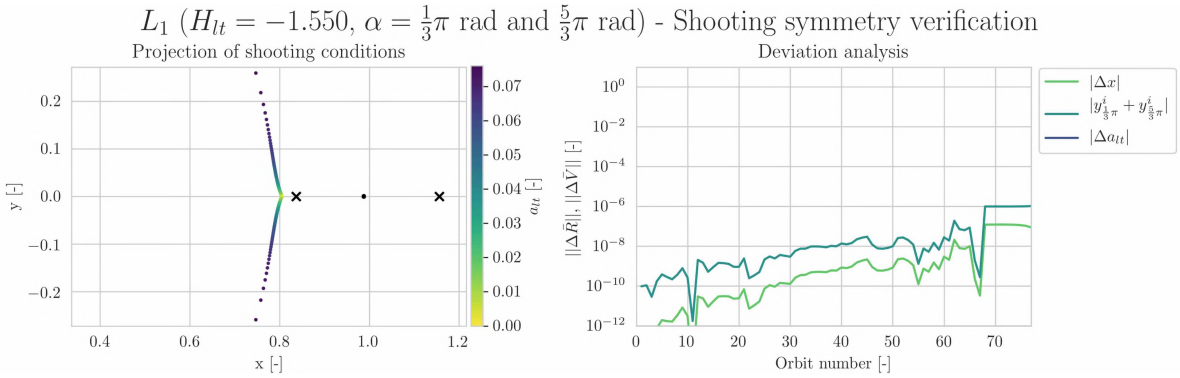

Figure F.53: Shooting symmetry analysis of the L_1 ($H_{lt} = -1.55$, $\alpha = \frac{1}{3}\pi$ and $\frac{5}{3}\pi$ rad) families. The left subfigure shows the evolution of the spatial conditions of both families. The upper branch shows the $\alpha = \frac{1}{3}\pi$ family whereas the lower branch denotes the $\alpha = \frac{5}{3}\pi$ family. The right subfigure shows the symmetry between the initial conditions of the family members.

Figure F.53 reveals that the degree of symmetry between the initial conditions of both families decreases as the acceleration magnitude of the family members increase. A possible explanation for this phenomenon is that truncation errors associated with the polynomial interpolation propagate along the numerical continuation procedure. This results in a decrease in symmetry between the shooting conditions of the families.

L_2 ($H_{lt} = -1.55$, $\alpha = \frac{1}{3}\pi$ rad) a_{lt}-varying family

The periodicity of the members that form the $L_2(H_{lt} = -1.55,\ \alpha = \frac{1}{3}\pi$ rad) family are established in Figure F.54. This Figure shows that the collocation procedure produces a converged solution with an equidistributed truncation error. The initial state of the resulting solution is explicitly propagated for the estimated orbital period which confirms the periodicity of the family members and a correct implementation of the collocation procedure. All family members adhere to the periodicity and equidistribution criteria listed in Table A.8.

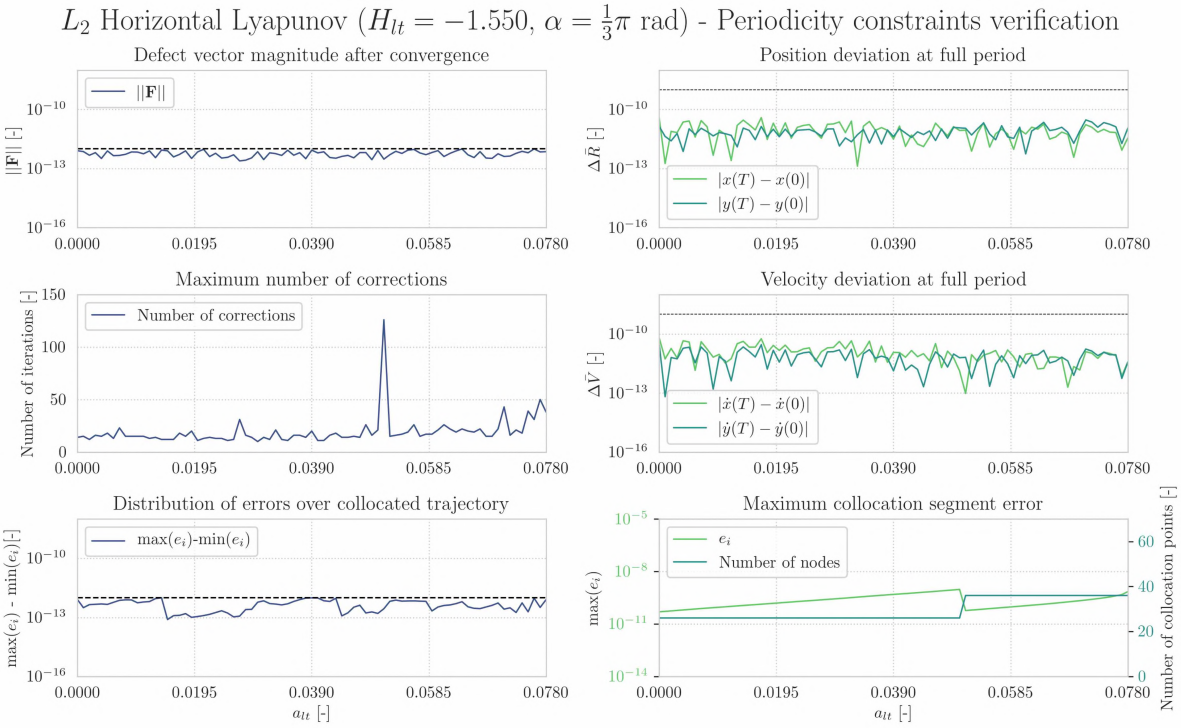

Figure F.54: Periodicity verification of the L_2 ($H_{lt} = -1.55$, $\alpha = \frac{1}{3}\pi$ rad) family. The three left subfigures and the bottom right subfigure demonstrate the characteristics of the collocation method whereas the upper and middle right subfigure show the full-period state discrepancy of the solution. These discrepancies are obtained via explicit propagation of the initial state forwarded by the collocation procedure.

Characteristics of the monodromy eigensystem of each member of the L_2 ($H_{lt} = -1.55$, $\alpha = \frac{1}{3}\pi$ rad) family are shown in Figure F.55. It can be concluded that the monodromy eigensystem of each family member adheres to the structure of a symplectic map.

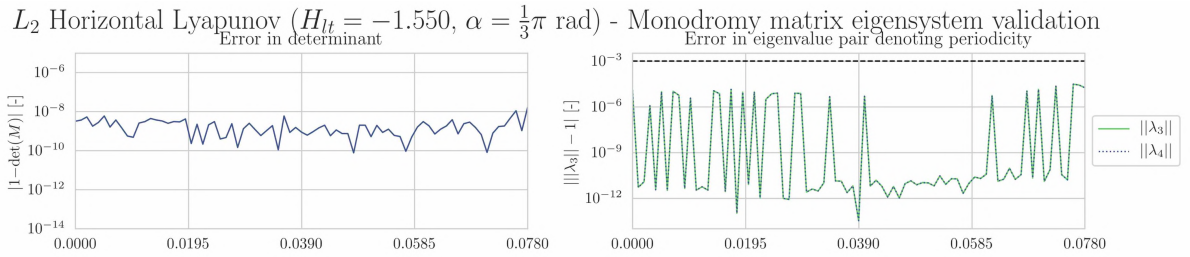

Figure F.55: Monodromy matrix eigensystem validation of the L_2 ($H_{lt} = -1.55$, $\alpha = \frac{1}{3}\pi$ rad) family. The left subfigure shows the deviation of the monodromy matrix determinant whereas the right subfigure demonstrates the deviation of the eigenvalue representing the in-plane center subspace.

Figure F.56 proves that the L_2 ($H_{lt} = -1.55$, $\alpha = \frac{1}{3}\pi$ rad) family is an a_{lt}-varying family since the Hamiltonian and acceleration orientation are constant.

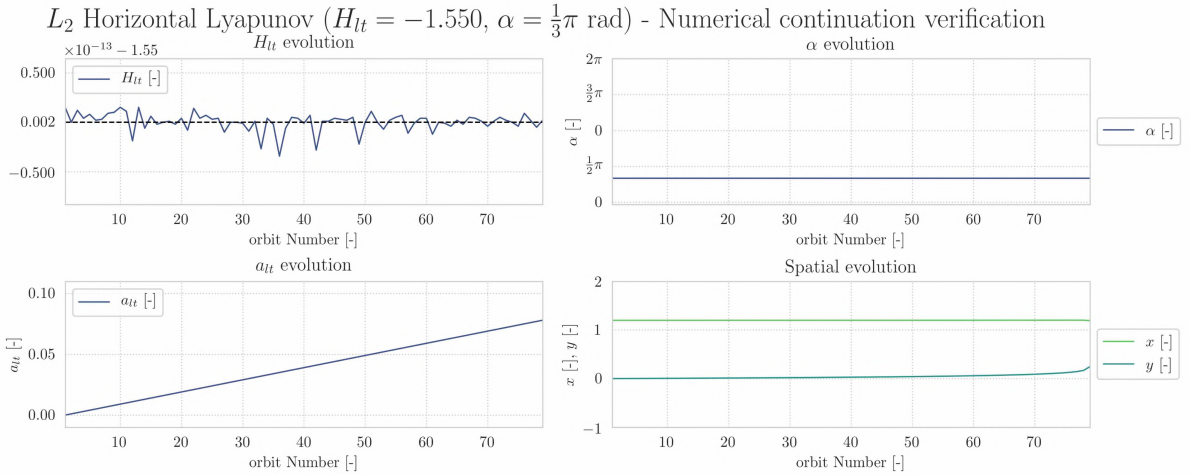

Figure F.56: Numerical continuation verification of the L_2 ($H_{lt} = -1.55$, $\alpha = \frac{1}{3}\pi$ rad) family. The top subfigures and bottom left subfigure demonstrate that the l.p.o family unfolds along the acceleration branch. The bottom right subfigure shows the spatial evolution of the initial condition along the family.

The symmetry shooting analysis that investigates the root cause between different termination points of the L_2 ($H_{lt} = -1.55$, $\alpha = \frac{1}{3}\pi$ rad and $\alpha = \frac{5}{3}\pi$ rad) families is presented in the next paragraph.

L_2 ($H_{lt} = -1.55$, $\alpha = \frac{5}{3}\pi$ rad) a_{lt}-varying family

The periodicity of the members that form the L_2($H_{lt} = -1.55$, $\alpha = \frac{5}{3}\pi$ rad) family are established in Figure F.57. This Figure shows that the collocation procedure produces a converged solution with an equidistributed truncation error. The initial state of the resulting solution is explicitly propagated for the estimated orbital period which confirms the periodicity of the family members and a correct implementation of the collocation procedure. All family members adhere to the periodicity and equidistribution criteria listed in Table A.8.

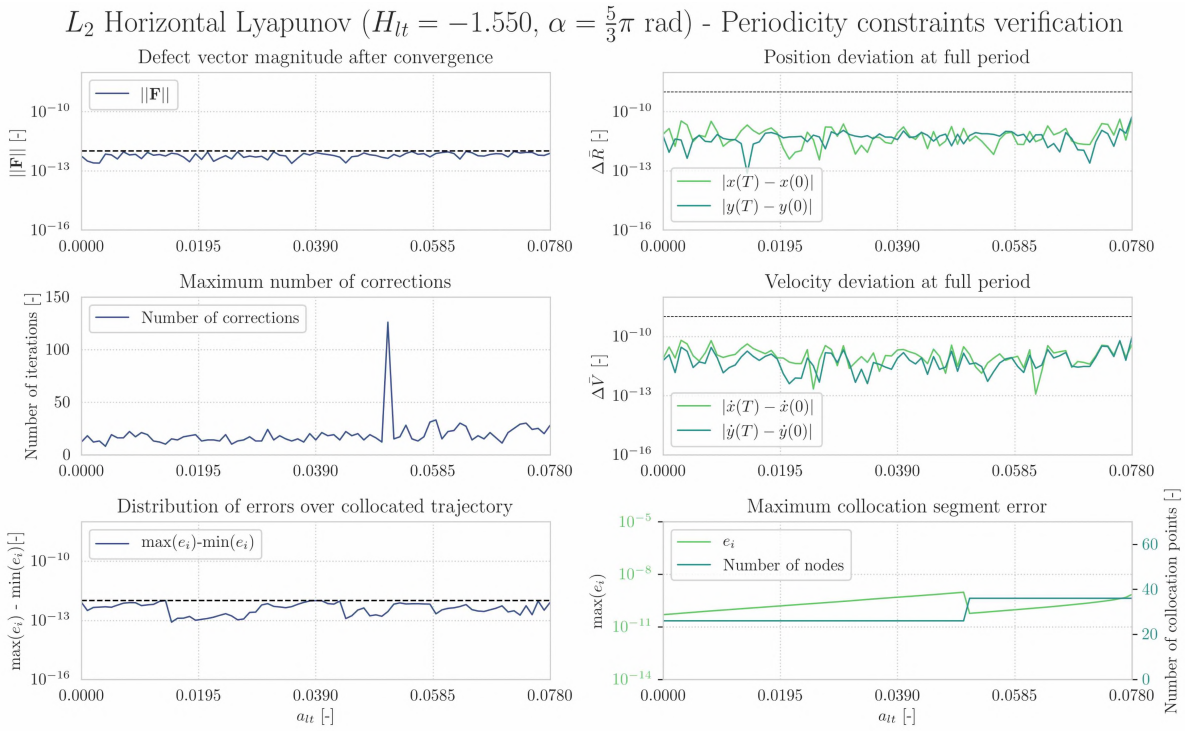

Figure F.57: Periodicity verification of the L_2 ($H_{lt} = -1.55$, $\alpha = \frac{5}{3}\pi$ rad) family. The three left subfigures and the bottom right subfigure demonstrate the characteristics of the collocation method whereas the upper and middle right subfigure show the full-period state discrepancy of the solution. These discrepancies are obtained via explicit propagation of the initial state forwarded by the collocation procedure.

Characteristics of the monodromy eigensystem of each member of the L_2 ($H_{lt} = -1.55$, $\alpha = \frac{5}{3}\pi$ rad) family are shown in Figure F.58. It can be concluded that the monodromy eigensystem of each family member adheres to the structure of a symplectic map.

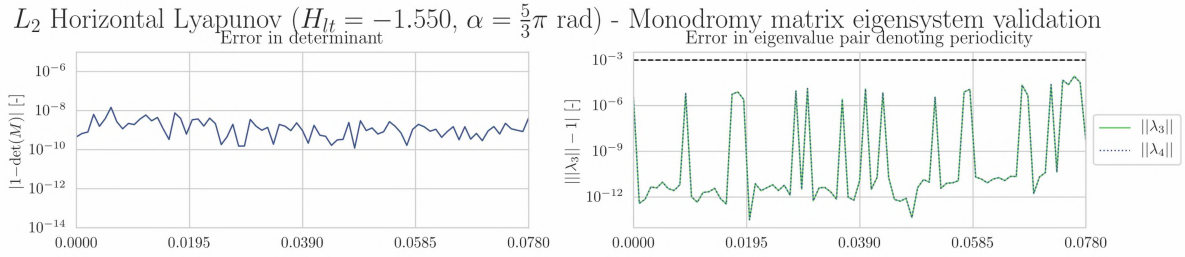

Figure F.58: Monodromy matrix eigensystem validation of the L_2 ($H_{lt} = -1.55$, $\alpha = \frac{5}{3}\pi$ rad) family. The left subfigure shows the deviation of the monodromy matrix determinant whereas the right subfigure demonstrates the deviation of the eigenvalue representing the in-plane center subspace.

Figure F.56 proves that the L_2 ($H_{lt} = -1.55$, $\alpha = \frac{5}{3}\pi$ rad) family is an a_{lt}-varying family since the Hamiltonian and acceleration orientation are constant.

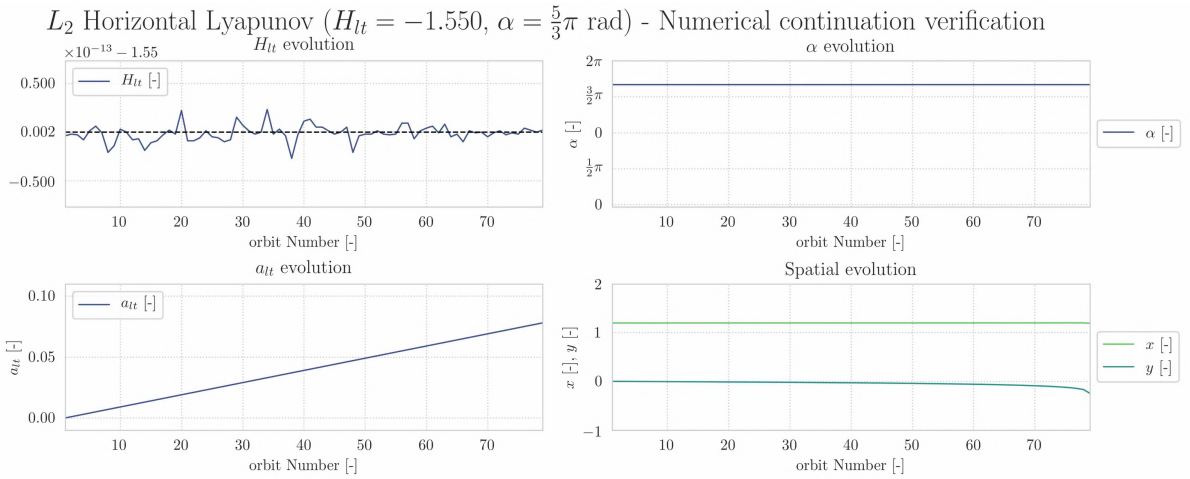

Figure F.59: Numerical continuation verification of the L_2 ($H_{lt} = -1.55$, $\alpha = \frac{5}{3}\pi$ rad) family. The top subfigures and bottom left subfigure demonstrate that the l.p.o family unfolds along the acceleration branch. The bottom right subfigure shows the spatial evolution of the initial condition along the family.

The verification of the L_2 ($H_{lt} = -1.55$, $\alpha = \frac{1}{3}\pi$ rad) and L_1 ($H_{lt} = -1.55$, $\alpha = \frac{5}{3}\pi$ rad) family is wrapped up by evaluating the degree of symmetry between their shooting conditions. This analysis can be found in Figure F.60.

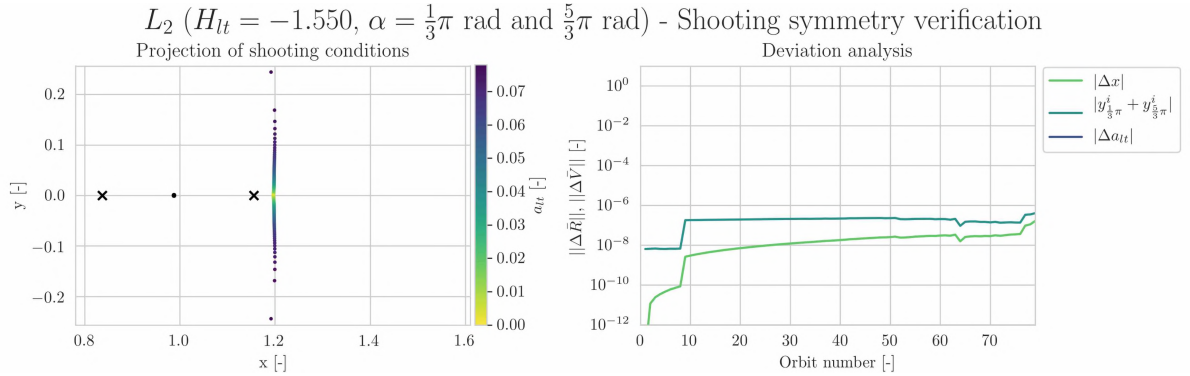

Figure F.60: Shooting symmetry analysis of the L_2 ($H_{lt} = -1.55$, $\alpha = \frac{1}{3}\pi$ and $\frac{5}{3}\pi$ rad) families. The left subfigure shows the evolution of the spatial conditions of both families. The upper branch shows the $\alpha = \frac{1}{3}\pi$ family whereas the lower branch denotes the $\alpha = \frac{5}{3}\pi$ family. The right subfigure shows the symmetry between the initial conditions of the family members.

Figure F.60 reveals that the degree of symmetry between the initial conditions the family members remains fairly constant over the families.A possible explanation for the asymmetries can be attributed to truncation errors that are inherent to the polynomial interpolation method of the collocation procedure.

L_2 ($H_{lt} = -1.50$, $\alpha = \frac{1}{3}\pi$ rad) a_{lt}-varying family

The periodicity of the members that form the L_2($H_{lt} = -1.50$, $\alpha = \frac{1}{3}\pi$ rad) family are established in Figure F.61. This Figure shows that the collocation procedure produces a converged solution with an equidistributed truncation error. The initial state of the resulting solution is explicitly propagated for the estimated orbital period which confirms the periodicity of the family members and a correct implementation of the collocation procedure. All family members adhere to the periodicity and equidistribution criteria listed in Table A.8.

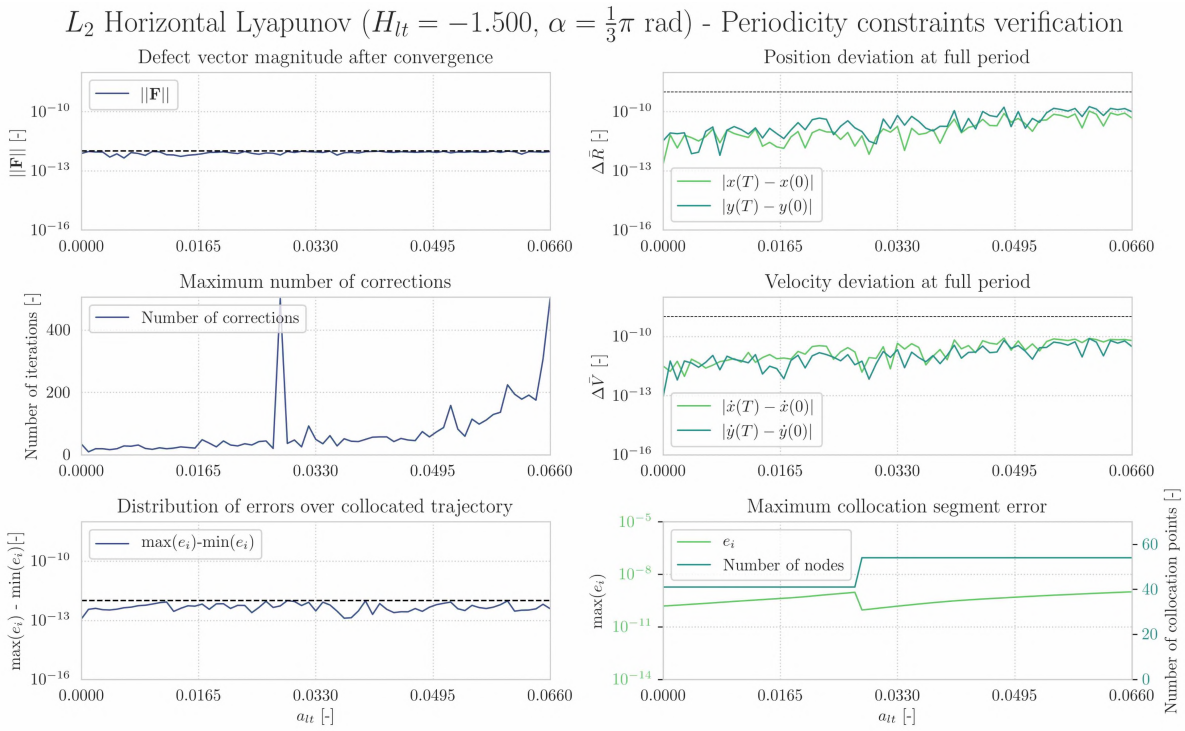

Figure F.61: Periodicity verification of the L_2 ($H_{lt} = -1.50$, $\alpha = \frac{1}{3}\pi$ rad) family. The three left subfigures and the bottom right subfigure demonstrate the characteristics of the collocation method whereas the upper and middle right subfigure show the full-period state discrepancy of the solution. These discrepancies are obtained via explicit propagation of the initial state forwarded by the collocation procedure.

Characteristics of the monodromy eigensystem of each member of the L_2 ($H_{lt} = -1.50$, $\alpha = \frac{1}{3}\pi$ rad) family are shown in Figure F.62. It can be concluded that the monodromy eigensystem of each family member adheres to the structure of a symplectic map.

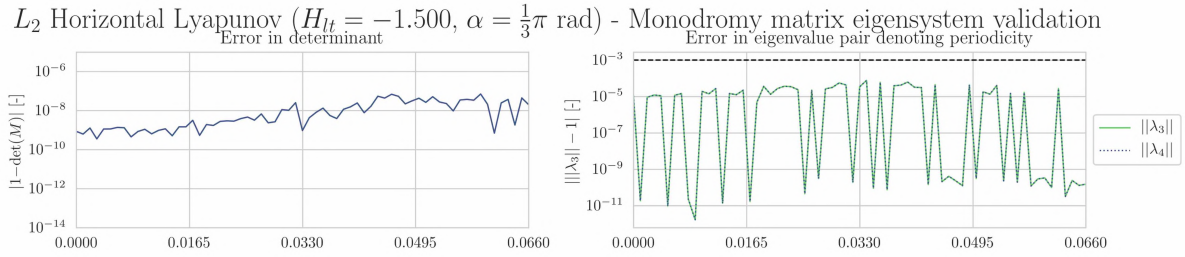

Figure F.62: Monodromy matrix eigensystem validation of the L_2 ($H_{lt} = -1.50$, $\alpha = \frac{1}{3}\pi$ rad) family. The left subfigure shows the deviation of the monodromy matrix determinant whereas the right subfigure demonstrates the deviation of the eigenvalue representing the in-plane center subspace.

Figure F.63 proves that the L_2 ($H_{lt} = -1.50$, $\alpha = \frac{1}{3}\pi$ rad) family is an a_{lt}-varying family since the Hamiltonian and acceleration orientation are constant.

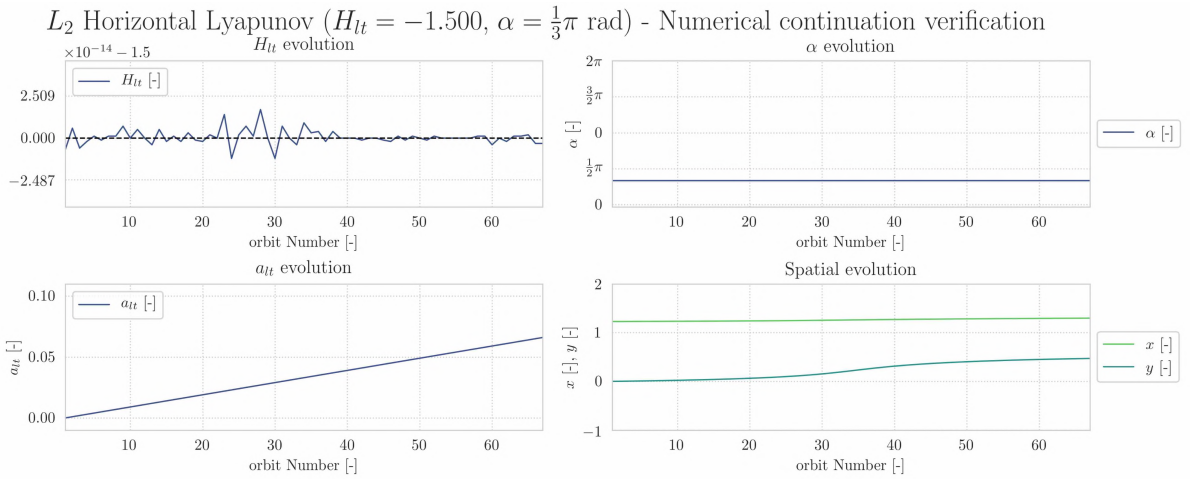

Figure F.63: Numerical continuation verification of the L_2 ($H_{lt} = -1.50$, $\alpha = \frac{1}{3}\pi$ rad) family. The top subfigures and bottom left subfigure demonstrate that the l.p.o family unfolds along the acceleration branch. The bottom right subfigure shows the spatial evolution of the initial condition along the family.

The symmetry shooting analysis that investigates the root cause between different termination points of the L_2 ($H_{lt} = -1.50$, $\alpha = \frac{1}{3}\pi$ rad and $\alpha = \frac{5}{3}\pi$ rad) families is presented in the next paragraph.

L_2 ($H_{lt} = -1.50$, $\alpha = \frac{5}{3}\pi$ rad) a_{lt}-varying family

The periodicity of the members that form the $L_2(H_{lt} = -1.50,\ \alpha = \frac{5}{3}\pi$ rad) family are established in Figure F.64. This Figure shows that the collocation procedure produces a converged solution with an equidistributed truncation error. The initial state of the resulting solution is explicitly propagated for the estimated orbital period which confirms the periodicity of the family members and a correct implementation of the collocation procedure. All family members adhere to the periodicity and equidistribution criteria listed in Table A.8.

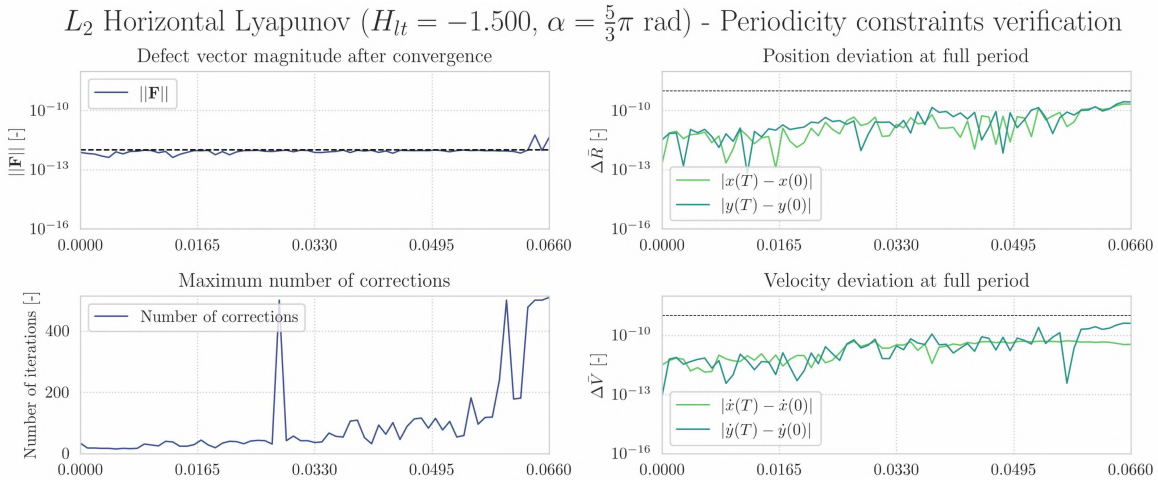

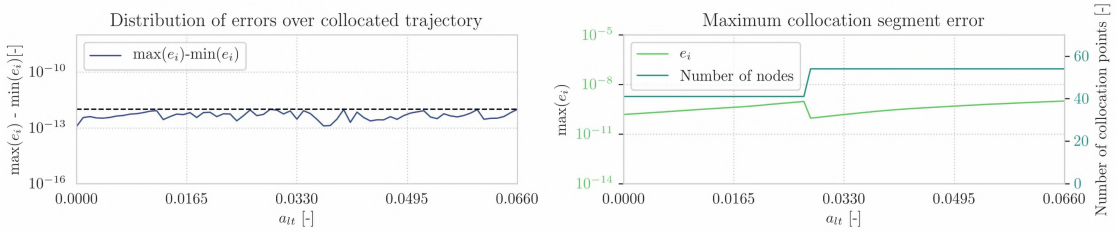

Figure F.64: Periodicity verification of the L_2 ($H_{lt} = -1.50$, $\alpha = \frac{5}{3}\pi$ rad) family. The three left subfigures and the bottom right subfigure demonstrate the characteristics of the collocation method whereas the upper and middle right subfigure show the full-period state discrepancy of the solution. These discrepancies are obtained via explicit propagation of the initial state forwarded by the collocation procedure.

Characteristics of the monodromy eigensystem of each member of the L_2 ($H_{lt} = -1.50$, $\alpha = \frac{5}{3}\pi$ rad) family are shown in Figure F.65. It can be concluded that the monodromy eigensystem of each family member adheres to the structure of a symplectic map.

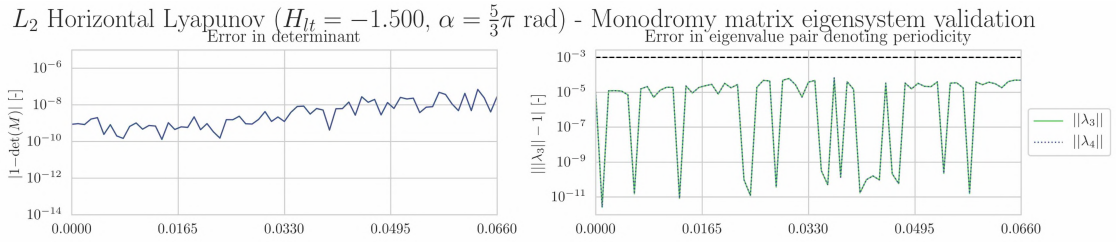

Figure F.65: Monodromy matrix eigensystem validation of the L_2 ($H_{lt} = -1.50$, $\alpha = \frac{5}{3}\pi$ rad) family. The left subfigure shows the deviation of the monodromy matrix determinant whereas the right subfigure demonstrates the deviation of the eigenvalue representing the in-plane center subspace.

Figure F.66 proves that the L_2 ($H_{lt} = -1.50$, $\alpha = \frac{5}{3}\pi$ rad) family is an a_{lt}-varying family since the Hamiltonian and acceleration orientation are constant.

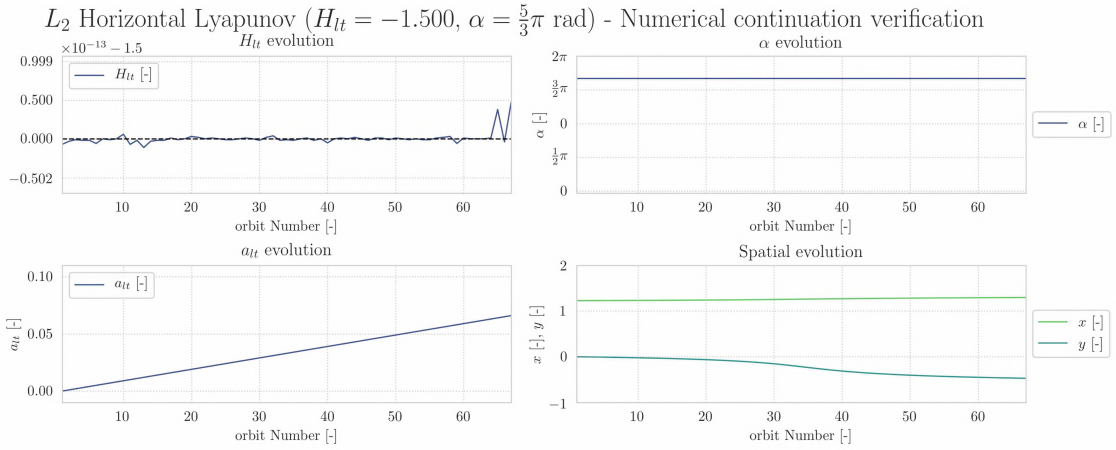

Figure F.66: Numerical continuation verification of the L_2 ($H_{lt} = -1.50$, $\alpha = \frac{5}{3}\pi$ rad) family. The top subfigures and bottom left subfigure demonstrate that the l.p.o family unfolds along the acceleration branch. The bottom right subfigure shows the spatial evolution of the initial condition along the family.

The verification of the L_2 ($H_{lt} = -1.50$, $\alpha = \frac{1}{3}\pi$ rad) and L_1 ($H_{lt} = -1.50$, $\alpha = \frac{5}{3}\pi$ rad) family is wrapped up by evaluating the degree of symmetry between their shooting conditions. This analysis can be found in Figure F.67.

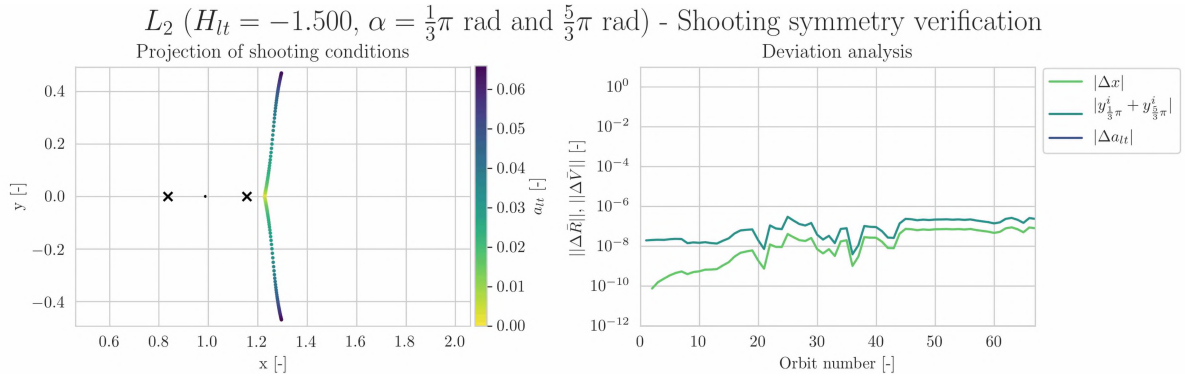

Figure F.67: Shooting symmetry analysis of the L_2 ($H_{lt} = -1.50$, $\alpha = \frac{1}{3}\pi$ and $\frac{5}{3}\pi$ rad) families. The left subfigure shows the evolution of the spatial conditions of both families. The upper branch shows the $\alpha = \frac{1}{3}\pi$ family whereas the lower branch denotes the $\alpha = \frac{5}{3}\pi$ family. The right subfigure shows the symmetry between the initial conditions of the family members.

Figure F.60 reveals that the degree of symmetry between the initial conditions the family members remains fairly constant over the families. A possible explanation for the asymmetries can be attributed to truncation errors that are inherent to the polynomial interpolation method of the collocation procedure.

F.5.3. Orientation-varying families

A total of eighteen α-varying families have been presented in Chapter 1. Their veracity is discussed in this Section. The termination cause of each numerical continuation procedure associated with construction of an α-varying family is presented in Table F.7.

	E_1			E_2		
a_{lt}	0.01	0.05	0.10	0.01	0.05	0.10
$H_{lt} = -1.55$	J	J	H	J*	H	J*
$H_{lt} = -1.525$	J	J	H	J*	J	I*
$H_{lt} = -1.50$	J	J*	J*	J	I*	I*

Table F.7: An overview of the termination causes of the numerical continuation procedures associated with α-varying families. The termination cause of some α-varying families is underlined, meaning that proof of their veracity is provided later in this Section. Families whose termination codes is augmented with an asterix subscript are generated via multiple continuation procedures.

The continuation procedures responsible for construction of the α-varying families are terminated due to various reasons. Most continuation procedures are terminated because the complete family has been calculated. Some families have been constructed via multiple continuation procedures that leverage different seed solutions. The remaining families could not be fully computed due to instabilities in the collocation procedure. The veracity of the families that have been fully computed via multiple numerical continuation procedures are discussed in the remainder of this Section.

L_1 ($H_{lt} = -1.50$, $a_{lt} = 0.05$) α-varying family

The degree of periodicity of the members that form the $L_1(H_{lt} = -1.50,\ a_{lt} = 0.05)$ family is shown in Figure F.68. This Figure shows that the collocation procedure produces a converged solution whose truncation error is not always equidistributed. The initial state of the resulting solution is explicitly propagated for the estimated orbital period. One member of the family does not meet the periodicity thresholds at full period but termination of the continuation procedure due to this violation is intentionally suppressed since α-varying families would otherwise be impossible to obtain. The family has been constructed via three continuation procedures where the first procedure has produced the partial family for $\alpha \in [0°, 134°]$. The second continuation procedure has computed the partial family for $\alpha \in [135°, 260°]$ and the third continuation procedure computes the partial family for $\alpha \in [261°, 359°]$. The piecewise construction is clearly observed in the right subfigures of F.68. A shift in full period state discrepancies and number of nodes is visible at 135° and 261°, which are indicated with red dotted lines.

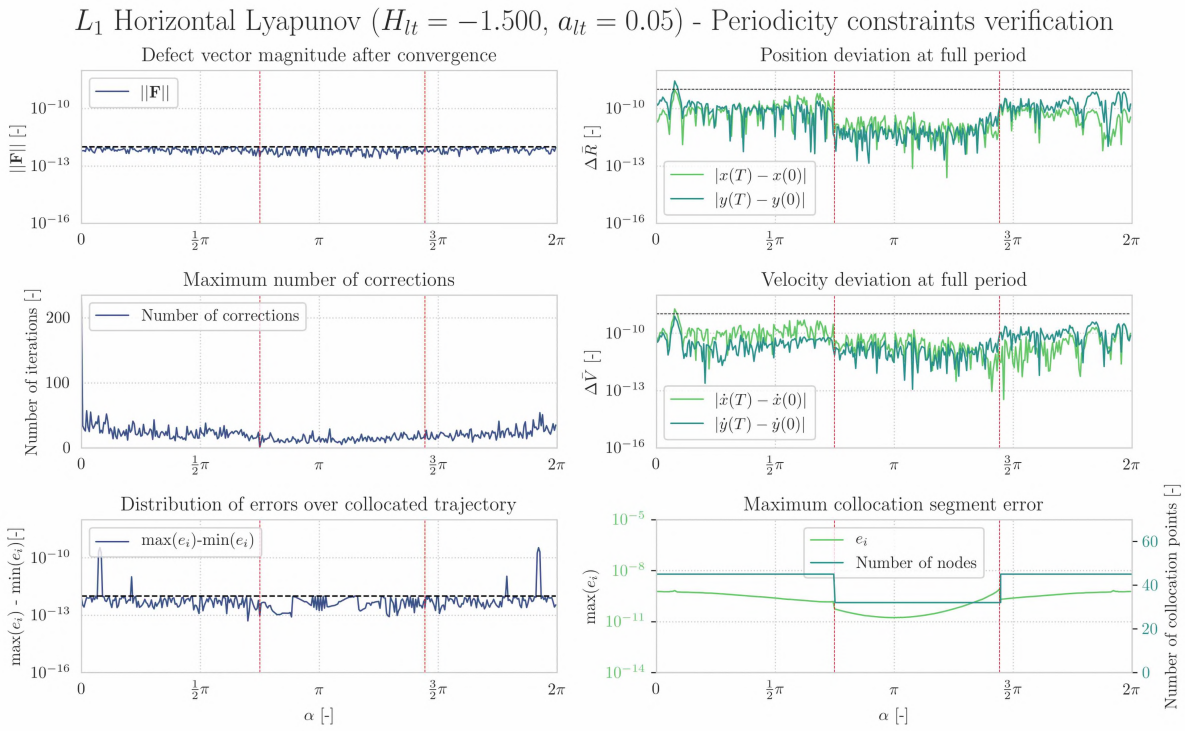

Figure F.68: Periodicity verification of the L_1 ($H_{lt} = -1.50$, $a_{lt} = 0.05$) family. The three left subfigures and the bottom right subfigure demonstrate the characteristics of the collocation method whereas the upper and middle right subfigure show the full-period state discrepancy of the solution. These discrepancies are obtained via explicit propagation of the initial state forwarded by the collocation procedure. The red dotted lines emphasize the piecewise construction of this family.

Characteristics of the monodromy eigensystem of each member of the L_1 ($H_{lt} = -1.50$, $a_{lt} = 0.05$) family are shown in Figure F.69. It can be concluded that the monodromy eigensystem of each family member adheres to the structure of a symplectic map. The piecewise construction of the family is also visible in the monodromy eigensystem deviations. A shift in the magnitude eigensystem deviations occur at 135° and 261°.

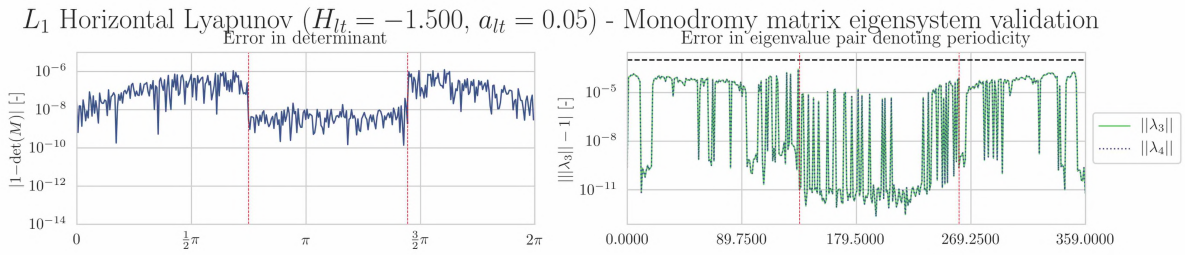

Figure F.69: Monodromy matrix eigensystem validation of the L_1 ($H_{lt} = -1.50$, $a_{lt} = 0.05$) family. The left subfigure shows the deviation of the monodromy matrix determinant whereas the right subfigure demonstrates the deviation of the eigenvalue representing the in-plane center subspace. The red dotted lines emphasize the piecewise construction of this family.

Figure F.70 proves that the L_1 ($H_{lt} = -1.50$, $a_{lt} = 0.05$) family is an α-varying family since the Hamiltonian and acceleration magnitude are constant. The piecewise construction of the family is also visible in this Figure since the deviation in Hamiltonian increases at the end of the first and third collocation procedure ($\alpha = 134°$) and at the beginning of the third collocation procedure ($\alpha = 261°$).

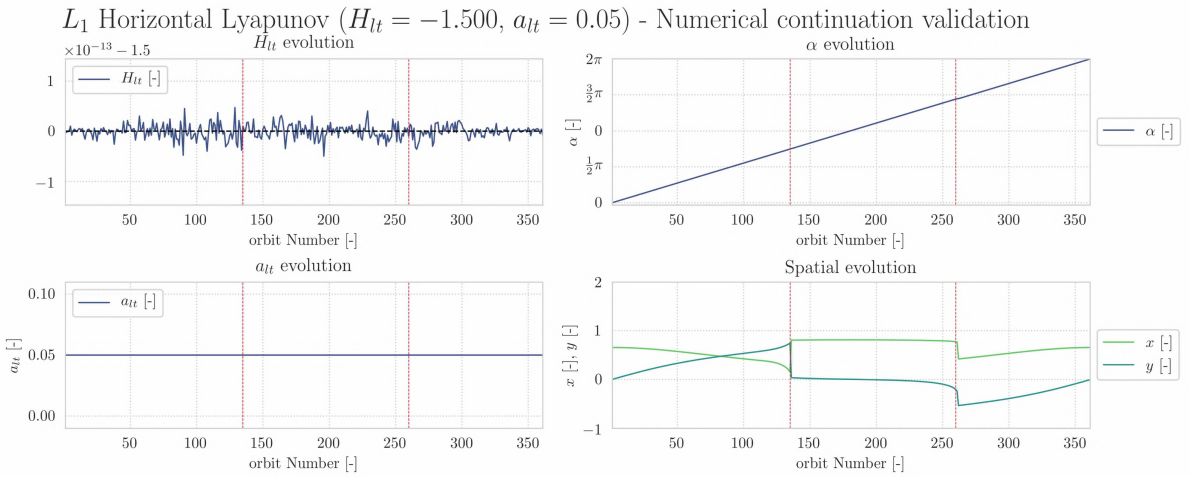

Figure F.70: Numerical continuation verification of the L_1 ($H_{lt} = -1.55$, $a_{lt} = 0.05$) family. The top subfigures and bottom left subfigure demonstrate that the l.p.o family unfolds along the acceleration branch. The bottom right subfigure shows the spatial evolution and phase drift of the initial condition along the family. The red dotted lines emphasize the piecewise construction of this family.

It is unlikely that the asymmetries observed in the L_1 ($H_{lt} = -1.50$, $a_{lt} = 0.05$) family are correct since symmetry exists in the CR3BP-LT[1]. These asymmetries are a consequence of the asymmetry in the shooting conditions of the family. Figure F.71 shows the degree of symmetry between family members with acceleration orientation α and $2\pi - \alpha$.

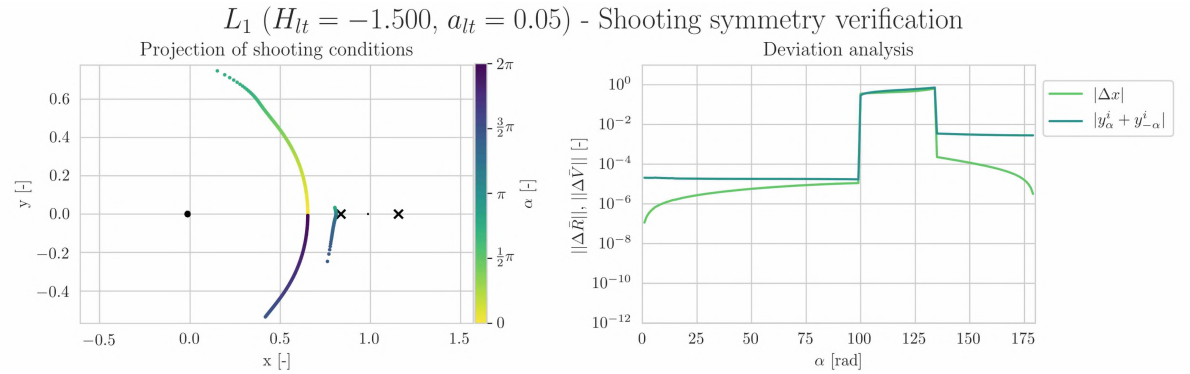

Figure F.71: Shooting symmetry analysis of the L_1 ($H_{lt} = -1.50$, $a_{lt} = 0.05$) family. The left subfigure shows the evolution of the shooting conditions of family. The right subfigure shows the symmetry between the initial conditions of the family members α and $2\pi - \alpha$.

Inspecting Figure F.71, it can be observed that the degree of asymmetry between members of the α-varying family is at least two orders of magnitude higher compared to the other two family types. Furthermore, the two spikes in degree of (a)symmetry are a consequence of the piecewise construction of this family. The fact that the resulting orbits depends heavily on the initial conditions means that the collocation procedure is not accurate enough to compute the α-varying families.

L_1 ($H_{lt} = -1.55$, $a_{lt} = 0.10$) α-varying family

The degree of periodicity of the members that form the L_1($H_{lt} = -1.55$, $a_{lt} = 0.10$) family is shown in Figure F.72. This particular family exists for $\alpha \in [238° \rightarrow 122°]$ which explains the straight line segment in each subfigure. This Figure shows that the collocation procedure produces a converged solution whose truncation error is not always equidistributed. The initial state of the resulting solution is explicitly propagated for the estimated orbital period. Several members of the family do not meet the periodicity thresholds at full period but termination of the continuation procedure due to this violation is intentionally suppressed since the α-varying families could not be obtained otherwise. The family has been constructed via four continuation procedures where the first procedure has produced the partial family for $\alpha \in [0°, 92°]$. The second continuation procedure has computed the partial family for $\alpha \in [93°, 122°]$ whereas the third and fourth continuation procedure compute parts of the family for $\alpha \in [238°, 267°]$ and $\alpha \in [268°, 359°]$. The piecewise construction

is clearly observed in the right subfigures of F.72. A shift in full period state discrepancies and patch points is visible at 93° and 268°.

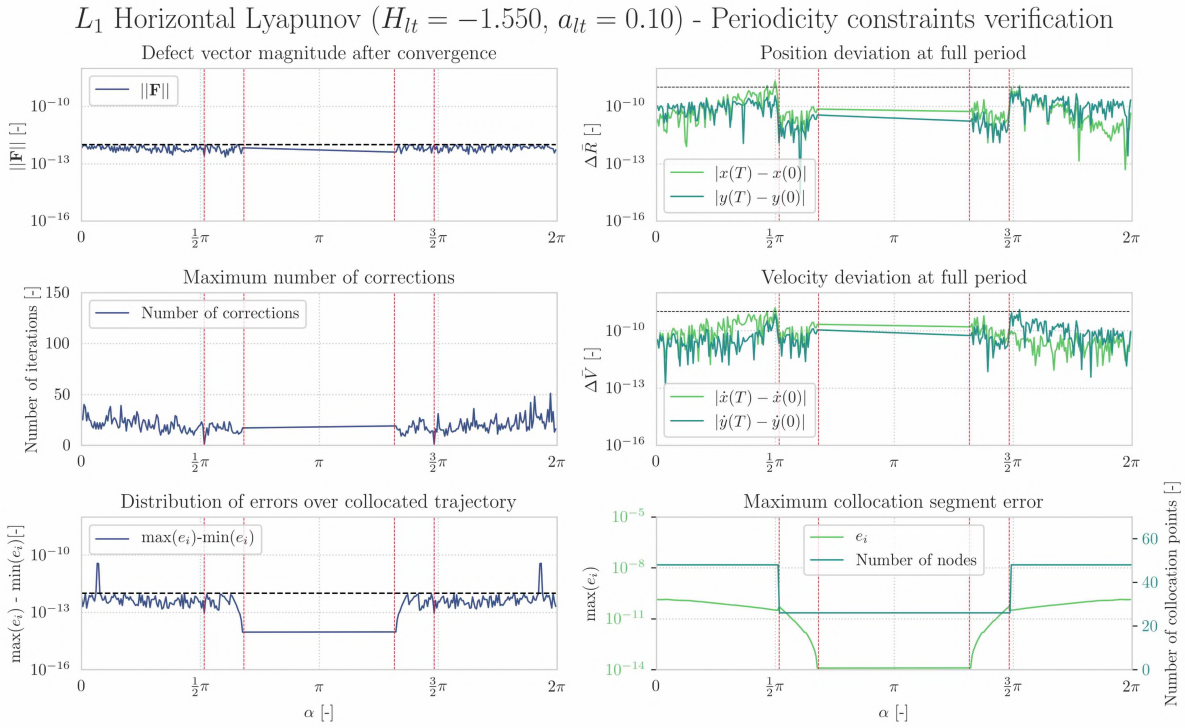

Figure F.72: Periodicity verification of the L_1 ($H_{lt} = -1.55$, $a_{lt} = 0.10$) family. The three left subfigures and the bottom right subfigure demonstrate the characteristics of the collocation method whereas the upper and middle right subfigure show the full-period state discrepancy of the solution. These discrepancies are obtained via explicit propagation of the initial state forwarded by the collocation procedure. The red dotted lines emphasize the piecewise construction of this family.

Characteristics of the monodromy eigensystem of each member of the L_1 ($H_{lt} = -1.55$, $a_{lt} = 0.10$) family are shown in Figure F.73. It can be concluded that the monodromy eigensystem of each family member adheres to the structure of a symplectic map. The piecewise construction of the family is also visible in the monodromy eigensystem deviations. A shift in the magnitude eigensystem deviations occur at 93° and 268°.

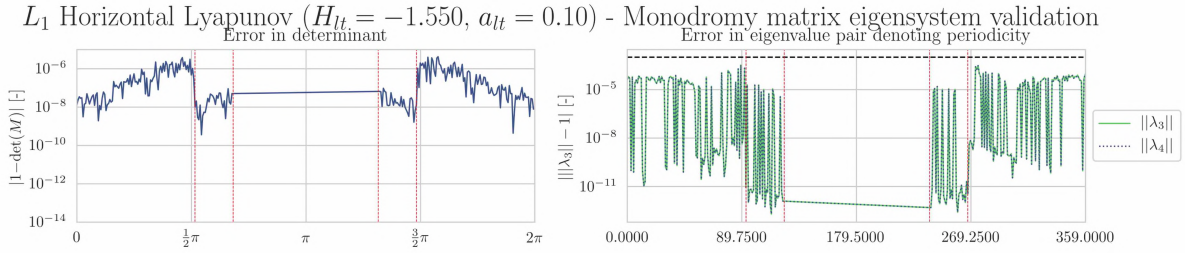

Figure F.73: Monodromy matrix eigensystem validation of the L_1 ($H_{lt} = -1.55$, $a_{lt} = 0.10$) family. The left subfigure shows the deviation of the monodromy matrix determinant whereas the right subfigure demonstrates the deviation of the eigenvalue representing the in-plane center subspace. The red dotted lines emphasize the piecewise construction of this family.

Figure F.74 proves that the L_1 ($H_{lt} = -1.55$, $a_{lt} = 0.1$) family is an α-varying family since the Hamiltonian and acceleration magnitude are constant. The piecewise construction of the family is also visible in the continuation verification since the deviation in Hamiltonian increases at the end of the first collocation procedure ($\alpha = 93°$) and at the beginning of the fourth collocation procedure ($\alpha = 268°$).

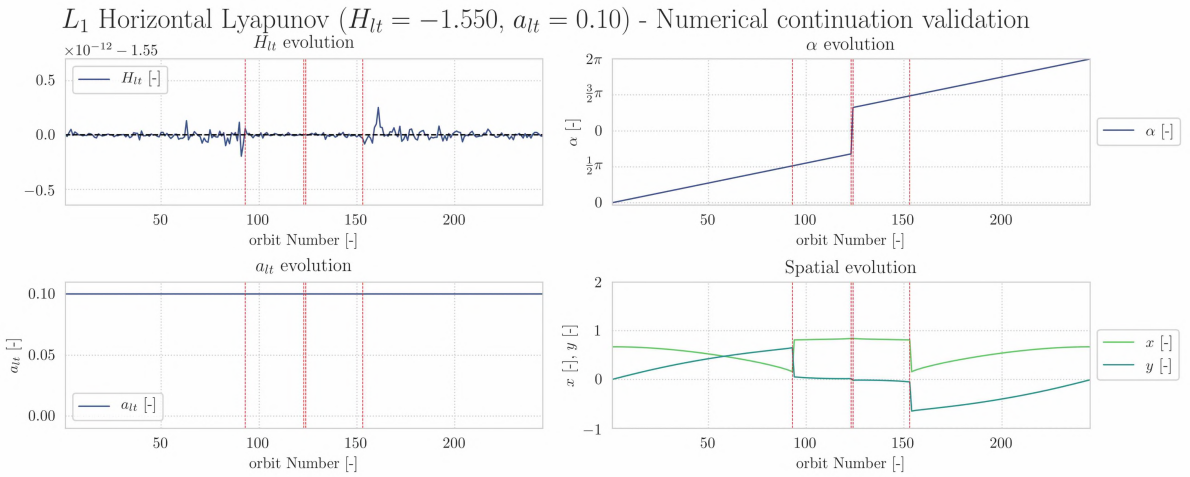

Figure F.74: Numerical continuation verification of the L_1 ($H_{lt} = -1.55$, $a_{lt} = 0.10$) family. The top subfigures and bottom left subfigure demonstrate that the l.p.o family unfolds along the acceleration branch. The bottom right subfigure shows the spatial evolution and phase drift of the initial condition along the family. The red dotted lines emphasize the piecewise construction of this family.

It is unlikely that the asymmetries observed in the L_1 ($H_{lt} = -1.55$, $a_{lt} = 0.10$) family are correct since symmetry exists in the CR3BP-LT [1]. These asymmetries are a consequence of the asymmetry in the shooting conditions of the family. Figure F.75 shows the degree of symmetry between family members with acceleration orientation α and $2\pi - \alpha$.

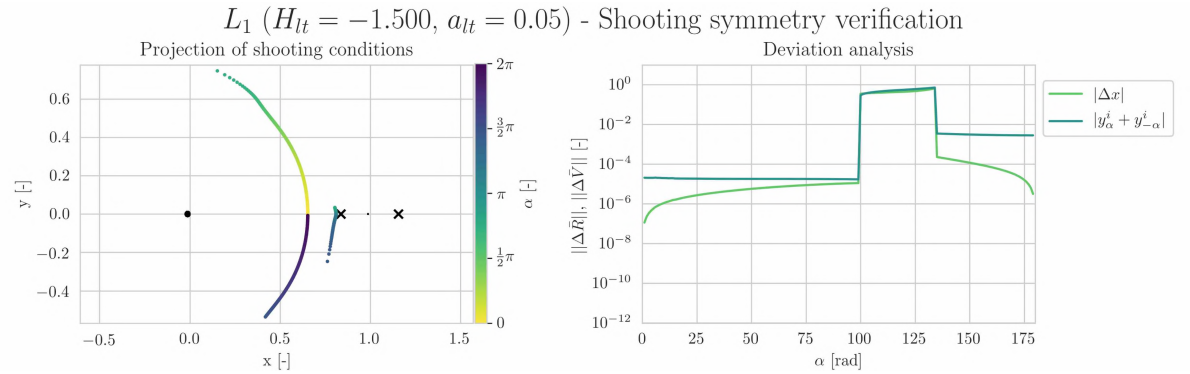

Figure F.75: Shooting symmetry analysis of the L_1 ($H_{lt} = -1.55$, $a_{lt} = 0.10$) family. The left subfigure shows the evolution of the shooting conditions of family. The right subfigure shows the symmetry between the initial conditions of the family members α and $2\pi - \alpha$.

Inspecting Figure F.75, it can be observed that the degree of asymmetry between members of the α-varying family is an order of magnitude higher compared to the other two family types. Furthermore, the two spikes in degree of asymmetry are a consequence of the piecewise construction of this family. The fact that the resulting orbits heavily depend on the initial conditions means that the collocation procedure is not accurate enough to compute the α-varying families for these settings.

L_1 ($H_{lt} = -1.525$, $a_{lt} = 0.10$) α-varying family

The degree of periodicity of the members that form the $L_1(H_{lt} = -1.525,\ a_{lt} = 0.1)$ family is shown in Figure F.76. This particular family exists for $\alpha \in [215° \rightarrow 145°]$ which explains the straight line segment in each subfigure. This Figure shows that the collocation procedure produces a converged solution whose truncation error is not always equidistributed. The initial state of the resulting solution is explicitly propagated for the estimated orbital period. Several members of the family do not meet the periodicity thresholds at full period but termination of the continuation procedure due to this violation is intentionally suppressed since construction of α-varying families would not be possible otherwise. The family has been constructed via four continuation procedures where the first procedure has produced the partial family for $\alpha \in [0°, 109°]$. The second continuation procedure has computed the partial family for $\alpha \in [110°, 145°]$ whereas the third and fourth continuation procedure compute parts of the family for $\alpha \in [215°, 253°]$ and $\alpha \in [254°, 359°]$.

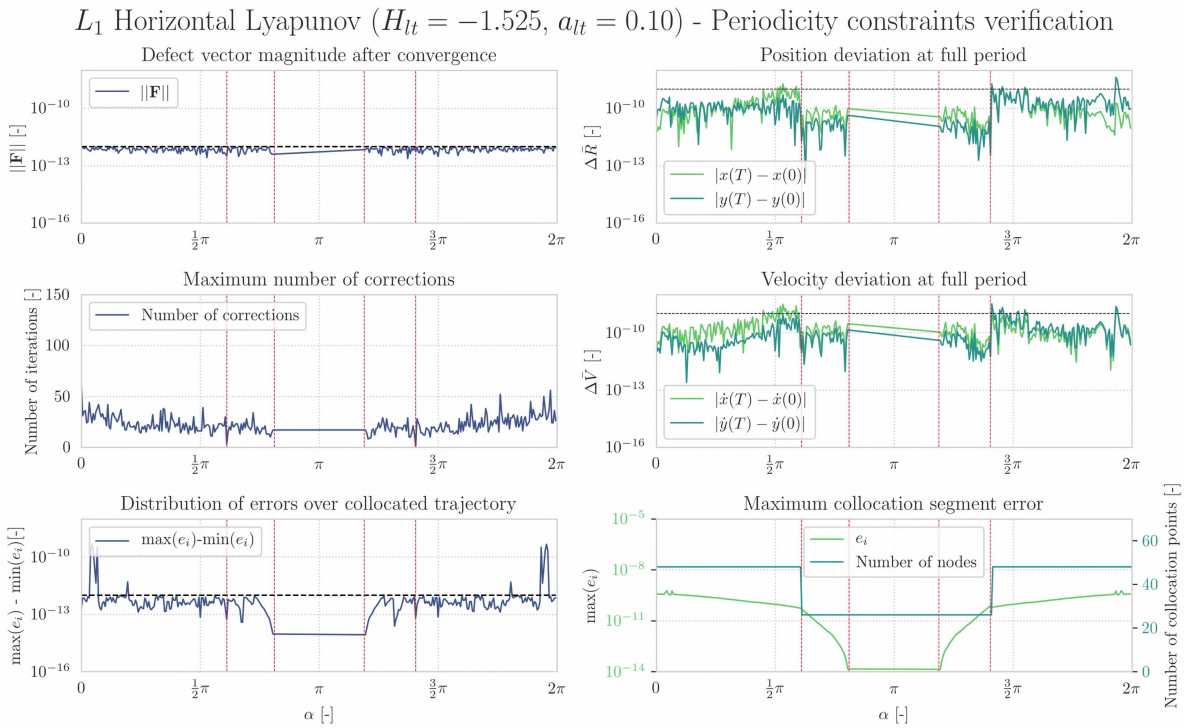

Figure F.76: Periodicity verification of the L_1 ($H_{lt} = -1.525$, $a_{lt} = 0.10$) family. The three left subfigures and the bottom right subfigure demonstrate the characteristics of the collocation method whereas the upper and middle right subfigure show the full-period state discrepancy of the solution. These discrepancies are obtained via explicit propagation of the initial state forwarded by the collocation procedure. The red dotted lines emphasize the piecewise construction of this family.

Characteristics of the monodromy eigensystem of each member of the L_1 ($H_{lt} = -1.525$, $a_{lt} = 0.10$) family are shown in Figure F.77. It can be concluded that the monodromy eigensystem of each family member adheres to the structure of a symplectic map. The piecewise construction of the family is also visible in the monodromy eigensystem deviations. A shift in the magnitude eigensystem deviations occur at 110° and 254°.

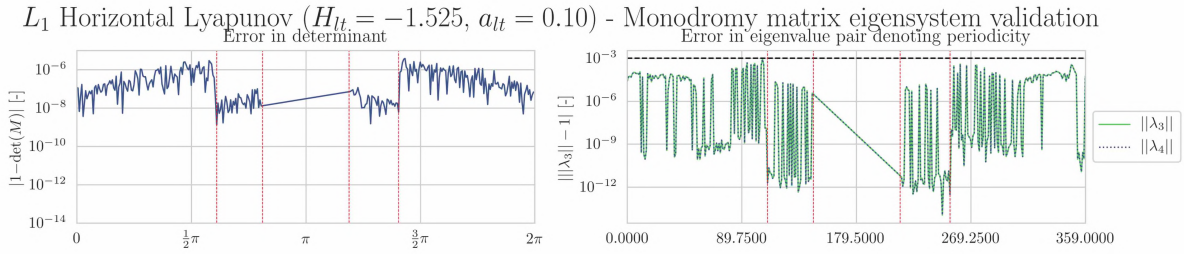

Figure F.77: Monodromy matrix eigensystem validation of the L_1 ($H_{lt} = -1.525$, $a_{lt} = 0.10$) family. The left subfigure shows the deviation of the monodromy matrix determinant whereas the right subfigure demonstrates the deviation of the eigenvalue representing the in-plane center subspace. The red dotted lines emphasize the piecewise construction of this family.

Figure F.78 proves that the L_1 ($H_{lt} = -1.525$, $a_{lt} = 0.10$) family is an α-varying family since the Hamiltonian and acceleration magnitude are constant. The piecewise construction of the family is also visible in the continuation verification since the deviation in Hamiltonian increases at the end of the first collocation procedure ($\alpha = 110°$) and at the beginning of the fourth collocation procedure ($\alpha = 254°$).

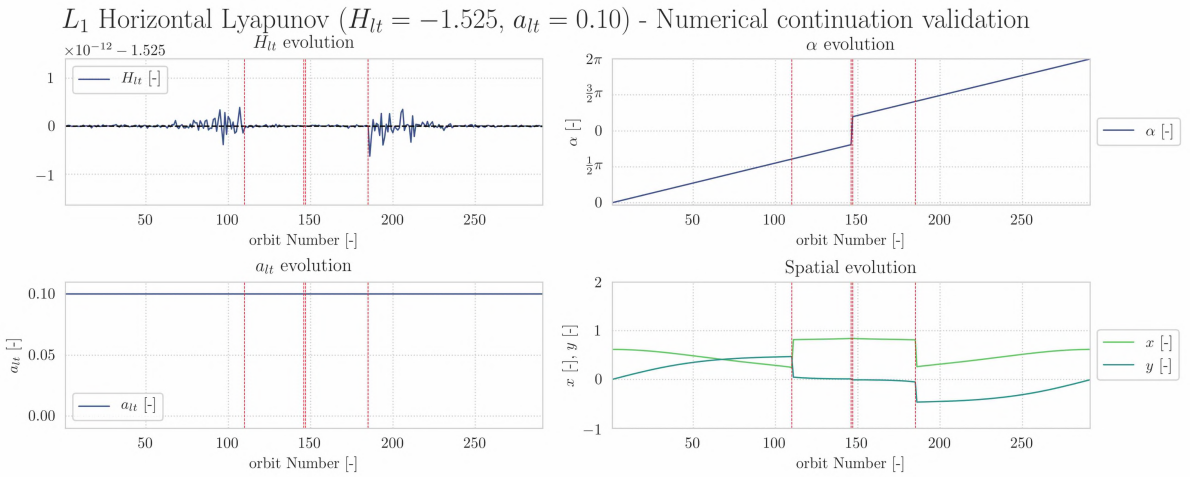

Figure F.78: Numerical continuation verification of the L_1 ($H_{lt} = -1.525$, $a_{lt} = 0.10$) family. The top subfigures and bottom left subfigure demonstrate that the l.p.o family unfolds along the acceleration branch. The bottom right subfigure shows the spatial evolution and phase drift of the initial condition along the family. The red dotted lines emphasize the piecewise construction of this family.

It is unlikely that the asymmetries observed in the L_1 ($H_{lt} = -1.525$, $a_{lt} = 0.10$) family are correct since symmetry exists in the CR3BP-LT [1]. These asymmetries are a consequence of the asymmetry in the shooting conditions of the family. Figure F.79 shows the degree of symmetry between family members with acceleration orientation α and $2\pi - \alpha$.

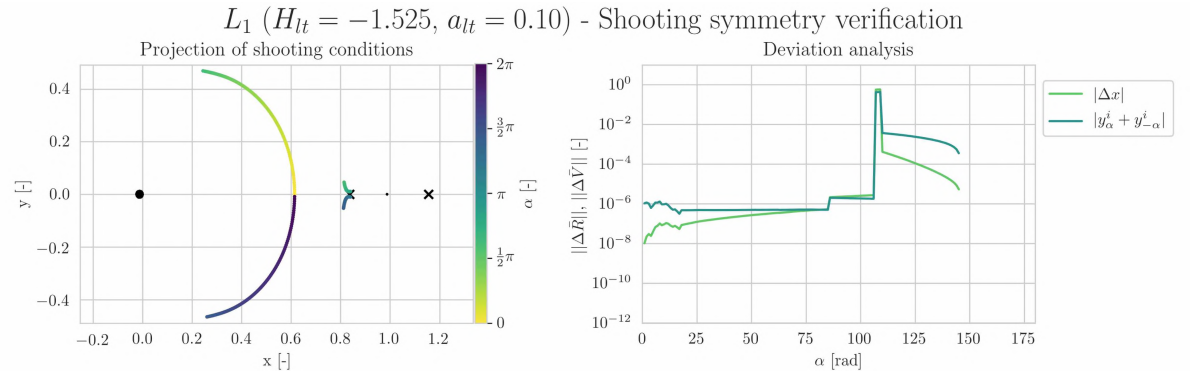

Figure F.79: Shooting symmetry analysis of the L_1 ($H_{lt} = -1.525$, $a_{lt} = 0.10$) family. The left subfigure shows the evolution of the shooting conditions of family. The right subfigure shows the symmetry between the initial conditions of the family members α and $2\pi - \alpha$.

Inspecting Figure F.79, it can be observed that the degree of asymmetry between members of the α-varying family is in the same order of magnitude as the until 110° where symmetry between the shooting conditions is lost. This is the result of the construction of the family in multiple numerical continuation procedures. The fact that the resulting orbits heavily depend on the initial conditions means that the collocation procedure is not accurate enough to compute the α-varying families for these settings.

L_1 ($H_{lt} = -1.50$, $a_{lt} = 0.10$) α-varying family

The degree of periodicity of the members that form the $L_1(H_{lt} = -1.50,\ a_{lt} = 0.10)$ family is shown in Figure F.80. This Figure shows that the collocation procedure produces a converged solution whose truncation error is not always equidistributed. The initial state of the resulting solution is explicitly propagated for the estimated orbital period. Several members of the family do not meet the periodicity thresholds at full period but termination of the continuation procedure due to this violation is intentionally suppressed since construction of α-varying families would not be possible otherwise. The family has been constructed via four continuation procedures where the first procedure has produced the partial family for $\alpha \in [0°, 125°]$. The second continuation procedure has computed the partial family for $\alpha \in [126°, 250°]$ whereas the third computes the family for $\alpha \in [251°, 359°]$.

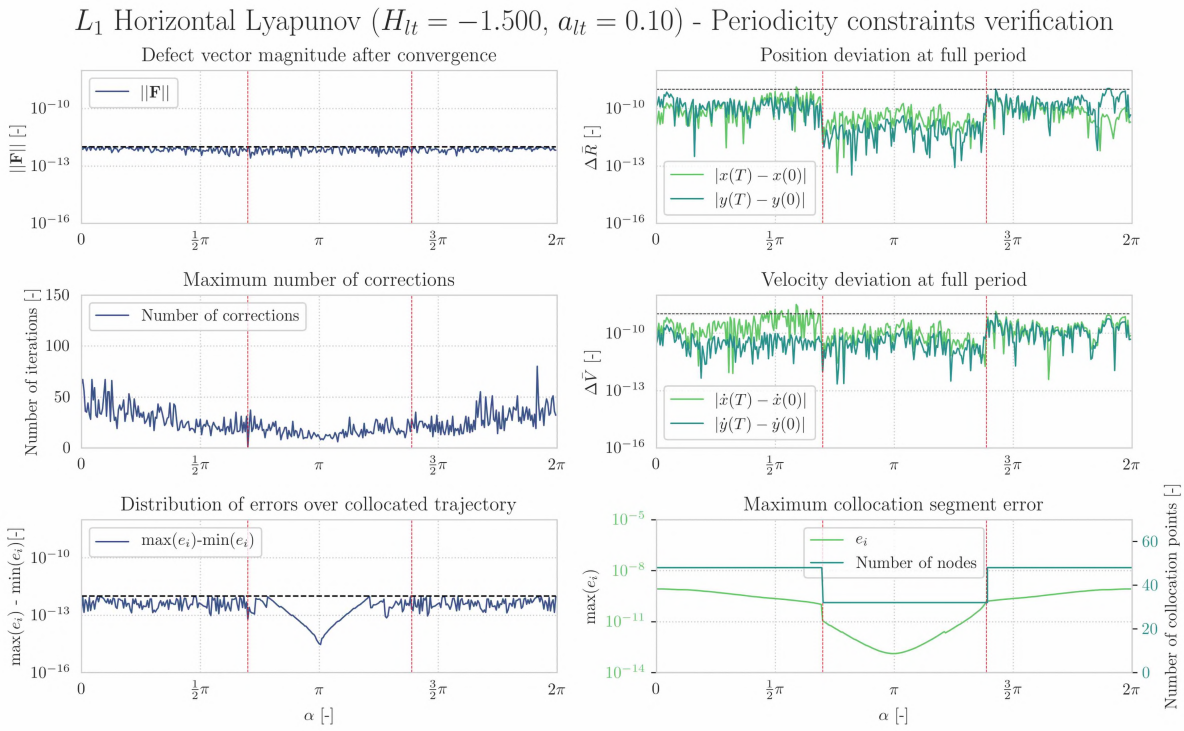

Figure F.80: Periodicity verification of the L_1 ($H_{lt} = -1.50$, $a_{lt} = 0.10$) family. The three left subfigures and the bottom right subfigure demonstrate the characteristics of the collocation method whereas the upper and middle right subfigure show the full-period state discrepancy of the solution. These discrepancies are obtained via explicit propagation of the initial state forwarded by the collocation procedure. The red dotted lines emphasize the piecewise construction of this family.

Characteristics of the monodromy eigensystem of each member of the L_1 ($H_{lt} = -1.50$,$a_{lt} = 0.10$) family are shown in Figure F.81. It can be concluded that the monodromy eigensystem of each family member adheres to the structure of a symplectic map. The piecewise construction of the family is also visible in the monodromy eigensystem deviations. A shift in the magnitude eigensystem deviations occur at 126° and 251°.

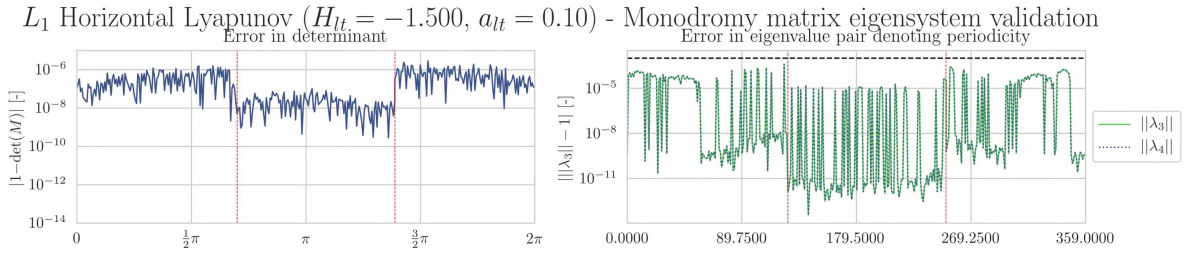

Figure F.81: Monodromy matrix eigensystem validation of the L_1 ($H_{lt} = -1.50$, $a_{lt} = 0.10$) family. The left subfigure shows the deviation of the monodromy matrix determinant whereas the right subfigure demonstrates the deviation of the eigenvalue representing the in-plane center subspace. The red dotted lines emphasize the piecewise construction of this family.

Figure F.82 proves that the L_1 ($H_{lt} = -1.50$, $a_{lt} = 0.1$) family is an α-varying family since the Hamiltonian and acceleration magnitude are constant. The piecewise construction of the family is also visible in the continuation verification since the deviation in Hamiltonian increases at the end of the first collocation procedure ($\alpha = 126°$) and at the beginning of the third collocation procedure ($\alpha = 251°$).

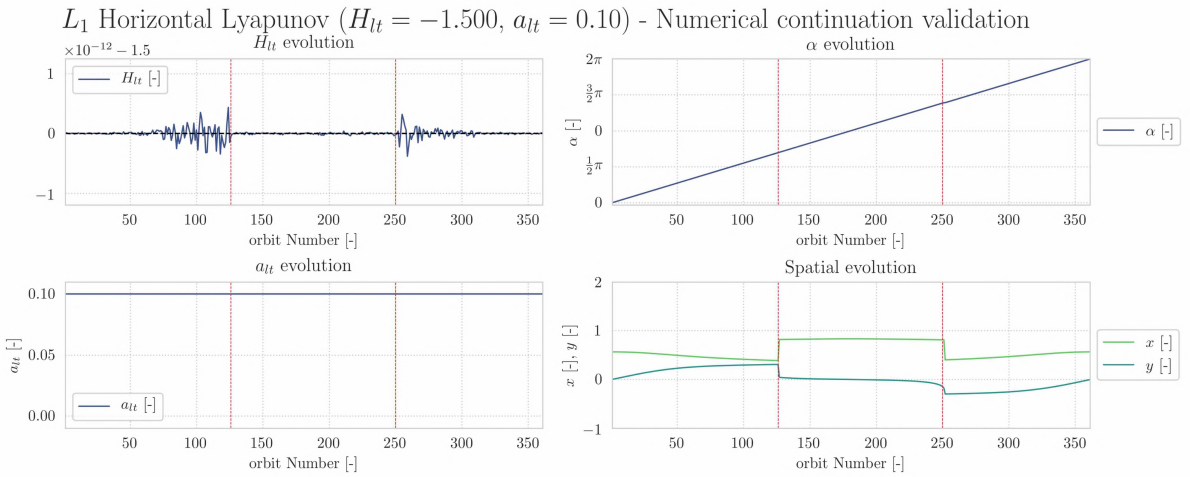

Figure F.82: Numerical continuation verification of the L_1 ($H_{lt} = -1.50$, $a_{lt} = 0.10$) family. The top subfigures and bottom left subfigure demonstrate that the l.p.o family unfolds along the acceleration branch. The bottom right subfigure shows the spatial evolution and phase drift of the initial condition along the family. The red dotted lines emphasize the piecewise construction of this family.

It is unlikely that the asymmetries observed in the L_1 ($H_{lt} = -1.50$, $a_{lt} = 0.10$) family are correct since symmetry exists in the CR3BP-LT [1]. These asymmetries are a consequence of the asymmetry in the shooting conditions of the family. Figure F.83 shows the degree of symmetry between family members with acceleration orientation α and $2\pi - \alpha$.

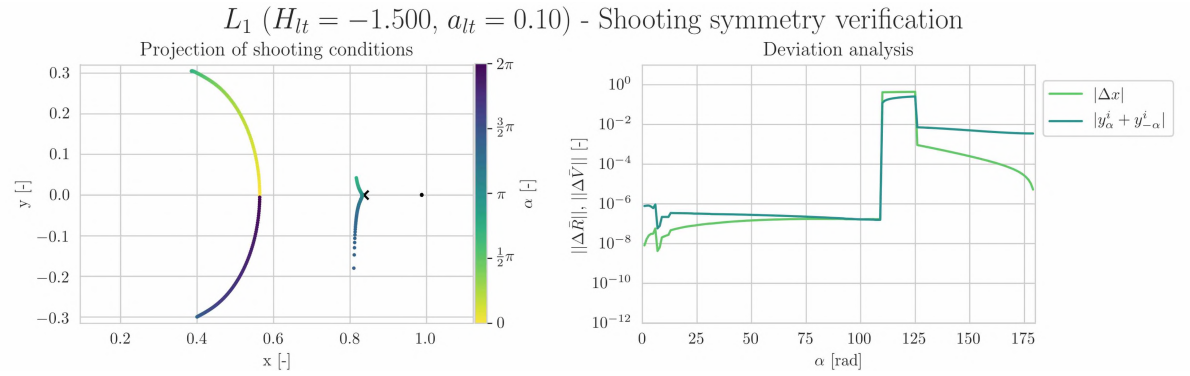

Figure F.83: Shooting symmetry analysis of the L_1 ($H_{lt} = -1.50$, $a_{lt} = 0.10$) family. The left subfigure shows the evolution of the shooting conditions of family. The right subfigure shows the symmetry between the initial conditions of the family members α and $2\pi - \alpha$.

Inspecting Figure F.83, it can be observed that the degree of asymmetry between members of the α-varying family is in the same order of magnitude as the until 126° where symmetry between the shooting conditions is lost. This is the result of the construction of the family in multiple numerical continuation procedures. The fact that the resulting orbits heavily depend on the initial conditions means that the collocation procedure is not accurate enough to compute the α-varying families for these settings.

L_2 ($H_{lt} = -1.55$, $a_{lt} = 0.10$) α-varying family

The degree of periodicity of the members that form the $L_2(H_{lt} = -1.55,\ a_{lt} = 0.10)$ family is shown in Figure F.84. This Figure show that the collocation procedure produces a converged solution whose defect vector does not always meet the desired threshold. This is caused by the fact that the numerical threshold is relaxed once the collocation algorithm takes more than 500 iterations to converge. The initial state of the resulting solution is explicitly propagated for the estimated orbital period. The family has been constructed via six continuation procedures. The first procedure has produced the partial family for $\alpha \in [0°, 60°]$. The second continuation procedure has computed the partial family for $\alpha \in [61°, 95°]$ whereas the third procedure computes the family for $\alpha \in [96°, 109°]$. The final three procedures produce parts of the family for $\alpha \in [251°, 264°]$, $\alpha \in [265°, 300°]$ and $\alpha \in [301°, 359°]$

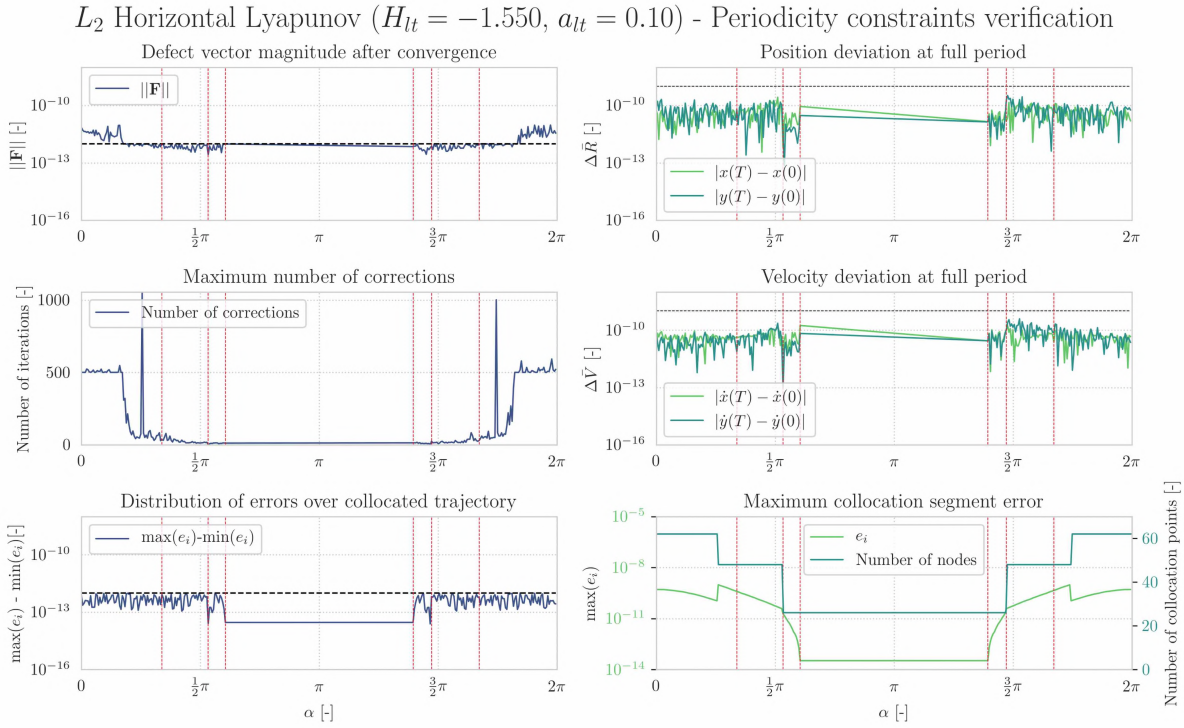

Figure F.84: Periodicity verification of the L_2 ($H_{lt} = -1.55$, $a_{lt} = 0.10$) family. The three left subfigures and the bottom right subfigure demonstrate the characteristics of the collocation method whereas the upper and middle right subfigure show the full-period state discrepancy of the solution. These discrepancies are obtained via explicit propagation of the initial state forwarded by the collocation procedure. The red dotted lines emphasize the piecewise construction of this family.

Characteristics of the monodromy eigensystem of each member of the L_2 ($H_{lt} = -1.55$, $a_{lt} = 0.10$) family are shown in Figure F.85. It can be concluded that the monodromy eigensystem of each family member adheres to the structure of a symplectic map. The piecewise construction of the family is also visible in the monodromy eigensystem deviations via the shifts that occur in both subfigures.

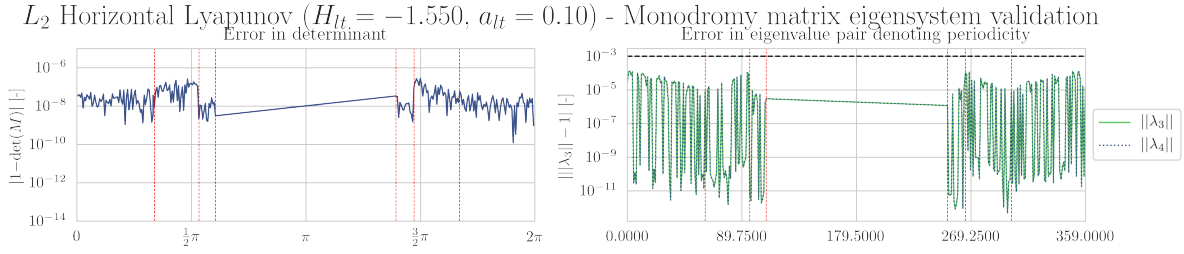

Figure F.85: Monodromy matrix eigensystem validation of the L_2 ($H_{lt} = -1.55$, $a_{lt} = 0.10$) family. The left subfigure shows the deviation of the monodromy matrix determinant whereas the right subfigure demonstrates the deviation of the eigenvalue representing the in-plane center subspace. The red dotted lines emphasize the piecewise construction of this family.

Figure F.86 proves that the L_2 ($H_{lt} = -1.55$, $a_{lt} = 0.10$) family is an α-varying family since the Hamiltonian and acceleration magnitude are constant. The piecewise construction of the family is also visible in the continuation verification from the shifts in each subfigure

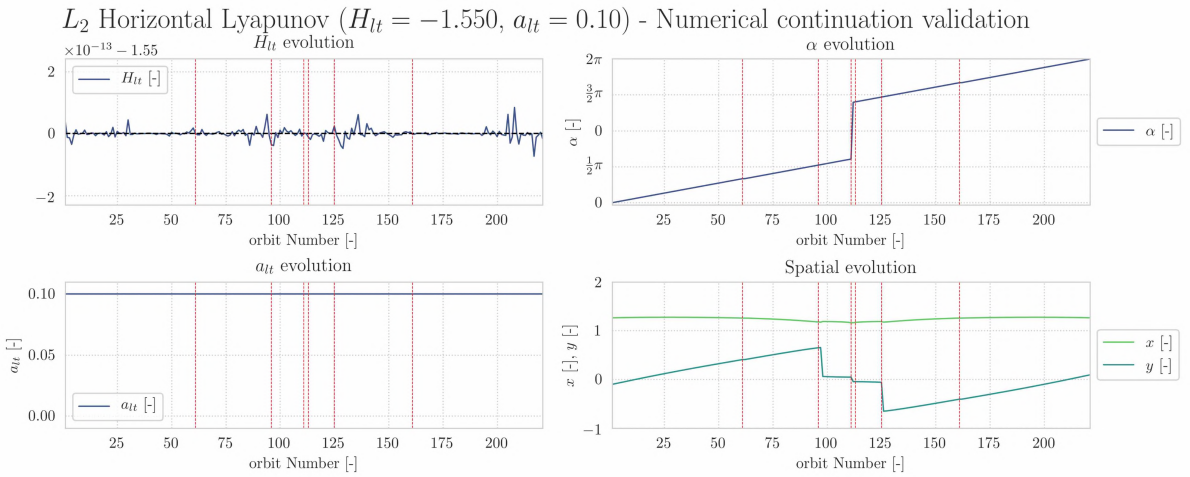

Figure F.86: Numerical continuation verification of the L_2 ($H_{lt} = -1.55$, $a_{lt} = 0.10$) family. The top subfigures and bottom left subfigure demonstrate that the l.p.o family unfolds along the acceleration branch. The bottom right subfigure shows the spatial evolution of the initial condition along the family. The red dotted lines emphasize the piecewise construction of this family.

It is unlikely that the asymmetries observed in the L_2 ($H_{lt} = -1.55$, $a_{lt} = 0.10$) family are correct since symmetry exists in the CR3BP-LT [1]. These asymmetries are a consequence of the asymmetry in the shooting conditions of the family. Figure F.87 shows the degree of symmetry between family members with acceleration orientation α and $2\pi - \alpha$.

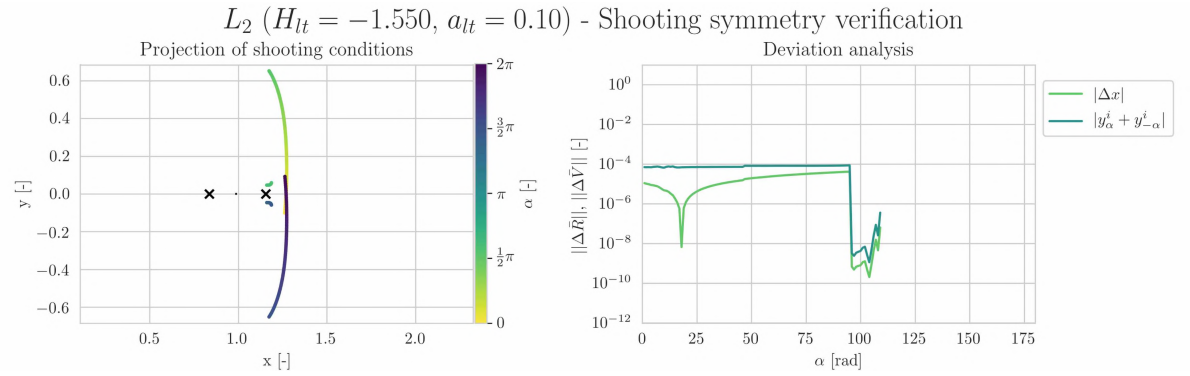

Figure F.87: Shooting symmetry analysis of the L_2 ($H_{lt} = -1.55$, $a_{lt} = 0.10$) family. The left subfigure shows the evolution of the shooting conditions of family. The right subfigure shows the symmetry between the initial conditions of the family members α and $2\pi - \alpha$.

Inspecting Figure F.87, it can be observed that the degree of asymmetry between members of the α-varying family is approximately two orders of magnitude larger compared to other family types. From 95° onward, the degree of symmetry between this family is similar to the other two family types. The discrepancy in degree of symmetry over the the family can be attributed to the piecewise of the family. The fact that the resulting orbits heavily depend on the initial conditions means that the collocation procedure is not accurate enough to compute the α-varying families for these settings.

F.5.4. Concluding statements on veracity of libration point orbit families

The majority of the results adhere to the tolerances as specified in Tables A.4 and A.8 which cultivates the credibility of the proposed numerical continuation methodology. However, the implemented numerical continuation procedure is not perfect as it can become unstable and asymmetry can sometimes be observed in the results. Following is an explanation of the encountered imperfections:

Phase shift of initial condition The adapted Poincaré phase condition prevents a phase drift during the construction of the H_{lt}-varying families with a collinear acceleration orientation. However, a phase drift cannot be prevented for H_{lt}-varying families with a noncollinear acceleration orientation. A possible explanation for the constraint failure is that the adapted Poincaré phase condition cannot cope with the geometry distortions that are observed for families with noncollinear acceleration orientations.

Outliers in required number of corrections It can be observed that maximum number of corrections evolves smoothly during the numerical continuation procedure. However, peaks in number of required corrections are observed in some cases. These peaks coincide with a change in number of nodes. A possible explanation for the excessive number of correction after a change in number of nodes is that the new number of nodes are equidistributed in time. This probably results in an initial guess far from the actual solution.

Asymmetry in α-varying families The observed asymmetries in the α-varying families are a result of the asymmetry in their shooting conditions. The asymmetry in the shooting conditions are a consequence of different seed solutions for the particular family member. This is surprising as collocation methods are generally praised for their wide radius of convergence [5]. A possible explanation for lack of robustness is that the order of the LGL node placement strategy is insufficient to correctly construct the α-varying families. The insufficient order of the collocation scheme is also a likely cause for the substantial full-period state discrepancies observed in the α-varying families.

Periodicity violation of initial family members The initial members of some H_{lt}-varying families do not always satisfy the full-period state discrepancy tolerances. A possible explanation for this phenomenon is that the tolerance for the maximum allowed truncation error per collocation segment is not strict enough.

G

Recommendations

The equilibria contours and periodic solution families presented in Chapter 1 and Appendix D allow the reader to understand the effects of constant low-thrust acceleration on dynamical structures in the circular restricted Earth-Moon system. However, the results presented in this thesis project only scratch the surface of the periodic solution structure of the CR3BP-LT. This Appendix provides the reader with suggestions how to further explore the low-thrust periodic solution structure and leverage the results presented in this report for other new research efforts. Section G.1 provides recommendations that concern the improvement of the numerical model as presented in Appendices A-C. Recommendations for new research directions can be found in Section G.2.

G.1. Technical recommendations

The construction of equilibria contours and periodic solution families rely heavily on the numerical techniques explained in Appendices A-C. Several ideas regarding performance improvement of these techniques emerged over the course of this thesis project. An exhaustive overview of these ideas can be found in the remainder of this Section.

Stochastic equilibria root-finding

The equilibria root-finding procedure provides robust performance as long as the equilibria contours do not merge. Stochastic root-finding procedures might provide a more reliable alternative with lower associated computational cost compared to classic multivariate root-finding procedures [30]. Alternatively, heuristic algorithms may provide additional seed solutions which could enable the equilibria root-finding procedure to compute equilibria contours at large acceleration values ($a_{lt} \geq 0.25$).

Perturbation based Floquet targeter

The floquet targeter scheme, as explained in Section C.3, provides a velocity correction after passing of a time interval as specified in Table A.6. Alternatively, a correction manoeuvre can be executed each time the perturbation along the unwanted motion components exceeds a certain threshold.

Extend Floquet targeter to other family types

The current implementation of the floquet targeter scheme generates approximate solutions for H-L type of libration point orbits. According to [4], Floquet targeter schemes can also be used to generate vertical Lyapunov orbits (V-L). If the floquet targeter scheme is augmented with this capability, l.p.o families of the V-L type can be investigated. It remains to be seen if approximate Halo orbits can be generated with the Floquet controller since this type of orbits is not a principle form of motion around the equilibria of the CR3BP-LT.

Variable number of nodes for the two-level targeter	The two-level targeter does not guarantee that its solution resembles the characteristics of the input trajectory. The reliability of the two-level targeter can be improved by providing it with the capability to automatically increase the number of nodes in case the solution does not meet user-specified criteria (i.e amplitude or distance to primaries).
Legendre Gauss node placement strategy	The choice of a Gauss-Legendre-Lobatto node placement strategy gives rise to a numerical continuation procedure with a high associated computational cost. This can be attributed to the number of nodes that are needed to achieve the orbits with the desired accuracy. A higher-order method like the Legendre-Gauss node placement strategy will require less nodes to achieve the desired accuracy which will result in a computationally less costly continuation procedure [8].
Collocation scheme with fixed node times	A common approach for collocation methods is to fix the node times during the root-finding procedure and only update them via mesh refinement techniques once a solution has been found [8]. The collocation method implemented during thesis project allows the node times to vary to enable estimation of the orbital period. The variable node time introduces an instability in the collocation procedure. Such an instability occurs when the sequence of the nodes is changed which results in an unsolvable problem. This instability is the root-cause for the termination of the majority of numerical continuation procedures. Fixed node times will circumvent this instability but this does not allow computation of the unknown orbital period of the solution. A possible solution might be to only vary the final node time. It remains to be seen how such a collocation scheme will produce a solution with an equidistributed error.
Extend TUDAT with implicit integration	One of the bottlenecks that prevents near-instant computation of l.p.o families is the use of the RK7(8) integrator in the verification procedure. Replacing the RK(7)8 integrator with an integration procedure based upon polynomial interpolation will significantly reduce the computational load of l.p.o family construction. In combination with a higher order node placement strategy, near-instant construction of l.p.o families might be achieved [29].
Higher order error estimation method	Boor's error control method does not always equidistribute the truncation error over the segments according to the desired constraints listed in Table A.4. A higher order error estimation method may solve this problem at the expense of increased computational cost.
Bifurcation detection via Broucke stability diagram	Bifurcations in the periodic solution families can be detected in a straightforward manner by analysis of monodromy eigensystem. However, determining the type of bifurcation is more cumbersome process that requires manual inspection of the eigenvalues. The Broucke stability diagram is a method for automatic detection and classification of bifurcations without the need for analysis of the monodromy eigenvalues [16, 37].

G.2. Scientific recommendations

The equilibria contours and periodic solution families presented in this thesis report provide an initial understanding of the low-thrust phase space in the circular restricted Earth-Moon system. At the same time, these dynamical structures give rise to numerous questions which could not be answered within the constraints of this thesis project. These questions provide opportunities for new research efforts and will be discussed in the remainder of this Section.

Investigate l.p.o families at large acceleration values

In, [1], equilibria contours have been investigated for low-thrust acceleration magnitudes that are unattainable for state-of-the-art low-thrust propulsion technology. However, these equilibria are positioned in close proximity to the moon which could be interesting for a variety of space missions. Studying the periodic solutions and invariant manifolds emanating from these equilibria might result in novel mission geometries for the distant future.

Analytical l.p.o approximation

Approximate solutions for libration point orbits are usually obtained via analytical expressions. These expressions exist for natural libration point orbits [31], solar-sail assisted libration point orbits [13], and even low-thrust libration point orbits [27, 32]. The common restriction of these methods is that they can only generate periodic solutions that emanate from equilibria located on the x-axis of the synodic frame. Literature suggests that an analytical expression for off-axis low-thrust libration point orbits exists [1] but this expression has not been published in literature. Deriving such an expression could allow the construction of low-thrust Halo orbits.

Investigate spatial periodic solutions in the CR3BP-LT

Results in Chapter 1 imply that Halo, Axial and vertical-Lyapunov families exist. These orbits provide an exciting topic for future research efforts. The current implementation of the two-level targeter and numerical continuation procedure are able to compute spatial libration point orbits. This cannot be said for the current implementation of the equilibria root-finding procedure and the Floquet targeter.

Investigate hyperbolic invariant manifolds emanating from low-thrust periodic solutions

The results of this thesis project show that some low-thrust periodic solution have a higher rate of hyperbolic unwinding behaviour compared to the ballistic periodic solutions. Investigating the hyperbolic flow emanating from low-thrust periodic solutions might lead to identification of novel transfer solutions in the Earth-Moon system.

This page is intentionally left blank.

Bibliography

The list below is an exhaustive list of references for the sources used the appendices A-G. A reference list for the citations in Chapter 1 can be found at the end of Chapter itself

[1] D. Folta A. Cox, K. Howell. Dynamical structures in a low-thrust, multi-body model with applications to trajectory design. *Celestial Mechanics and Dynamical Astronomy*, 131(:12), 2019. - ISBN: 0923-2958.

[2] F. Saleri A. Quarteroni, R. Sacco. *Numerical Mathematics*. Springer-Verlag, Berlin, 2001. - ISBN 978-0-387-95116-4.

[3] K. Atkinson. *An Introduction To Numerical Analysis*. John Wiley & Sons, Canada, 1978. - ISBN: 0-471-62489-6.

[4] R. Wilson B. Marchand, K. Howell. An improved corrections process for constrained trajectory design in the n-body problem. *Journal of Spacecraft and Rockets*, 44(4), 2007. - eISSN: 1533-6794.

[5] J. Betts. Survey of numerical methods for trajectory optimization. *Journal of Guidance, Control and Dynamics*, 21(2), 1998.

[6] A. Björk. *Numerical methods for least squares problems*. Society for Industrial and Applied Mathematics, Philadelphia, 1998. -ISBN 0-89871-360-9.

[7] K. Howell C. York. A two-level differential corrections algorithm for low-thrust spacecraft trajectory targeting. In *Spaceflight Mechanics Meeting*, volume 168 of *Advances in Astronautical Sciences*, 2019. - ISBN: 978-0-87703-660-9.

[8] T. Pavlak D. Grebow. Mcoll: Monte collocation trajectory design tool. In *Astrodynamics Specialist Conference 2017*, volume 162 of *Advances in the Astronautical Sciences Series*, pages 677–696, 2017. - ISBN: 978-0-87703-646-3.

[9] C. de Boor. Good approximation by splines with variable knots. In Springer-Verlag, editor, *Spline Functions and Approximation Theory*, pages 57–72, Basel, 1973. - ISBN: 978-3-0348-5979-0.

[10] H. Keller D. Dichmann-J. Galan-Vioque A. Vanderbrauwhede E. Doedel, R. Paffenroth. Continuation of periodic solutions in conservative systems with application to the 3-body problem. *International Journal of Bifurcation and Chaos,*, 13(6):1353–1381, jan 2003.

[11] G. Wanner E. Hairer, S. Nørset. *Solving Ordinary Differential Equations I*. Springer-Verlag, Berlin, 1993. - ISBN: 3-540-56670-8.

[12] K. Kumar et al. Tudat: a modular and robust astrodynamics toolbox. In *Fifth ICATT, International Conference on Astrodynamics Tools and Techniques*, pages 1–8, 2012.

[13] C. McInnes H. Baoyin. Solar sail halo orbits at the sun-earth artificial l1 point. *Celestial Mechanics and Dynamical Astronomy*, 94(2), 2006. - ISSN: 0923-2958.

[14] J. Herman. *Improved Collocation Methods to Optimize Low- rust, Low-Energy Transfers in the Earth-Moon System*. PhD thesis, University of Colorado, Boulder, 2015.

[15] K. Howell. Three-dimensional, periodic, 'halo' orbits. *Celestial Mechanics & Dynamical Astronomy*, 32 (1):51–73, 1984. - ISSN: 0923-2958.

[16] K. Howell and E. Campbell. Three-dimensional periodic solutions that bifurcate from halo families in the circular restricted three-body problem. In *AIAA/AAS Astrodynamics Specialist Conference*, 1998.

[17] M. Macdonald J. Heiligers, J. Parker. Extension of earth-moon libration point orbits with solar sail propulsion. *Astrophysics and Space Science*, 361(241), jun 2016.

[18] C. Moler J. Lyness. Numerical differentiation of analytic functions. *SIAM Journal on Numerical Analysis*, 4(2):202–210, 1967. - ISSN: 0036-1429.

[19] J. Alonso J. Martins, P. Sturda. The complex-step derivative approximation. *ACM Transactions on Mathematical Software*, 29(3), sep 2003. - ISSN: 0098-3500.

[20] W. Rheinboldt J. Ortega. *Iterative Solution of Nonlinear Equations in Several Variables*. Academic Press, 1970. - ISBN: 1483244334.

[21] B. Marchand K. Howell. Natural and non-natural spacecraft formations near the l1 and l2 libration points in the sun–earth/moon ephemeris system. *Dynamical Systems: An International Journal*, 201(1):149–173, mar 2005.

[22] H. Pernicka K. Howell. Numerical determination of lissajous trajectories in the restricted three-body problem. *Celestial Mechanics and Dynamical Astronomy*, 41(1):107–124, 1978. - ISSN: 0923-2958.

[23] H. Keller. *Numerical Methods for Two-Point Boundary-Value Problems*. Dover, New York, 1992. -ISBN 13: 9780486669250.

[24] C. Kelley. *Solving Nonlinear Equations with Newton's method*. Society for Industrial and Applied Mathematics, Philadelphia, 2003. - ISBN: 0-89871-546-6.

[25] K. Langemeijer. Connecting hyperbolic invariant manifolds at variations of the poincaré section orientation. Master's thesis, TU Delft, 2018.

[26] L. Massarweh. Linear stability and bifurcations of periodic lagrange orbits in the elliptic restricted 3-body problem. Master's thesis, Delft University of Technology, 2016.

[27] M. Morimoto. Periodic orbits with low-thrust propulsion in the restricted three-body problem. *Journal of Guidance, Control and Dynamics*, 29(5), 2006. - eISSN: 1533-3884.

[28] E. Gill O. Montenbruck. *Satellite Orbits: Models, Methods and Applications*. Springer-Verlag, Berlin, 2000. - ISBN: 978-3540672807.

[29] A. Humphries A. Lemus-Rodríguez E. Oldeman R. Calleja, E. Doedel. Boundary-value problem formulations for computing invariant manifolds and connecting orbits in the circular restricted three body problem. *Celestial Mechanics and Dynamical Astronomy*, 114(12):77–106, 2012. - ISSN: 0923-2958.

[30] S. Kim R. Pasupathy. The stochastic root-finding problem: Overview, solutions, and open questions. *ACM Transactions on Modeling and Computer Simulation*, 21, 2011. - ISSN: 1049-3301.

[31] D. Richardson. Analytic construction of periodic orbits about the collinear points. *Celestial Mechanics and Dynamical Astronomy*, 22:241–253, 1980. - ISSN: 0008-8714/80/0223-0241.

[32] C. McInnes S. Baig. Artificial halo orbits for low-thrust propulsion spacecraft. *Celestial Mechanics and Dynamical Astronomy*, 104:321–355, 2000. ISSN: 0923-2958.

[33] L. Petzold U. Ascher. *Computer Methods For Ordinary Differential Equations and Differential-Algebraic Equations*. Society for Industrial and Applied Mathematics, Philadelphia, 1998. -ISBN: 0-89871-412-5.

[34] S. Ross W. Koon. M. Lo, J. Marsden. *Dynamical Systems, the Three-Body Problem and Space Mission Design*. Springer-Verlag, New York, 2007. - ISBN: 978-0387495156.

[35] K. Wakker. *Fundamentals of Astrodynamics*. TU Delft Library, 2015. - ISBN: 978-94-6186-419-2.

[36] P. Zhou. *Numerical Analysis of Electromagnetic Fields*. Springer-Verlag, Berlin, 1993. - ISBN: 978-3-642-50321-4.

[37] E. Zimovan-Spreem, K. Howell, and D. Davis. Near rectilinear halo orbits and their application in cislunar space. In *3rd International Academy of Astronautics Conference on Dynamics and Control of Space Systems*, Moscow, Russia, 2017.